NATIONAL AERONAUTICS AND SPACE ADMINISTRATION

Space Programs Summary 37-64, Vol. III

Supporting Research and Advanced Development

For the Period June 1 to July 31, 1970

JET PROPULSION LABORATORY
CALIFORNIA INSTITUTE OF TECHNOLOGY
PASADENA, CALIFORNIA

August 31, 1970

NATIONAL AERONAUTICS AND SPACE ADMINISTRATION

Space Programs Summary 37-64, Vol. III

Supporting Research and Advanced Development

For the Period June 1 to July 31, 1970

JET PROPULSION LABORATORY
CALIFORNIA INSTITUTE OF TECHNOLOGY
PASADENA, CALIFORNIA

August 31, 1970

SPACE PROGRAMS SUMMARY 37-64, VOL. III

Prepared Under Contract No. NAS 7-100
National Aeronautics and Space Administration

Preface

The Space Programs Summary is a multivolume, bimonthly publication that presents a review of technical information resulting from current engineering and scientific work performed, or managed, by the Jet Propulsion Laboratory for the National Aeronautics and Space Administration. The Space Programs Summary is currently composed of four volumes:

Vol. I. *Flight Projects* (Unclassified)
Vol. II. *The Deep Space Network* (Unclassified)
Vol. III. *Supporting Research and Advanced Development* (Unclassified)
Vol. IV. *Flight Projects and Supporting Research and Advanced Development* (Confidential)

Contents

PLANS AND PROGRAMS

PROJECT ENGINEERING DIVISION

DATA SYSTEM DIVISION

TELECOMMUNICATIONS DIVISION

Contents (contd)

GUIDANCE AND CONTROL DIVISION

ENGINEERING MECHANICS DIVISION

Contents (contd)

ASTRIONICS DIVISION

PROPULSION DIVISION

Contents (contd)

MISSION ANALYSIS DIVISION

I. Advanced Studies

PLANS AND PROGRAMS

A. Mission Objectives for a Lunar Roving Vehicle, *R. G. Brereton*

1. Introduction

There are two ways to define the objectives for roving vehicles in lunar research. The first way involves fundamental ideas about the origin of life or the solar system in terms of lunar research. The second is empirical, deriving rover objectives from terrestrial field geology experience. In other words, where surface mobile systems or traverses have been required for terrestrial exploration, like systems may be required for lunar exploration, and there should be a definite correlation between the useful types of experiments and instruments. The first way is deductive in nature while the second is inductive. Both ways should lead to compatible results.

We do not now have a complete scientific rationale for lunar exploration, especially one that takes account of *Apollo 11* and *12* results. Therefore, rover objectives must be defined empirically and we must be prepared to do some basic thinking about lunar roving vehicles (LRVs) in order to understand what special contribution an LRV can make to lunar science and the penalties inherent in not developing and utilizing the rover concept to its full potential. Using this empirical approach, it should be possible to define several missions for LRVs in terms of terrestrial experience and then using these missions to define specific scientific experiments, applicable instruments, and an appropriate *modus operandi.* It should be realized that there probably isn't a single set of experiments for an LRV that can provide a unique solution to a major lunar problem. Rather, the LRV must be considered as an adaptive tool that can be variously instrumented to provide certain kinds of data for furthering the whole scientific picture of the moon—as it is today, how it was, and how it evolved.

2. Mission Objectives

Table 1 shows some of the likely objectives, which may be more appropriately called field tasks, for an LRV. These represent important uses for a properly designed

Table 1. LRV utility chart

Mission objectives or field tasks	Remarks	Experiments
Field geology	Vehicle would be expected to provide the on-site capability of a field geologist for both reconnaissance and detailed area investigation. Experiments (1), (2), and (3) would be required for all missions of this type, while sample return missions would require the addition of a fourth experiment.	(1) Eyeball-type imaging (a) Panoramic (b) Textural (2) Limited *in situ* sample analysis (a) Mineral (b) Elemental (3) Sample storage
Traverse geophysics	Vehicle would serve as an automated mobile platform for crustal geophysical studies. Both local and regional investigations may be required. It is not likely that all of these experiments will be included in a particular mission, but rather that select ones would be used with the field geology package to investigate specific science questions.	(1) Gravity survey (2) Magnetic survey (3) Seismic survey (4) Electrical survey (5) Radioactivity survey
Field assistant	To serve as a mobility aid, shelter, and pack-vehicle for manned operations.	As specified by mission objectives.
Instrument deployment	To place scientific instruments or packages in areas that cannot otherwise be reached. This would include the deployment of sensors, remote geophysical monitor packages, or even a series of charges for an active seismic experiment.	As specified by mission objectives.
Search	To provide a means for investigating the nooks and crannies of the lunar surface in the search for evidence of lunar life, degassing, or other phenomena.	Various

and instrumented LRV in a lunar exploration program. In fact, without some method of accomplishing these tasks, our knowledge of the moon cannot approach our knowledge of the earth and answers to the major scientific questions that have been proposed will not be forthcoming. These tasks have been performed by field investigators on earth and they must be performed by field investigation on the moon. The capability to automate a vehicle to accomplish these tasks represents a tool for lunar research, and is a way of getting at lunar scientific objectives analogous to the operational methods of terrestrial geologists and geophysicists.

a. Field geology. Our terrestrial experience indicates that one of the principal tasks for an LRV will be in substituting for the field geologist. The degree of success that can be hoped for in this type of mission will depend on the mobility, sensing, sample handling, and other functions of the field geologist that can be automated to a remotely controlled vehicle. The LRV will be expected to provide eyes, hands, and mobility for a crew of geologists in a control center on earth. We have not yet demonstrated that an LRV can do this task; Therefore, it must be demonstrated by laboratory and field testing that an LRV can be a useful tool for lunar field geology investigations.

A field test (SPS 37-55, Vol. III, pp. 258–263) to determine the practicability and examine some of the operating procedures and scientific instruments for doing geology from an automated vehicle was conducted in the late fall of 1968. The test vehicle was a camper–truck that was capable of limited mobility over rough terrain. The test vehicle was instrumented with an array of TV cameras and sample acquisition instruments that could be operated remotely from inside the vehicle by the geoscience observer. For the field test, the geoscience observer was enclosed in the test vehicle where he observed the geology and carried out the sampling operations remotely. It was assumed that the vehicle was on a mission of geological reconnaissance on an alien planetary surface with all the data and observations actually being seen in a control center on earth by a science or payload performance analysis and control team.

The conclusions from the field test were very favorable, and it would seem that a roving vehicle can serve many of the functions of a field geologist. One important result from the field program was that it provided information on requirements for the imaging system, surface-sampling systems, and sample-storage system for an automated LRV (SPS 37-60, Vol. III, pp. 1–3). Further laboratory and field tests are desirable.

b. Traverse geophysics. Traverse geophysics has a special place in the lunar exploration program. It can provide data on problems amenable to solution only by the combined techniques of surface mobility and geophysical instrumentation. Traverse geophysics using automated LRV is a powerful tool for providing data on the subsurface of the moon. When these data are correlated with lunar geology and multiple working hypotheses, they can provide an informative picture of the possible structure and processes of the lunar crust. The choice of scientific instruments for a traverse task is quite large due to both the diversification of geophysical techniques and instrumentation through the effect of space-age technology and the revolutionary growth of science that has taken place since 1940.

Several practical geophysical experiments for an automated traverse rover have been discussed in SPS 37-56, Vol. III, pp. 213–216 and SPS 37-62, Vol. III, pp. 1–5. Further LRV geophysical applications are discussed in SPS 37-51, Vol. III, pp. 335–341; SPS 37-57, Vol. III, pp. 1–6; and SPS 37-61, Vol. III, pp. 1–4.

Instruments to provide the geophysical traverse data can be assembled; however, system and field tests to determine the practicability of conducting these types of experiments on an automated vehicle are required. There is no question that the active seismic experiment described in SPS 37-56, Vol. III can be built; however, the practicability and technique of operating it as a part of an LRV system needs to be studied in both the laboratory and the field. The same is true for the other traverse geophysics experiments—field and laboratory system tests should be carried out.

c. Manned vehicles. A small LRV is presently being built by NASA to serve as an astronaut lunar mobility aid. In its initial concept, the vehicle weighs about 400 lb and is capable of carrying approximately 1000 lb of extra equipment including astronauts, scientific experiments, and lunar rock samples. Future lunar missions involving a man as the exploration agent are expected to require a more advanced vehicle to provide not only the basic transport capability of the present LRV, but also a shelter for extended traverse missions.

The requirements for an LRV to carry out tasks of instrument deployment and search are shown in Table 1 and have been discussed in other articles (SPS 37-61, Vol. III); therefore, these missions are not described further here.

3. Conclusions

The need for LRVs in a lunar science program has been here established on the bases of function, utility, or mission requirements, rather than from fundamental science objectives. The lunar science program will be incomplete, i.e., unable to investigate many critical aspects of the lunar surface and interior, without such vehicles. Field geologists and traverse geophysical experiments have been required to investigate the terrestrial environment and they will be required to answer many fundamental questions about the moon. To determine the feasibility of such an exploration system is an objective for future field tests.

The techniques and procedures to be developed for automated lunar exploration are a step towards automated surface operations on all the terrestrial planets. In the same vein, sample return missions from the terrestrial planets will not be as practical as they have been from the moon; therefore, special instrumentation for *in situ* analysis of mineralogy, texture, age, etc., of surface materials will be required.

II. Environmental Requirements

PROJECT ENGINEERING DIVISION

A. Multi-Phase Ammonia Water System,

C. Haudenschild

1. Introduction

In conjunction with the SR/AD Space Vehicle Design Criteria Monograph Program JPL develops monographs on various planetary environments. In the specific problem of modeling atmospheres of Jupiter and Saturn for the monographs one needs to consider the properties of the major condensible constituents—ammonia and water.

Pertinent information in references is primarily in a scattered tabular form.

In Ref. 1 Lewis makes a graphical representation of the NH_3–H_2O system from data in Refs. 2 and 3. For the production of model atmospheres it was felt that analytic expressions, in addition to a graphical display, would be very useful. So, an attempt was made to produce empirical equations relating quantities of interest displayed in Table 1. The equations give partial vapor pressure over solid NH_3, solid $(NH_3)_2H_2O$ hydrate, solid NH_3H_2O hydrate, solid H_2O, and NH_3–H_2O solution phases. In addition, along boundaries of the regions, equations for freezing curve temperatures as a function of concentration are given. Finally a phase diagram similar to Lewis's is produced, displaying the equations graphically.

Table 1. Definition of terms

Symbol	Units	Definition
T	°K	Temperature
C	$0.0 \leqq C \leqq 1.0$	Molar concentration of NH_3 in H_2O solution
P_2	Torr	H_2O vapor partial pressure
P_3	Torr	NH_3 vapor partial pressure

2. Forms Relating the Quantities of Interest

To proceed, we must choose appropriate equation forms that can be fitted to the data available and incorporate our understanding of the physics of the situation. The following forms were chosen:

In the pure solid regions of NH_3 or H_2O, equations of the form of the Clausius Clapeyron equation are chosen to relate P and T (Ref. 1):

$$\log P = \alpha - \beta/T \tag{1}$$

The constants α and β can be determined numerically from any two data points at which P and T are specified.

Forms for the hydrate regions were taken from Ref. 1. For $(NH_3)_2H_2O$ we get the equation

$$(2/3)\log P_3 + (1/3)\log P_2 = \alpha - \beta/T \tag{2}$$

Here the ratio of the coefficients of the logarithms of the pressures is the same as the ratio of NH_3 and H_2O in the hydrate—that is, two to one—and the basic form of the Clausius Clapeyron equation is retained. For NH_3H_2O the appropriate equation is

$$(1/2)\log P_2 + (1/2)\log P_3 = \alpha - \beta/T \tag{3}$$

In each hydrate region one can obtain the two constants α and β numerically from two data points, just as for the pure solid regions.

From the phase diagram displayed in Ref. 1 (p. 367) we infer that solution region equations obey:

$$\left(\frac{\partial \log P_3}{\partial \log P_2}\right)_c = \text{constant, independent of temperature} \tag{4}$$

That is, the isoconcentration lines are straight. Also, we infer that

$$\left(\frac{\partial \log P_3}{\partial \log P_2}\right)_T = -\frac{1-C}{C}, \text{ also independent of temperature.} \tag{5}$$

This matches the slope of the solution region isotherm with the slopes in the hydrate regions, at those points where the molecular number ratios are identical in the two regions. Equations were chosen which retain a Clausius Clapeyron dependence and satisfy the above requirements; namely

$$\log P_2 = \log(1-C) + A_0 + A_2C^2 - \frac{a_0 + a_2C^2}{T} \tag{6}$$

and

$$\log P_3 = \log C + B_0 + A_2(C^2 - 2C) - \frac{b_0 + a_2(C^2 - 2C)}{T} \tag{7}$$

The six constants A_0, A_2, B_0, a_0, a_2, and b_0 can be obtained numerically from appropriately chosen combinations of tabular values of C, T, $\log P_2$, and $\log P_3$.

Finally, freezing curves can be obtained by equating the solution region partial pressures to solid region ones, and eliminating the pressures. There result equations which give T as a function of C.

3. Numerical Relations Among Quantities of Interest

Table 2 lists numerical equations for regions of solid and solution phases. Partial pressures of ammonia and water are given as function of temperature or of temperature

Table 2. Solid and solution equations

Region	Data source	Form	Equation
Solid H_2O	Table 3 (underlined entries)	Eq. (1)	$\log P_2 = 10.447 - 2673.01/T$ (8)
Solid NH_3	Table 4 (underlined entries)	Eq. (1)	$\log P_3 = 10.312 - 1691.77/T$ (9)
$(NH_3)_2H_2O$	Table 2 († entries)	Eq. (2)	$(2/3)\log P_3 + (1/3)\log P_2 = 9.777 - \frac{2051.185}{T}$ (10)
NH_3H_2O	Table 5 (‡ entries)	Eq. (3)	$(1/2)\log P_2 + (1/2)\log P_3 = 9.790 - \frac{2219.28}{T}$ (11)
Solution	Table 5 (underlined entries)	Eq. (6)	$\log P_2 = \log(1 - C) + 9.488 + 1.743C^2 - \left(\frac{2406.2 + 878.192C^2}{T}\right)$ (12)
		Eq. (7)	$\log P_3 = \log C + 9.906 + 1.743(C^2 - 2C) - \left(\frac{2149.65 + 878.192(C^2 - 2C)}{T}\right)$ (13)

and concentration. The data from which the numerical coefficients in Table 2 were derived are found in Tables 3, 4, and 5.

Table 6 lists numerical freezing curves temperature equations as functions of concentration. These are formed by equating the source equation and eliminating log P_2, log P_3, or both.

4. Comparison With Data

Table 3 compares the values of log P_2 for solid H_2O from the tabular sources listed with log P_2 from Eq. (8). The largest discrepancy shown is near −20.1°C and amounts to 0.002 in log P_2.

Table 3. Vapor pressure over solid H_2O ice

Reference and page	T, °C	T, °K	P_2, torr (From Ref.)	log P_2, torr (From Ref.)	log P_2, torr (From Eq. 8)
4, 1474	−99.0	174.16	1.2×10^{-5}	−4.92	−4.901
4, 1474	−68.0	204.46	2.36×10^{-3}	−2.627	−2.627
4, 1474	−46.0	227.16	0.0481	−1.318	−1.320
4, 1474	−20.1	253.06	0.0769	−0.111	−0.116
4, 1475	0.0	273.16	4.579	0.661	0.661

Underlined entries indicate data used to obtain constants in Eq. (8).

Table 4. Vapor pressure over solid NH_3 ice

Reference and page	T, °C	T, °K	P_2, torr (From Ref.)	log P_2, torr (From Ref.)	log P_2, torr (From Eq. 8)
2, 362	−77.6	195.56	45.82	1.661	1.661
3, D-140	−79.2	193.96	38.90	1.602	1.590
2, 362	−84.4	188.76	22.36	1.367	1.349
4, D-140	−91.9	181.26	9.52	1.000	0.979
3, D-140	−109.1	164.06	1.00	0.000	0.000

Underlined entries are data used to obtain constants in Eq. (9).

Table 4 compares values of log P_3 for solid NH_3 from the tabular sources listed with log P_3 from Eq. (9). The largest discrepancy shown is near −91.9°C and amounts also to 0.02 in log P_3.

Table 5 was produced to display the accuracy of the solution and freezing curve equations. Column 1 gives the concentration considered on any particular line. Column 2 lists the tabular source from which T (°K), log P_2, and log P_3 in Cols. 3, 4, and 5 were obtained. When an S in the "remarks" column appears, we are considering the solution region and the temperature in Col. 3 is transferred to Col. 7. F denotes freezing curve; hence, T in Col. 7 is computed from the appropriate freezing curve equation. Finally, based on the values of C in Col. 1 and T in Col. 7, log P_2 and log P_3 in Cols. 8 and 9 are obtained from Eqs. (12) and (13).

The largest discrepancy in log P_3 (Cols. 5 and 9 in Table 5) in the solution region occurs at $C = 0.60$ and $T = 189.31$ and is 0.15 (a factor of 1.4). Table values for log P_2 are only given in the interval $0 \leqq C \leqq 0.2395$. The largest discrepancy in log P_2 (Cols. 4 and 8 in Table 5) in the solution region occurs at $C = 0.2181$ and $T = 316.16$ and is 0.14 (a factor of 1.4).

For points along the freezing curves, discrepancies of log P_2 and log P_3 are magnified. That is, the freezing curve temperature is used to calculate the log pressure instead of the table temperature, as in the solution region. Hence, a double error is produced. The largest discrepancy in log P_3, listed in Table 5, occurs at $C = 0.25$ and is 0.387 (a factor of 2.4). Values of log P_2 are listed in the tables at only five points along the freezing curve, all of which have $0 \leqq C \leqq 0.2$. Among these the largest discrepancy occurs at $C = 0.20$ with log P_2 0.33 below the tabular value (a factor of 2.1). One would expect relatively large discrepancies along the freezing curve in the region of $0.2 \leqq C \leqq 0.35$, because T is a very sensitive function of C there (Fig. 1). In fact, if one scans the freezing curve temperature, the largest discrepancy of 9.8°K occurs at

Table 5. Vapor pressure over NH_3–H_2O solution

C	Reference and page	T, °K (from Ref.)	log P_2, torr (from Ref.)	log P_3 (from Ref.)	Area	T, °K (See Subsection 4.)	log P_2, torr (Eq. 12)	log P_3, torr (Eq. 13)
1.00	2, 362	—	—	—	S	273.16	$-\infty$	3.508
1.00		195.56	—	1.661	F	195.59	$-\infty$	1.662
0.95		192.66	—	1.537	F	192.95	−6.818	1.544
0.95		213.16	—	2.194	S	213.16	−5.246	2.170

Table 5 (contd)

C	Reference and page	T, °K (from Ref.)	log P_2, torr (from Ref.)	log P_3 (from Ref.)	Area	T, °K (See *Subsection 4.*)	log P_2, torr (Eq. 12)	log P_3, torr (Eq. 13)
0.90	2, 362	213.16	—	2.167	S	213.16	−4.726	2.129
0.90		188.76	—	1.367	F	189.01	−6.594	1.361
0.85		184.16	—	1.155	F	183.71	−6.628	1.103
0.85		213.16	—	2.135	S	213.16	−4.341	2.074
0.812		180.16	—	0.956	Q, F	178.74†	−6.790†	0.847†
0.80		181.96	—	1.022	F	181.35	−6.463	0.931
0.80		223.16	—	2.365	S	223.16	−3.396	2.281
0.75		189.31	—	1.248	F	189.45	−5.442	1.146
0.70		223.16	—	2.245	S	223.16	−2.891	2.113
0.70		193.46	—	1.320	F	193.61	−4.831	1.190
0.6667		194.36	—	1.306	N, F	194.36	−4.603†	1.137†
0.65		194.16	—	1.240	F	194.19	−4.533	1.088
0.65		223.16	—	2.156	S	223.16	−2.677	2.010
0.60		223.16	—	2.043	S	223.16	−2.482	1.893
0.60		189.31	—	0.934	F	191.36	−4.509	0.841
0.5855		186.81	—	0.813	Q, F	189.91	−4.553	0.740
0.55		191.16	—	0.0820	F	191.77	−4.264	0.699
0.50		193.96	—	0.732	N, F	193.91‡	−3.918‡	0.609‡
0.50		243.16	—	2.278	S	243.16	−1.176	2.166
0.45		193.16	—	0.508	S	193.16	−3.796	0.386
0.45		191.31	—	0.432	F	191.76	−3.894	0.328
0.40		184.16	—	−0.174	F	185.24	−4.203	−0.178
0.35		263.16	—	2.248	S	263.16	−0.038	2.202
0.35		173.26	—	−1.046	S	174.03	−4.930	−0.995
0.346		172.86	—	−1.081	Q, F	$\underline{172.96}$‡	$\underline{-5.007}$‡	$\underline{-1.075}$‡
0.30		273.16	—	2.292	S	273.16	0.392	2.264
0.30		204.46	—	0.204	F	196.20	−3.177	−0.179
0.25	↓	227.16	—	0.806	F	217.36	−1.851	0.419
0.2395	3, 1467	273.16	0.448	2.067	S	273.16	0.476	2.036
0.2181		316.16	1.578	2.760	S	316.16	1.721	2.848
0.2054		273.16	0.477	1.916	S	273.16	0.517	1.892
0.20		241.91	−0.600	1.045	F	234.93	−0.931	0.775
0.1546	↓	273.16	0.613	1.710	S	273.16	0.571	1.646
0.15	2, 362	253.00	—	0.125	F	249.46	−0.268	0.958
0.10	2, 362	261.21	0.215	1.076	F	$\underline{261.34}$	$\underline{0.219}$	0.988
0.0987	3, 1467	333.16	2.132	2.575	S	333.16	2.212	2.616
0.0964		273.16	0.724	1.394	S	273.16	0.622	1.291
0.05		267.81	0.466	0.868	F	270.87	0.578	0.815
0.0408		333.16	2.159	2.136	S	$\underline{333.16}$	2.246	$\underline{2.136}$
0.00	↓	—	—	—	S	373.16	3.040	−∞
0.00	2, 363	273.16	0.661	—	F	278.22	0.839	−∞

†Data used to obtain constants in Eq. (10) for $(NH_3)_2H_2O$ hydrate.

‡Data used to obtain constants in Eq. (11) for $(NH_3)H_2O$ hydrate.

Underlined entries indicate data used to obtain constants in Eqs. (12) and (13) for solution region.

S = point of consideration lies in solution region.

F = point of consideration lies on freezing curve.

Q = quadrupole point.

N = nose of freezing curve where the H_2O and NH_3 number ratio are equal in the solution and adjacent hydrate regions.

Table 6. Freezing curve equations

Region of concentration	Quantities eliminated	Source equations	Freezing curves
$0.812 \leqq C \leqq 1.00$ Solid NH_3	$\log P_3$	(9), (13)	$T = \frac{457.88 + 878.192 (C^2 - 2C)}{\log C - 0.406 + 1.743 (C^2 - 2C)} \qquad (14)$
$0.5855 \leqq C \leqq 0.812$ $(NH_3)_2H_2O$	$\log P_2$ $\log P_3$	(10), (12), (13)	$T = \frac{183.982 - 1170.92C + 878.192C^2}{(1/3) \log [C^2 (1 - C)] - 0.01033 - 2.324C + 1.743C^2} \qquad (15)$
$0.346 \leqq C \leqq 0.5855$ NH_3H_2O	$\log P_2$ $\log P_3$	(11), (12), (13)	$T = \frac{117.29 + 1756.384 (C^2 - C)}{\log [-(C^2 - C)] - 0.186 + 3.486 (C^2 - C)} \qquad (16)$
$0.0 \leqq C \leqq 0.346$ Solid H_2O	$\log P_2$	(8), (12)	$T = \frac{-266.81 + 878.192C^2}{\log (1 - C) - 0.959 + 1.743C^2} \qquad (17)$

$C = 0.25$. The next largest freezing curve discrepancies occur at the quadrupole points: at $C = 0.5855$, T is 3°K below table values and at $C = 0.812$, T is 1.4°K below table value. However, the $\log P_3$ values remain within 0.11 of the tabular values there.

A phase diagram of the NH_3–H_2O system was constructed (Fig. 1) for comparison with the phase diagram from Ref. 1. Lines of constant concentration are straight and range from $0.01 \leqq C \leqq 0.999$. Isothermal curves range from $T = -100°C$ to $T = +40°C$. Equations (12) and (13) were used to plot the solution region. The freezing curves (Eqs. 14 to 17) were used to plot the solid–solution boundaries. The lines separating two solid phases are found by equating two adjacent solid pressure equations and finding the ratio of $\log P_2$ to $\log P_3$.

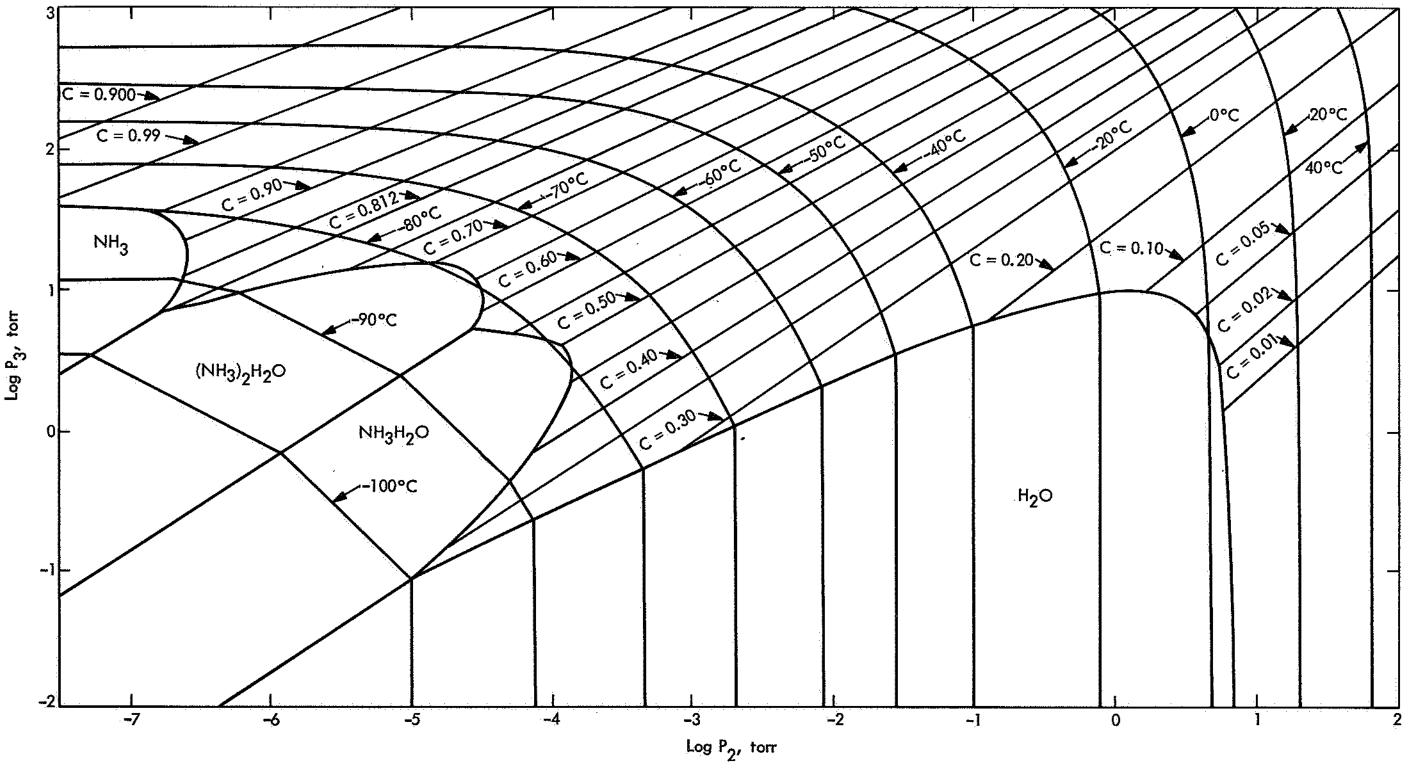

Fig. 1. Phase diagram for the NH_3–H_2O system prepared from Eqs. (8) through (17)

5. Conclusions

Empirical equations produced for all regions agree remarkably well with the table values. Discrepancies over the entire region shown in Fig. 1 are within a factor of about 2.5, with the poorest fit occurring along the freezing curve in the vicinity of $C \simeq 0.25$. Qualitatively the results agree with those of Lewis (Ref. 1), who employed graphical representations of the NH_3–H_2O system rather than analytic ones such as those discussed above. It appears likely that much better fits cannot be obtained without more data and more complicated relations among the quantities of interest.

The relations derived enable one to predict cloud composition and temperature of formation in a model atmosphere containing ammonia and water required for space vehicle design criteria. In particular, the equations were used in preparation of the Jupiter and Saturn environmental design criteria monograph atmospheric models.[1]

---

[1] Divine, T. N., *The Planet Jupiter (1970)*, Monograph to be published by National Aeronautics and Space Administration, Washington, D.C.

References

1. Lewis, J. S., "The Clouds of Jupiter and the NH_3–H_2O and NH_3–H_2S System," *Icarus*, Vol. 10, No. 3, 1969, pp. 365–378.
2. *International Critical Tables*, Vol. 3. Edited by F. W. Washburn. McGraw-Hill Book Co., New York, 1928.
3. *Handbook of Chemistry and Physics*, (50th Ed.), Chemical Rubber Pub. Co., Cleveland, Ohio, 1969.
4. *Handbook of Chemistry*, (Rev. 10th Ed.). Edited by N. A. Lange. McGraw-Hill Book Co., New York, 1967.

III. Computation and Analysis

DATA SYSTEM DIVISION

A. Some Mathematical and Computational Properties for the Incomplete Gamma Functions, *E. W. Ng*

It has been pointed out that the need for computation of the incomplete gamma functions has recently arisen, both at JPL and elsewhere.[1] Applications include stochastic processes in structural mechanics, probability calculations in statistics, and study of droplet size distribution in material science. Several well-known functions can be identified as special cases of the incomplete gamma functions, examples being given subsequently.

In the following, we first define the functions and express them in various forms that have been brought up in applications. We shall summarize the important properties of these functions and discuss an algorithm, which we shall implement for the use of a general-purpose program. Throughout this article we shall adhere to the notations used in the NBS Handbook of Mathematical Functions (Ref. 1).

$$\gamma(a,x) = \int_0^x t^{a-1} e^{-t}\, dt \qquad R(a) > 0 \tag{1}$$

$$\begin{aligned}\Gamma(a,x) &= \int_x^\infty t^{a-1} e^{-t}\, dt \\ &= \Gamma(a) - \gamma(a,x)\end{aligned} \tag{2}$$

$$P(a,x) = \frac{\gamma(a,x)}{\Gamma(a)} \tag{3}$$

$$I(u,p) = P(p+1, u\sqrt{p+1}) \tag{4}$$

and

$$Q(x^2/\nu) = \frac{\Gamma(\nu/2, x^2/2)}{\Gamma(\nu/2)} \tag{5}$$

Q is known as the chi-square probability function. The incomplete gamma functions have also appeared in the literature as

$$\gamma(a,x) = x^a \operatorname{cosec} \pi a \int_0^\pi e^{x\cos\theta} \cos(a\theta + \sin\theta)\, d\theta \qquad a \neq 1, 2, \cdots, \tag{6}$$

$$= x^{a/2} \int_0^\infty e^{-t}\, t^{(a/2)-1} J_a(2\sqrt{xt})\, dt \qquad R(a) > 0 \tag{7}$$

---

[1] Private communications from J. Yang and R. Kushida of JPL, W. J. Cody of the Argonne National Laboratory, and H. Kuki of the University of Chicago.

$$\Gamma(a,x) = \frac{2x^{a/2} e^{-x}}{\Gamma(1-a)} \int_0^\infty e^{-t} t^{-a/2} K_a (2\sqrt{xt})\, dt$$

$$R(a) < 1 \qquad (8)$$

Various well-known special functions are particular cases of the incomplete gamma functions (Ref. 2). For example,

$$\Gamma(0,x) = E_1(x) \qquad (9)$$

$$\gamma(\tfrac{1}{2}, x) = \sqrt{\pi}\, \mathrm{erf}(s) \qquad x = s^2 \qquad (10)$$

$$\Gamma(n+1, x) = n!\, e^{-x} e_n(x) \qquad (11)$$

$$\Gamma(1-n, x) = x^{1-n} E_n(x) \qquad (12)$$

where E_n, erf and e_n are the exponential integrals, the error function, and the truncated exponential, respectively. γ and Γ, in turn, are special cases of the confluent hypergeometric functions.

$$\gamma(a,x) = \frac{x^a}{a} e^{-x} {}_1F_1(1; a+1; x) \qquad (13)$$

$$\Gamma(a,x) = x^a e^{-x} U(1; a+1; x) \qquad (14)$$

The following properties are useful for the computational problem.

$$\gamma(a,x) = x^a e^{-x} \sum_{n=0}^{\infty} \frac{x^n}{(a)_{n+1}}$$

$$(a)_0 = 1, (a)_n = a(a+1), \cdots, (a+n-1) \qquad (15)$$

which is just a trivial re-arrangement of Eq. (13).

$$\Gamma(a,x) \approx x^{a-1} e^{-x} \sum_k \frac{(a-1)_k}{x^k} \qquad \text{for large } x \qquad (16)$$

$$\Gamma(a,x) = x^a e^{-x} \left[\frac{1}{x+} \frac{1-a}{1+} \frac{1}{x+} \frac{2-a}{1+} \frac{2}{x+} \cdots \right]$$

$$x > 0, a \text{ finite} \qquad (17)$$

Recently, Luke (Ref. 3) derived rational expansion for the incomplete gamma function

$$H(\nu, z) = {}_1F_1(1; \nu+1; -z)$$

He obtains an approximation of the form

$$H(\nu, z) = \left[\frac{A_n(\nu, z)}{B_n(\nu, z)} \right] + V_n(\nu, z) \qquad (18)$$

$$A_n(\nu, z) = \frac{z^n}{(n+\nu+1)_n} \sum_{k=0}^{n} \frac{(-n)_k (n+\nu+1) k}{(\nu+1)_k k!} \qquad (19)$$

$$x\, {}_3F_1 \left(\begin{matrix} -n+k, n+\nu+k+1, 1 \\ k+1 \end{matrix} \,\middle|\, -\frac{1}{z} \right)$$

$$B_n(\nu, z) = {}_1F_1(-n; -2n-\nu; z) \qquad (20)$$

where both A_n and B_n satisfy a recurrence relation of the form

$$A_{n+1} = \left\{ 1 + \frac{\nu z}{(2n+\nu)(2n+\nu+2)} \right\} A_n + \frac{n(n+\nu) z^2}{(2n+\nu-1)(2n+\nu)^2(2n+\nu+1)} A_{n-1} \qquad (21)$$

and $V_n(\nu, z)$ is an error term given as

$$V_n(\nu, z) = \mathcal{C}_n [1 + 0(n^{-3})] \qquad (22)$$

where $\mathcal{C}_n$ is a given coefficient depending on n. Luke presents similar rational expansion for $\Gamma(\nu, z)$.

Still another method of computation of these functions can be derived based on the analyses of Gautschi (Ref. 4) and Olver (Ref. 5). Consider the function $P(a, x)$ defined in Eq. (3). Integration by parts yields

$$P(a,x) = P(a-1, x) - \frac{a^{-1} e^{-x}}{\Gamma(a)} \qquad (23)$$

which, by elimination of the inhomogeneous term, can be expressed as

$$aP(a+1, x) - (x+a) P(a,x) + xP(a-1, x) = 0 \qquad (24)$$

or, more generally, as

$$(a+n) Y_{n+1} - (x+a+n) Y_n + xY_{n-1} = 0$$

$$n - 1, 2, 3 \cdots \qquad (25)$$

Equation (25) is obviously solved by the two linearly independent solutions

$$Y_n = P(a+n,x)$$

and

$$\widetilde{Y}_n = \widetilde{P}(a+n,x) = 1 - P(a+n,x)$$

and as a second-order difference equation, can be computed by any version of Miller's algorithm (Ref. 5, p. 121). In the following, we shall discuss one version of such an algorithm. Consider Eq. (25), which is an infinite system of linear algebraic equations. From Eq. (15), it is obvious that

$$\lim_{n\to\infty} Y_n = 0$$

Therefore, for some large N, we may approximate Eq. (25) by a finite system of N equations. Furthermore, it can be shown that for

$$\lambda_m = \frac{(a)_m}{m!} \qquad \sum_{m=0}^{\infty} \lambda_m Y_m = \frac{x^a}{\Gamma(a+1)} \tag{26}$$

Thus, we can approximate our solutions $Y_0, Y_1, \cdots Y_{N-1}$ by solving the linear system

---

$$\left.\begin{array}{rl} (a+n)Y_{n+1} - (x+a+n)Y_n + xY_{n-1} = 0 & n = 1,2,\cdots,N-1 \\ Y_N = 0 & \displaystyle\sum_{m=0}^{N-1} \lambda_m Y_m = \frac{x^a}{\Gamma(a+1)} \end{array}\right\} \tag{27}$$

In the above, we have summarized all the important properties that have been used or are of potential use for the computation of the incomplete gamma functions. Naturally, any one mathematical expression cannot be optimal for all situations. For example, Eq. (15) is extremely efficient when x is small compared to a, and Eq. (24) is convenient for computing a sequence of values $P(a+n,x)$. Here we shall mention a few considerations for a general-purpose program. First, for a given parameter a, both γ and Γ range in values from 0 to $\Gamma(a)$, and this can be a very wide range for large a, to the extent that overflow problems may occur. The normalized functions P and $\widetilde{P}$ avoid this predicament. On the other hand, given a program for P and $\widetilde{P}$, one needs a program for $\Gamma(a)$ if interested in γ and Γ. Second, to avoid loss of significance, one should compute γ for x small compared to a, and Γ for the other case. Third, consideration must be given as to whether one is interested in computing sequences $P(a_n, x)$ or $P(a, x_n)$. Fourth, the trade-off between efficiency and computer storage requirement must be taken into account (e.g., should one reasonable algorithm be used for all values of a and x, or should a combination of algorithms for different ranges of values?) Based on the above considerations, we shall briefly mention the merits and demerits of the various expressions for the use of computation. As mentioned above, Eq. (15) is most suitable for x/a small, and Eqs. (16) and (17) for a/x small. Luke's rational expansion is quite easy to implement, but it is not fast convergent. For example, for $\Gamma(a,x)$, the order of convergence is even worse than that indicated by Eq. (22). Furthermore, it is not clear that computation of the rational function via recurrences like Eq. (21) is always stable. The last method described is most suitable for the computation of a sequence $P(a+n,x)$, $n = 1, 2, 3, \cdots$,. In using this method, three types of errors need be considered. There are truncation errors in approximating the Infinite Sequence (25) by a finite one and in replacing the Series (26) by a finite sum. There is also round-off error in the computation of Eq. (27).

In summary, we are currently investigating all the above mathematical properties or processes in an attempt to achieve an optimal algorithm for the implementation of a general-purpose computer program. Results of these investigations will be reported in the near future.

References

1. *Handbook of Mathematical Functions with Formulas, Graphs, and Mathematical Tables.* Edited by M. Abramowitz and I. Stegun. Applied Mathematics Series 55, U.S. Government Printing Office, Washington, 1964.

2. Magnus, W., and Oberhettinger, F., *Formulas and Theorems for the Special Functions of Mathematical Physics.* Springer-Verlag, Berlin, 1966.

3. Luke, Y. L., "The Special Functions and Their Approximations," *Math. Sci. Eng.*, Vol. 53-II, 1969.

4. Gautschi, W., "Computational Aspects of Three-Term Recurrences," *SIAM Rev.*, Vol. 9, pp. 24–82, 1969.

5. Olver, F. W. J., "Numerical Solution of Second-Order Linear Difference Equations," *NBS J. Res., Math. Sci.*, Vol. 71B, pp. 111–129, 1967.

B. Chebyshev Polynomial Expansions of Emden Functions, *C. J. Devine and E. W. Ng*

1. Introduction

Traditionally, Emden functions arose from astrophysical problems in the structure of stars and planets (Refs. 1, 2, and 3). They are defined as solutions of the Lane–Emden equation

$$\frac{d^2y}{dx^2} + \frac{2}{x}\frac{dy}{dx} + y^\nu = 0 \qquad (1)$$

subject to the initial conditions that at

$$x = 0, \qquad y = 1, \qquad \frac{dy}{dx} = 0$$

Essentially, these functions are used in two ways in problems of applications. First, a function y_ν for some parameter ν corresponding to Eq. (1) is used to describe the temperature or pressure variation of some region in a star or planet. Second, they appear as given functions in differential equations describing the density and mass variation in stars:

$$\frac{d^2z}{dx^2} + \frac{2}{x}\frac{dz}{dx} + \nu y_\nu^{\nu-1} z = f(x)\, z \qquad (2)$$

In both cases, one most frequently needs integral and half-integral values for ν between 1 and 5. Miller and Sadler (Ref. 4) have generated values for $\nu = 1.0(0.5)5.0$ using finite difference methods, but only at evenly spaced points of x in the range $0 \leqq x \leqq x_0$, with the exception of $n = 3$ where the integration was carried to the third root.

This article will concern truncated Chebyshev polynomial approximations to the solution of Eq. (1) for values of $\nu = 1.0(0.1)4.5$, which will allow evaluation of the solution $f(x)$ at any point x in the range $0 \leqq x \leqq x_0$.

The solutions all have at least one zero at some point x_0, in the range $[0, \infty_0]$, with the value of x_0 increasing with that of ν. For $\nu = 1$ and $\nu = 5$, the equation admits of integration in terms of simple functions. With the initial conditions stated above,

$$y = \frac{\sin x}{x} \qquad \text{for } \nu = 1$$

and

$$y = \frac{1}{\sqrt{1 + (x^2/3)}} \qquad \text{for } \nu = 5$$

For illustrative purposes, Chebyshev coefficients of the polynomial approximation of $\sin x/x$ are given in this article for $\nu = 1$.

2. Method of Computation

Equation (1), with the given initial conditions, was solved by numerical integration and the integration was carried out to the first root x_0 for each value of ν. A Chebyshev polynomial was then fit to the integrated solution $f(x)$ in the range $[0, x_0]$ using the appropriate transformation to transform the interval to the range $[-1, 1]$ (Ref. 5).

If the desired accuracy was not attainable with a single polynomial approximation, a point $\bar{x}\,(0 \leqq \bar{x} \leqq x_0)$ was chosen and approximations were generated for the interval $[0, \bar{x}]$ and for the interval $[\bar{x}, x_0]$ with suitable transformations t of the independent variable x. Transformations for the interval $[0, u]$, where $u = x_0$ or $u = \bar{x}$, were of the form

$$t = 2\left(\frac{x}{u}\right)^\alpha - 1$$

where $\alpha = 2$ or $\alpha = 1$, while transformations t' for the interval $[\bar{x}, x_0]$ were of the form

$$t' = 1 - \left(\frac{2}{\beta}\right) \cdot \left(\frac{1}{x} - \frac{1}{x_0}\right)$$

where $\beta = (1/\bar{x}) - (1/x_0)$. The asymptotic nature of the solution $f(x)$ near the zero root x_0 determined the unusual nature of the transformation t'. A general-purpose program (*Fortran IV*, IBM 7094) was written to do most of the above automatically, given the desired error tolerances.

3. Sample Coefficients and Usage

The solution $f(x)$ for any point x may be generated by a subroutine (CHBPOL) available in the JPL *Fortran* V Subroutine Directory.[1] The user must consider the transformation t when calling the subroutine. For example, if a solution was desired for some $x, 0 \leqq x \leqq x_0$, a typical *Fortran* coding segment would be:

```
DIMENSION   COEF(N)
T = 2*(x/xz)**2-1.0
POLYX = CHBPOL (COEF, NDEGP1, T)
```

---

[1] *JPL Fortran V Subroutine Directory.* Edition 3.0, pp. 900–921, Apr. 1, 1970 (JPL internal document).

POLYX would then contain the value of the solution evaluated at the point x, using the transformation

$$t = 2\left(\frac{x}{x_0}\right)^2 - 1$$

Table 1 lists the Chebyshev polynomial coefficients, together with the needed transformations and the maximum error generated. The tabulated error listed in Table 1 is the result of evaluating the truncated Chebyshev polynomial for points x, $(0 \leqq x \leqq x_0)$, and considering the maximum absolute error defined by $|\Sigma\, a_r T_r(t) - f(x)|$, where $f(x)$ is the true solution and t is the appropriate transformation. Coefficients for the cases not reported will be published in a JPL Technical Report.

References

1. Menzel, D. H., et al., *Stellar Interiors.* John Wiley & Sons, Inc., New York, 1963.
2. Kovetz, A., "Slowly Rotating Polytropes," *Astrophys. J.*, Vol. 154, pp. 999–1003, 1968.
3. Lyttleton, R. A., *On the Internal Constitution of the Terrestrial Planets,* Technical Report 32-522. Jet Propulsion Laboratory, Pasadena, Calif., Sept. 21, 1963.
4. *Mathematical Tables: Volume 2. Emden Functions.* British Association for the Advancement of Science, University Press, Cambridge, 1932.
5. Clenshaw, C. W., "Chebyshev Series for Mathematical Functions," in *National Physical Laboratory Mathematical Tables: Volume 5.* Her Majesty's Stationary Office, London, 1962.

Table 1. Truncated Chebyshev polynomial coefficients for the Emden function for $\nu = 1.0(0.5)4.5$

$\nu = 1.0$

$f(x) = \sin x / x$

$0 \leqq x \leqq x_0$

$x_0 = \pi$

$t = 2\,(x/x_0)^2 - 1$

Maximum error $= 1.5^{-10}$

r	a_r
0	(00) 0.42893 09479
1	(00) −0.49547 83857
2	(−01) 0.70906 0456
3	(−02) −0.45178 277
4	(−03) 0.16294 51
5	(−05) −0.37858
6	(−07) 0.614
7	(−09) −0.7

$\nu = 1.5$

$0 \leqq x \leqq x_0$

$x_0 = 3.6537537362191 21$

$t = 2\,(x/x_0)^2 - 1$

Maximum error $= 2.331^{-10}$

r	a_r
0	(00) 0.39148 81658
1	(00) −0.48196 63052
2	(00) 0.10611 82523
3	(−01) −0.17737 8084
4	(−02) 0.23625 488
5	(−03) −0.29211 52
6	(−04) 0.30842 0
7	(−05) −0.36784
8	(−06) 0.2156
9	(−07) −0.790
10	(−07) −0.174
11	(−08) −0.99
12	(−08) −0.48
13	(−08) −0.26
14	(−08) −0.14
15	(−09) −0.8
16	(−09) −0.5
17	(−09) −0.3
18	(−09) −0.2
19	(−09) −0.1
20	(−09) −0.1

$\nu = 2.0$

$0 \leqq x \leqq x_0$

$x_0 = 4.352874595946112$

$t = 2\,(x/x_0)^2 - 1$

Maximum error $= 2.122^{-10}$

r	a_r
0	(00) 0.35235 07213
1	(00) −0.46020 55579
2	(00) 0.13780 19803
3	(−01) −0.37463 8746
4	(−02) 0.93127 658
5	(−02) −0.22106 840
6	(−03) 0.50809 76
7	(−03) −0.11413 12
8	(−04) 0.25196 5
9	(−05) −0.54880
10	(−05) 0.11824
11	(−06) −0.2525
12	(−07) 0.535
13	(−07) −0.113
14	(−08) 0.24
15	(−09) −0.5
16	(−09) 0.1

Table 1 (contd)

$\nu = 2.5$

$0 \leq x \leq x_0$

$x_0 = 5.355275459010755$

$t = 2\,(x/x_0)^2 - 1$

Maximum error $= 2.086^{-10}$

r	a_r
0	(00) 0.46309 44094
1	(00) −0.54427 47467
2	(−01) 0.59922 7281
3	(−01) 0.40293 7390
4	(−01) −0.24090 6063
5	(−02) 0.48446 285
6	(−03) 0.85811 68
7	(−03) −0.87581 86
8	(−03) 0.24351 68
9	(−05) 0.27432
10	(−04) −0.27604 9
11	(−04) 0.10256 3
12	(−06) −0.9251
13	(−06) −0.7492
14	(−06) 0.3841
15	(−07) −0.652
16	(−07) −0.160
17	(−07) 0.131
18	(−08) −0.32
19	(−09) −0.2
20	(−09) 0.4
21	(−09) −0.1

$\nu = 3.0$

$0 \leq x \leq x_0$

$x_0 = 6.896848619376899$

$t = 2\,(x/x_0) - 1$

Maximum error $= 3.196^{-10}$

r	a_r
0	(00) 0.42086 86792
1	(00) −0.53263 22023
2	(00) 0.11060 27253
3	(−01) 0.20231 5651
4	(−01) −0.29653 0115
5	(−01) 0.13401 3379
6	(−02) −0.26752 364
7	(−03) −0.68362 73
8	(−03) 0.81875 92
9	(−03) −0.34737 78
10	(−04) 0.61263 6
11	(−04) 0.22254 3
12	(−04) −0.22444 9
13	(−05) 0.89496
14	(−05) −0.13582
15	(−06) −0.6966
16	(−06) 0.6115
17	(−06) −0.2291
18	(−07) 0.288
19	(−07) 0.212
20	(−07) −0.166
21	(−08) 0.58
22	(−09) −0.6
23	(−09) −0.6
24	(−09) 0.5
25	(−09) −0.1

$\nu = 3.5$

$0 \leq x \leq x_0$

$x_0 = 9.535805344244662$

$t = 2\,(x/x_0) - 1$

Maximum error $= 3.123^{-10}$

r	a_r
0	(00) 0.37184 06549
1	(00) −0.50799 67252
2	(00) 0.16172 12608
3	(−01) −0.15271 2420
4	(−01) −0.23659 4229
5	(−01) 0.21091 5535
6	(−01) −0.10521 8311
7	(−02) 0.31466 151
8	(−04) 0.25134 0
9	(−03) −0.74279 17
10	(−03) 0.55902 15
11	(−03) −0.25358 88
12	(−04) 0.63422 1
13	(−04) 0.10700 4
14	(−04) −0.23009 6
15	(−04) 0.15107 2
16	(−05) −0.61754
17	(−05) 0.11848
18	(−06) 0.5441
19	(−06) −0.6967
20	(−06) 0.4068
21	(−06) −0.1481
22	(−07) 0.178
23	(−07) 0.214
24	(−07) −0.206
25	(−07) 0.108
26	(−08) −0.34
27	(−09) 0.1
28	(−09) 0.7
29	(−09) −0.6
30	(−09) 0.3
31	(−09) −0.1

$\nu = 4.0$

$0 \leq x \leq \bar{x}$

$\bar{x} = 2.5$

$t = 2\,(x/\bar{x}) - 1$

Maximum error $= 1.123^{-10}$

r	a_r
0	(00) 0.78366 45165
1	(00) −0.25501 94013
2	(−01) −0.19891 2183
3	(−01) 0.16736 7163
4	(−02) −0.26378 177
5	(−03) −0.33327 69
6	(−03) 0.22545 78

Table 1 (contd)

r	a_r
7	(−04) −0.32363 5
8	(−05) −0.57536
9	(−05) 0.32483
10	(−06) −0.4117
11	(−07) −0.991
12	(−07) 0.480
13	(−08) −0.52
14	(−08) −0.17
15	(−09) 0.7
16	(−09) −0.1

$\nu = 4.0$

$\bar{x} \leqq x \leqq x_0$

$\bar{x} = 2.5$

$t = 1 - (2/\beta) \cdot [(1/x) - (1/x_0)]$

$\beta = (1/\bar{x}) - (1/x_0)$

Maximum error $= 2.600^{-10}$

r	a_r
0	(00) 0.27598 91790
1	(00) −0.26356 07646
2	(−01) −0.15005 1712
3	(−02) 0.22610 425
4	(−03) 0.40143 59
5	(−04) −0.48813 3
6	(−04) −0.30141 8
7	(−05) −0.65978
8	(−06) −0.7426
9	(−06) 0.1755
10	(−06) 0.1997
11	(−06) 0.1160
12	(−07) 0.539
13	(−07) 0.213
14	(−08) 0.71
15	(−08) 0.16
16	(−09) −0.1
17	(−09) −0.4
18	(−09) −0.4
19	(−09) −0.2
20	(−09) −0.1
21	(−09) −0.1
22	(−09) −0.1

$\nu = 4.5$

$0 \leqq x \leqq \bar{x}$

$\bar{x} = \pi$

$t = 2\,(x/\bar{x}) - 1$

Maximum error $= 1.475^{-10}$

r	a_r
0	(00) 0.73576 88435
1	(00) −0.29488 18306
2	(−02) −0.29852 385
3	(−01) 0.21321 0218
4	(−02) −0.65374 936
5	(−03) 0.40226 48
6	(−03) 0.41379 10
7	(−03) −0.17254 30
8	(−04) 0.22011 6
9	(−05) 0.77785
10	(−05) −0.46108
11	(−06) 0.8757
12	(−06) 0.1175
13	(−06) −0.1202
14	(−07) 0.307
15	(−09) 0.5
16	(−08) −0.30
17	(−08) 0.10
18	(−09) −0.1
19	(−09) −0.1
20	(−10) 0

$\nu = 4.5$

$\bar{x} \leqq x \leqq x_0$

$\bar{x} = \pi$

$x_0 = 31.83646324469206$

$t = 1 - (2/\beta) \cdot [(1/x) - (1/x_0)]$

$\beta = (1/\bar{x}) - (1/x_0)$

Maximum error $= 1.919^{-10}$

r	a_r
0	(00) 0.23553 85677
1	(00) −0.22816 21290
2	(−02) −0.90116 390
3	(−02) 0.15169 975
4	(−03) 0.16325 36
5	(−04) −0.29415 0
6	(−04) −0.12187 6
7	(−05) −0.28924
8	(−06) −0.6274
9	(−07) −0.747
10	(−07) 0.435
11	(−07) 0.470
12	(−07) 0.297
13	(−07) 0.155
14	(−08) 0.71
15	(−08) 0.28
16	(−09) 0.9
17	(−09) 0.2
18	(−09) −0.1
19	(−09) −0.1
20	(−09) −0.1
21	(−09) −0.1
22	(−09) −0.1

IV. Communications Systems Research

TELECOMMUNICATIONS DIVISION

A. Coding and Synchronization Research: Performance of an All-Digital Command System Timing Loop, *J. Holmes*

1. Introduction

This article continues the analysis (SPS 37-63, Vol. III, pp. 28–34) of a digital phase-locked loop that is used on a single-channel command system (Mark I) which is being developed as part of the Thermoelectric Outer-Planet Spacecraft Project.

The previous article (SPS 37-63, Vol. III) dealt with the case in which the subcarrier was unmodulated and the transitions were instantaneous. This article extends the theory to a PN code-modulated subcarrier with "soft transitions," that is, when the transitions are linear in shape and of duration 1/16 of a subcarrier cycle (Fig. 1). This is a considerably better approximation to the transition of the filtered signal observed in the laboratory. Three aspects of performance are considered: (1) the stationary timing error variance, (2) the signal-to-noise ratio (SNR) degradation due to timing jitter and, (3) the bias due to doppler.

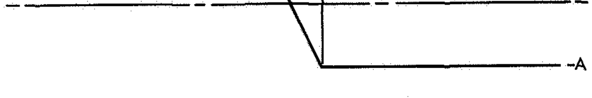

Fig. 1. Typical transition

2. Description of the Digital Phase-Locked Loop

The timing system that functions with a modulated subcarrier is diagrammed in Fig. 2. The input waveform $y(t)$ consists of the signal plus white gaussian noise with one-sided spectral density N_0. The signal is a 60-Hz square wave subcarrier biphase-modulated by a length-15 PN

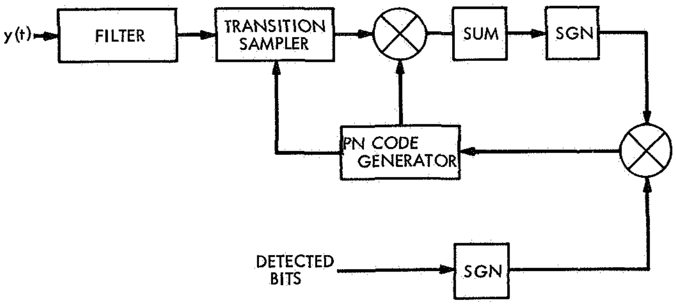

Fig. 2. Timing update or digital phase-locked loop block diagram

sequence. The filter is modeled as an ideal low-pass filter of a one-sided bandwidth of 480 Hz. It filters the input so that the input can be sampled at the Nyquist rate of 960 samples per second and then quantized. The quantization causes a negligible amount of degradation and is not considered further. The transition sampler obtains a sample at each location where the digital phase-locked loop thinks the center of the current transition occurs. Further filterings are performed digitally by the SUM block, which adds the 22 transition samples per bit from the transition sampler. [The number 22 is determined from the number of transitions in a length-15 PN sequence (Fig. 3)]. Updating of the local timing reference is accomplished by modifying the PN code generator timing every bit time by a fixed fraction Δ of a subcarrier cycle. The sign of the correction depends on the output of the SGN block. Positive slope and negative slope transitions are resolved by the PN code generator, which, by means of an internally generated PN code, produces a plus *one* when the transition is negative-going and a negative *one* if the transition is positive-going. The bit detector determines whether a *one* or a *zero* was detected and modifies the algebraic sign only if a *zero* was sent. In the analysis of the next two subsections, it is assumed that there is no drift between the received subcarrier and the locally generated subcarrier used in the PN code generator.

Fig. 3. Bit waveform: length-15 pseudonoise sequence modulating a square wave subcarrier

3. Random Walk Model

Figure 1 illustrates the model used for a typical soft transition. For this soft transition case, it is also possible to model the timing error sequence as a single-step, homogeneous Markov chain. This is due to the fact that the amplitude and, therefore, the transition probabilities vary with the states in the transition region. Again the error between the sampling point and the center of the present PN transition is defined as the "state" of the loop at the present time. Since the timing correction is a fixed amount Δ, we see that the state of the error is a random walk with a countable number of possible states. Assuming zero offset error ($\mu = 0$, SPS 37-63, Vol. III, Fig. 3, p. 29), state *one* corresponds to a positive error of Δ/2, state *minus one* to a negative error of Δ/2, and state *two* corresponds to a positive error of 3Δ/2, etc. It can be shown that the case when $\mu = 0$ corresponds to the best possible alignment of the error states. This in turn leads to the smallest timing variance. However, for small Δ ($\Delta \leqq 1/128$) the result is essentially independent of the alignment.

4. Stationary Probabilities and Variance

Before we obtain the difference equation that defines the stationary probabilities, we shall calculate the parameters of the random walk.

White noise, passed through an ideal low-pass filter of bandwidth W and then sampled at a rate $2W$ samples per second, produces independent gaussian samples. These samples have a variance of N_0W where the spectral density N_0 and the bandwidth W are both one-sided parameters. In the transition region, each sample has a signal-to-noise ratio given by

$$\mathrm{SNR}_{\mathrm{sample}} = c_k^2 \frac{A^2}{N_0 W} \tag{1}$$

where c_k is the ratio of the waveform at the sample point to the maximum value A. Since the 22 transition samples are statistically independent, the sum over one bit time has a SNR given by

$$\mathrm{SNR}_{\Delta} = c_k^2 \frac{22A^2}{N_0 W} \tag{2}$$

This is the SNR of the statistic that updates the timing. The PN code is modulated by command bits of period T_b (T_b is 15 times the subcarrier period T_{sc}) so that the bit detection SNR, assuming a perfectly synchronized digital integrate-and-dump circuit, is given by

$$\mathrm{SNR}_b = \frac{2A^2 T_b}{N_0} \tag{3}$$

This ratio neglects the small loss of signal energy due to the low-pass filter.

The probability p of being updated in the correct direction, assuming no bit errors, and given the error state is outside the transition region, is given by

$$p = \mathrm{erf}\left[\left(\frac{22A^2}{N_0 W}\right)^{1/2}\right] \tag{4}$$

However, in the transition region, the probability p_k of being updated in the correct direction is given by

$$p_k = \mathrm{erf}\left[c_k\left(\frac{22A^2}{N_0 W}\right)^{1/2}\right] \tag{5}$$

where

$$c_k = 16\Delta(2k-1), \quad \Delta = \frac{1}{32}(\tfrac{1}{2})^t, \qquad \begin{array}{l} k = 1, 2, \cdots, (32\Delta)^{-1}, \\ t = 0, 1, \cdots \end{array}$$

The probabilities of updating in the wrong direction are given by $q = 1 - p$ and $q_k = 1 - p_k$. If it is desired to take into account the effect of bit errors, let PE_k denote the bit error probability, given that the timing error is in state k. Further denote p'_k as the probability (taking into account bit errors) of reducing the timing error, given that the error state is k. Also, let q'_k denote the probability of increasing the timing error, given that the error state is k. Then

$$\left.\begin{array}{l} p'_k = (1 - PE_k)\,p + PE_k q \\ q'_k = (1 - PE_k)\,q + PE_k p \end{array}\right\} \qquad (6)$$

In Eq. (6), the correlation between bit decisions and the timing direction statistic are neglected. However, this is a negligible effect since the correlation is only 1/16. It can be shown, moreover, that for the conditions of this problem there is a negligible error in assuming $p'_k = p_k$ and $q'_k = q_k$. We now have the parameters necessary to complete our random walk model. As was pointed out in *Subsection 3*, there are a countable number of states. In the limit as the time increases without bound, the stationary probabilities would all tend to zero and the phase error variance would be unbounded. To overcome this difficulty, we shall compute the stationary (steady-state) phase error variance modulo one full cycle, as was done in SPS 37-63, Vol. III.

Figure 4 illustrates the resulting reduced state transition diagram for arbitrary N, which we may now use to determine the mean-squared timing error. Define the steady-state probabilities by

$$P_k = \text{Prob}\,(\text{error is in state } k), \qquad 1 \leq k \leq N$$

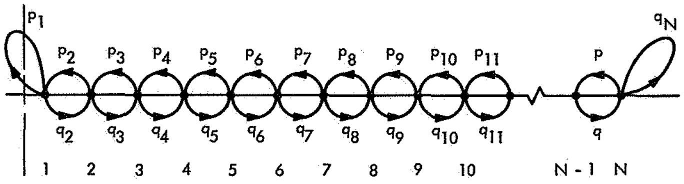

Fig. 4. Reduced-state transition diagram showing the transition probabilities with reflecting states at each end

and, in addition, let

$$p_k = \text{Prob}\,(\text{of reducing the error} \,|\, \text{error is in state } k)$$

$$q_k = \text{Prob}\,(\text{of increasing the error} \,|\, \text{error is in state } k)$$

then the steady-state probabilities, for the positive states, must satisfy the following second-order difference equation:

$$P_k = q_{k-1}P_{k-1} + p_{k+1}P_{k+1}, \qquad 1 < k < N \qquad (7)$$

The boundary conditions for Eq. (7) are

$$\left.\begin{array}{l} P_1 = p_1 P_1 + p_2 P_2 \\ P_N = q_{N-1}P_{N-1} + q_N P_N \end{array}\right\} \qquad (8)$$

It is not difficult to show that the unique solution of Eq. (7), employing the boundary conditions in Expression (8), satisfies the recursive relationship

$$P_{k+1} = \frac{q_k}{p_{k+1}} P_k, \qquad k = 1, \cdots, N \qquad (9)$$

so that in terms of P_1 the solution becomes

$$P_k = P_1 \prod_{j=1}^{k-1} \left(\frac{q_j}{p_{j+1}} \right), \qquad k = 2, \cdots, N \qquad (10)$$

A similar set of equations can be written for the negative states. However, symmetry will be used since we consider only the zero offset case. To evaluate Eq. (10), the set of p_j's must be computed. Their values depend on the signal amplitude associated with that particular state and the value of Δ. The constant P_1 is found from the normalization condition

$$\sum_{k=1}^{N} P_k = 1 \qquad (11)$$

(From symmetry, all the probability mass can be assigned to the positive states.) Once the stationary probabilities are known, the timing error variance can be computed from

$$\sigma_{TE}^2 = \Delta^2 \sum_{1}^{N} (k - \tfrac{1}{2})^2 P_k \qquad (12)$$

Using the threshold of $E_b/N_0 = 9.6$ dB, the timing error variance was computed for the case when $\Delta = 1/16, 1/32, 1/64, 1/128$, and $1/256$ as a function of SNR above threshold. As can be seen in Fig. 5, where the results are plotted,

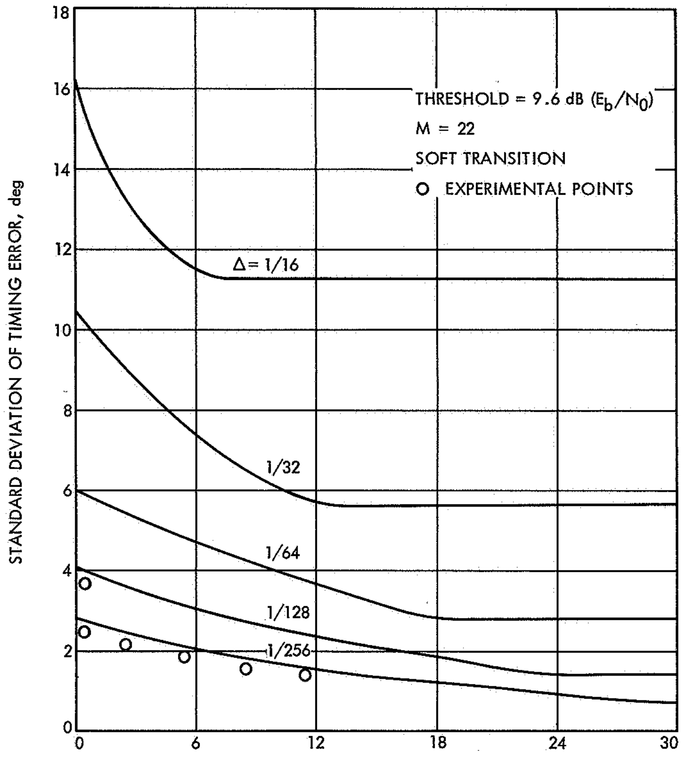

Fig. 5. Timing loop error performance

there exists a SNR value above which the timing error is no longer reduced. This SNR value depends on Δ. The larger the Δ, the smaller the SNR to reach this minimum variance. For example, for $\Delta = 1/16$ a signal-to-noise ratio 7 dB above threshold essentially achieves the minimum timing error variance. Some experimental points obtained by the Spacecraft Telemetry and Command Group are also plotted in Fig. 5, for the cases when $\Delta = 1/256$ and 1/128.

5. Doppler Frequency Effect

We now consider the important question of what influence the doppler frequency has on the timing error of the transition sampler. We shall find that in an environment of no noise the timing error is essentially unaffected by the presence of doppler up to a point, above which, timing synchronization cannot be maintained. This is in contrast to the continuous first-order loop which, without noise, but in the presence of a doppler frequency, has a phase error that increases with the doppler frequency. When the doppler frequency is non-zero, the effect, as viewed on the error state diagram (SPS 37-63, Vol. III), is to continuously move the error states to left if the sampling rate is greater than the subcarrier transition rate and to the right if it is less. Consequently, steady-state probabilities are no longer meaningful for our problem since the transition probabilities now depend on time as well as the state. However, a meaningful result can be obtained to describe the effect of the doppler frequency.

First, we consider the case that the system is such that the error lies away from the transition region. Conceptually, we may assume that we have a state diagram with each state spaced Δ fractions of a subcarrier cycle apart and, in addition, that the state diagram is moving to the left at a rate of Δ_d fractions of a cycle per bit time. This movement to the left accounts for the doppler frequency. The transition probability of moving to the right is p and to the left is q, independent of which state the system is in as long as it is not in a transition region. Then, denoting the mean distance from an arbitrary starting point in this region at time n by $\bar{d}_n$, we see that $\bar{d}_n$ satisfies

$$\bar{d}_n = (\bar{d}_{n-1} + \Delta - \Delta_d)\, p + (\bar{d}_{n-1} - \Delta - \Delta_d)\, q \qquad (13)$$

That is, the mean distance at time n is equal to the mean distance at time $n - 1$ plus $\Delta - \Delta_d$ with probability p plus the distance at time $n - 1$ minus $(\Delta + \Delta_d)$ with probability q. Equation (13) is easily solved to yield

$$\bar{d}_n = n\,[(p - q)\,\Delta - \Delta_d] \qquad (14)$$

as long as the system does not enter a transition region. Hence, by symmetry it is clear that as long as

$$(p - q) > \frac{|\Delta_d|}{\Delta}$$

then the system will be more likely to return to the transition region than slip one cycle. Conversely, if

$$(p - q) < \frac{|\Delta_d|}{\Delta}$$

the system will be more likely to slip than return to the correct transition region. So, whenever $|\Delta_d| > \Delta\,(p - q)$ the effect of the doppler frequency will be, on the average, to force the system out of synchronization. We now obtain a bound on how far up the transition the doppler will tend to bias the system.

In the transition region, the error state configuration depends on the timing correction size Δ. Even though the error states move relative to the transition due to doppler, a worst-case configuration can be used to determine for what states the expected change is towards zero error. The worst-case configuration, given the system is in a negative state, corresponds to a shift of the error states from the one of symmetry to the right until state -1 is located at the zero crossing. Figure 6 illustrates the configuration for the case $\Delta = 1/256$. By symmetry, the results will apply to the right side of zero if the doppler is in the opposite direction. Let $\tilde{p}_k$ denote the probability of moving toward the zero crossing, given that the system is in state k for this worst-case configuration. Now denote by Δd_k the change of position from state k at time n to a new position at time $n + 1$. We have

$$\Delta d_k = i_k - \Delta_d \tag{15}$$

where

$$\begin{aligned} i_k &= \Delta \text{ with probability } \tilde{p}_k \\ &= -\Delta \text{ with probability } \tilde{q}_k \end{aligned}$$

So the average change at time $n + 1$ is

$$\overline{\Delta d_k} = (\tilde{p}_k - \tilde{q}_k)\,\Delta - \Delta_d \tag{16}$$

Since we have picked the worst-case configuration, it follows that if there exists a k such that

$$(\tilde{p}_k - \tilde{q}_k) > \frac{|\Delta_d|}{\Delta}$$

then the upper bound on the doppler-induced bias is $k'\Delta$ where k' is the smallest k such that

$$(\tilde{p}_k - \tilde{q}_k) > \frac{|\Delta_d|}{\Delta}$$

Note that if the effect of the doppler is to cause a timing error of Δ_d fractions of a cycle in one bit time and we let D be the allowable relative doppler rate, and T_b the duration of one bit, then it can be shown that D must satisfy

$$D < \frac{\Delta}{f_{sc} T_b} (\tilde{p}_k - \tilde{q}_k) \tag{17}$$

in order that the bias be no more $k\Delta$. The upper bound is plotted in Fig. 7 as a function of the relative doppler frequency. Notice from the figure that if the design specifications call for a $D \leqq 10^{-5}$, the upper bound yields a bias of Δ. When the relative doppler frequency exceeds 20.8×10^{-5}, the bound becomes "exact" and the bias becomes unbounded. This implies that, on the average, the system will continually lose sync. Some experimental points obtained by the Telemetry and Command Development Group are shown in Fig. 7 and indicate the tightness of the bound.

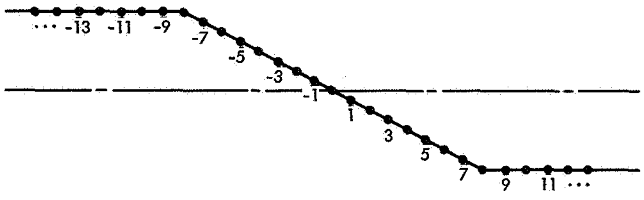

Fig. 6. Worst-state configuration of the error state diagram superimposed on a negative-going transition

6. SNR Degradation Due to Timing Jitter

An important parameter that measures the effectiveness of the timing loop in providing timing is the degradation

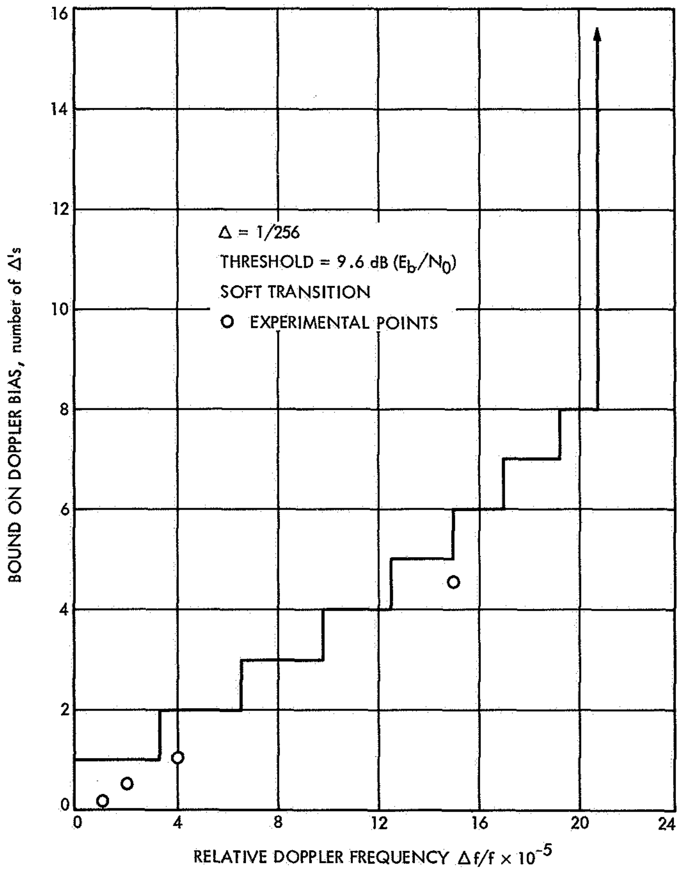

Fig. 7. Upper bound of doppler bias vs relative doppler frequency

in the average bit error probability. Alternately, this can be converted to degradation in SNR. The computation made here assumes the sign of the detected bit is known perfectly, as far as the timing loop operation is concerned. Since the timing loop, in actual operation, is decision-directed, bit detection errors in general will tend to degrade the loop operation more than predicted from the assumption of no bit errors. However, calculations indicate that if the nominal bit error rate is 1×10^{-5}, the difference will be negligible. The average bit error probability must be computed for each state, which, in turn, requires the correlation function of the bit waveform. It was found that the correlation function of the PN-modulated subcarrier is almost as sharp, between zero and 1/4 of a subcarrier cycle, as the unmodulated subcarrier and considerably sharper than the correlation peak of the unmodulated PN code. Four values of Δ were considered, assuming no doppler and zero offset. The average error probability PE was computed from the following equation:

$$PE = \sum_{k=1}^{N} PE_k P_k$$

where PE_k is the bit error probability conditional on being in state k and P_k is the stationary probability of being in state k or $-k$. Because of the assumption of zero offset, the negative states can be folded over onto the positive ones. The parameter N is given by

$$N = \frac{1}{2\Delta}, \qquad \Delta = 1/16, 1/32, 1/64, 1/256$$

After the PE was found for each of the four values of Δ, the corresponding SNR was determined. From this SNR, the degradation from the value needed to produce a PE of 1×10^{-5} was computed. The results are shown in Table 1 and the degradation is plotted in Fig. 8.

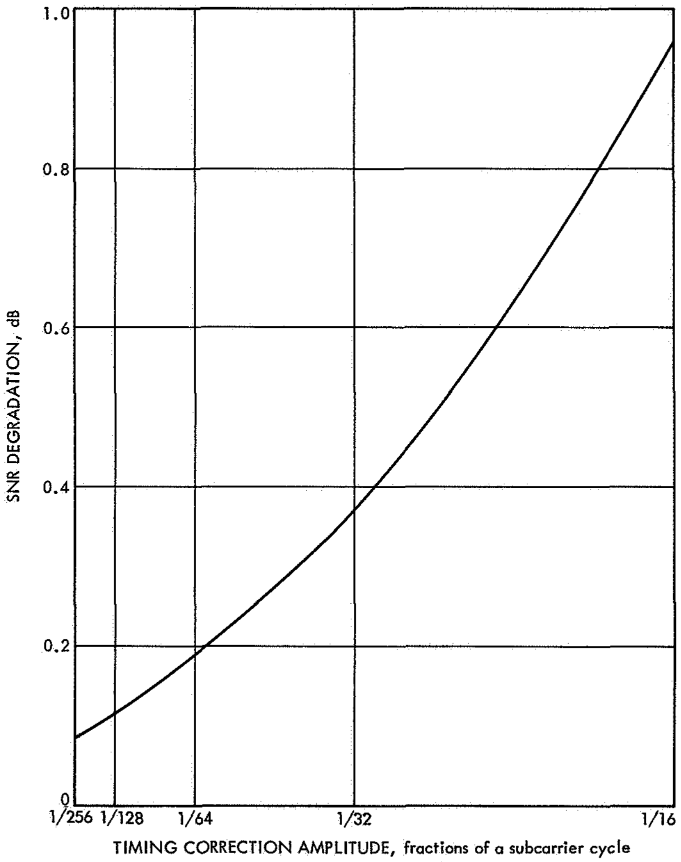

Fig. 8. SNR degradation vs timing update size

Table 1. Computation of PE and SNR degradation

Δ	$PE \times 10^{-5}$	SNR degradation, dB
1/16	6.751	0.963
1/32	2.285	0.374
1/64	1.020	0.191
1/256	1.207	0.086
Perfect system	1.000	0.000

B. Space Station Unified Communication: Optimum Modulation Indexes and Maximum Data Rates for the Interplex Modem, *J. La Frieda*

1. Introduction

This article is concerned with the determination of the optimum modulation indexes, and the corresponding maximum rate-to-bandwidth ratios for the interplex modem, introduced in *SPS 37-62*, Vol. III, pp. 57–60, when the bit error probabilities of the data channels are equal. The results, which are presented in the form of design curves, are of practical interest, since the interplex modem yields significantly improved performance over the existing modem.

2. Analysis of the System

A basic simplified diagram of the interplex modem is depicted in Fig. 1. In the transmitter portion of the system, the data signals $s_i(t) = \pm 1$, $i = 1, 2$, are processed, i.e., "interplexed", such that the frequency-multiplexed, square-wave subcarrier waveforms $\mathrm{sq}\,(\omega_i t) = \pm 1$, $i = 1, 2$, are biphase-modulated by $s_1(t)$ and $s_2(t)\, s_1(t)\, \mathrm{sq}\,(\omega_1 t)$, respectively, where $\mathrm{sq}\,(\omega_i t)$ denotes a square wave of frequency ω_i. With this modulation scheme assumed, the output of the phase modulator is given by

$$s(t) = (2P)^{1/2} \sin\left[\omega_c t + \theta_1 s_1(t)\, \mathrm{sq}\,(\omega_1 t) + \theta_2 s_2(t)\, s_1(t)\, \mathrm{sq}\,(\omega_1 t)\, \mathrm{sq}\,(\omega_2 t)\right] \tag{1}$$

where P is the overall average transmitted power, and where θ_1 and θ_2 are the modulation indices of the high and low data rate channels, respectively. The received waveform is then given by

$$y(t) = (2P)^{1/2} \sin\left[\omega_c t + \theta_1 s_1(t)\, \mathrm{sq}\,(\omega_1 t) + \theta_2 s_1(t)\, s_2(t)\, \mathrm{sq}\,(\omega_1 t)\, \mathrm{sq}\,(\omega_2 t) + \theta\right] + n(t) \tag{2}$$

where $n(t)$ is assumed to be white gaussian noise with one-sided spectral density N_0 watts/hertz, and θ is some arbitrary (but unknown) phase shift. The coherent carrier tracking loop generates the reference signal

$$r(t) = (2)^{1/2} \cos(\omega_c t + \hat{\theta}) \tag{3}$$

where $\hat{\theta}$ is the loop's estimate of θ.

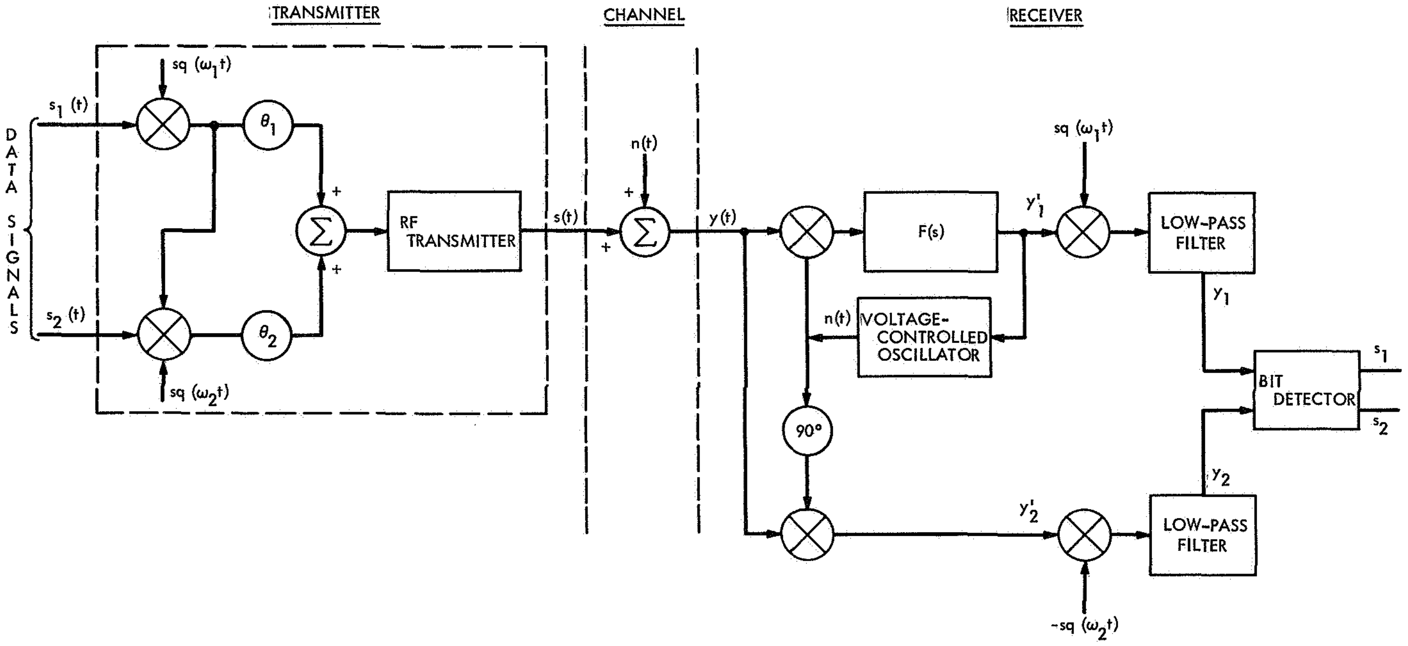

Fig. 1. Interplex modem

Assuming that the data-bearing subcarriers are at frequencies outside the bandwidth of the carrier phase-locked loop (PLL) and disregarding terms of frequency $2\omega_c$, the output data bearing signals, which go into the subcarrier demodulators, are given by

$$y_1'(t) = (P)^{1/2} \sin\left[\theta_1 s_1(t)\,\mathrm{sq}(\omega_1 t) + \theta_2 s_2(t)\, s_1(t)\,\mathrm{sq}(\omega_1 t)\,\mathrm{sq}(\omega_2 t) + \phi\right] + n_1'(t) \tag{4}$$

$$y_2'(t) = (P)^{1/2} \cos\left[\theta_1 s_1(t)\,\mathrm{sq}(\omega_1 t) + \theta_2 s_2(t)\, s_1(t)\,\mathrm{sq}(\omega_1 t)\,\mathrm{sq}(\omega_2 t) + \phi\right] + n_2'(t) \tag{5}$$

where $\phi \overset{\Delta}{=} \theta - \hat{\theta}$ is the PLL phase error, and where $n_i'(t), i = 1, 2$, are statistically independent white gaussian noise processes of single-sided spectral density N_0 watts/hertz.

Using simple trigonometric expansions and the fact that $s_i(t) = \pm 1$, $\mathrm{sq}(\omega_i t) = \pm 1$, $i = 1, 2$, Eqs. (4) and (5) may be written as follows:

$$\begin{aligned} y_1'(t) = {} & \underbrace{(P)^{1/2} \cos\phi \sin\theta_1 \cos\theta_2 s_1(t)\,\mathrm{sq}(\omega_1 t)}_{\text{high data rate component}} + \underbrace{(P)^{1/2} \cos\phi \cos\theta_1 \sin\theta_2 s_1(t)\, s_2(t)\,\mathrm{sq}(\omega_1 t)\,\mathrm{sq}(\omega_2 t)}_{\text{cross-modulation loss component}} \\ & + \underbrace{(P)^{1/2} \sin\phi \left[\cos\theta_1 \cos\theta_2 - \sin\theta_1 \sin\theta_2 s_2(t)\,\mathrm{sq}(\omega_2 t)\right]}_{\text{leakage component}} + n_1'(t) \end{aligned} \tag{6}$$

$$\begin{aligned} y_2'(t) = {} & \underbrace{(P)^{1/2} \cos\phi \cos\theta_1 \cos\theta_2}_{\text{dc component}} - \underbrace{(P)^{1/2} \cos\phi \sin\theta_1 \sin\theta_2 s_2(t)\,\mathrm{sq}(\omega_2 t)}_{\text{low data rate component}} \\ & \underbrace{- (P)^{1/2} \sin\phi \left[\sin\theta_1 \cos\theta_2 + \cos\theta_1 \sin\theta_2 s_2(t)\,\mathrm{sq}(\omega_2 t)\right] s_1(t)\,\mathrm{sq}(\omega_1 t)}_{\text{leakage component}} + n_2'(t) \end{aligned} \tag{7}$$

Note that the leakage components exist as a result of the imperfect RF carrier loop performance.

With the subcarrier frequencies chosen such that $\mathrm{sq}(\omega_1 t)$ is orthogonal to $\mathrm{sq}(\omega_2 t)$, the demodulated low-pass filtered output signals are, respectively,

$$\left.\begin{aligned} y_1(t) &= (P)^{1/2} \cos\phi \sin\theta_1 \cos\theta_2 s_1(t) + n_1(t) \\ y_2(t) &= (P)^{1/2} \cos\phi \sin\theta_1 \sin\theta_2 s_2(t) + n_2(t) \end{aligned}\right\} \tag{8}$$

where $n_1(t)$ and $n_2(t)$ have the same statistics as $n_1'(t)$ and $n_2'(t)$, respectively. Rewriting Eq. (2) as

$$\begin{aligned} y(t) = {} & (2P)^{1/2} \cos\theta_1 \cos\theta_2 \sin(\omega_c t + \theta) - (2P)^{1/2} \sin\theta_1 \sin\theta_2 \sin(\omega_c t + \theta)\, s_2(t)\,\mathrm{sq}(\omega_2 t) \\ & + (2P)^{1/2} \sin\left[\theta_1 s_1(t)\,\mathrm{sq}(\omega_1 t) + \theta_2 s_1(t)\, s_2(t)\,\mathrm{sq}(\omega_1 t)\,\mathrm{sq}(\omega_2 t)\right] \cos(\omega_c t + \theta) + n(t) \end{aligned} \tag{9}$$

it follows that the average power of the received signal at the carrier frequency ω_c is

$$P_c = P \cos^2 \theta_1 \cos^2 \theta_2 \tag{10}$$

while from Eqs. (6) and (8) it follows that the average power in the data components, and the cross-modulation loss component, is, respectively,

$$P_1 = P \sin^2 \theta_1 \cos^2 \theta_2 \cos^2 \phi$$

$$P_2 = P \sin^2 \theta_1 \sin^2 \theta_2 \cos^2 \phi$$

$$P_L = P \cos^2 \theta_1 \sin^2 \theta_2 \cos^2 \phi \tag{11}$$

3. Selection of Optimum Modulation Indices for the Interplex Modem

In this subsection, we make use of the results given in the previous subsection and present a method whereby the modulation indices $\theta_i, i = 1, 2$, can be determined.

Let the data rate (bit/s) of $s_1(t)$ and $s_2(t)$ be $R_1 = 1/T_1$ and $R_2 = 1/T_2$, respectively, where T_1 and T_2 are the bit times. With the assumption that $\phi(t)$ is constant over the bit times and that the data signals are uncoded and antipodal, the probability of a bit error is then given by

$$P_{e_i} = \int_{-\pi}^{\pi} \frac{\exp(\rho \cos \phi)}{2\pi I_0(\rho)} \operatorname{erfc}\left(\frac{2P_iT_i}{N_0}\right)^{1/2} d\phi, \qquad i = 1, 2 \tag{12}$$

where

$$\rho \overset{\Delta}{=} \frac{P_c}{N_0 B_L} \tag{13}$$

is the signal-to-noise ratio (SNR) of the carrier tracking loop, and B_L is the one-sided noise bandwidth (BW) of the carrier PLL. The overall SNR of the received signal is defined to be

$$\beta \overset{\Delta}{=} \frac{P}{N_0 B_L} \tag{14}$$

and, in terms of the parameters which describe the carrier PLL, the signal energy per bit to noise spectral density can be expressed as

$$\frac{P_iT_i}{N_0} = \beta \frac{P_i}{P} \frac{1}{\delta_i}, \qquad i = 1, 2 \tag{15}$$

where

$$\delta_i \overset{\Delta}{=} \frac{R_i}{B_L} \tag{16}$$

is the rate-to-BW ratio.

If the system is designed such that the bit error probability of both channels are equal, viz., similar to *Mariner* Mars 1969 specifications, then

$$\frac{P_1T_1}{N_0} = \frac{P_2T_2}{N_0} \tag{17}$$

Defining the ratio

$$\alpha = \frac{R_2}{R_1} = \frac{\delta_2}{\delta_1} = \frac{T_1}{T_2} \tag{18}$$

and enforcing the requirement of Eq. (17) on the system yields

$$\frac{P_1T_1}{P_2T_2} = \alpha \cot^2 \theta_2 = 1 \tag{19}$$

so that the low data rate modulation index

$$\theta_2 = \tan^{-1}(\alpha)^{1/2} \tag{20}$$

Let P_e denote the required bit error probability. Then, for given values of α and the independent variable β, δ_1 is solely a function of the modulation index θ_1, implicitly defined by the integral equation

$$P_e = \int_{-\pi}^{\pi} \frac{\exp(\rho \cos \phi)}{2\pi I_0(\rho)} \operatorname{erfc}\left\{\left[\frac{2\beta \sin^2 \theta_1}{\delta_1(1+\alpha)}\right]^{1/2} \cos \phi\right\} d\phi \tag{21}$$

where

$$\rho = \beta \frac{P_c}{P} = \frac{\beta}{1+\alpha} \cos^2 \theta_1$$

In particular, because of Eq. (20), we are interested in determining the optimum index $\hat{\theta}_1(\beta, P_e)$, which yields the maximum rate-to-BW ratios $\hat{\delta}_1(\beta, P_e, \hat{\theta}_1)$ and $\hat{\delta}_2(\beta, P_e, \hat{\theta}_1)$. Note that it suffices to determine only $\hat{\delta}_1(\beta, P_e, \hat{\theta}_1)$ since $\hat{\delta}_2 = \alpha\hat{\delta}_1$.

Since $\delta \overset{\Delta}{=} \delta_1(\beta, P_e, \theta_1)$ cannot be expressed analytically in terms of θ_1, the optimization must be performed numerically. The following iterative method was employed:

(1) P_e, α, and β are fixed, and coarse iterations are made to restrict $\hat{\theta}_1$ to an interval of length 2Δ. Namely, starting with an arbitrary initial value $\theta_1 = \theta_0$ and an increment Δ_0, the integral equation is solved for $\delta_0(\theta_0)$ and $\delta_1(\theta_0 + \Delta_0)$. If $\delta_1 > \delta_0$, the values

$$\delta_2(\theta_0 + 2\Delta_0), \cdots, \delta_k(\theta_0 + k\Delta_0)$$

are computed until $\delta_{k-1} < \delta_k$, so that

$$\hat{\theta}_1 \in [\theta_0 + (k-2)\Delta_0, \theta_0 + k\Delta_0]$$

Conversely, if $\delta_1 < \delta_0$, then the values

$$\delta_{-1}(\theta_0 - \Delta_0), \cdots, \delta_{-k}(\theta_0 - k\Delta_0)$$

are computed until $\delta_{-k} < \delta_{-(k-1)}$, so that

$$\hat{\theta}_1 \in [\theta_0 - k\Delta_0, \theta_0 - (k-2)\Delta_0]$$

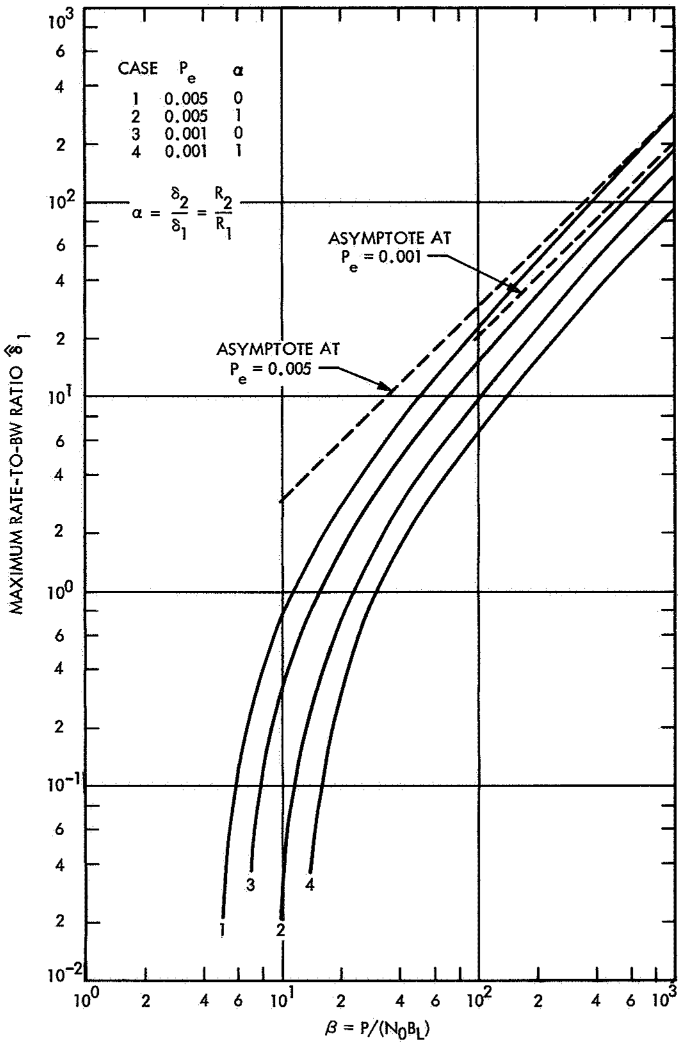

Fig. 2. Maximum rate-to-BW ratio $\hat{\delta}_1$ vs received SNR β (both channels uncoded)

(2) Selecting some new initial value of θ_1 within the above interval, and repeating the procedure with the increment $\Delta_1 < \Delta_0$, e.g., $\Delta_1 = \Delta_0/5$, $\hat{\theta}_1$ can be determined within an accuracy $\pm\Delta_1$, while

$$\delta_{k-1} \leqq \hat{\delta}_1(\beta, P_e, \hat{\theta}_1) \leqq \delta_{k-1} + \Delta\delta$$

where

$$\Delta\delta = \max[(\delta_{k-1} - \delta_{k-2}), (\delta_{k-1} - \delta_k)]$$

The procedure is then repeated with $\Delta_k < \Delta_{k-1}$, until the tolerances Δ_k and $\Delta\delta$ are acceptable. In the computations, we set $\Delta_0 = 0.087$, $\Delta_k = \Delta_{k-1}/5$, and determined $\hat{\delta}_1(\beta, P_e, \hat{\theta}_1)$ within 0.1%.

(3) The computations are made for other values of β.

4. Numerical Results

In the limiting case $\beta \to \infty$, Eq. (19) becomes

$$P_e = \operatorname{erfc}\left\{\left[\frac{2\beta \sin^2\theta_1}{\delta_1(1+\alpha)}\right]^{1/2}\right\}$$

so that asymptotically we have

$$\hat{\theta}_1(\beta, P_e) = 90\,\text{deg}$$

and

$$\hat{\delta}_1(\beta, P_e, \hat{\theta}_1) = \frac{2\beta}{1+\alpha}(\operatorname{erfc}^{-1} P_e)^{-2} \tag{22}$$

For other values of β, numerical calculations are necessary. The maximum rate-to-BW ratio $\hat{\delta}_1(\beta, P_e, \hat{\theta}_1)$ and the corresponding optimum modulation index $\hat{\theta}_1(\beta, P_e)$ are shown plotted in Figs. 2 and 3, respectively, as a function of β for selected values of α and P_e. Note that $\hat{\delta}_1$ is approximately given by Eq. (22) for $\beta > 1000$.

5. Conclusion

The results presented in Figs. 2 and 3 can be used to choose telemetry data rates and optimum modulation indexes such that the most economical use of spacecraft power is employed.

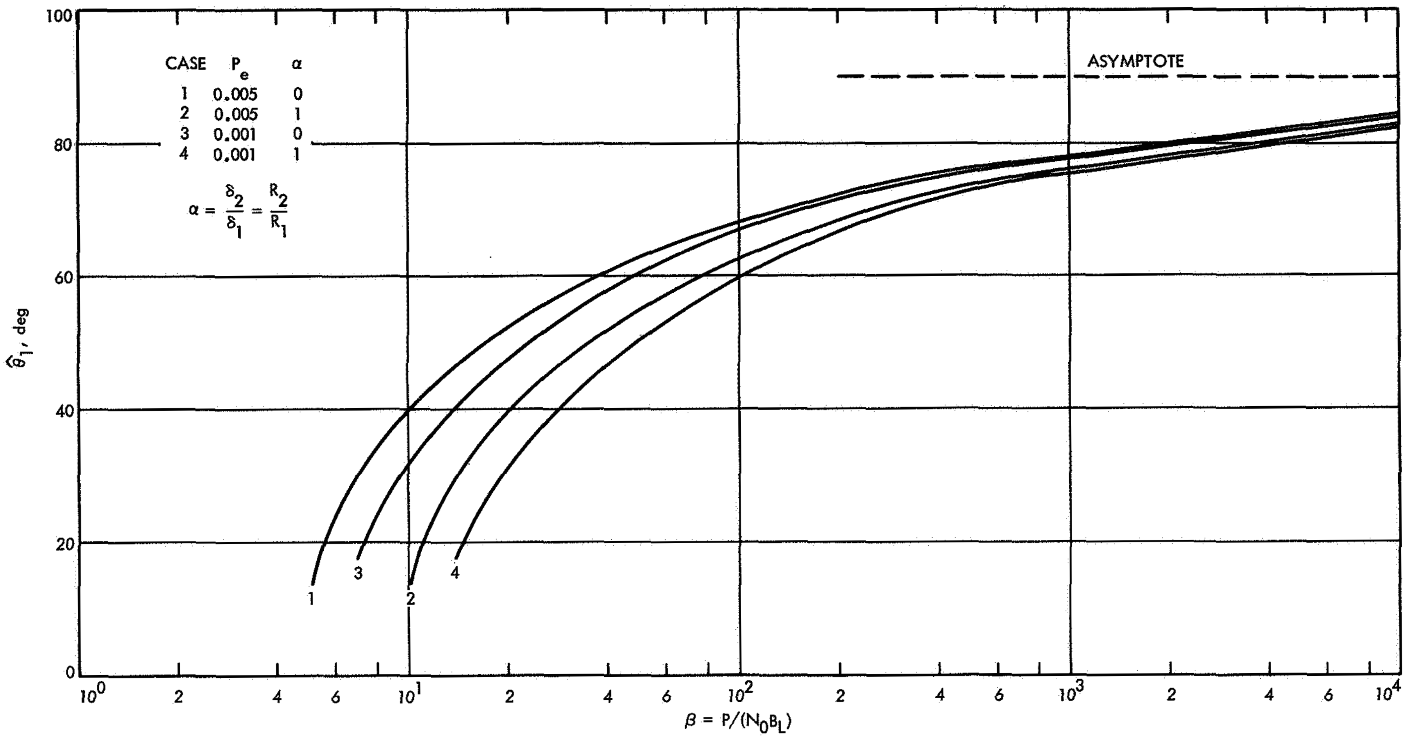

Fig. 3. Optimum high data rate modulation index $\hat{\theta}_1$ vs received SNR β (both channels uncoded)

C. Space Station Unified Communication: Suppressed-Carrier Two-Channel Interplex Modulation System,

U. Timor and S. Butman

1. Introduction

It is well known that maximum efficiency of a coherent single-channel PCM/PSK/PM system is achieved by completely suppressing the RF carrier, and that a coherent local carrier reference required to demodulate can be established by means of a Costas loop (Ref. 1), a squaring loop (Ref. 2), or another type of decision-directed tracking loop. However, in the existing two-channel system, it is theoretically not possible to completely suppress the RF carrier without simultaneously eliminating one of the channels. In fact, the best choice of modulation angles for maximizing the power in the data sidebands produces enough unsuppressed RF carrier power to obviate the need for data-aided tracking. A standard phase-locked loop is sufficient to provide frequency and phase synchronization. Also, the intermodulation loss in the existing system is actually greater than the power in the low-rate channel.

Recently, a new two-channel modulation scheme called Interplex (SPS 37-62, Vol. III, pp. 57–60) has been suggested where the intermodulation loss and the RF carrier power can be eliminated without compromising any of the advantages of the existing system. Not only is the Interplex system more efficient than the existing system, when some unsuppressed RF power is transmitted, but it permits 100% of the transmitted power to be allocated to data-bearing sidebands while preserving two-channel PCM/PSK/PM operation at all ratios of channel rates. In this mode, the RF carrier is completely suppressed; therefore, it is necessary to develop a method for maintaining frequency and phase sync at the receiver by methods other than the standard phase-locked loop.

In this article, a new and efficient phase tracking method for a two-channel, suppressed-carrier Interplex system is discussed and system performance is analyzed. It is shown that although Costas or squaring loops can be used, their performance deteriorates rapidly as the ratio of channel powers (or data rates) $\alpha = P_2/P_1$ increases until no tracking is feasible when $\alpha = 1$. However, the new technique presented here is insensitive to α, and is as efficient as the single-channel Costas loop.

2. Phase Tracking with the Costas Loop

Let $a(t) = \hat{a}(t)\,\mathrm{sq}(\omega_1 t)$ and $b(t) = \hat{b}(t)\,\mathrm{sq}(\omega_2 t)$ be square-wave subcarriers of frequencies ω_1 and ω_2, modulated by binary data streams $\hat{a}(t)$ and $\hat{b}(t)$, respectively. The suppressed-carrier transmitted waveform is

$$\left.\begin{aligned} s(t) &= \sqrt{2P_T}\sin\left(\omega_c t + \frac{\pi}{2}a(t) + \theta a(t)\,b(t)\right) \\ &= \sqrt{2P_T}a(t)\cos\left(\omega_c t + \theta a(t)\,b(t)\right) \end{aligned}\right. \qquad (1)$$

where P_T is the transmitted power, ω_c is the carrier frequency, and θ is determined by the required ratio of the powers in the data channels (see *Section B* of this chapter and SPS 37-62, Vol. III, pp. 57–60)

$$\tan^2\theta = \frac{P_2}{P_1} = \alpha \qquad \text{for } 0 \leqq \alpha \leqq 1 \qquad (2)$$

The Costas loop (Fig. 1) correlates $s(t)$ with a local reference $\cos(\omega_c t + \phi)$ and its quadrature $\sin(\omega_c t + \phi)$ to yield (filtering out terms of frequency $2\omega_c$)

$$\left.\begin{aligned} x(t) &= \sqrt{P_T}\,a(t)\cos[\phi - \theta a(t)\,b(t)] \\ y(t) &= \sqrt{P_T}\,a(t)\sin[\phi - \theta a(t)\,b(t)] \end{aligned}\right\} \qquad (3)$$

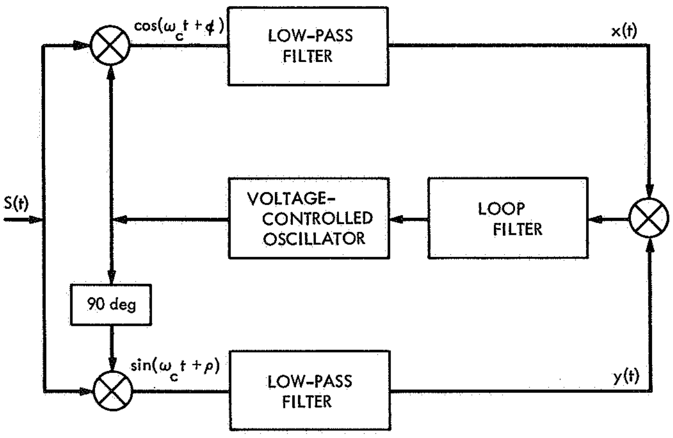

Fig. 1. Costas loop block diagram

Multiplying $x(t)$ and $y(t)$ and passing through the loop low-pass filter, we get the control signal

$$x(t)\,y(t) = \frac{1}{2}P_T\cos(2\theta)\sin 2\phi$$

Thus, we get an effective RF power for tracking 2ϕ

$$P_{RF} = \frac{P_T^2}{4}\cos^2(2\theta) = \frac{P_T^2}{4}\cdot\left(\frac{1-\alpha}{1+\alpha}\right)^2 \qquad (4)$$

which is a decreasing function of α and is zero for $\alpha = 1$ (when $P_1 = P_2$), i.e., no tracking is possible when both data channels have equal power.

It can be shown that the squaring method yields the same results. Thus, the suppressed carrier methods for a single data channel cannot be applied to the two-channel case, unless $\alpha << 1$.

3. Suppressed Carrier Tracking for Two-Channel Interplex

Let $x(t)$ and $y(t)$ be as in Eq. (3). Then we can write

$$\left.\begin{aligned} x(t) &= P_T[a(t)\cos\phi\cos\theta + b(t)\sin\phi\sin\theta] \\ y(t) &= P_T[a(t)\sin\phi\cos\theta - b(t)\cos\phi\sin\theta] \end{aligned}\right\} \qquad (5)$$

Since $a(t)$ and $b(t)$ are modulated subcarriers of different frequencies, we can use bandpass filters centered at ω_1 and ω_2 to separate them. Let the bandwidth of these filters, W_a and W_b, be chosen to pass the data around the first harmonic of the subcarrier. We get (Fig. 2)

$$\left.\begin{aligned} x_1(t) &= \sqrt{P_T}(\cos\phi\cdot\cos\theta)\,\hat{a}(t)\cos(\omega_1 t + \phi_a) \\ x_2(t) &= \sqrt{P_T}(\sin\phi\cdot\sin\theta)\,\hat{b}(t)\cos(\omega_2 t + \phi_b) \\ y_1(t) &= \sqrt{P_T}(\sin\phi\cdot\sin\theta)\,\hat{a}(t)\cos(\omega_1 t + \phi_a) \\ -y_2(t) &= \sqrt{P_T}(\cos\phi\cdot\sin\theta)\,\hat{b}(t)\cos(\omega_2 t + \phi_b) \end{aligned}\right\} \qquad (6)$$

Multiplying $x_1(t)\,y_1(t)$ and $x_2(t)\,y_2(t)$, and using low-pass filter of bandwidth B_L, we get

$$\left.\begin{aligned} \mathcal{Z}_1(t) &= x_1(t)\,y_1(t) = \frac{1}{4}P_T\cos^2\theta\sin 2\phi \\ \mathcal{Z}_2(t) &= x_2(t)\,y_2(t) = \frac{1}{4}P_T\sin^2\theta\sin 2\phi \end{aligned}\right. \qquad (7)$$

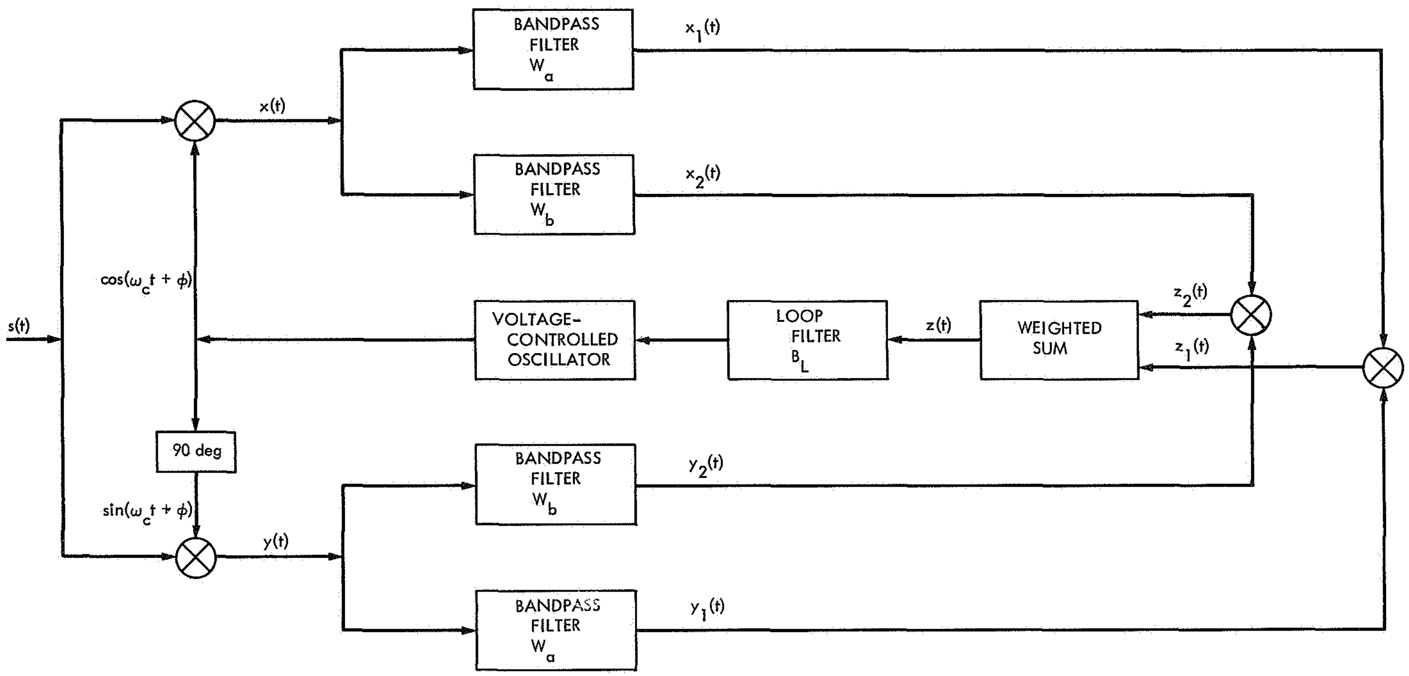

Fig. 2. Suppressed carrier two-channel Interplex tracking loop

If the control signal is taken to be

$$\tilde{z}_1(t) + \tilde{z}_2(t) = \frac{1}{4} P_T \sin 2\phi$$

the RF power will be independent of α. In general, taking the noise into consideration, we can find the best linear combination of $\tilde{z}_1(t)$ and $\tilde{z}_2(t)$ to minimize the variance of the phase error in tracking.

4. Analysis of Tracking Loop With Noise

We assume that the channel adds white gaussian noise with one-sided spectral density N_0. The received signal will be

$$r(t) = s(t) + n(t)$$

and the control signals at the output of the lowpass filter (B_L) are

$$\left.\begin{aligned} z_1(t) &= \tilde{z}_1(t) + n_1(t) \\ z_2(t) &= \tilde{z}_2(t) + n_2(t) \end{aligned}\right. \qquad (8)$$

where $n_1(t)$ and $n_2(t)$ are independent.

Since $B_L << W_a$ and $B_L << W_b$, the effective one-sided spectral densities of $n_1(t)$ and $n_2(t)$ in the low frequency band are, respectively (Ref. 2)

$$\left.\begin{aligned} N_1 &= \frac{1}{4} N_0 P_T \cos^2\theta + \frac{N_0^2 W_a}{2} \\ N_2 &= \frac{1}{4} N_0 P_T \sin^2\theta + \frac{N_0^2 W_b}{2} \end{aligned}\right\} \qquad (9)$$

Let

$$z(t) = \gamma z_1(t) + (1-\gamma) z_2(t) \qquad 0 \leqq \gamma \leqq 1 \qquad (10)$$

from Eqs. (7) and (8)

$$z(t) = \frac{1}{4} P_T [\gamma \cos^2\theta + (1-\gamma)\sin^2\theta] \sin 2\phi + \tilde{n}(t) \qquad (11)$$

where

$$\tilde{n}(t) = \gamma n_1(t) + (1-\gamma) n_2(t)$$

is zero mean process with spectral density in the low frequency band

$$N = \gamma^2 N_1 + (1-\gamma)^2 N_2 \qquad (12)$$

Assuming that the phase error ϕ is small enough that the linear model is a good approximation to the phase-locked loop, we obtain the variance of ϕ (Ref. 2)

$$\sigma_\phi^2 = \frac{1}{4}\sigma_{2\phi}^2 = \frac{1}{4}\frac{NB_L}{\left\{\frac{1}{4}P_T\left[\gamma\cos^2\theta + (1-\gamma)\sin^2\theta\right]\right\}^2}$$

From Eqs. (9) and (12)

$$\sigma_\phi^2 = \frac{N_0B_L}{P_T}\cdot\frac{\gamma^2\cos^2\theta + (1-\gamma)^2\sin^2\theta + K\left(\gamma^2 + d(1-\gamma)^2\right)}{\left[\gamma\cos^2\theta + (1-\gamma)\sin^2\theta\right]^2} \tag{13}$$

where

$$K \triangleq \frac{2N_0W_a}{P_T}$$

and

$$d \triangleq \frac{W_b}{W_a}$$

We want to find the optimum γ (as a function of θ) to minimize σ_ϕ^2.

5. Optimization of γ

If only $z_1(t)$ is used as control signal (i.e., $\gamma = 1$), then

$$\sigma_\phi^2 = \frac{N_0B_L}{P_T}\cdot\sec^2\theta\,(1 + K\sec^2\theta) \tag{14}$$

Using both $z_1(t)$ and $z_2(t)$ and minimizing σ_ϕ^2 we get

$$\gamma_{\text{opt}} = \frac{(Kd + \sin^2\theta)\cos^2\theta}{K\sin^2\theta + dK\cos^2\theta + 2\sin^2\theta\cos^2\theta} \tag{15}$$

$$\sigma_\phi^2(\gamma_{\text{opt}}) = \frac{N_0B_L}{P_T}\left(1 + K\frac{Kd + (1+d)\sin^2\theta\cos^2\theta}{K(d\cos^4\theta + \sin^4\theta) + \sin^2\theta\cos^2\theta}\right) \tag{16}$$

The relation between K, d, and θ depend on the type of coding and the error probabilities of the two channels. For the case where both channels use the same type of code (or are uncoded), and have the same error probabilities, we get

$$d = \frac{W_b}{W_a} = \frac{R_b}{R_a} = \frac{P_2}{P_1} = \tan^2\theta \tag{17}$$

where R_a, R_b are the bit rates of the two data streams. In this case, substituting d in Eqs. (15) and (16) yields

$$\gamma_{\text{opt}} = \frac{1}{2} \tag{18}$$

$$\sigma_\phi^2 = \frac{N_0B_L}{P_T}(1 + K\sec^2\theta) \tag{19}$$

But

$$\frac{K}{\cos^2\theta} = \frac{2N_0W_a}{P_T\cos^2\theta} = \frac{2N_0W_a}{P_1} \propto \frac{2N_0R_a}{P_1} \tag{20}$$

which is independent of θ.

Thus, for a given total signal-to-noise ratio (SNR), the performance of the system is independent of the division of power between the two channels. Note that by taking

$$z(t) = z_1(t) + z_2(t)$$

instead of

$$z(t) = z_1(t)$$

we reduce the phase error variance by a factor of $\cos^2\theta$.

6. The Performance of the System

We assume that both channels are uncoded and the error probabilities are equal, i.e., Eq. (17) is satisfied. Let

$$\rho_L \triangleq \frac{P_T}{N_0B_L} \tag{21a}$$

and

$$\delta \triangleq \frac{R_a}{B_L} \tag{21b}$$

Assuming that the phase error is small so that the linear approximation holds, we get (Ref. 2)

$$P_E = \frac{1}{\pi I_0(u)} \int_0^{\pi} \exp(u\cos\phi)\,\mathrm{erfc}\left(\sqrt{\frac{2\rho_L\cos^2\theta}{\delta}}\cos\phi\right) d\phi \tag{22}$$

where

$$u = \frac{1}{\sigma_\phi^2} = \frac{\rho_L}{1 + K\sec^2\theta} \tag{23}$$

Also, $W_a = \lambda R_a$, where λ depends on the rate of the code, and we can take $\lambda = 6$ for the uncoded case. Therefore,

$$K = \frac{2\lambda\delta}{\rho_L}$$

and

$$u = \frac{\rho_L}{1 + (2\lambda\delta/\rho_L\cos^2\theta)} \tag{24}$$

Thus, given ρ_L, θ, and δ we can find P_E from Eq. (22). Conversely, given ρ_L, θ, and P_E we can find the maximum data rate that yields error probability $\leqq P_E$.

For large ρ_L we have the asymptotic result

$$\frac{\delta}{\rho_L} \xrightarrow[\rho_L\to\infty]{} \frac{2\cos^2\theta}{[\mathrm{erfc}^{-1}(P_E)]^2} \tag{25}$$

which is identical to the asymptotic value of the Interplex system without carrier suppression (*Section B*). In general, the suppressed carrier method yields higher rates. The advantage is more significant for comparable rates in the two-channel system. Results for the extreme case of $\alpha = 0\,(\theta = 0)$ and $\alpha = 1\,(\theta = \pi/4)$ are given in Fig. 3, together with the results for optimum non-suppressed carrier system.

References

1. Costas, J. P., "Synchronous Communication," *Proc. IRE*, Vol. 44, No. 12, pp. 1713–1718, Dec. 1956.
2. Viterbi, A. J., *Principles of Coherent Communication*, McGraw-Hill Book Co., Inc., New York, 1966.

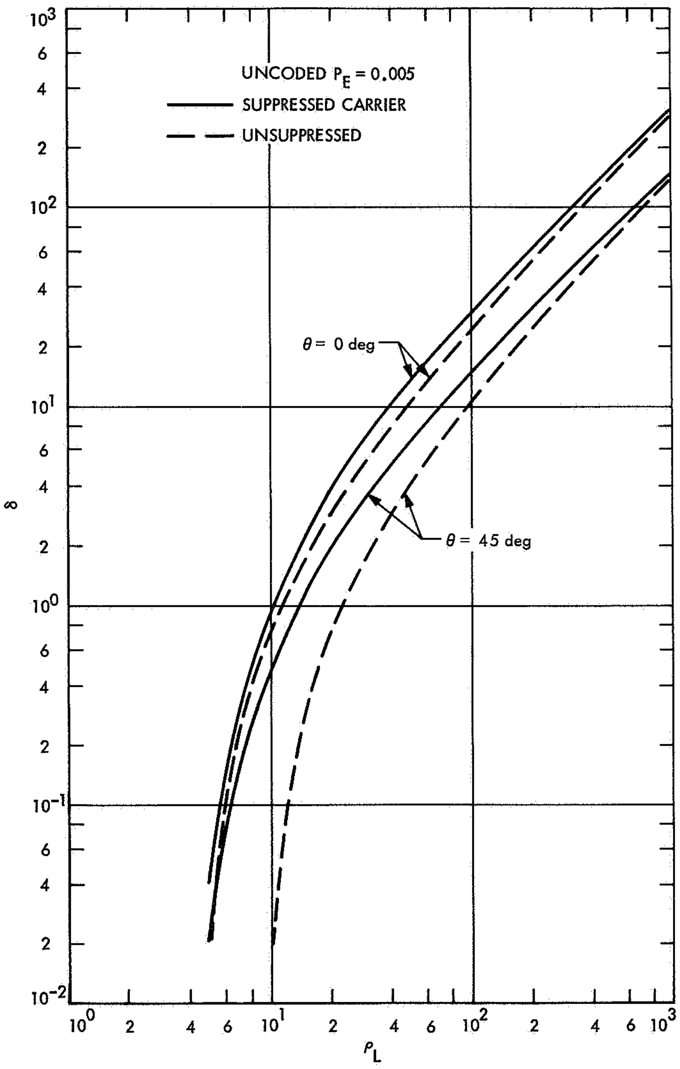

Fig. 3. Rate/bandwidth vs loop SNR for two-channel Interplex system

D. Discretionary Research: Uniform Permutation of Sequences, *L. Kleinrock*

1. Introduction

In SPS 37-62, Vol. III, pp. 75–79, a simple sequence permuter for disguising speech was described. It was pointed out that a single stage of this simple coder–decoder spread the samples only over three adjacent positions; in order to increase the range of permutation, a concatenation of many stages of the simple coder was considered. In this article, the behavior of this system is analyzed and experimental results showing performance of the permutation algorithm are given.

A new network structure (namely, a ternary tree) for connecting these simple coders is then analyzed, and experimental results are also given for that case. As predicted, the performance of the tree structure is far superior to that of the concatenation.

2. Performance of the Simple Coders

From SPS 37-62, Vol. III, a *simple coder* is defined as an $n = 2$ sequence-permutation coder (for which it was shown that the decoder is essentially the same as the encoder). Recall that this device generates a "key" sequence $\{k_i\}$ where $k_i \in \{1, 2\}$. This key sequence directs a sequence of speech samples $\{X_i\}$ into one of two cells of a register $P = (P_2, P_1)$. Whenever $k_i = j$, then X_i is placed in P_j $(j = 1, 2)$, and the previous occupant of that cell is "bumped out," creating a permuted sequence $\{Y_i\}$. Also recall that the key sequence has the property that in every string of three key symbols, both 1 and 2 must each appear at least once. This last is accomplished by using a four-stage shift-register $S = (S_4, S_3, S_2, S_1)$ that contains two 1's and two 2's, which are circulated in one of two cyclic fashions depending upon a pseudorandom sequence $\{c_i\}$ $(c_i \in \{0, 1\})$. If $c_i = 0$, then the sequence in S is shifted one position to the right and the contents of S_4 is replaced by the contents of S_1 (denoted $S_1 \rightarrow S_4$); if $c_i = 1$, then the three rightmost stages are shifted one position to the right and $S_1 \rightarrow S_3$, $S_4 \rightarrow S_4$. The key symbol k_i is taken as the contents of S_1 at the ith shift. This gives rise to the state diagram given in Fig. 1 where the directed branches are labelled with two symbols, the first being c_i and the second being the k_i generated in passing out of the indicated state. Within each state, the contents of $S = (S_4, S_3, S_2, S_1)$ and a state number are given. Note that the k_i generated from a state is independent of c_i.

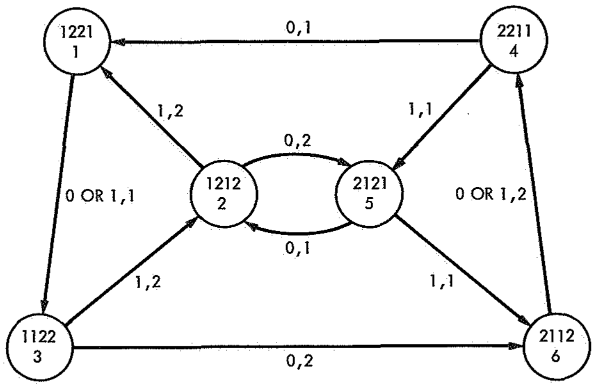

Fig. 1. State diagram for the simple coder

Let us now analyze the behavior of the simple coder. We assume that adjacent symbols in $\{c_i\}$ are independent and that $c_i = 0$ with probability ½. From this, we may construct the following probability transition matrix $H = (h_{jk})$ for this six-state Markov process where $h_{jk} = P$ [next state is k | present state is j] as follows:

$$H = \begin{bmatrix} 0 & 0 & 1 & 0 & 0 & 0 \\ \frac{1}{2} & 0 & 0 & 0 & \frac{1}{2} & 0 \\ 0 & \frac{1}{2} & 0 & 0 & 0 & \frac{1}{2} \\ \frac{1}{2} & 0 & 0 & 0 & \frac{1}{2} & 0 \\ 0 & \frac{1}{2} & 0 & 0 & 0 & \frac{1}{2} \\ 0 & 0 & 0 & 1 & 0 & 0 \end{bmatrix} \qquad (1)$$

Note that this is a doubly stochastic matrix (rows as well as columns each sum to unity). Let $\boldsymbol{\pi} = (\pi_1, \cdots, \pi_6)$ be the probability vector of stationary state probabilities where

$$\pi_m = \lim_{n \rightarrow \infty} P\,[\text{process is in } m\text{th state on } n\text{th step}] \qquad (2)$$

As is well known, we solve for $\boldsymbol{\pi}$ from the eigenvector equation

$$\boldsymbol{\pi} = \boldsymbol{\pi} H \qquad (3)$$

Also, since H is doubly stochastic, the solution is immediately that

$$\pi_m = \frac{1}{6} \qquad 1 \leq m \leq 6 \qquad (4)$$

(where, of course,

$$\sum_m \pi_m = 1$$

has been used). Note that states 1, 4, and 5 give $k_i = 1$ whereas states 2, 3, and 6 give $k_i = 2$.

We are interested in calculating two probability distributions. The first is for the random variable U_i where

$$U_i = j - i \tag{5}$$

if $Y_j = X_i$. That is, U_i is equal to the relative shift of X_i from its original position (i) in the unpermuted sequence to its new position (j) in the permuted sequence. In SPS 37-62, Vol. III, it was shown that X_i will be "bumped out" of the P register at step $i + d_i - 2$ if k_i is next repeated d_i steps later, where $d_i \in \{1, 2, 3\}$. Thus,

$$U_i = d_i - 2$$

and so $U_i \in \{-1, 0, 1\}$. The second distribution of interest is for the random variable V_i where

$$V_i = n - m \tag{6}$$

if $Y_i = X_m$ and $Y_{i+1} = X_n$. That is, V_i is the difference in positions in the original (unpermuted) sequence of the ith and $(i + 1)$th samples which appear in the permuted sequence. For example, if $\{X_i\}$ permutes into $\{Y_i\}$ as shown in Table 1, then $\{U_i\}$ and $\{V_i\}$ are as given in that table.

Table 1. Example of sequences $\{U_i\}$ and $\{V_i\}$

i	X_i	Y_i	U_i	V_i
1	X_1	X_2	1	−1
2	X_2	X_1	−1	3
3	X_3	X_4	1	−1
4	X_4	X_3	−1	2
5	X_5	X_5	0	1
6	X_6	X_6	0	1
7	X_7	X_7	0	
•	•	•	•	•
•	•	•	•	•
•	•	•	•	•

We now compute $P[U_i = k]$ and $P[V_i = k]$. From the state diagram in Fig. 1, we immediately see that beginning in each state, there is a short *deterministic* sequence of key symbols that are generated independently of $\{c_i\}$. These are listed in Table 2 where it is assumed that we are in state m just prior to step i and generate the key symbol k_i upon leaving that state. Note the duality between states 1 and 6, 2 and 5, and 3 and 4.

Table 2. Deterministic portion of $\{k_i\}$ given state at step i

Initial state m	k_i	k_{i+1}	k_{i+2}	k_{i+3}
1	1	2	2	1
2	2	1	2	
3	2	2		
4	1	1		
5	1	2	1	
6	2	1	1	2

In order to calculate the distributions for U_i and V_i, we only need the distribution of the next four key symbols from a given state. We already know the length-4 sequence (which is deterministic) following states 1 and 6. From state 2, we go to states 1 or 5 (each with probability ½) which, from Table 2, must then give the length-4 sequences (following state 2) as 2122 and 2121, respectively. By duality, state 5 must give 1211 and 1212 (each with probability ½). From state 3, we go to states 2 or 6, which give 2212 and 2211, respectively (each with probability ½). Thus, the probability of length-4 sequences from each state is known (Table 3).

Table 3. Length-4 sequences of key symbols from various states

Initial state	Possible length-4 sequences of key symbols	Conditional probability of sequence
1	1 2 2 1	1
2	2 1 2 2	½
2	2 1 2 1	½
3	2 2 1 2	½
3	2 2 1 1	½
4	1 1 2 2	½
4	1 1 2 1	½
5	1 2 1 2	½
5	1 2 1 1	½
6	2 1 1 2	1

Now to find $P[U_i = k]$, $k = -1, 0, 1$, recall that $U_i = d_i - 2$. From this last and from Table 3 we have

$$\begin{aligned} P[U_i = -1] &= P[d_i = 1] \\ &= P[k_i = k_{i+1}] \\ &= \pi_3 + \pi_4 \\ &= \frac{1}{3} \end{aligned} \tag{7}$$

$$\begin{aligned} P[U_i = 0] &= P[d_i = 2] \\ &= P[k_i = k_{i+2} \neq k_{i+1}] \\ &= \pi_2 + \pi_5 \\ &= \frac{1}{3} \end{aligned} \tag{8}$$

$$\begin{aligned} P[U_i = 1] &= [d_i = 3] \\ &= [k_i = k_{i+3} \neq k_{i+1} = k_{i+2}] \\ &= \pi_1 + \pi_6 \\ &= \frac{1}{3} \end{aligned} \tag{9}$$

Thus, from Eqs. (7), (8), and (9), we have

$$P[U_i = k] = \frac{1}{3} \qquad k = -1, 0, 1 \tag{10}$$

Now we calculate $P[V_i = k]$. We are interested in observing two adjacent symbols in the $\{Y_i\}$ sequence. These may be studied by inspecting Table 3 and observing the samples generated as a result of the third and fourth key symbols in each sequence shown. Recall that if the key sequence is $k_{i-1}, 1, 1, 2$ (or $k_{i-1}, 2, 2, 1$) then k_{i-1} must be 2 (or 1) since each key symbol must occur at least once in each string of three. Thus, from state 1, the key sequence $k_i = 1$, $k_{i+1} = 2$, $k_{i+2} = 2$, $k_{i+3} = 1$ would produce $Y_i = X_{i+1}$, $Y_{i+1} = X_i$ giving $V_i = -1$ from Eq. (6). Similar calculations are possible for the other states, and are summarized in Table 4 in a fashion similar to Table 3.

Since $\pi_m = 1/6$ for $m = 1, 2, \cdots, 6$, we may then calculate $P[V_i = k]$ from

$$P[V_i = k] = \sum_{m=1}^{6} P[V_i = k | m]\, \pi_m \tag{11}$$

where $P[V_i = k|m]$ is given as the last column in Table 4 for all non-zero terms. Thus,

$$P[V_i = k] = \left\{ \begin{array}{ll} \frac{1}{3} & k = -1 \\ \frac{1}{6} & k = 1 \\ \frac{1}{3} & k = 2 \\ \frac{1}{6} & k = 3 \\ 0 & \text{otherwise} \end{array} \right\} \tag{12}$$

Equations (10) and (12) give the distributions for U_i and V_i, respectively. Of more importance is the fact that U_i is *uniformly* distributed over $\{-1, 0, 1\}$. Figure 2 shows the experimentally obtained histograms for U_i (Fig. 2a) and V_i (Fig. 2b) where a sequence of 7500 samples X_i was used. This figure corresponds to our calculations in Eqs. (10) and (12).

3. The Concatenation of Simple Coders

In order to increase the span of samples over which we permute, it was suggested in SPS 37-62, Vol. III that we form a concatenation of M simple coders as shown in

Table 4. Calculation of V_i

Initial state	k_i	k_{i+1}	k_{i+2}	k_{i+3}	Y_i	Y_{i+1}	V_i	Conditional probability
1	1	2	2	1	X_{i+1}	X_i	-1	1
2	2	1	2	2	X_i	X_{i+2}	2	½
2	2	1	2	1	X_i	X_{i+1}	1	½
3	2	2	1	2	X_{i-1}	X_{i+1}	2	½
3	2	2	1	1	X_{i-1}	X_{i+2}	3	½
4	1	1	2	2	X_{i-1}	X_{i+2}	3	½
4	1	1	2	1	X_{i-1}	X_{i+1}	2	½
5	1	2	1	2	X_i	X_{i+1}	1	½
5	1	2	1	1	X_i	X_{i+2}	2	½
6	2	1	1	2	X_{i+1}	X_i	-1	1

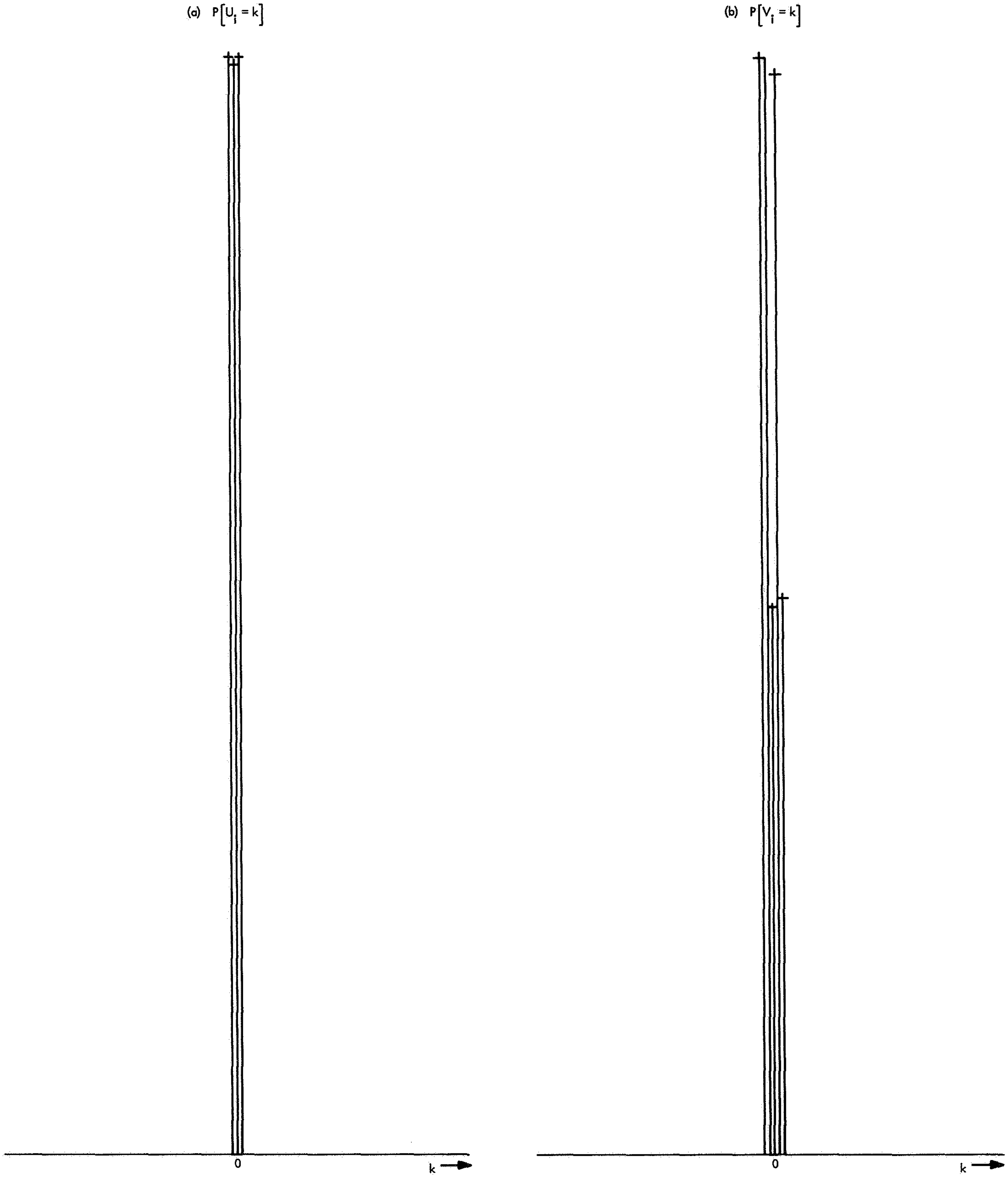

Fig. 2. Histograms for U_i and V_i

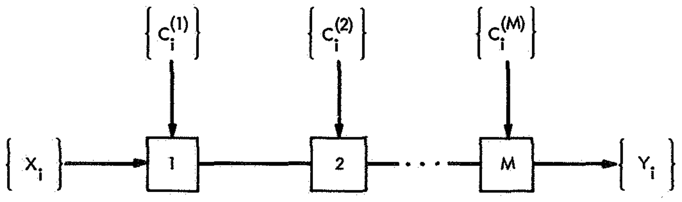

Fig. 3. *M*-level encoder concatenation

Fig. 3. In this configuration, the mth stage uses the pseudorandom sequence $\{C_i^{(m)}\}$ to generate the mth key sequence $\{k_i^{(m)}\}$. The decoder is again a chain of encoders in the reverse order such that the mth decoder key sequence, $\{K_i^{(m)}\} = \{k_i^{(M-m+1)}\}$ (SPS 37-62, Vol. III).

We may analyze the mixing behavior of this chain of M simple coders as follows: From Eq. (10) we know that $U_i = -1, 0, 1$, each with probability ⅓. If we take the permuted output from stage 1 of Fig. 3 and feed it into a second independent stage as shown, the output sequence $\{Y_i^{(2)}\}$ from the second stage will be a permutation of the first permuted sequence. Define $U_i^{(2)}$ as

$$U_i^{(2)} = j - i \qquad (13)$$

if $Y_j^{(2)} = X_i$, and so $U_i^{(2)}$ is the relative shift of X_i from its original position, i, in the unpermuted sequence to its new position, j, in the twice permuted sequence. Similarly, we define

$$U_i^{(m)} = j - i \qquad (14)$$

if $Y_j^{(m)} = X_i$ where $\{Y_i^{(m)}\}$ is the m-times permuted output sequence from the mth stage.

Since all the permutations are independent of each other (i.e., $\{C_i^{(m)}\}$ are independent pseudorandom sequences), then the random variable $U_i^{(2)}$ is merely the sum of two independent random shifts giving

$$P\,[U_i^{(2)} = k] = \sum_{j=-1}^{1} P_1\,[U_i = j]\,P_2\,[U_{i+j} = k - j] \qquad (15)$$

where $P_\alpha\,[U_i = j]$ is the probability distribution for the relative shift of position to the ith input sample in the αth stage ($\alpha = 1, 2, \cdots, M$). Clearly, the summation in Eq. (15) is the convolution of the distribution $P\,[U_i = k]$, which is itself evaluated at the kth position. Let us denote convolution by $*$, giving

$$P\,[U_i^{(2)} = k] = P\,[U_i = k_1] * P\,[U_1 = k_2] \qquad (16)$$

Clearly, also

$$P\,[U_i^{(m)} = k] = \overbrace{P\,[U_i = k_1] * P\,[U_i = k_2] * \cdots * P\,[U_i = k_m]}^{m\text{ times}} \qquad (17)$$

since the $U_i^{(m)}$ is the sum of m independent random shifts. The author knows no simple form for expressing the probability in Eq. (17). One may define the generating function for $P\,[U_i^{(m)} = k]$ as

$$G_m(Z) \equiv \sum_{k=-m}^{m} P\,[U_i^{(m)} = k]\,Z^k \qquad (18)$$

We may then use the usual properties of generating functions for sums of independent random variables to get

$$G_m(Z) = [G_1(Z)]^m \qquad (19)$$

From Eqs. (10) and (18), we then obtain

$$G_1(Z) = \frac{Z^{-1} + 1 + Z}{3} \qquad (20)$$

and, thus, from Eq. (19),

$$G_m(Z) = \left(\frac{1 + Z + Z^2}{3Z}\right)^m \qquad (21)$$

From Eq. (18), the value for $P\,[U_i^{(m)} = k]$ may be obtained as the coefficient of Z^k ($k = 0, \pm 1, \cdots, \pm m$) in Eq. (21). We may also write

$$G_m(Z) = \left(\frac{1}{3}\right)^m \sum_{i=0}^{m} \sum_{j=0}^{i} \binom{m}{i} \binom{i}{j} Z^{m-i-j} \qquad (22)$$

Inversion of Eq. (22) has not been carried out. However, we may compute $P\,[U_i^{(m)} = k]$ from the following Pascal-like triangle:

$$\begin{array}{ccccccccccccc}
 & & & & & & 1 & & & & & & \\
 & & & & & 1 & 1 & 1 & & & & & \\
 & & & & 1 & 2 & 3 & 2 & 1 & & & & \\
 & & & 1 & 3 & 6 & 7 & 6 & 3 & 1 & & & \\
 & & 1 & 4 & 10 & 16 & 19 & 16 & 10 & 4 & 1 & & \\
 & 1 & 5 & 15 & 30 & 45 & 51 & 45 & 30 & 15 & 5 & 1 & \\
1 & 6 & 21 & 50 & 90 & 126 & 141 & 126 & 90 & 50 & 21 & 6 & 1
\end{array}$$

This triangle is created by making an element equal to the sum of its *three* immediate neighbors in the row above it. Thus, to find $P\,[U_i^{(m)} = k]$, we first locate the kth element (from the center vertical column) in the mth row; the top element of the triangle corresponds to $n = k = 0$. We then take this element and divide by 3^m. For example,

$$P\,[U_i^{(5)} = -4] = \frac{5}{3^5} = \frac{5}{243}$$

Obviously, however, the distribution $P\,[U_i^{(m)} = k]$ is tending to the gaussian distribution in the limit as $m \to \infty$. Therefore, the cumulative distribution can easily be approximated. In any case, however, we have *not* achieved the performance we were seeking; namely, a *uniform* permutation over a large number of shifts. We have obtained a near-gaussian shape that does not spread fast enough as M increases (it spreads like $\sqrt{M}$ instead of like M). Empirical results from simulation are given in Fig. 4, where we show the histograms for $U_i^{(m)}$ for $m = 2$, 3, 5, 10, and 30 ($m = 1$ is given in Fig. 2). Also shown are the histograms for $V_i^{(m)}$ where

$$V_i^{(m)} = n - p \tag{23}$$

if $Y_i^{(m)} = X_p$ and $Y_{i+1}^{(m)} = X_n$ with the same interpretation as for V_i in Eq. (6). (The computation of $P\,[V_i^{(m)} = k]$ is very difficult and is not discussed further.) Note the rapid convergence to gaussian for both distributions.

4. An Improved Configuration—the Ternary Tree

The concatenation of M simple coders leads to a permutation that is not distributed uniformly over the range $[-M, M]$, as was seen in *Subsection 3*.

We now consider the ternary tree configuration shown in Fig. 5. This figure shows the case $M = 13$ where each square box corresponds to a simple coder whose properties are discussed in *Subsection 2*. The interpretations of the connections is as follows: Consider Coder 10; the three inputs to this coder come from the outputs of coders 1, 2, and 3. The connection notation means that coder 10 receives an input from coder 1, followed by an input from coder 2, followed by an input from coder 3 (this sequence is repeated indefinitely). The input sequence

$$\{X_1, X_2, X_3, \cdots,\}$$

is separated into nine sequences:

$$\{X_1, X_{10}, X_{19}, \cdots,\}, \{X_2, X_{11}, X_{20}, \cdots,\}, \cdots, \{X_9, X_{18}, X_{27}, \cdots,\}$$

In general, we have A tiers of coders where the ath tier contains 3^{a-1} simple coders ($a = 1, 2, \cdots, A$). In this case, we have

$$M = \frac{3^A - 1}{2} \tag{24}$$

The input stream is separated into 3^{A-1} sequences. Figure 5 shows the case $A = 3$, $M = 13$.

As for decoding, we merely create a matching decoding ternary tree in the reverse configuration. As an example, consider the two-tier ($A = 2$) case shown in Fig. 6. Here, the input sequence $\{X_i\}$ is passed through a splitting box σ that creates 3 streams (3^{2-1}) as shown. The coder creates the permuted output sequence $\{Y_i\}$. The decoder accepts the sequence $\{Y_i\}$ as input after transmission over some channel and passes it through the reverse tree decoder. This produces three output streams that are then passed through the merging box μ to recreate the original sequence $\{X_i\}$. The pseudorandom sequence $\{C_i^{(m)}\}$ for coder box m is also used for decoder box m'.

We now consider the shift $U_i^{(A)}$ defined for the A-tier system as

$$U_i^{(A)} = j - i \tag{25}$$

if $Y_j = X_i$ where the overall output sequence is $\{Y_i\}$. We will show that

$$P\,[U_i^{(A)} = k] = \left\{ \begin{array}{ll} 3^{-A} & k = 0, \pm 1, \cdots, \pm M \\ 0 & \text{otherwise} \end{array} \right\} \tag{26}$$

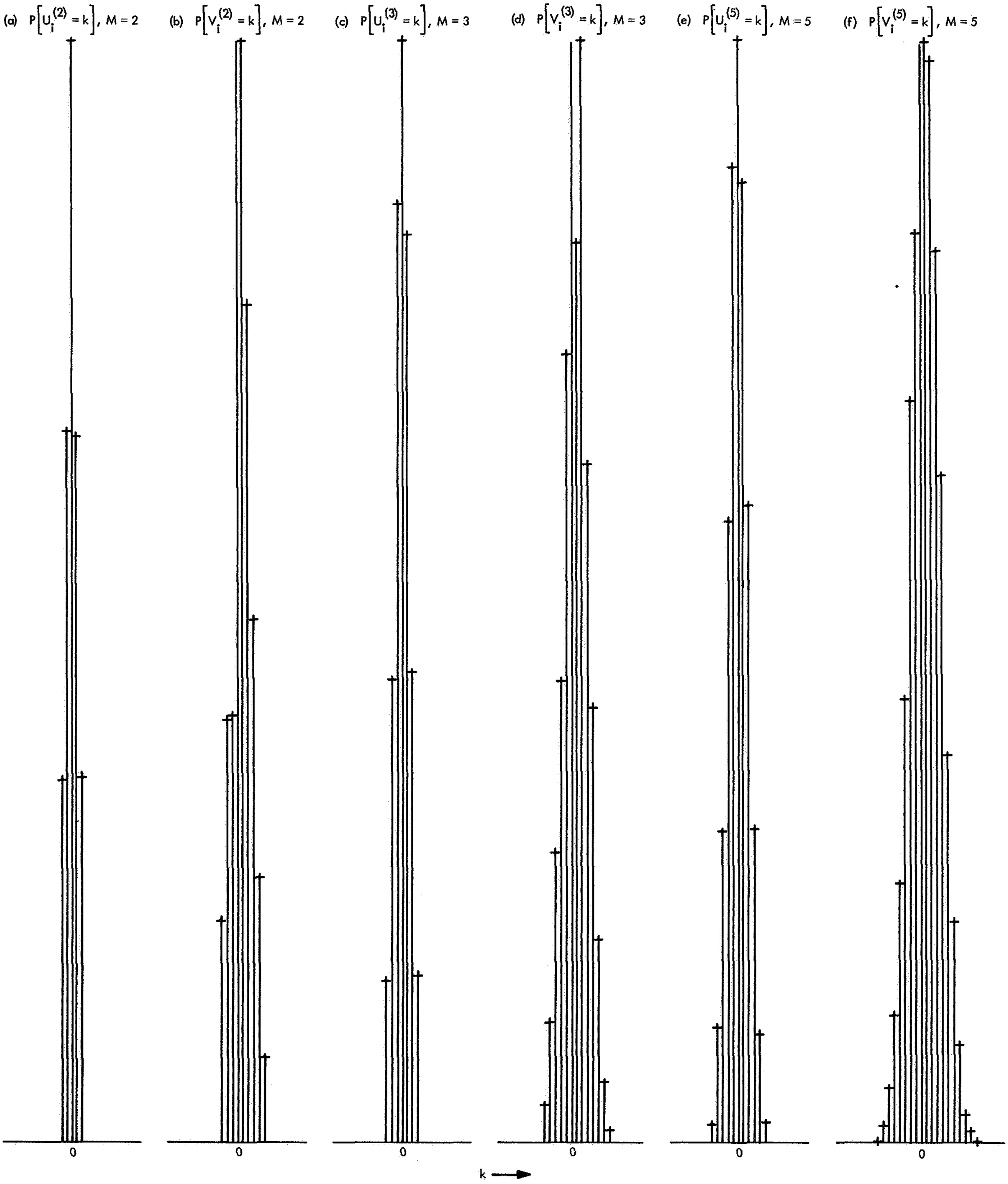

Fig. 4. Histograms for $U_i^{(m)}$ and $V_i^{(m)}$ for $m = 2, 3, 5, 10$, and 30 (for the concatenated structure)

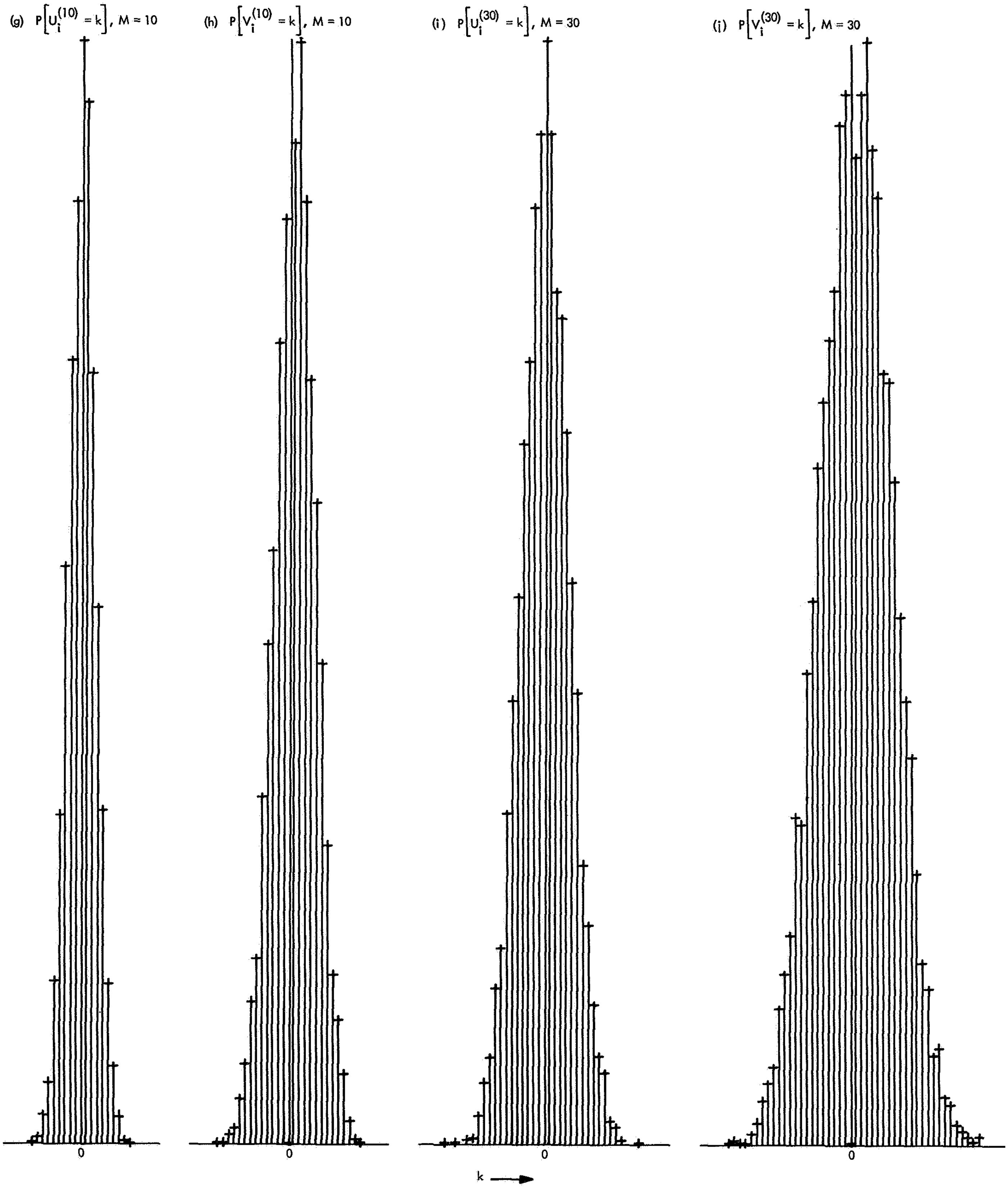

(g) $P\left[U_i^{(10)} = k\right]$, $M = 10$

(h) $P\left[V_i^{(10)} = k\right]$, $M = 10$

(i) $P\left[U_i^{(30)} = k\right]$, $M = 30$

(j) $P\left[V_i^{(30)} = k\right]$, $M = 30$

Fig. 4 (contd)

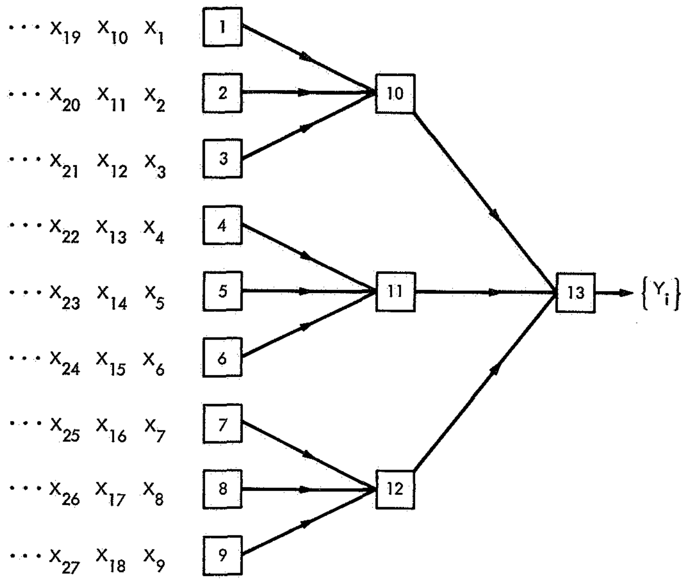

Fig. 5. The ternary tree structure

That is, $U_i^{(A)}$ is *uniformly* distributed over $3^A = 2M + 1$ positions. From Eq. (10), we know for $A = 1$ that

$$P\,[U_i^{(1)} = k] = 3^{-1} \qquad k = -1, 0, 1 \tag{27}$$

Now consider $A = 2$. For this case, we separate the input sequence into three subsequences as shown in Fig. 6. Consider X_8. In passing through coder 2, we have (from Eq. 27) that X_8 will appear in place of X_5, X_8, or X_{11}, each with probability ⅓. Then, when each of the singly permuted subsequences leave the first tier, the elements are interlaced as an input to coder 4. In that case, we have the following: if X_8 had moved to position 5 in passing through coder 2, then (in passing through coder 4) it will move to original positions 4, 5, or 6 (each with probability ⅓). If X_8 had remained in position 8, it will move to positions 7, 8, or 9. If X_8 had moved to position 11, it will now move to positions 10, 11, or 12. Since each of these nine possibilities is equally likely, we have proved Eq. (26) for $A = 2$. Thus, for $A = 3$ in Fig. 5, X_{14} will move to positions 4, 5, 6, 13, 14, 15, 22, 23, or 24 (each with probability ⅑) in passing through the first two tiers as just proven. Now, in a similar fashion, each of those nine possible positions moves is equally likely to three others in passing through the third tier. Thus X_{14} moves to positions $1, 2, 3, \cdots, 26$, or 27 (each with probability $1/27$) for $A = 3$. By induction, proof of Eq. (26) follows.

Define $V_i^{(A)}$ for A tiers as

$$V_i^{(A)} = n - p \tag{28}$$

if $Y_i = X_p$ and $Y_{i+1} = X_n$. The computation of $P\,[V_i^{(A)} = k]$ is also difficult in this case and is not carried out.

Figure 7 gives empirical results for the ternary tree. Histograms are shown for $U_i^{(A)}$ and $V_i^{(A)}$ for $A = 2, 3, 4$. Note the essentially uniform distribution for $U_i^{(A)}$, as we had been seeking! The distribution for $V_i^{(A)}$ remains gaussian-like with every third entry of larger value.

5. Conclusions

We have analyzed and experimented with the M-stage concatenation of simple coders for use in speech scrambling. As predicted, the performance is far below that which we require for effective scrambling.

We proposed a new topology, the ternary tree, for more effective scrambling and found that this structure produced the sought-after uniform distribution over $2M + 1$ positions (for M simple coders). The simple coders are such that the decoders are identical to the encoders. Thus, we propose to use this method for permuting sequences of speech samples.

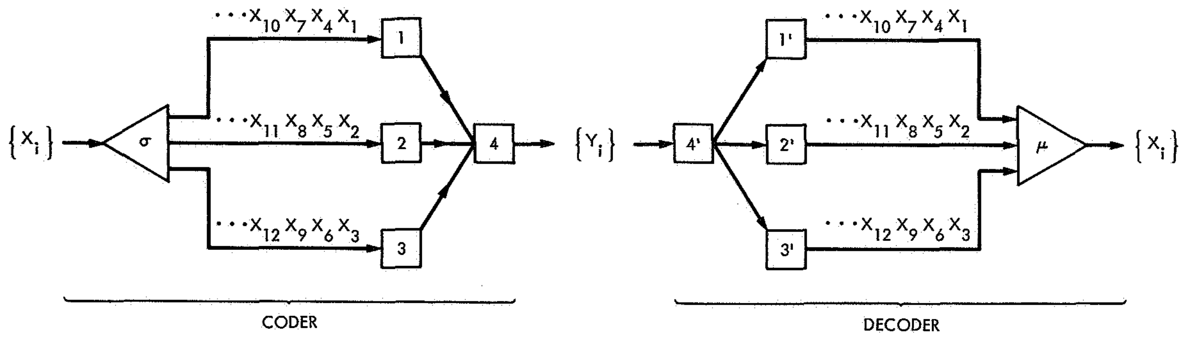

Fig. 6. Coder–decoder for $A = 2$

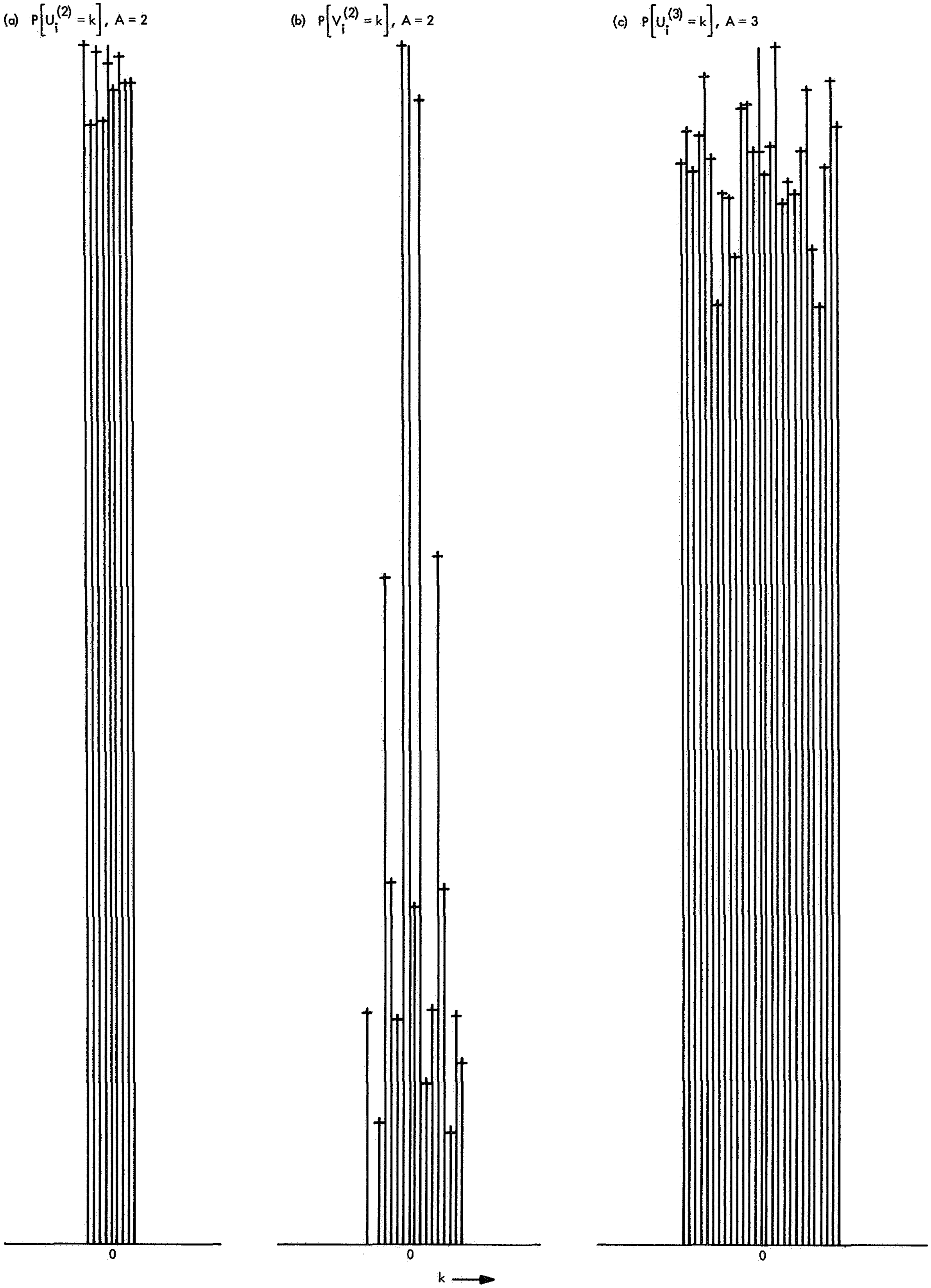

Fig. 7. Histograms for $U_i^{(A)}$ and $V_i^{(A)}$ for $A = 2$, 3, and 4 (for the ternary tree)

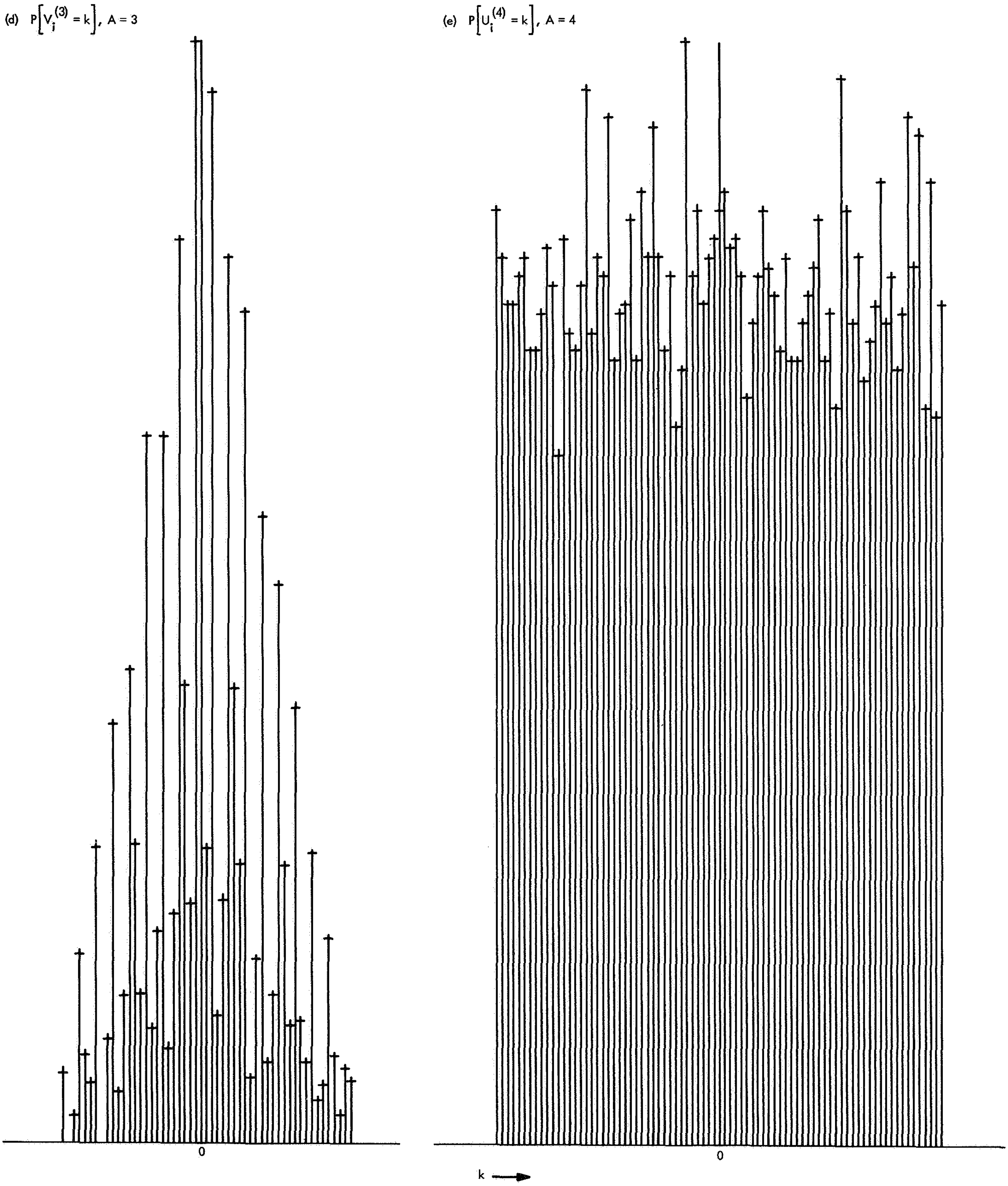

(d) $P\left[V_i^{(3)} = k\right]$, A = 3

(e) $P\left[U_i^{(4)} = k\right]$, A = 4

Fig. 7 (contd)

(f) $P\left[V_i^{(4)} = k\right]$, A = 4

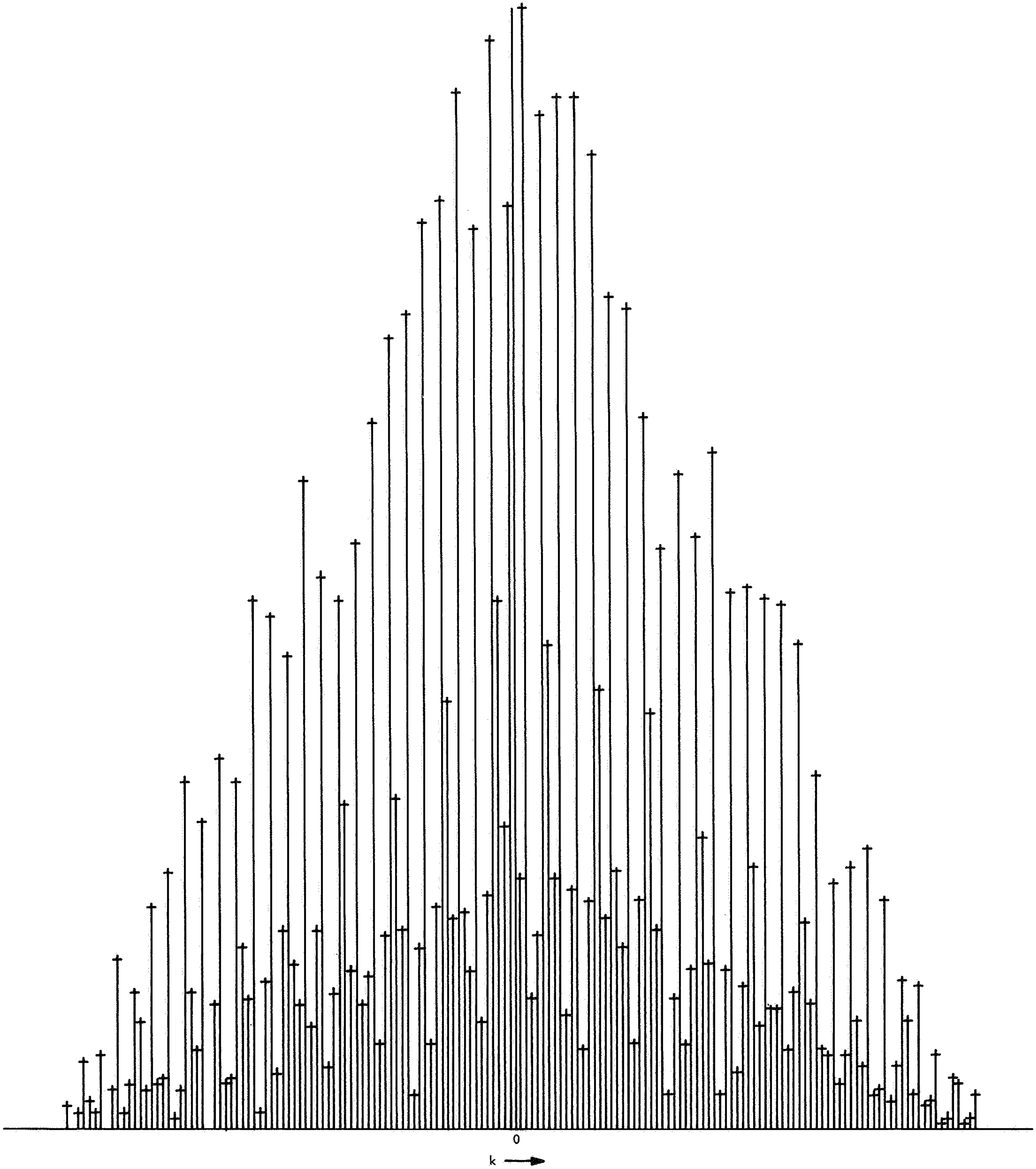

Fig. 7 (contd)

V. Communications Elements Research

TELECOMMUNICATIONS DIVISION

A. Large Spacecraft Antennas: Slotted Lens Antenna Study, *R. Woo*

1. Introduction

In SPS 37-59, Vol. III, pp. 57–61, a large zone-plate lens was described for use as a high-gain spacecraft antenna. This zone plate possessed an inherently low efficiency. Despite this low efficiency, the simplicity of construction and large error tolerances could allow an increase in size to compensate for the loss in efficiency and make the zone plate a feasible spacecraft antenna. In this article, a slotted lens antenna is proposed. This slotted lens also possesses the attractive feature of simple construction. The purpose of this article is to show that the potential efficiency of the slotted lens antenna offers an improvement over the zone-plate lens.

2. Principle of the Slotted Lens

Consider a thin planar surface illuminated by a spherical wave from a feed as shown in Fig. 1. The objective is to locate some slots on the planar surface such that the fields transmitted through the surface will experience a phase shift, designed to convert the spherical phase front to a nearly planar phase front. This will provide gain in the normal direction. A slotted lens is therefore simply a diffraction lens. It can be seen that, in principle, the surface on which the slots are located need not be planar.

3. Analysis of the Slotted Lens

Although the principle of the slotted lens is simple, analysis of this antenna is very complicated. The problem can be solved in three different ways. The first way consists of solving the boundary value problem for the most general configuration, i.e., arbitrary slots in arbitrary locations. A closed form solution of such a problem would be most difficult, if not impossible. The second way involves obtaining the solution for one slot and then combining such solutions for several slots. This method is rather impractical since the solution for one slot is complicated enough. When additional slots are considered, mutual coupling effects must be included and this would be a

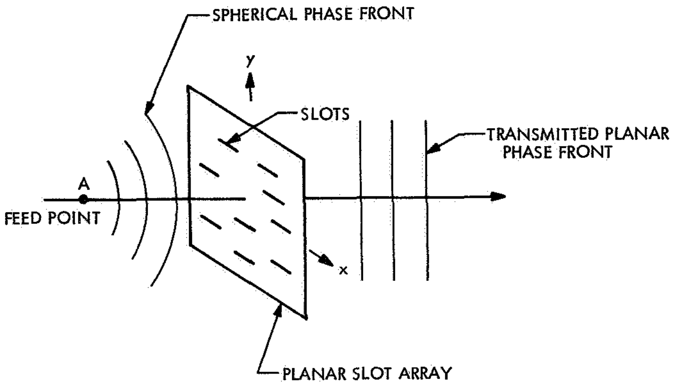

Fig. 1. Slotted lens antenna

difficult task. The third and most attractive way consists of first considering an infinite two-dimensional array of similar slots. Because of the periodicity and symmetry of this configuration, expressions giving a reasonable description of the transmitted wave can be obtained. The lens can then be designed in the following manner: First, the periodic pattern (*c* and *d* in Fig. 2) is chosen. The dimensions *a* and *b* of each slot are then determined to produce the desired transmission through that particular slot. These dimensions are computed on the basis that all other slots in the array are the same size. It is expected that the error introduced by this approximation is small since this closely represents the situation as seen by the slot.

4. Two-Dimensional Array of Slots

If the slots on a thin and infinite two-dimensional array of similar slots are smaller than one wavelength, then no higher order modes will propagate and the array can be represented by a shunt admittance across a transmission line (see Fig. 3). The value of this shunt admittance can be determined by a variational method (Ref. 1) and a point matching technique (Ref. 2). For the purpose of this article, no specific expressions need be considered. Instead, it is only necessary to use the fact that the array can be represented by a shunt admittance and that the desired value of shunt admittance can be controlled by adjusting the dimensions of the slot. The transmission coefficient T for the transmission line in Fig. 3 is simply given by

$$T = \frac{2}{2 + jB} \tag{1}$$

where B is the admittance normalized to the characteristic admittance of the transmission line. The amplitude $|T|$ and phase ϕ of T are then

$$|T| = \sqrt{\frac{4}{4 + B^2}} \tag{2}$$

$$\phi = -\tan^{-1}\frac{B}{2} \tag{3}$$

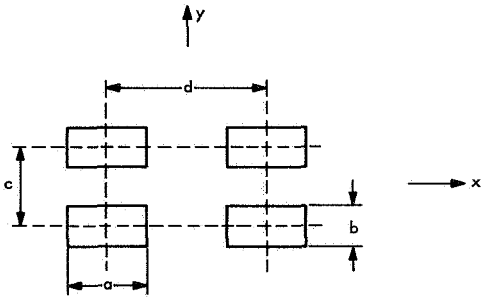

Fig. 2. Periodic pattern

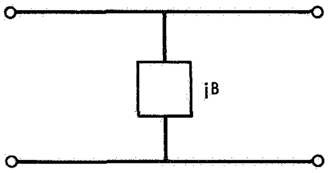

Fig. 3. Equivalent circuit representation

Plots of Eqs. (2) and (3) as a function of B are shown in Fig. 4. Several points are worth mentioning. It can be seen that the slots may only be used to produce phase shifts up to ±90 deg (±180 deg would be ideal). Moreover, amplitude and phase are related to each other in such a manner that the greater the phase change the smaller the amplitude. Thus, amplitude must be sacrificed at the expense of a phase change.

5. Efficiency of the Slotted Lens

To determine the design criteria for the slots and to compute the efficiency of the slotted antenna, the reciprocal of the situation depicted in Fig. 1 will be examined. In other words, a plane wave is assumed incident on the slotted lens from the right and the resultant field at point A is studied. If the array is transparent, then the resultant field and its components at point A are shown in the complex plane in Fig. 5. As can be seen, the component vectors *dr* form a spiral. This spiral converges to the point (1, 0) since the resultant field is normalized in magnitude and phase to the incident field. The component vectors at the beginning of the spiral are due to contributions from the aperture area nearest the axis. As the off-axis distance on the aperture is increased, component vectors of increasing phase and diminishing magnitude are added and the spiral eventually converges to the point (1, 0).

In optimizing the gain of the slotted lens antenna, phase is not the sole criterion that must be considered. As discussed previously, phase and amplitude are interdependent, and optimizing one does not ensure gain maximization. The correct procedure is to re-orient the vectors *dr* in Fig. 5 in view of Eqs. (2) and (3) so as to maximize their components in the *x* direction. The first turn of the spiral in Fig. 5 is shown in Fig. 6. A component vector *dr* with amplitude $|dr|$ and phase θ is also shown. The adjusted vector dr' then has magnitude $|dr|\,|T|$ and phase $\theta + \phi$, where $|T|$ and ϕ are given in Eqs. (2) and (3). The component of dr' in the x direction is

$$dx = |dr|\,|T|\cos(\theta + \phi)$$

$$= \frac{4}{4 + B^2}\cos\theta + \frac{2B}{4 + B^2}\sin\theta \tag{4}$$

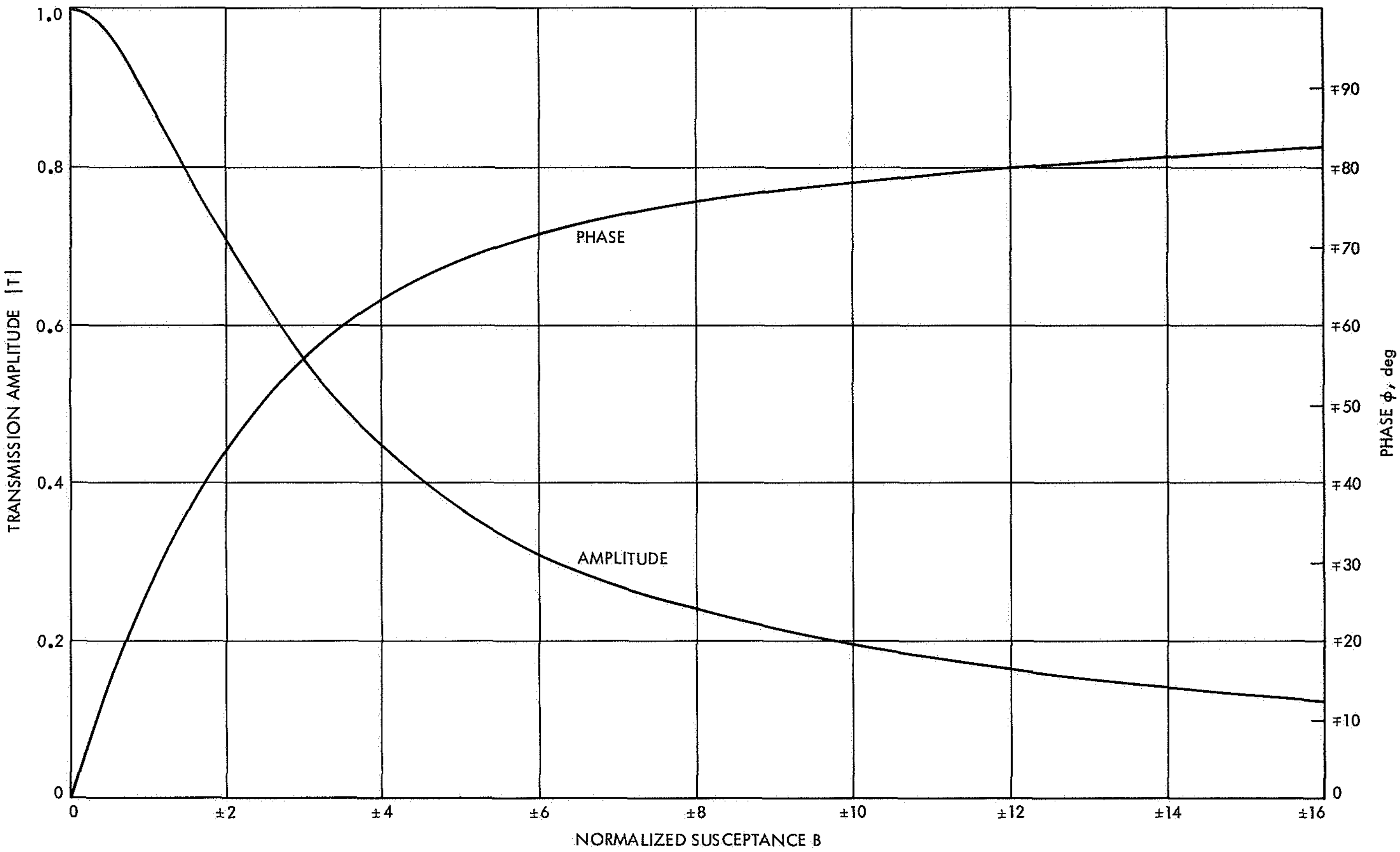

Fig. 4. Phase and amplitude vs *B*

In order to maximize *dx*, Eq. (4) is differentiated with respect to *B* and set to zero. The following condition results:

$$B^2 + 4B \cot\theta - 4 = 0 \qquad (5)$$

Equation (5) is a quadratic equation and therefore has two solutions, i.e.,

$$B = 2\tan\frac{\theta}{2}$$

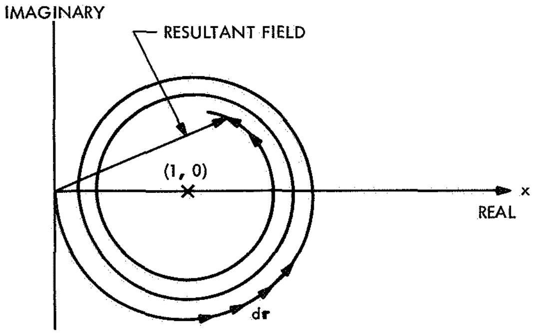

Fig. 5. Field at point A

and

$$B = -\frac{2}{\tan\frac{\theta}{2}}$$

Using Fig. 6 and Eq. (3), it can be shown that the appropriate solution is

$$B = 2\tan\frac{\theta}{2} \qquad (6)$$

Substitution of Eq. (6) into Eqs. (2) and (3) yields

$$|T| = \cos\frac{\theta}{2} \qquad (7)$$

and

$$\phi = \begin{cases} -\dfrac{\theta}{2}, & 0 \leqq \theta \leqq \pi \\ -\dfrac{\theta}{2} + \pi, & \pi \leqq \theta \leqq 2\pi \end{cases} \qquad (8)$$

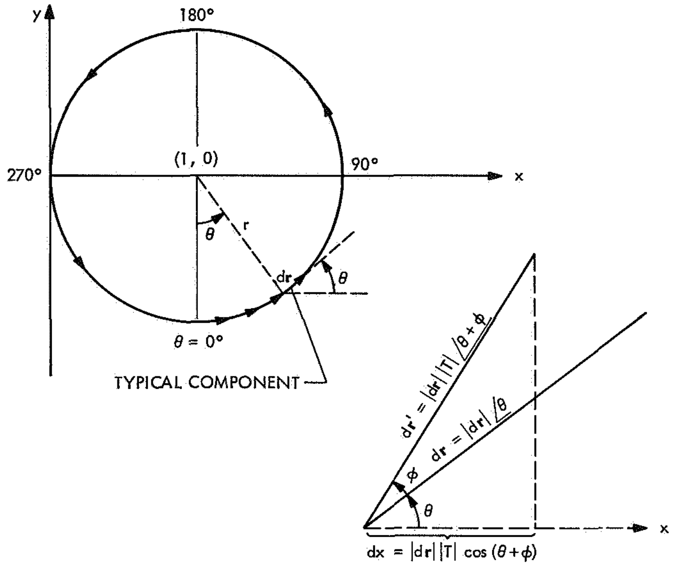

Fig. 6. First spiral

Also, Eq. (4) becomes

$$dx = |\,dr\,|\ \frac{1}{2}(1+\cos\theta) \tag{9}$$

Now, $|dr| = r d\theta$. Therefore, the resultant vector in the x direction for $0 \leqq \theta \leqq 2\pi$ is

$$\int_0^{2\pi} \frac{1}{2}(1+\cos\theta)\,r\,d\theta = \pi r \tag{10}$$

Efficiency is defined as the ratio of the power intensity at a far-field point to the intensity that would exist if the field across the aperture were uniform in amplitude and phase. If the field across the aperture were uniform in amplitude and phase, the resultant vector would be $2\pi r$. The ideal slotted lens then has an efficiency of

$$\left(\frac{\pi r}{2\pi r}\right)^2 = 25\% \tag{11}$$

For comparison, in the ideal zone plate, the resultant vector in the x direction is

$$\int_{3\pi/2}^{2\pi} r\cos\theta\, d\theta + \int_0^{\pi/2} r\cos\theta\, d\theta = 2r \tag{12}$$

and the efficiency is

$$\left(\frac{2r}{2\pi r}\right)^2 = 10.1\% \tag{13}$$

The above results are summarized in Fig. 7, where the first spiral of Fig. 5 is shown for (a) the zone-plate lens, (b) the slotted lens, and (c) the perfect lens. Relative results are to scale. Each spiral is divided into 12 component vectors and the adjusted vectors are dashed. The resultant vectors are also shown.

6. Conclusion

It has been shown that the slotted lens has a theoretical efficiency over twice that of a zone-plate lens. Before a proper slotted lens can be designed, a practical slot size range that gives the range of $B(-\infty \text{ to } +\infty)$ must be determined. With this information secured, an experimental slotted lens can then be built. It must be emphasized that because of the assumptions made, the feasibility of the slotted lens can only be checked after an experimental model is built and tested.

References

1. Kieburtz, R. B., and Ishimaru, A., "Scattering by a Periodically Apertured Conducting Screen," *IRE Trans. Ant. Propagation*, AP-9, No. 6, pp. 506–514, Nov. 1961.

2. Ott, R. H., Kouyoumjian, R. G., and Peters, L., Jr., "Scattering by a Two-Dimensional Periodic Array of Narrow Plates," *Radio Science*, Vol. 2 (new series), No. 11, pp. 1347–1359, Nov. 1967.

(a) ZONE-PLATE LENS

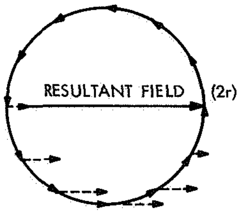

(b) SLOTTED LENS

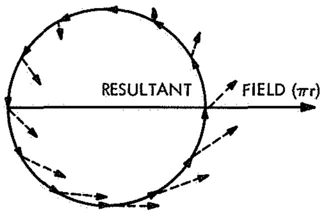

(c) PERFECT LENS

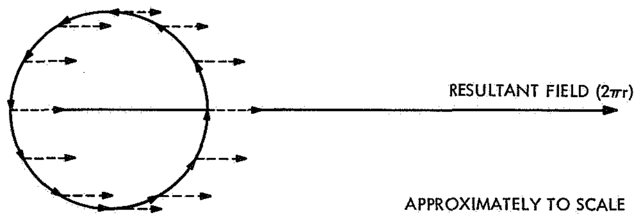

APPROXIMATELY TO SCALE

Fig. 7. Vector diagrams

VI. Spacecraft Telecommunications Systems

TELECOMMUNICATIONS DIVISION

A. Outer Planet Telemetry and Command: Exact Power Spectrum of PN Codes, *D. James*

1. *Introduction*

This article describes a method for finding the power spectrum of a PN-coded square wave modulated with a square wave subcarrier of a frequency that is an integer multiple of the PN clocking frequency. Similar work was done by G. D. Hase (Ref. 1) computing the power spectrum of an unmodulated PN-coded square wave, and several modulated waveforms. However, his method involved tedious integrations and trigonometric substitutions. Some analysis was done by Titsworth and Welch (Ref. 2) for randomly coded square waves, which can be approximated by a PN code. Unlike these references, the solution presented here solves the problem in a simple and exact method.

After solving for the general case, the solution is used to analyze the power spectrum of a waveform used in a digital spacecraft command system.

2. The General Case

For generality, consider the problem of computing the power spectrum of a PN square waveform of p bits modulated with a subcarrier with a frequency of n times the PN clocking frequency.

The method for solving this problem will be to consider the modulated PN waveform as the output $y(t)$ of the system:

$$x(t) \rightarrow \boxed{h_0(t)} \rightarrow \boxed{h_1(t)} \rightarrow y(t)$$

where $x(t)$ is a PN type of impulse train. A *one* in the PN code corresponds to a positive impulse, and a *zero* corresponds to a negative impulse (Fig. 1); $h_0(t)$ consists of

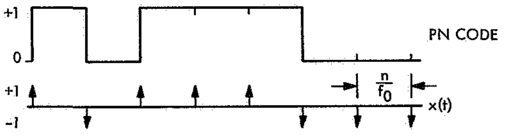

Fig. 1. PN-generated impulse train

impulses spaced $1/f_0$ apart (Fig. 2); $h_1(t)$ is the impulse response shown in Fig. 3.

Looking at the system in terms of the power density spectrum, it can be described by

$$S_0(f) \rightarrow \boxed{H_0(f)} \rightarrow \boxed{H_1(f)} \rightarrow S_2(f)$$

$S_0(f)$ and $S_2(f)$ are the power spectrums of the input and output. From this analysis it is clear that

$$S_2(f) = S_0(f)\,|H_0(f)|^2\,|H_1(f)|^2$$

The problem reduces to finding $S_0(f)$, $|H_0(f)|^2$ and $|H_1(f)|^2$. The procedure is straightforward, and the results are as follows:

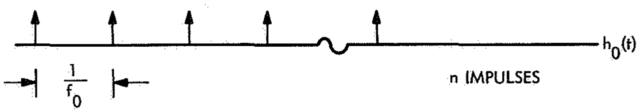

Fig. 2. Impulse response $h_0(t)$

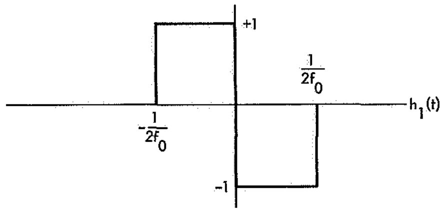

Fig. 3. Impulse response $h_1(t)$

---

a. $S_0(f)$

$$S_0(f) = \frac{f_0^2(p+1)}{n^2p^2} \sum_{\substack{m=-\infty \\ m \neq kp,\, k = \cdots -1, 0, +1, \cdots}}^{\infty} u_0\left(f - \frac{mf_0}{np}\right) + \frac{f_0^2}{n^2p^2} \sum_{m=-\infty}^{\infty} u_0\left(f - \frac{mf_0}{n}\right)$$

u_0 is the impulse function

b. $|H_0(f)|^2$

For n odd

$$\left|H_0\left(\frac{kf_0}{np}\right)\right|^2 = \left[1 + 2\sum_{m=1}^{\frac{n-1}{2}} \cos\left(2\pi\frac{km}{np}\right)\right]^2$$

For n even

$$\left|H_0\left(\frac{kf_0}{np}\right)\right|^2 = \left[2\sum_{\substack{m=1 \\ \text{odd}}}^{n-1} \cos\left(\pi\frac{km}{np}\right)\right]^2$$

c. $\left|H_1\left(\frac{kf_0}{np}\right)\right|^2$

$$\left|H_1\left(\frac{kf_0}{np}\right)\right|^2 = \frac{1}{f_0^2}\sin\left(\frac{k\pi}{2np}\right)\Big/\left(\frac{k\pi}{2np}\right)^2$$

$S_2(f)$ consists of impulses of area $S_2'(f)$, determined by the equations:

For n odd

$$k = \ell p, \qquad \ell = \cdots, -1, 0, +1, \cdots$$

$$S_2'\left(\frac{kf_0}{np}\right) = \left(\frac{2}{k\pi}\right)^2 \left[\sin^4\left(\frac{k\pi}{2np}\right)\right]\left[1 + 2\sum_{m=1}^{\frac{n-1}{2}} \cos\left(\pi\frac{mk}{np}\right)\right]^2$$

$$k \neq \ell p, \qquad \ell = \cdots, -1, 0, +1, \cdots$$

$$S_2'\left(\frac{kf_0}{np}\right) = (p+1)\left(\frac{2}{k\pi}\right)^2 \left[\sin^4\left(\frac{k\pi}{2np}\right)\right]\left[1 + 2\sum_{m=1}^{\frac{n-1}{2}} \cos\left(2\pi\frac{mk}{np}\right)\right]^2$$

For n even

$$k = \ell p, \qquad \ell = \cdots, -1, 0, +1, \cdots$$

$$S_2'\left(\frac{kf_0}{np}\right) = \left(\frac{2}{k\pi}\right)^2 \left[\sin^4\left(\frac{k\pi}{2np}\right)\right]\left[2\sum_{\substack{m=1\\ \text{odd}}}^{n-1} \cos\left(\pi\frac{km}{np}\right)\right]^2$$

$$k \neq \ell p$$

$$S_2'\left(\frac{kf_0}{np}\right) = (p+1)\left(\frac{2}{k\pi}\right)^2 \left[\sin^4\left(\frac{k\pi}{2np}\right)\right]\left[2\sum_{\substack{m=1\\ \text{odd}}}^{n-1} \cos\left(\pi\frac{km}{np}\right)\right]^2$$

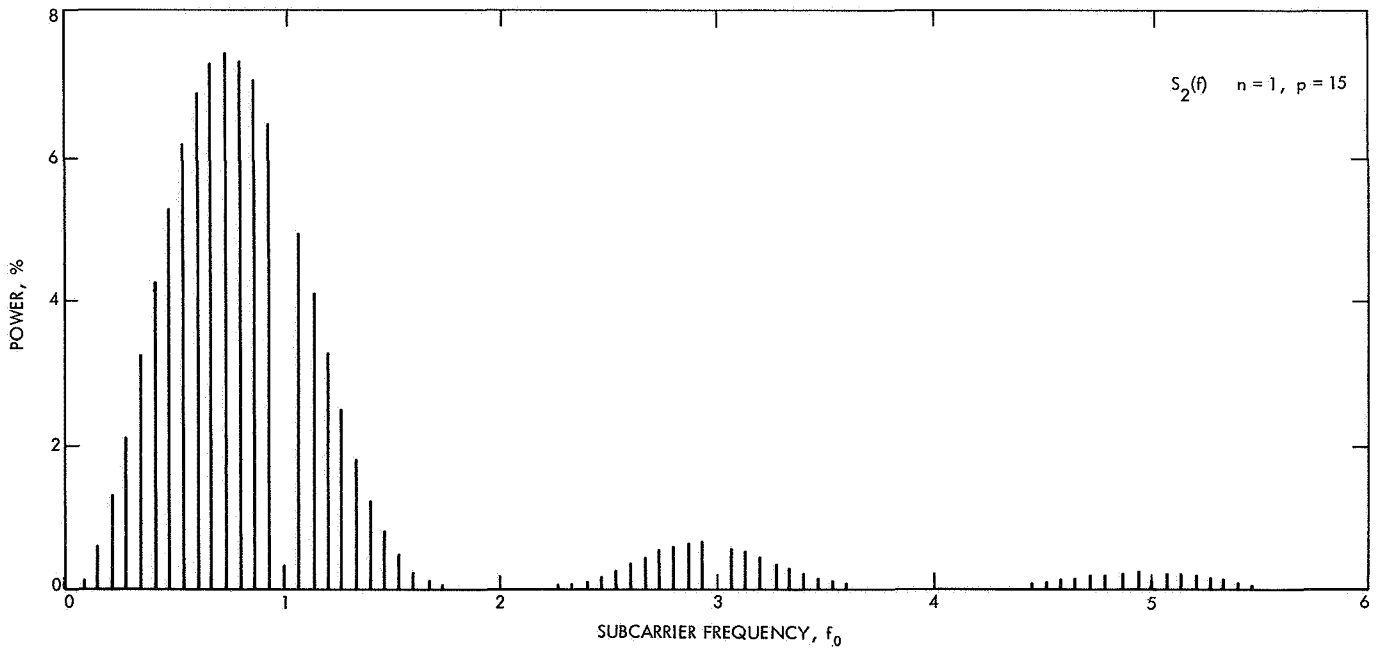

Fig. 4. Power density spectrum for a 15-bit PN-coded square wave modulated with a square wave subcarrier of a frequency equal to the PN clocking frequency

3. Example

The general problem was solved to find the power spectrums of a 15-bit PN-coded square wave modulated with a square wave subcarrier of the same frequency as the PN clocking frequency. In this case, the power spectrum is found to consist of impulses in frequency of height $S_2'(f)$ (Fig. 4).

Example

$$n = 1$$

$$p = 15$$

For $k = 15(2\ell + 1)$, $\ell = \cdots, -1, 0, +1, \cdots$

$$S_2'\left(\frac{kf_0}{15}\right) = \left(\frac{2}{k\pi}\right)^2$$

For $k \neq 15\ell$, $\ell = \cdots, -1, 0, +1, \cdots$

$$S_2'\left(\frac{kf_0}{15}\right) = 16\left(\frac{2}{k\pi}\right)^2 \sin^4\left(\frac{k\pi}{30}\right)$$

References

1. Hase, G. D., "Analysis of Power Spectrums of Pseudo-Noise Waveforms," Technical Memorandum 530-2853-1, Apollo Transponder Section, Telecommunications Laboratory, Military Electronics Division, Western Center, Scottsdale, Ariz.
2. Titsworth, R. C., and Welch, L. R., "Power Spectra of Signals Modulated by Random and Pseudorandom Sequence," Technical Report 32-140, Jet Propulsion Laboratory, Pasadena, Calif., July 24, 1961.

B. Effect of Predemodulation Filtering on the Correlation and Error Signals in a Pseudonoise Receiver, *M. A. Koerner*

1. Introduction

Spread spectrum techniques are commonly used in communication and radio tracking systems to provide security against interfering signals. The system considered in this article is a communication and radio tracking link for a Tracking and Data Relay Satellite Network (TDRSN).[1] This application requires a radio link having immunity against both multipath signals and interfering signals from external sources.

The effectiveness of the frequency spreading will be limited by the frequency response of the channel through which the wide-band signal must be transmitted. The frequency response of the channel may be imperfect for several reasons. A filter may be required at the transmitter to reduce the signal power outside the allocated frequency band to an acceptable level. A filter may be required at the receiver to remove interfering out-of-band signals. The frequency response of the channel may be limited by the bandwidth attainable in the radio equipment itself. Finally, the frequency response of the channel may be impaired by band-reject filters inserted in the receiver IF amplifier to augment the interference-rejection capability of the receiver over narrow frequency bands.

This analysis examines the effect of predemodulation filtering on a system where the frequency spreading is achieved by multiplying a phase-modulated carrier with a binary-valued (± 1) signal. The receiver for this communication link synchronizes a locally generated replica of this binary-valued (± 1) modulation with that carried by the received signal and recovers the phase-modulated carrier by multiplying the received signal with the locally generated binary signal. A conventional phase-locked-loop receiver then demodulates the subcarrier signals which were phase-modulated on the carrier signal.

The receiver for this communication system computes two observables, the correlation $C(\hat{\tau})$ and the error signal $E(\hat{\tau})$. $C(\hat{\tau})$ and $E(\hat{\tau})$ are functions of $\hat{\tau}$, the receiver

---

[1] *Tracking and Data Relay Satellite Network (TDRSN) Final Study Report*, Sept. 30, 1969 (JPL internal document).

estimate of τ, the time phase of the binary modulation carried by the received signal. $C(\hat{\tau})$ will be non-zero only where the synchronization error $\hat{\tau} - \tau = \delta T$ is small. During initial acquisition $\hat{\tau}$ is varied, and $C(\hat{\tau})$ is observed to coarsely determine correct synchronization. The second observable, the error signal $E(\hat{\tau})$, is then used as an error signal in a phase-locked loop to remove the remaining synchronization error. The primary effect of predemodulation filtering on this communication link is distortion of the functions $C(\hat{\tau})$ and $E(\hat{\tau})$.

This article presents an analysis which can be used to evaluate the functions $C(\hat{\tau})$ and $E(\hat{\tau})$ for specified predemodulation filtering. This article considers Butterworth and Tchebycheff low-pass filters and the high-pass, band-pass, and band-reject filters which can be synthesized from these low-pass filters, using simple frequency transformations. Computer programs have been written to provide numerical results. The analysis can be extended to other types of filters without difficulty, provided the filter transfer functions have only simple poles. Further analysis and substantial modification of the computer programs would be required for filter transfer functions having multiple-order poles.

2. System Description

Functional block diagrams of the system to be analyzed are presented in Figs. 1 and 2. At the transmitter (Fig. 1), a phase-modulated carrier is multiplied by a binary signal $a(t)\,c(t - \alpha T)$, where $a(t)$ is a binary-valued (± 1) signal with L symbols of equal duration T and $c(t)$ is a binary-valued clock signal whose transitions are synchronous with those of $a(t)$. The timing relationship between $a(t)$ and $c(t)$ is illustrated in Fig. 3. This analysis assumes the binary sequence $a(t)$ has a two-level autocorrelation function with negligible out-of-phase correlation. Maximal length linear shift register sequences with $L >> 1$ have these properties.

The receiver (Fig. 2) recovers the carrier signal and generates the observables $C(\hat{\tau})$ and $E(\hat{\tau})$. The filter $H(s)$ represents the predemodulation filtering. For most applications, the nominal values of α_C and α_E will be α and $\alpha + 1/2$.

3. Effect of Predemodulation Filtering on Correlation and Error Signal

The effect of the predemodulation filter on the correlation $C(\hat{\tau})$ and the error signal $E(\hat{\tau})$ is determined by the impulse response of the predemodulation filter. If $h(\tau)$ is

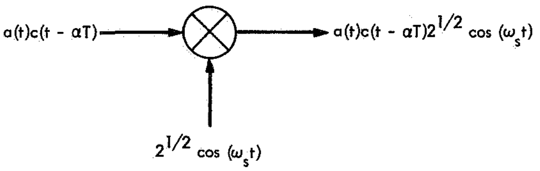

Fig. 1. Transmitter functional block diagram

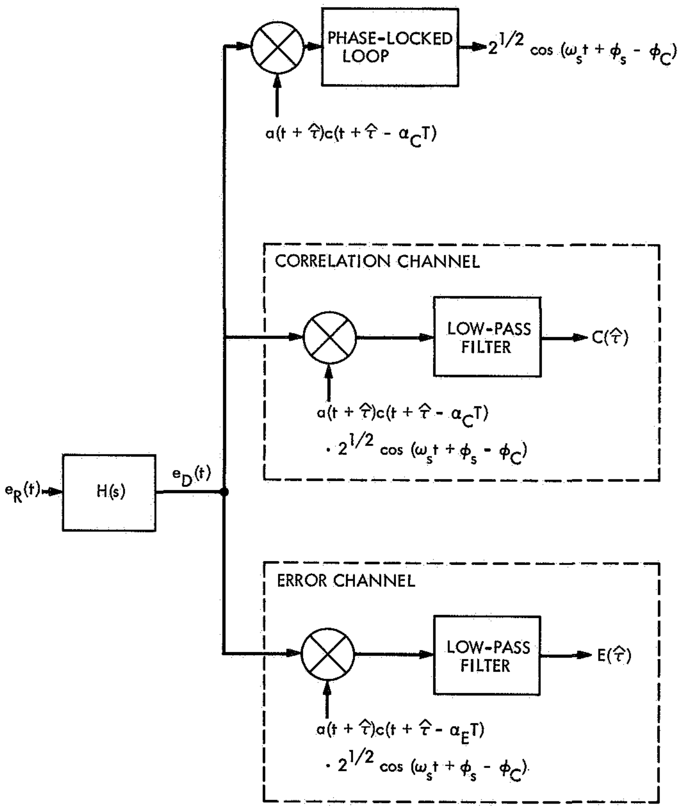

Fig. 2. Receiver functional block diagram

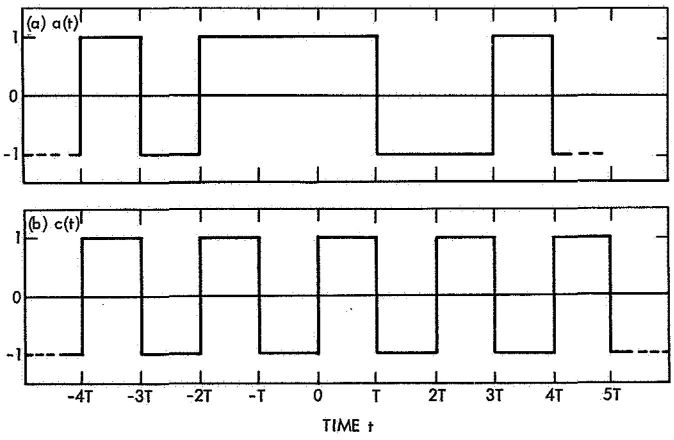

Fig. 3. Timing relationships between a (t) and c (t)

the impulse response of the predemodulation filter and $\beta_s = f_s T$, where $f_s = (2\pi)^{-1}\omega_s$,

$$P^{-1/2} C(\tau + \delta T) = \left\{ \left[\int_0^\infty Th(uT)\cos(2\pi\beta_s u) R(\alpha, \alpha_C, \delta + u)\, du \right]^2 + \left[\int_0^\infty Th(uT)\sin(2\pi\beta_s u) R(\alpha, \alpha_C, \delta + u)\, du \right]^2 \right\}^{1/2} \tag{1}$$

and

$$P^{-1/2} E(\tau + \delta T) = \cos(\phi_C) \int_0^\infty Th(uT)\cos(2\pi\beta_s u) R(\alpha, \alpha_E, \delta + u)\, du + \sin(\phi_C) \int_0^\infty Th(uT)\sin(2\pi\beta_s u) R(\alpha, \alpha_E, \delta + u)\, du \tag{2}$$

where

$$\phi_C = \tan^{-1} \frac{\int_0^\infty Th(uT)\sin(2\pi\beta_s u) R(\alpha, \alpha_C, \delta + u)\, du}{\int_0^\infty Th(uT)\cos(2\pi\beta_s u) R(\alpha, \alpha_C, \delta + u)\, du} \tag{3}$$

and

$$R(\alpha, \alpha', \delta) = (2LT)^{-1} \int_0^{2LT} a(t)\, c(t - \alpha T)\, a(t + \delta T)\, c[t + (\delta - \alpha')T]\, dt \tag{4}$$

In the absence of predemodulation filtering, $Th(uT)$ is the Dirac delta function $\delta(u)$, and

$$P^{-1/2} C(\tau + \delta T) = |R(\alpha, \alpha_C, \delta)| \tag{5}$$

and

$$P^{-1/2} E(\tau + \delta T) = \begin{cases} R(\alpha, \alpha_E, \delta), & R(\alpha, \alpha_C, \delta) > 0 \\ -R(\alpha, \alpha_E, \delta), & R(\alpha, \alpha_C, \delta) < 0 \end{cases} \tag{6}$$

4. The Correlation Function $R_0(\alpha, \alpha', \delta)$

This analysis assumes that

$$R_a(mT) = \begin{cases} 1, & m = \ell L \\ -L^{-1}, & m \neq \ell L \end{cases} \tag{7}$$

Then, for $L >> 1$,

$$R(\alpha, \alpha', \delta) = R_0(\alpha, \alpha', \delta) \tag{8}$$

where, if k, k', and ℓ are integers and $0 \leqq \alpha \leqq 1$, $0 \leqq \alpha' \leqq 1$, $-(L-1) \leqq \delta \leqq 1$,

$$R_0(k+\alpha, k'+\alpha', \delta+\ell L) = (-1)^{k+k'+\ell} \times \begin{cases} 0, & -(L-1) \leqq \delta \leqq -1 \\ |1+\delta-\alpha'| - \alpha', & -1 \leqq \delta \leqq -\alpha \\ \alpha' + |1+\delta-\alpha'| - 2|\delta-(\alpha'-\alpha)|, & -\alpha \leqq \delta \leqq 0 \\ |\delta-\alpha'| - 2|\delta-(\alpha'-\alpha)| + 1 - \alpha', & 0 \leqq \delta \leqq 1-\alpha \\ |\delta-\alpha'| - (1-\alpha'), & 1-\alpha \leqq \delta \leqq 1 \end{cases} \qquad (9)$$

The function $R_0(k+\alpha, k'+\alpha', \delta)$, where k and k' are integers and $0 \leqq \alpha \leqq 1$ and $0 \leqq \alpha' \leqq 1$, is a piecewise linear function of δ having discontinuities in slope at $-(L-1)$, -1, 0, 1, $\alpha'-1$, α', $\alpha'-\alpha$, $-\alpha$, and $1-\alpha$. In the following equations $\delta_0, \delta_1, \cdots, \delta_M$, where

$$\delta_0 < \delta_1 < \cdots < \delta_M$$

are used to denote the values of δ, $-(L-1) \leqq \delta \leqq 1$, where the slope of the function $R_0(k+\alpha, k'+\alpha', \delta)$ is discontinuous. Clearly $\delta_0 = -(L-1)$, $\delta_1 = -1$, $\delta_M = 1$, and, if

$$R_h = R_0(\alpha, \alpha', \delta_h), \qquad 0 \leqq h \leqq M \qquad (10)$$

and

$$S_h = \frac{R_h - R_{h-1}}{\delta_h - \delta_{h-1}}, \qquad 1 \leqq h \leqq M \qquad (11)$$

$$R_0(\alpha, \alpha', \delta) = R_{h-1} + S_h(\delta - \delta_{h-1}),$$

$$\delta_{h-1} \leqq \delta \leqq \delta_h, \qquad 1 \leqq h \leqq M \qquad (12)$$

Note that R_0, R_1, R_M, and S_1 are zero. To simplify the equations in *Subsection 5*, the symbol

$$S_{M+1} = 0 \qquad (13)$$

is used.

5. Integral Evaluation

From Eqs. (1), (2), and (3), it is evident that the basic computation required in this analysis is evaluation of an integral having the form

$$I_0(\alpha, \alpha', \delta) = \int_0^\infty g(u)\, R_0(\alpha, \alpha', \delta+u)\, du \qquad (14)$$

where $g(u)$ is either

$$Th(uT)\cos(2\pi\beta_s u) \quad \text{or} \quad Th(uT)\sin(2\pi\beta_s u)$$

For the predemodulation filters considered in this article, the Laplace transform of $g(u)$, $\mathcal{L}[g(u)]$, can be expressed in the form

$$\mathcal{L}[g(u)] = Q_0 + \sum_{k=1}^{N} \frac{Q_k}{s - P_k} \qquad (15)$$

Q_0 is the response of the transfer function $\mathcal{L}[g(u)]$ at infinity and P_k and Q_k, $1 \leqq k \leqq N$, are its poles and residues. Then, assuming that

$$\exp(P_k L) << 1, \qquad 1 \leqq k \leqq N \qquad (16)$$

$$I_0(\alpha, \alpha', \delta) = \left(Q_0 - \sum_{k=1}^{N} \frac{Q_k}{P_k}\right) R_0(\alpha, \alpha', \delta) + S_h \sum_{k=1}^{N} \frac{Q_k}{P_k^2}$$

$$- \sum_{k=1}^{N} \left[\frac{Q_k}{P_k^2} \sum_{\ell=h}^{M} (S_\ell - S_{\ell+1}) \exp(P_k \delta_\ell)\right] \exp(-P_k \delta), \qquad \delta_{h-1} \leqq \delta < \delta_h \qquad (17)$$

6. Predemodulation Filter

This section considers predemodulation filters which are Butterworth or Tchebycheff low-pass filters or the high-pass, band-pass, and band-reject filters which can be synthesized from Butterworth or Tchebycheff low-pass filters using simple frequency transformations. From the preceding analysis it is evident that the correlation $C(\hat{\tau})$ and the error signal $E(\hat{\tau})$ depend on the parameters of the predemodulation filter only through the response at infinity and the poles and residues of

$$\mathcal{L}\,[Th(uT)\cos(2\pi\beta_s u)]$$

and

$$\mathcal{L}\,[Th(uT)\sin(2\pi\beta_s u)]$$

In this analysis, the response at infinity and the poles and residues of these transfer functions are determined by: (1) calculating the poles and residues of a low-pass Butterworth or Tchebycheff filter; (2) calculating, if necessary, the response at infinity and the poles and residues of the high-pass, band-pass, or band-reject filter; and (3) calculating the response at infinity and the poles and residues of $\mathcal{L}\,[Th(uT)\cos(2\pi\beta_s u)]$ and $\mathcal{L}\,[Th(uT)\sin(2\pi\beta_s u)]$. Of course, the second step will not be required if the predemodulation filter is a low-pass filter.

a. Low-pass filters. This analysis considers both Butterworth and Tchebycheff filters. To facilitate comparison the transfer functions of both Butterworth and Tchebycheff filters will be adjusted to have unit response at zero frequency and amplitude response A at frequency f_A.

An N-pole Butterworth filter has amplitude response

$$A_B(\omega) = \frac{1}{\left[1 + \left(\frac{f}{f_B}\right)^{2N}\right]^{1/2}} \tag{18}$$

where $f_B = (2\pi)^{-1}\omega_B$ is the half-power bandwidth of the filter. Consequently, a Butterworth filter having amplitude response A at frequency $f_A = (2\pi)^{-1}\omega_A$ will have

$$f_B = (A^{-2} - 1)^{1/(2N)} f_A \tag{19}$$

The Butterworth transfer function $H_B(s)$ has poles at

$$P_k = -\omega_B \sin\left[(2k-1)\frac{\pi}{2N}\right] - i\omega_B \cos\left[(2k-1)\frac{\pi}{2N}\right], \qquad k = 1, 2, \cdots, N \tag{20}$$

and no zeros.

An N-pole Tchebycheff filter, adjusted to have unit response at zero frequency, has amplitude response

$$A_T(\omega) = \begin{cases} \dfrac{1}{\left[1 + \epsilon^2 C_N^2\left(\dfrac{f}{f_T}\right)\right]^{1/2}}, & N = \text{odd} \\[2ex] \dfrac{(1+\epsilon^2)^{1/2}}{\left[1 + \epsilon^2 C_N^2\left(\dfrac{f}{f_T}\right)\right]^{1/2}}, & N = \text{even} \end{cases} \tag{21}$$

where $C_N(x)$ is the Nth order Tchebycheff polynomial and $f_T = (2\pi)^{-1}\omega_T$ is the cutoff frequency of the Tchebycheff filter.

$$\epsilon = (\rho^2 - 1)^{1/2} \tag{22}$$

where $10\log_{10}(\rho^2)$ is the amount of ripple allowed in the pass-band of the Tchebycheff filter. A Butterworth filter is equivalent to a Tchebycheff filter having zero ripple. A Tchebycheff filter having amplitude response A at frequency f_A will have cutoff frequency

$$f_T = \begin{cases} \dfrac{1}{\cosh\{N^{-1}\cosh^{-1}[\epsilon^{-1}(A^{-2}-1)^{1/2}]\}} f_A, & N = \text{odd} \\[2ex] \dfrac{1}{\cosh\{N^{-1}\cosh^{-1}[\epsilon^{-1}(A^{-2}(1+\epsilon^2)-1)^{1/2}]\}} f_A, & N = \text{even} \end{cases} \tag{23}$$

The Tchebycheff transfer function $H_T(s)$ has poles at

$$P_k = -\omega_T \sinh\left[\frac{\sinh\left(\frac{1}{\epsilon}\right)}{N}\right]\sin\left[(2k-1)\frac{\pi}{2N}\right] - i\omega_T\cosh\left[\frac{\sinh\left(\frac{1}{\epsilon}\right)}{N}\right]\cos\left[(2k-1)\frac{\pi}{2N}\right], \qquad k = 1, 2, \cdots, N \tag{24}$$

As both Butterworth and Tchebycheff filters have only simple poles, their transfer functions can be expressed in the form

$$H_{LP}(s) = \sum_{k=1}^{N} \frac{Q_k}{s - P_k} \tag{25}$$

where

$$Q_k = -P_k \prod_{\substack{l=1 \\ l \neq k}}^{N} \left(1 - \frac{P_k}{P_l}\right)^{-1} \tag{26}$$

b. High-pass filters. A high-pass filter can be synthesized from a low-pass filter using the transformation

$$H_{HP}(s) = H_{LP}\left(\frac{\omega_A^2}{s}\right) \tag{27}$$

If the low-pass filter has unit response at zero frequency, amplitude response A at frequency f_A, and zero response at infinite frequency, the high-pass filter will have zero response at zero frequency, amplitude response A at frequency f_A, and unit response at infinite frequency.

If the low-pass filter transfer function is given by Eq. (25), the high-pass transfer function is

$$H_{HP}(s) = Q_0' + \sum_{k=1}^{N} \frac{Q_k'}{s - P_k'} \tag{28}$$

where

$$Q_0' = -\sum_{k=1}^{N} \frac{Q_k}{P_k} \tag{29}$$

$$Q_k' = -\frac{\omega_A^2}{P_k^2} Q_k \tag{30}$$

and

$$P_k' = \frac{\omega_A^2}{P_k} \tag{31}$$

c. Band-pass filters. A band-pass filter can be synthesized from a low-pass filter using the transformation

$$H_{BP}(s) = H_{LP}\left(s + \frac{\omega_R^2}{s}\right) \tag{32}$$

If the low-pass filter has unit response at zero frequency, amplitude response A at frequency f_A, and zero response at infinite frequency, the band-pass filter will have zero response at zero and infinite frequency, unit response at frequency $f_R = (2\pi)^{-1}\omega_R$, and bandwidth f_A between frequencies where the filter amplitude response is A.

If the low-pass filter transfer function is given by Eq. (25), the band-pass filter transfer function is

$$H_{BP}(s) = Q_0' + \sum_{k=1}^{N} \frac{Q_k'}{s - P_k'} + \frac{Q_k''}{s - P_k''} \tag{33}$$

where

$$P_k' = \frac{1}{2} P_k + i\omega_R \left[1 - \left(\frac{P_k}{2\omega_R}\right)^2\right]^{1/2} \tag{34}$$

$$P_k'' = \frac{1}{2} P_k - i\omega_R \left[1 - \left(\frac{P_k}{2\omega_R}\right)^2\right]^{1/2} \tag{35}$$

$$Q_0' = 0 \tag{36}$$

$$Q_k' = \frac{Q_k}{1 - \dfrac{P_k''}{P_k'}} \tag{37}$$

$$Q_k'' = \frac{Q_k}{1 - \dfrac{P_k'}{P_k''}} \tag{38}$$

d. Band-reject filters. A band-reject filter can be synthesized from a low-pass filter using the transformation

$$H_{BR}(s) = H_{LP}\left(\frac{\omega_A^2}{s + \dfrac{\omega_R^2}{s}}\right) \tag{39}$$

If the low-pass filter has unit response at zero frequency, amplitude response A at frequency f_A, and zero response at infinite frequency, the band-reject filter will have unit response at zero and infinite frequency, zero response at frequency f_R, and bandwidth f_A between frequencies where the filter amplitude response is A.

If the low-pass filter transfer function is given by Eq. (25), the band-reject filter transfer function is

$$H_{BR}(s) = Q_0' + \sum_{k=1}^{N} \frac{Q_k'}{s - P_k'} + \frac{Q_k''}{s - P_k''} \tag{40}$$

where

$$P'_k = \frac{\omega_A^2}{2P_k} + i\omega_R\left[1 - \left(\frac{\omega_A^2}{2P_{k\omega_R}}\right)^2\right]^{1/2} \tag{41}$$

$$P''_k = \frac{\omega_A^2}{2P_k} - i\omega_R\left[1 - \left(\frac{\omega_A^2}{2P_{k\omega_R}}\right)^2\right]^{1/2} \tag{42}$$

$$Q'_0 = -\sum_{k=1}^{N}\frac{Q_k}{P_k} \tag{43}$$

$$Q'_k = -\frac{\dfrac{\omega_A^2}{P_k^2}Q_k}{1 - \dfrac{P''_k}{P'_k}} \tag{44}$$

$$Q''_k = -\frac{\dfrac{\omega_A^2}{P_k^2}Q_k}{1 - \dfrac{P'_k}{P''_k}} \tag{45}$$

e. Partial fraction expansion for $\mathcal{L}\,[Th\,(uT)\cos(2\pi\beta_s u)]$ ***and*** $\mathcal{L}[Th\,(uT)\sin(2_\pi\beta_s u)]$. Assuming the predemodulation filter transfer function can be expressed in the form

$$H\left(\frac{s}{T^{-1}}\right) = \mathcal{L}\,[Th\,(uT)] = Q_0 + \sum_{k=1}^{N}\frac{Q_k}{s - P_k} \tag{46}$$

$$\mathcal{L}\,[Th\,(uT)\cos(2\pi\beta_s u)] = Q'_0 + \sum_{k=1}^{N}\frac{Q'_k}{s - P'_k} + \frac{Q''_k}{s - P''_k} \tag{47}$$

where

$$P'_k = P_k + i2\pi\beta_s \tag{48}$$

$$P''_k = P_k - i2\pi\beta_s \tag{49}$$

$$Q'_0 = Q_0 \tag{50}$$

and

$$Q'_k = Q''_k = \frac{1}{2}Q_k \tag{51}$$

Similarly

$$\mathcal{L}\,[Th\,(uT)\sin(2\pi\beta_s u)] = Q'_0 + \sum_{k=1}^{N}\frac{Q'_k}{s - P'_k} + \frac{Q''_k}{s - P''_k} \tag{52}$$

where P'_k and P''_k are given by Eqs. (48) and (49),

$$Q'_0 = 0 \tag{53}$$

and

$$Q'_k = -Q''_k = (2i)^{-1}Q_k \tag{54}$$

The frequency parameters of $H\,(s/T^{-1})$ will be the frequency parameters of $H\,(s)$ normalized by the factor T^{-1}. Assume, for example, that $H\,(s)$ is a band-pass filter with unit response at the resonant frequency f_R and bandwidth f_A between points at which the amplitude response is A. Then $H\,(s/T^{-1})$ will be a band-pass filter of the same type with resonant frequency $\beta_R = f_R T$ and bandwidth $\beta_A = f_A T$ between points at which the amplitude response of $H\,(s/T^{-1})$ is A.

7. Numerical Results

Computer programs have been written to provide numerical data and graphs. One program evaluates the amplitude and phase response of the predemodulation filter. The graphs presented in Figs. 4 and 5 were produced by this program. Figure 4 shows the amplitude response and Fig. 5 the phase response of Butterworth and Tchebycheff band-pass filters which have a 10-MHz center frequency and a 2-MHz 3-dB bandwidth. These

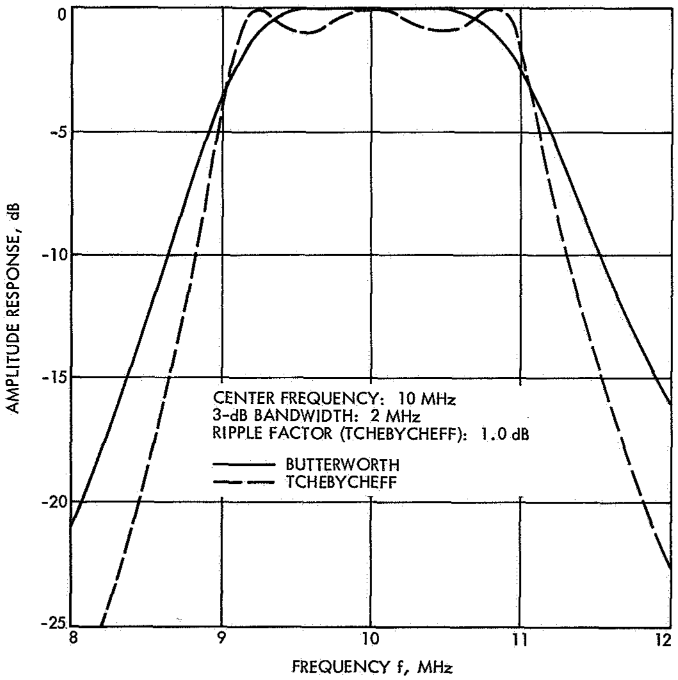

Fig. 4. Amplitude response of 6-pole Butterworth and Tchebycheff band-pass filters

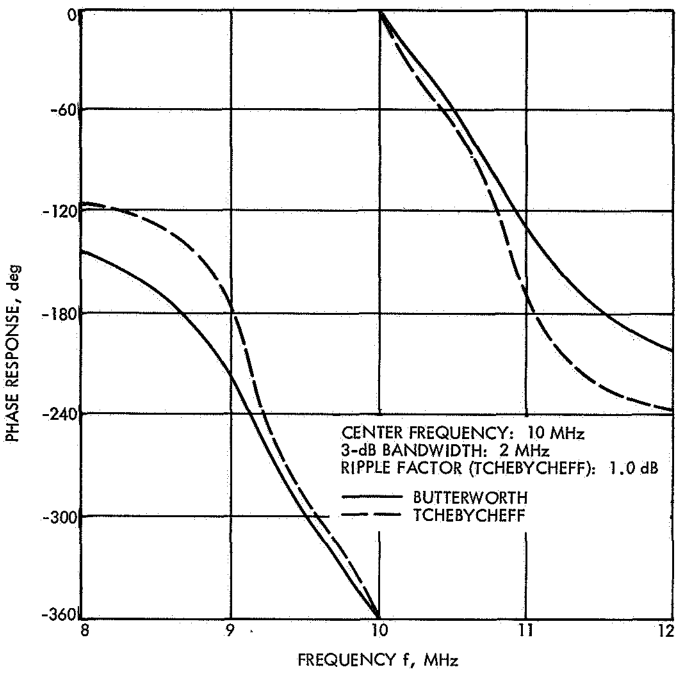

Fig. 5. Phase response of 6-pole Butterworth and Tchebycheff band-pass filters

parameters are typical of those used for the TDRSN system. Both filters were synthesized from low-pass Butterworth and Tchebycheff filters having 3 poles; consequently, both band-pass filters have 6 poles. The ripple factor allowed for the Tchebycheff filter was 1.0 dB.

A second computer program evaluates $P^{-1/2} C(\tau + \delta T)$ and $P^{-1/2} E(\tau + \delta T)$. The graphs presented in Figs. 6 and 7 were produced by this program. In this example $\alpha = \alpha_C = 0$, $\alpha_E = 0.5$, and $T^{-1} = 0.8$ MHz. Figure 6 shows the correlation $P^{-1/2} C(\tau + \delta T)$ for the two filters specified above. For comparison, Fig. 6 also shows $P^{-1/2} C(\tau + \delta T)$ for no predemodulation filtering. Figure 7 shows the error signal $P^{-1/2} E(\tau + \delta T)$ for the two filters specified above. For comparison Fig. 7 also shows $P^{-1/2} E(\tau + \delta T)$ for no predemodulation filtering.

8. Conclusion

The analysis summarized in this article provides a means of evaluating the effect of predemodulation filtering on the correlation and error signals in a pseudonoise receiver. Computer programs have been written to evaluate the amplitude and phase response of the predemodulation filter and to evaluate the correlation $P^{-1/2} C(\tau + \delta T)$ and the error signal $P^{-1/2} E(\tau + \delta T)$. Sample results are presented in Figs. 4–7.

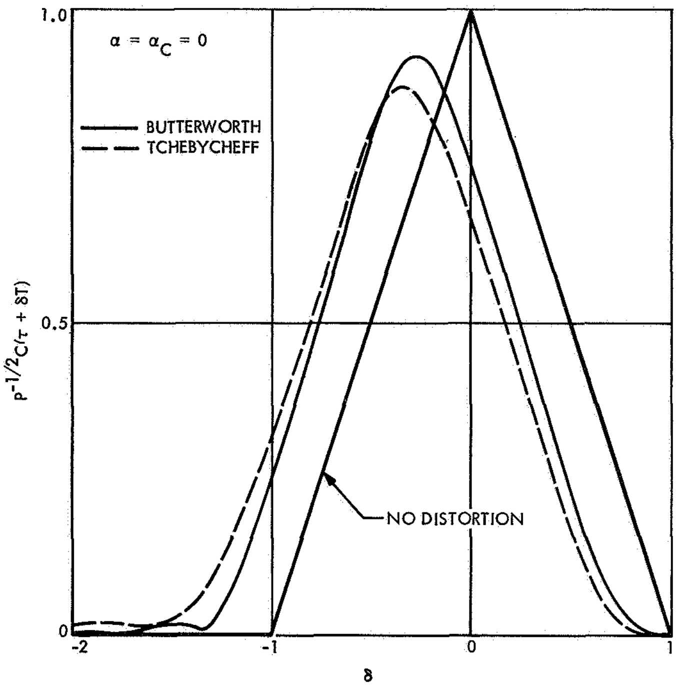

Fig. 6. Effect of Butterworth and Tchebycheff band-pass filters on correlation $P^{-1/2}C(\tau + \delta T)$

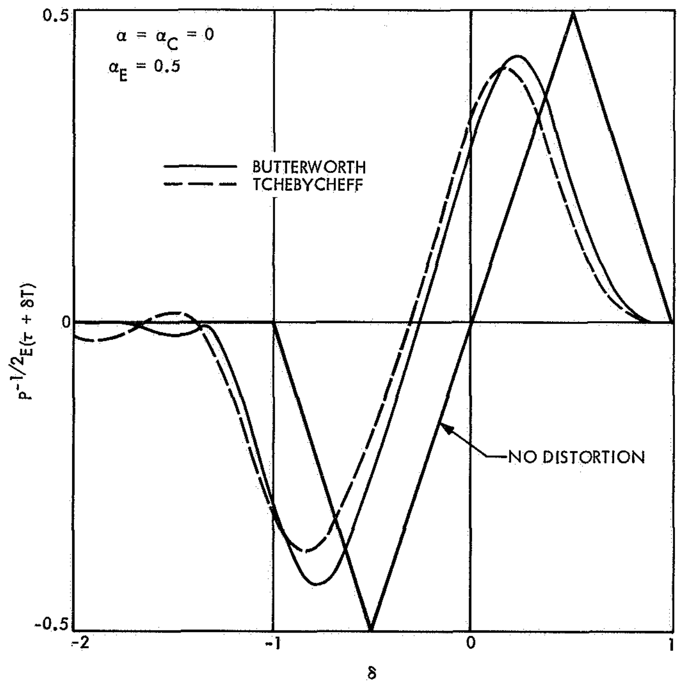

Fig. 7. Effect of Butterworth and Tchebycheff band-pass filters on error signal $P^{-1/2}E(\tau + \delta T)$

This article considered only Butterworth and Tchebycheff low-pass filters and high-pass, band-pass, and band-reject filters which can be synthesized from these low-pass filters using simple frequency transformations. No provision was made in the analysis or computer programs to handle several filters in series. For example, it would be useful to evaluate the effect of a band-pass filter and one or more band-reject filters in series. Addition of capability for handling several filters in series is an obvious area for future work.

There are four attributes caused by the filters shown in this analysis which are of significance to the system application. Illustrated in Fig. 6 are two of these. Firstly, there is a reduction in peak correlation or equivalently a reduction in the energy available for lockup of the system. Secondly, there is partial correlation outside of the desired region which allows lockup of the RF loop. Illustrated in Fig. 7 are the remaining two attributes. Thirdly, the partial correlation illustrated in Fig. 6 additionally shows up in the error signal. The Tchebycheff filter causes crossovers of the zero axis in such a manner to give undesirable stable lock points. Fourthly, the desired lock point has been shifted. This causes a delay which must be accounted for in the system when used for ranging measurements. By proper choice of parameters, system mechanizations, and filter type, undesirable effects can be avoided.

The material presented in this article will form the basis for a parameter study of the effects of the predemodulation filter characteristics on the receiver correlation and error signals. Characteristics of specific interest are: (1) the filter bandwidth and the attenuation at which this bandwidth is specified, (2) the steepness of the filter skirts and the associated phase-nonlinearities, (3) the offset between the signal and filter center frequency, and (4) the amount of in-band ripple (Tchebycheff filters) that can be tolerated. The parameter study will provide a basis for final selection of TDRSN receiver predemodulation filter parameters.

VII. Spacecraft Power

GUIDANCE AND CONTROL DIVISION

A. Analytical Calculation of the Neutron Yield From (α, n) Reactions of Low-Z Impurities,

M. Taherzadeh

1. Introduction

Impurities are usually found in a plutonium heat source, due to the lack of a technique to remove them completely. Since plutonium isotopes are natural α-emitters, (α, n) reactions can take place in the fuel as a result of the concentration of these undesirable impurities, and thus the neutron yield of a given heat source is increased. It is desirable to know the contribution of this factor to the overall neutron yield of a nuclear power source, such as the radioisotope thermoelectric generator adopted by the Thermoelectric Outer Planet Spacecraft (TOPS) Project. In order to evaluate the neutron yield of such impurities, a scheme has been developed and is discussed here. Even though this method yields an approximate result, the result is satisfactory because of the small concentration of impurities in the fuel (i.e., much less than 1%).

2. Impurity Characteristics

Clearly (α, n) reactions can take place with light-element impurities when the energy of the incoming α particle is greater than the threshold energy of the reaction. In addition, both the height of the potential barrier of the target nucleus and the α-ray energy should be within an acceptable range.

Table 1 summarizes the radiation characteristics of α-rays emitted from plutonium isotopes. The contribution to the neutron yield is generally taken to be primarily from the α-rays from plutonium-238; in Table 1, an energy of 5.48 MeV for this isotope is indicated (Ref. 1).

Table 1. Alpha-radiation from plutonium isotopes

Isotope	Energy, MeV	N_α/disintegration	Energy/disintegration, MeV
Pu^{238}	5.495	0.72	3.95
	5.452	0.28	1.53
	5.352	1.3×10^{-3}	6.95×10^{-3}
	Others	$<10^{-4}$	—
Pu^{239}	5.147	0.720	3.71
	5.134	0.168	0.86
	5.095	0.107	0.55
	Others	$<6.9 \times 10^{-4}$	—
Pu^{240}	5.159	0.75	3.87
	5.115	0.75	1.28
	Others	$<0.85 \times 10^{-4}$	—

Table 2. (α, n) reaction with impurities

Impurity	Z	A	$(m - A) \times 10^3$, amu	$(E_\alpha)_{th}$, MeV	$(E_n)_{max}$, MeV	Q, MeV	B, MeV	Abundance, %	Reaction
Li	3	7	18.223	4.39	3.57	−2.79	2.33	92.1	$Li^7 (\alpha, n) B^{10}$
	3	8	25.018	—	13.54	6.63	2.27	~0.0	$Li^8 (\alpha, n) B^{11}$
Be	4	9	15.043	—	12.47	5.71	2.95	100.0	$Be^9 (\alpha, n) C^{12}$
	4	10	16.711	—	10.45	3.85	2.88	~0.0	$Be^{10} (\alpha, n) C^{13}$
B	5	10	16.114	—	7.55	1.07	3.60	18.4	$B^{10} (\alpha, n) N^{13}$
	5	11	12.789	—	6.51	0.15	3.52	81.6	$B^{11} (\alpha, n) N^{14}$
	5	12	18.162	—	14.17	7.36	3.45	0.0	$B^{12} (\alpha, n) N^{15}$
C	6	13	7.473	—	8.54	2.20	4.06	1.1	$C^{13} (\alpha, n) O^{16}$
	6	14	7.515	2.55	4.07	−1.98	3.99	0.0	$C^{14} (\alpha, n) O^{17}$
O	8	17	4.533	—	6.71	0.60	5.07	0.04	$O^{17} (\alpha, n) Ne^{20}$
	8	18	4.857	0.86	5.31	−0.70	5.00	0.204	$O^{18} (\alpha, n) Ne^{21}$
F	9	18	6.651	3.12	3.34	−2.56	5.63	0.0	$F^{18} (\alpha, n) Na^{21}$
	9	19	4.456	2.33	4.00	−1.92	5.55	100.0	$F^{19} (\alpha, n) Na^{22}$
	9	20	6.350	—	10.14	3.90	5.48	0.0	$F^{20} (\alpha, n) Na^{23}$
Na	11	23	−2.945	—	9.16	3.15	6.40	100.0	$Na^{24} (\alpha, n) Al^{27}$
Mg	12	25	−6.255	—	8.52	2.67	6.90	11.5	$Mg^{25} (\alpha, n) Si^{28}$
	12	26	−9.198	—	5.93	3.99	6.84	11.1	$Mg^{26} (\alpha, n) Si^{29}$
	12	27	−7.124	—	10.19	4.22	6.78	0.0	$Mg^{27} (\alpha, n) Si^{30}$
Al	13	28	−9.230	—	7.88	1.96	7.27	100.0	$Al^{28} (\alpha, n) P^{31}$
Si	14	29	−14.340	1.80	4.22	−1.58	7.76	6.2	$Si^{29} (\alpha, n) S^{32}$
	14	30	−16.763	4.22	1.94	−3.73	7.70	4.2	$Si^{30} (\alpha, n) S^{33}$
	14	31	−14.850	—	7.05	1.18	7.63	0.0	$Si^{31} (\alpha, n) S^{34}$

Table 2 summarizes the list of low-Z impurities which have an acceptable threshold energy for (α, n) reactions. The potential barrier height B is equal to

$$Zz\,e^2/(r_0\,A^{1/3} + 1.2),$$

where $e^2 = 1.44$ MeV • fermi and $r_0 = 1.3$ fermi. The terms Z and z are the target and α-particle atomic number, respectively, r_0 is the nuclear radius, A is the atomic number, m is the mass number, $(E_\alpha)_{\text{th}}$ is the threshold energy of the (α, n) reaction, $(E_n)_{\max}$ is the maximum energy of the neutrons, and Q is the Q-value of the reaction.

3. (α, n) Neutron Yield

The neutron yield from impurities y_i in a mixture can be written in terms of the experimentally measured neutron yield from target impurity atoms, the activity of the plutonium radioactive nuclei, and the straggling ratio; that is,

$$y_i = K(\lambda N)_{\text{Pu}}\, y_{0_i} \left(\frac{S_i N_i}{\sum_j S_j N_j + S_{\text{Pu}} N_{\text{Pu}}} \right) \qquad (1)$$

where K is the percent fraction of the α-emitter, $(\lambda N)_{\text{Pu}}$ is called the α-activity of the emitter source, and y_{0_i} is the experimentally measured neutron yield for the impurity in question. The last fraction in the expression above accounts for the effect of competition between the (α, n) reactions and other unwanted ionization processes by which α particles also lose energy (Ref. 2) and is termed the straggling ratio. (Therefore, the neutron source density depends upon the degree of mixing of the α-particle source and impurities.)

The term λ is the disintegration constant and is equal to $0.693/T_{1/2}$; N is the total number of radioactive atoms of the emitter. The term (λN) is given in units of curies (the curie is equal to 3.7×10^{10} disintegrations per second) and $\lambda N = dN(t)/dt$, where $N(t)/N(0) = \exp(-\lambda t)$ is the number of radioactive atoms left at time t. The term S_i is the ith element atomic stopping power and is proportional to $Z_i/\sqrt{7 + Z_i}$.

Table 3 presents the experimental values of the n/α yield (y_0) for different low-Z materials as reported by different groups. Since the results of Gorshkov (Ref. 3)

Table 3. Observed neutron yield for low-Z impurities

Impurity	Z	A	Atomic neutron yield, $Y_0 n/10^6 \alpha$		
			Gorshkov (Ref. 3)	Roberts (Ref. 4) (corrected)	Breen and Hertz (Ref. 5)
Li	3	7	—	2.6	1.0
Be	4	9	84.4 ±0.9	80	59
B	5	10	19.6 ±0.2	24	15
C	6	12	0.113 ±0.015	0.11	—
O	8	16	0.068 ±0.011	0.07	—
F	9	19	11.6 ±0.2	12	—
Na	11	23	—	1.5	1.1
Mg	12	25	1.33 ±0.04	1.4	0.80
Al	13	27	0.76 ±0.03	0.74	0.53
Si	14	28	0.168 ±0.02	0.16	—
Cl	17	35	—	0.11	—
A	18	36	—	0.38	—
P[a]	15	31	—	—	—
S[a]	16	32	—	—	—

[a] $Y_P \simeq Y_S < 0.03$.

appear superior, they have been adopted for this calculation. Equation (1) will be used to evaluate neutron yields for all the impurities involved, and the yields will be compared with other measured data.

In order to simplify Eq. (1), it may be assumed that $(SN)_i << (SN)_{\mathrm{Pu}}$ and since Avogadro's number N_0 is equal to (NA/ρ), thus,

$$\left.\begin{aligned} y_i &= K\lambda_{\mathrm{Pu}} y_0 \frac{S_i}{S_{\mathrm{Pu}}} \frac{m_i N_0}{A_i} \\ \frac{y_i}{m_{\mathrm{Pu}}} &= K\lambda_{\mathrm{Pu}} y_{0_i} \frac{S_i}{S_{\mathrm{Pu}}} \frac{m_i}{m_{\mathrm{Pu}}} \frac{N_0}{A_i} \end{aligned}\right\} \qquad (2)$$

$$Y_i \equiv \frac{\dfrac{y_i}{m_{\mathrm{Pu}}}}{\dfrac{m_i}{m_{\mathrm{Pu}}}} = K\lambda_{\mathrm{Pu}} N_0 \left(\frac{y_0}{A}\right)_i \left(\frac{S_i}{S_{\mathrm{Pu}}}\right) \qquad (3)$$

where Y_i is the neutron yield of the ith impurity per gram of plutonium and per part ratio of the impurity and y_{0_i} is the observed atomic neutron yield of the ith impurity and is given in neutron yield/α particle. Thus, the total neutron yield of an impurity is given by Eq. (3) in neutrons/gram of plutonium/second/part of impurity.

4. Total Neutron Yield

The observed number of neutrons per α-particle in the (α, n) reaction with impurities has been reported by different groups. Table 3 shows the observed atomic neutron yield in $n/10^6\alpha$ for impurities up to silicon.

Through the use of Eq. (3) and Tables 2 and 3, neutron yields of all impurities capable of producing neutrons can be obtained. By knowing the neutron yield of each impurity, the total neutron yield of the actual fuel, where the α-emitter is mixed with other impurities, can be calculated. This is achieved simply by adding the contributions from all the impurities to obtain the total yield, namely

$$Y = \sum_i f_i Y_i = K\lambda_{\mathrm{Pu}} N_0 \sum_i \left(\frac{y_0}{A}\right)_i \left(\frac{S_i}{S_{\mathrm{Pu}}}\right) f_i \qquad (4)$$

where f_i is the fractional weight of the ith impurity, $K\lambda_{\mathrm{Pu}}$ depends on the α-emitter, y_0 is the measured number of neutrons/α and S_i/S_{Pu} depends on the Z-number of each impurity. Since S_i is proportional to $Z/(Z + 7)^{1/2}$, thus

$$Y = K\lambda_{\mathrm{Pu}} N_0 \sum_i \left[\left(\frac{y_0}{A}\right)_i f_i \left(\frac{Z_i}{Z_{\mathrm{Pu}}}\right) \sqrt{\frac{7 + Z_{\mathrm{Pu}}}{7 + Z_i}} \right] \qquad (5)$$

5. Results

Through the use of Eq. (3) and Tables 2 and (3), the neutron yield for one gram of plutonium-238 and one part per million (1 ppm) of each impurity has been calculated by the aid of a computer code; the results are presented in Table 4. Since we need only to make use of α particles emitted by Pu^{238}, the disintegration constant λ of this isotope is used. The half-life of Pu^{238} is 86.4 years, and 1 year is 3.15×10^7 seconds; therefore

$$\lambda = 0.693/T_{1/2}\,(\text{seconds})$$

$$= 2.54 \times 10^{-10}\ \text{seconds}$$

$$\lambda N_0 = 1.52 \times 10^{14}\ \text{second}^{-1}\,\text{mole}^{-1}$$

If one takes K as 81% plutonium-238 in the fuel, Eq. (5) can be rewritten in the form of

$Y\,(n/\text{gram } \mathrm{Pu}^{238}/\text{second}/\text{ppm})$

$$= 1.2 \times 10^8 \sum_i \left[\left(\frac{y_0}{A}\right)_i \left(\frac{Z_i}{Z_{\mathrm{Pu}}}\right) \sqrt{\frac{7 + Z_{\mathrm{Pu}}}{7 + Z_i}} \right] \qquad (6)$$

Table 4. Neutron yield of (α, n) reactions with impurities of Pu^{238} heat source (1 ppm)

Impurity	Z	A	y_{0_1} $n/10^6\alpha$	$\frac{S_i}{S_{Pu}}$	$\left(\frac{y_0}{A}\right)_i$	Y, (n/second/gram Pu/ppm) Calculated	Y, (n/second/gram Pu/ppm) Ref. 6
Li	3	7	2.6 ±1	0.10	3.72×10^{-1}	4.64 ±1.78	4.6
Be	4	9	84.4 ±0.9	0.13	9.35	148.80 ±1.55	133
B	5	11	19.6 ±0.2	0.15	1.78	32.80 ±0.33	41
C	6	13	0.113 ±0.015	0.18	8.7×10^{-3}	0.20 ±0.03	0.2
O	8	16	0.068 ±0.011	0.20	4.27×10^{-3}	0.10 ±0.01	0.1
F	9	19	11.6 ±0.2	0.24	6.10×10^{-1}	18.07 ±0.31	18
Na	11	23	1.5 ±0.4	0.28	6.55×10^{-2}	2.22 ±0.58	2.2
Mg	12	25	1.33 ±0.04	0.29	5.33×10^{-2}	1.93 ±0.06	2.1
Al	13	28	0.76 ±0.03	0.31	2.82×10^{-2}	1.08 ±0.04	1.0
Si	14	29	0.168 ±0.02	0.32	5.8×10^{-3}	0.24 ±0.03	0.2
P	—	—				—	<0.03
S	—	—				—	<0.03

for 1 ppm of the *i*th impurity, i.e., $f_i = 1$. Table 4 summarizes the computer results obtained from this equation.

In the calculation of neutron yield, the experimental values obtained by Gorshkov (Ref. 3) were used. The absolute errors on the neutron yields given in Table 4 are about 1.5%, and this is due to the small errors given by Gorshkov.

The data in Table 4 indicate that the light elements such as Be, B, and F must be eliminated or minimized in the fuel to preclude large neutron emission rates. It should be noted that although the yield from oxygen per ppm is relatively low, the percent concentration of this element in PuO_2 fuel is substantial and will tend to contribute significantly to the overall neutron yield. Clearly, for a given fuel source the neutron yield of each impurity should be calculated according to its contribution in parts per million to the overall fuel concentration. In the last column of Table 4, the results reported by Matlack and Metz (Ref. 6) are presented.

References

1. Stoddard, D. H., and Albensius, E. L., "Radiation Properties of Pu 238 Produced for Isotopic Power Generators," DP984. Atomic Energy Commission, Savannah River Laboratory, Aiken, S. C., July 1965.
2. Morrion, J. B., and Fowler, J. L., *Fast Neutron Physics*, Vol. 1, p. 61. Interscience Publications, Inc., John Wiley & Sons, Inc., New York, 1960.
3. Gorshkov, V. A., et al., "Neutron Yield From the Reaction (α, n) in Be, B, C, O, F, Mg, Al, Si and Granite Irradiated with Polonium α Particles," *Soviet J. At. Energy*, Vol. 13, p. 654–657, July 1962.
4. Roberts, J. H., *Neutron Yields for Several Light Elements Bombarded With Polonium α-Particles*, AEC MDDC-731. Atomic Energy Commission, Jan. 7, 1947.
5. Breen, R. J., Hertz, M. R., and Wright, D. V., *The Spectrum of Polonium-Beryllium Neutron Sources*, Report MLN 1054(54). Atomic Energy Commission, Mound Laboratory, Miamisburg, O., June 13, 1955.
6. Matlack, G. M., and Metz, C. F., *Radiation Characteristics of Plutonium 238*, LA 3696. Atomic Energy Commission, Los Alamos Scientific Laboratory, Los Alamos, N. Mex., 1967.

B. Design of a Thick-film Microcircuit DC-to-DC Converter, *H. Wick and S. Capodici*[1]

1. Introduction

Since the inception of earth-orbiting and interplanetary space vehicles, reduction of size and weight of flight electronic equipment has received considerable attention. Various packaging technologies and state-of-the-art techniques have been applied to space vehicle subsystems. Large strides have been taken in weight reduction, and increased packaging densities have been achieved for most spacecraft subsystems.

Although some progress has been made in increasing the density of power processing equipment, it has not kept pace with the advancements in other subsystems. Two considerations that have inhibited progress are: (1) the nonuniform sizes of the electronic components associated with power equipment do not always lend themselves to efficient use of the available volume and (2) as the packaging density of power processing equipment is increased, the thermal density is also increased, thereby causing design conflicts. Through the application of both thin- and thick-film microcircuit techniques, progress in the standardization and packaging of spacecraft power processing equipment has been accelerated. Only recently have these techniques been applied to power subsystem circuits, even though the technology has been available for nearly 10 years.

One task of the Thermoelectric Outer Planet Spacecraft (TOPS) power subsystem study, conducted by the General Electric Company, was to investigate the feasibility of applying thick-film techniques to the electronics portion of a dc-to-dc converter (Ref. 1). One basic multipurpose circuit was used to satisfy load power requirements ranging from 1 to 25 W. The microcircuit for each load in this power range was built using the same substrate conductor layout. The converters were optimized for efficiency by "fine tuning" the values of the thick-film resistors.

This article describes the design of a thick-film microcircuit dc-to-dc converter and discusses the advantages of using this approach in a spacecraft power subsystem.

2. Circuit Description

The circuit for which the hybrid thick film microcircuit was developed is a basic Jensen square-wave oscillator (Ref. 2). A schematic diagram of the circuit is given in Fig. 1. The components contained within the dotted lines are contained within the thick-film microcircuit.

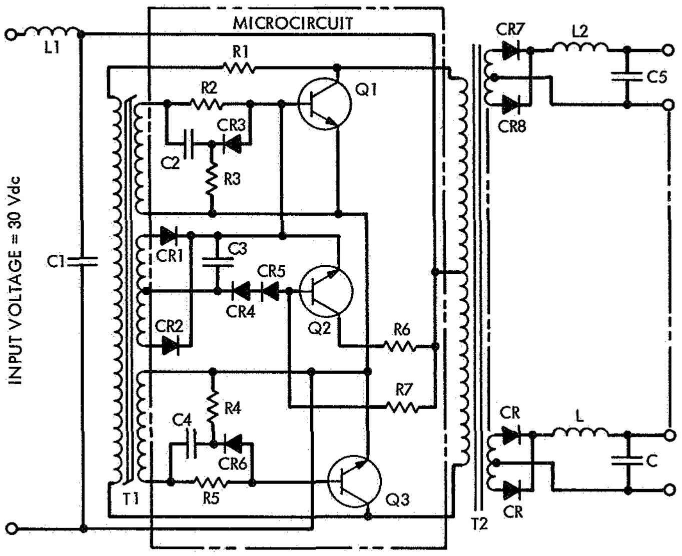

Fig. 1. Schematic diagram of dc-to-dc converter

Transformer T1 and resistor R1 determine the operating frequency of the oscillator: R1 acts to limit the current when T1 saturates. Resistors R2 and R5 limit the current to the bases of transistors Q1 and Q3, respectively. Capacitor C2 and diode CR3 as well as C4 and CR6, form "speed-up" networks to decrease the switching times of Q1 and Q3, the main switching transistors. Transistor Q2 and resistors R6 and R7 comprise the starting circuit, which provides an initial current pulse to the base of Q1, ensuring that the dc-to-dc converter will begin to oscillate. After oscillation begins, the starting circuit is automatically disabled by the application of back-bias to the base of transistor Q2. The negative "turn-off" voltage for Q2 is developed by a secondary winding of T1, diodes CR1 and CR2, and capacitor C3.

The power transformer T2 transforms the input voltage to the desired output voltage levels and also provides isolation between the input and output circuits. A silicon–iron tape-wound cut core with an inherent air gap is used for T2. This type of core does not saturate easily and therefore does not produce large current spikes when the switching transistors are not closely matched.

The output voltages of transformer T2 are rectified and then are filtered by passive LC filters. The filtering smooths the commutation notches produced during the switching intervals and reduces the output voltage ripple to the

---

[1] Space Systems Division, General Electric Co., Philadelphia, Pa.

limits required by the particular loads. In addition to the low-frequency LC filter networks shown in Fig. 1, each output contains a radio frequency interference filter to remove spikes produced by the switching transistors.

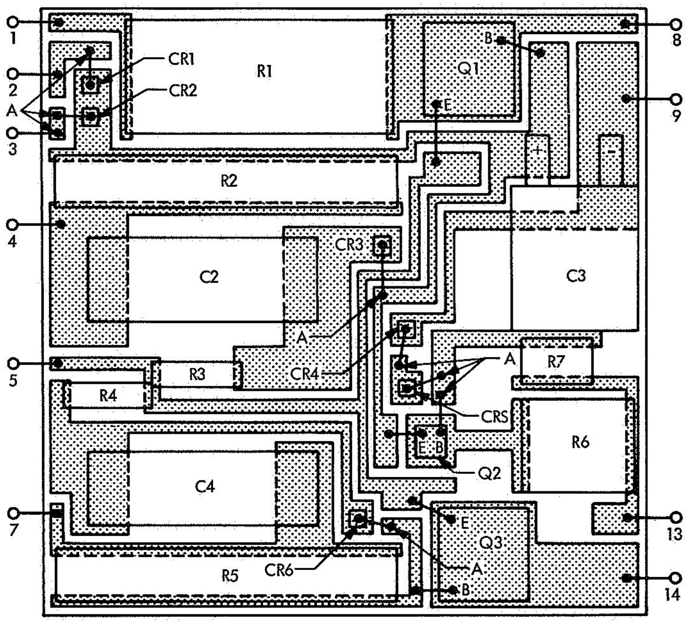

Fig. 2. Scale layout of thick-film microcircuit

3. Thermal Characteristics

The physical properties of the substrate material and the thick-film construction techniques enhance heat transfer from the electronic components of the microcircuit to an adjacent heat sink and balance the increased thermal density with higher thermal conductivity. Figure 2 is a scale layout of the microcircuit substrate showing the position and relative sizes of the various electronic components that make up the electronics portion of the dc-to-dc converter. Figure 3 shows the fabricated microcircuit.

The alumina substrate, which is the means by which the circuit interconnections and electronic piece parts are held within the microcircuit flat pack, has a high thermal conductivity and is an excellent electrical insulator. This property provides a more direct and efficient path for heat flow from the internally mounted power transistor chips and the other substrate-mounted circuit elements to the bottom of the metal flat pack. The flat pack in turn is then mounted or bonded to a metal heat sink with either a heat-conductive paste or a low-temperature solder. The small number of highly efficient thermal interfaces provides excellent heat transfer. The flat pack is rated at 25 W/in.^{2} of mounting surface based on the assumption that it is bonded to a heat sink that will adequately remove this much power.

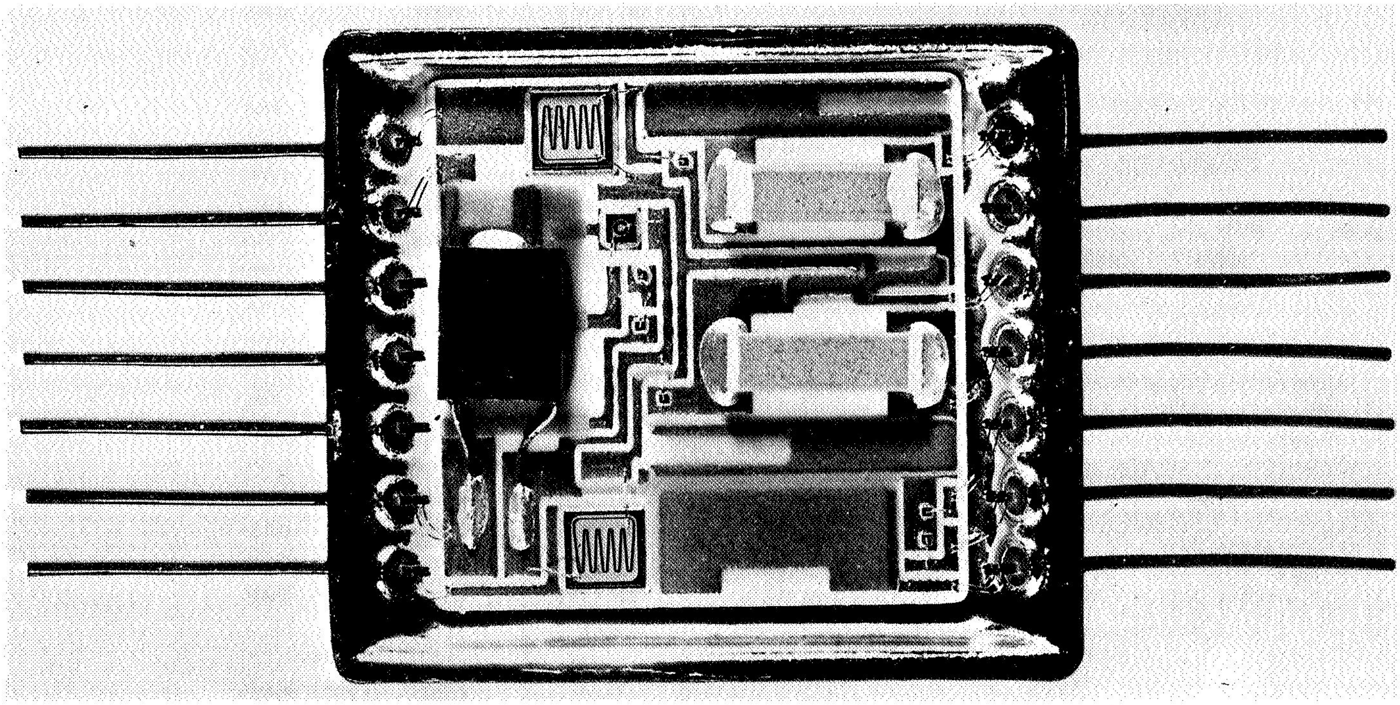

Fig. 3. Photograph of thick-film microcircuit

Standard spacecraft packaging techniques for power processing equipment use printed circuit boards and/or cordwood module construction for the mounting of discrete electronic components. Both of these techniques require additional means for removing excess heat from the package to limit the temperature of electronic components to some allowable range. Through the use of thick-film construction methods, each component is bonded to a thermally conductive substrate which provides an excellent means for removing any excess heat. Furthermore, standard construction techniques lead to longer circuit interconnections and increased opportunity for noise coupling to adjacent circuitry. These disadvantages are eliminated through the use of thick-film techniques.

4. Weight and Volume Comparison

Figure 4 shows the size of the conventionally packaged discrete electronic components for a 5-W dc-to-dc converter in relation to the same components packaged using thick-film technology. As the power level of the dc-to-dc converter increases, the size of the discrete components increase accordingly. Therefore, one would expect the size of the conventionally packaged converter to increase. The thick-film package shown in Fig. 4, however, will not increase in size for power levels up to 25 W, thereby realizing more saving in weight and volume. A weight analysis for the electronics portion of a 5-W and 16-W dc-to-dc converter was performed; the results are shown in Table 1, along with the weight of the hybrid thick-film microcircuit that contains the same number of electronic components.

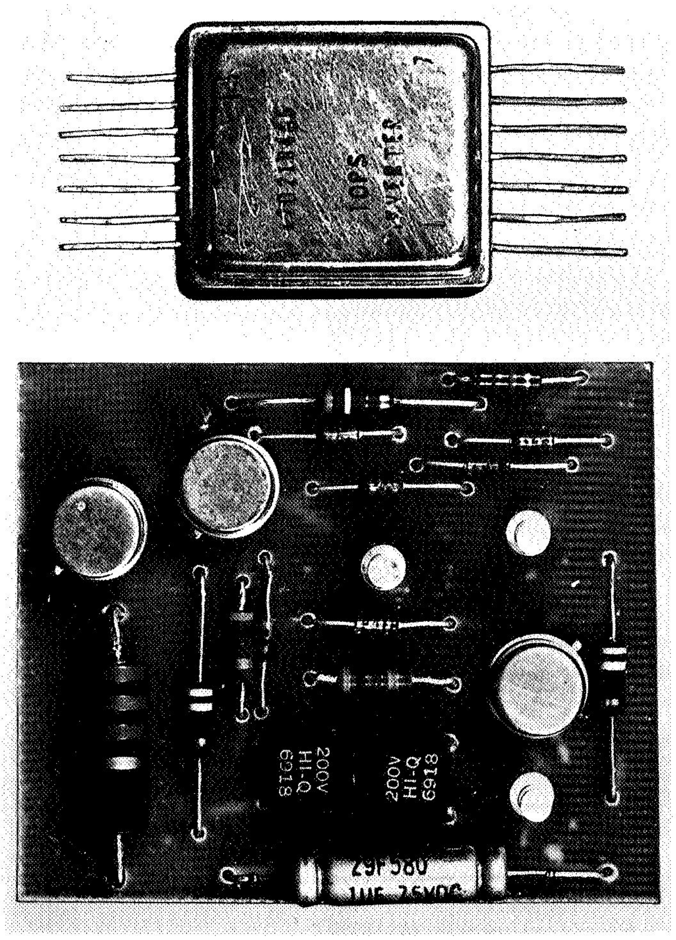

Fig. 4. Comparison of conventionally packaged 5-W dc-to-dc converter electronics and the thick-film microcircuit

5. Reliability Considerations

The thick-film dc-to-dc converter inherently has a higher reliability than the same circuit using discrete parts and standard construction methods. The higher reliability of the microcircuit is due to the following:

(1) The circuit elements in the microcircuit are more uniform and more standardized.

Table 1. Weight comparison of discrete parts vs hybrid thick-film microcircuit flatpack

Weight of discrete parts, lb			Weight of flatpack, lb
Component	5-W converter	16-W converter	
R1	0.003	0.005	
R2	0.001	0.003	
R3	0.001	0.001	
R4	0.001	0.001	
R5	0.001	0.003	
R6	0.001	0.001	
R7	0.001	0.001	
CR1	0.0005	0.0005	
CR2	0.0005	0.0005	
CR3	0.0005	0.0005	
CR4	0.0005	0.0005	
CR5	0.0005	0.0005	
CR6	0.0005	0.0005	
C2	0.002	0.002	
C3	0.005	0.005	
C4	0.002	0.002	
Q1	0.007	0.020	
Q2	0.007	0.020	
Q3	0.007	0.007	
Printed circuit board	0.020	0.020	
Total	0.062	0.0940	0.0125

(2) The electronic components are deposited directly on the interconnecting substrate and are metallurgically bonded to it directly, without the multiple interconnections required by the mechanical package of the discrete piece parts.

(3) Interconnections are standardized on the microcircuit. The dissimilar-metal problems associated with a wide variety of termination methods are eliminated. Also, the hazards of oxidation, contamination, and electrolysis are removed.

(4) The fabrication process is usually automated and continuous and is not subject to human operator error to the same extent as discrete circuitry fabrication.

(5) The thick-film process is more tightly controlled; 100% inspection is performed under magnification by comparator techniques.

(6) The number of circuit connections that pass the microcircuit interface is minimized.

(7) The integrated circuit performs a complete electrical function and is fully tested with all its piece parts in place, sealed in a controlled environment, with established physical interrelationships.

(8) The single substrate and high thermal conductivity assure a common operating temperature and reduce the possibility of differential thermal expansion or parameter drift due to temperature differences between individual piece parts.

(9) The substrate enclosure protects the piece parts within the integrated circuit from oxidation, contamination, and mechanical abuse.

6. Conclusions

A comparison of microcircuit thick-film construction with discrete piece part circuit construction indicates a minimum weight reduction of 80%, as shown for the 5-W converter in Table 1, a volume reduction of 80%, an inherently higher reliability with respect to fabrication, contamination, and elemental circuit chips, and minimization of the number of circuit connections that pass the microcircuit interface.

References

1. Hayden, J. H., et al., *Power Conditioning Equipment for a Thermoelectric Outer Planet Spacecraft Power Subsystem*, Quarterly Technical Report 1J86-TOPS-513, JPL Contract 952536. General Electric Company, Space Systems Division, Philadelphia, Pennsylvania, Feb. 15, 1970.
2. Jensen, J. L., "An Improved Square-Wave Oscillator Circuit," *IRE Trans. on CT*, Sept. 1957.

C. Electrochemical Cells Incorporating Liquid Amalgam Electrodes, *G. L. Juvinall*

1. Introduction

One major objective of the JPL battery advanced development effort is the investigation of the power-producing reactions involved in the operation of liquid amalgam electrodes and their possible applications to space power systems. Some of the unusual properties exhibited by liquid amalgam electrode systems have been described previously in SPS 37-61, Vol. III, pp. 133–134, SPS 37-55, Vol. III, pp. 105–107, and SPS 37-57, Vol. III, pp. 88–89. Dr. G. Myron Arcand of Idaho State University is the principal investigator on this development effort.

One of the most remarkable properties exhibited by these systems is a very high rate charge and discharge capability, coupled with good charge recovery. However, a suitable cathode possessing comparable capabilities must be developed if this aspect of the liquid amalgam systems is to be exploited. At present, development of a high-energy-density cell which does not contain the soluble zinc electrode, and therefore would not be subject to dendritic shorting or excessive variations in capacity from cycle to cycle, would be in direct support of JPL's need for a long-life spacecraft battery. Consequently, this effort is directed toward complete cell development with special emphasis on the cathode. The properties of the first cells incorporating rechargeable liquid amalgam electrodes are reported here.

2. Experimental Approach

Several cells containing liquid potassium amalgam anodes and silver oxide cathodes have been fabricated. The construction details are shown in Fig. 1. The plate electrode was mounted in a holder constructed according to the specifications of France (Ref. 1), except that nylon was used for the holder body. The nominal area of exposed electrode surface was 1 cm^2. The silver oxide electrode was prepared by pressing commercial silver powder onto an expanded silver grid and sintering the plaque at 700° in a furnace. The plaque was then mounted in the holder with two layers of fiber sausage casing separator. Formation charging of the electrode was performed in a 10 N potassium hydroxide electrolyte at 10 mA.

The amalgam electrode was contained in a filter tube bent as shown in Fig. 1. The tube had an inside diameter of 7 mm and a medium frit disc sealed on the end. Triply distilled mercury was placed in the tube and covered with a layer of carbon tetrachloride to inhibit air oxidation of the active metal. The electrode was formation charged in 10 N potassium hydroxide.

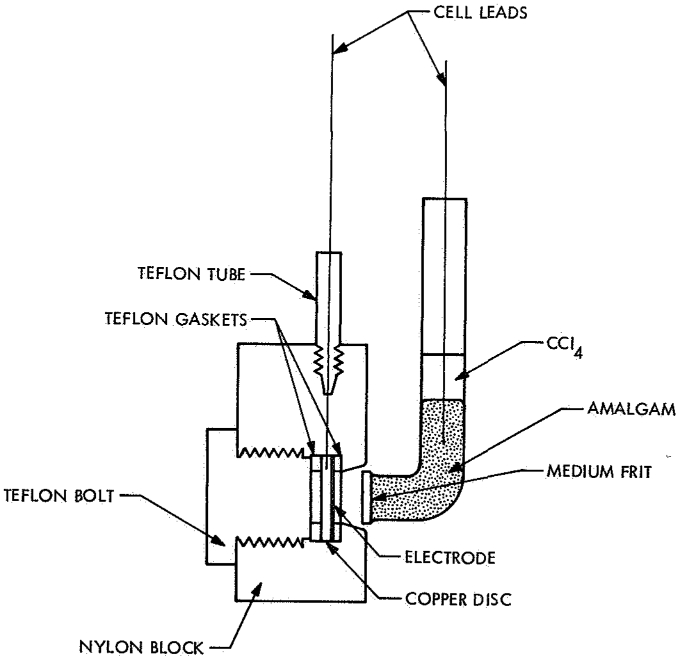

Fig. 1. Cross section of electrode assembly

The two electrodes were mounted in a beaker containing 10 N potassium hydroxide electrolyte so that the distance between them was 5 mm. The cell was left in an open-circuit condition except for the monitoring recorder.

3. Discussion and Results

The open-circuit voltage of these cells lies typically in the range of 2.3 to 2.5 V, depending upon the total charge. The cells have not been heavily loaded; discharge currents have been of the order of 9 mA. Because of a cell resistance of 60 Ω, the cell design must be modified before high-rate discharges are attempted.

Preliminary stand life data have been obtained for a cell which exhibited an open-circuit voltage of 2.08 V initially. After 77 h, the voltage was down to 0.5 V. These results are summarized in Fig. 2.

It should be noted that the recorder impedance was approximately 1 MΩ. On this basis, a current of about 2 μA and approximately 0.00014 A-h of discharge through the recorder would be expected during the period of the experiment. Thus, direct self-discharge at the amalgam–solution interface may be only a small part of the total discharge observed. Previous data obtained solely on the amalgam electrode support this conclusion.

One cell combining liquid potassium amalgam and nickel electrodes has been constructed. This cell, which exhibited an open-circuit voltage of 2.25 V, was capable

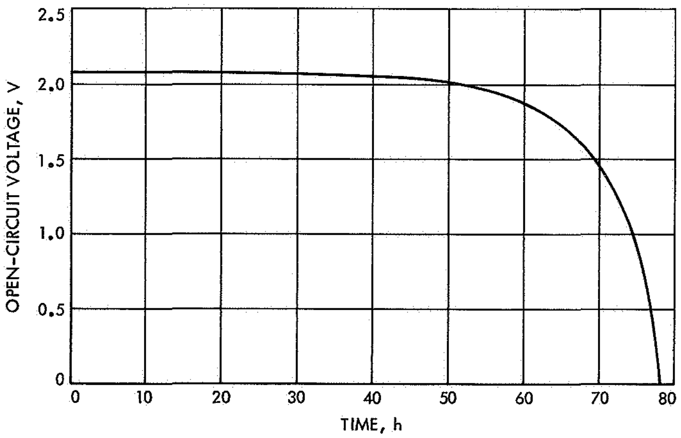

Fig. 2. Stand life characteristic of cell with silver oxide electrode

of supporting a discharge current of 7 A for approximately 30 s. The voltage remained above 1 V throughout the major portion of the discharge.

It may be concluded that, on the basis of work done to date, the amalgam electrode systems show promise as working electrodes in electrochemical cells. Further experiments conducted with complete cells will permit a final evaluation to be made.

Reference

1. France, W. D., "A Specimen Holder for Precise Electrochemical Polarization Measurements on Metal Sheets and Foils," *J. Electrochem. Soc.*, Vol. 114, p. 818, 1967.

D. Heat-Sterilizable Battery Development,

R. Lutwack

1. JPL Contract With Texas Instruments Inc.

The program for the development of heat-sterilizable Ni–Cd cells has ended with the delivery of 25-A-h cylindrical cells but without the completion of a large segment of the development of the high-impact-resistant cell. The progress that was made is illustrated by these results:

(1) The delivered capacity of the engineering model cells was not decreased by sterilization. The data that support this conclusion are: the capacities of 4-A-h 17-plate and 18-plate cells and of 25-A-h cylindrical cells after 248, 189, and 65 deep discharges respectively were unaffected by sterilization.

(2) Marked increases in the end-of-charge voltage, the open-circuit voltage, and the efficiency occurred with increases in the time of sterilization, indicating that permanent electrode changes are caused by sterilization.

(3) Through the use of gas analyses and single-electrode potential measurements, an increase of 30 to 60 mV in the end-of-charge voltage after sterilization was shown to be associated with the Ni electrode. It is believed that sterilization results in a reduction in electrochemical surface and consequently in a higher current density and/or higher oxygen overvoltage at the Ni electrode.

(4) A crimped polymer seal, patterned after the Ziegler seal, was fabricated and successfully leak tested down to 10^{-10} std cm^3 He s^{-1} atm^{-1}. However, the seal could not be maintained after sterilization, since the polymer flowed enough during sterilization to cause leaks. Polymers with better properties under stress and high temperature are needed to secure an adequate seal under sterilization conditions.

A considerable amount of data and information was obtained relative to the design of a high-impact-resistant cell. In the constant deformation static testing, the modulus of elasticity, the yield strength, and the ultimate strength were measured with these results:

(1) The positive plaque has a much higher yield strength than does the negative plaque. The increased strength is caused by the positive plate having less porosity and a higher sintering temperature as well as a higher area density, although the plates have the same slurry formulation and the same thickness.

(2) A reduction in strength of the positive plate occurs as a result of the electrochemical forming process; this is apparently caused by the 30 % wt corrosion of the sinter matrix which takes place during the process and despite a reduction in porosity to 33%.

(3) The negative plate has a higher yield strength than does the initial negative plaque, although corrosion (20–25%) of the sintered matrix occurs during the electrochemical forming process; the porosity is decreased to 56% in the process. In a comparison of the factors leading to the opposite results for the two plates, these conclusions were made: (a) the amount of sintered matrix corrosion is less for the negative plate than for the positive plate; (b) the negative active material has more strength, because it is partly a metal.

(4) The positive plate has a higher yield strength than the negative plate; this is apparently due to the great differences in their parent plaque structures.

(5) In the ultimate strength measurements it was shown that the greater corrosion of the positive plate leads to a lower ultimate strength than that of the negative plate.

Constant-load static testing was used to more accurately determine the modulus of elasticity and to examine the yield phenomena. The values of yield strength and ultimate strength agree well with those obtained using the constant-deformation type of loading. It was also shown that: (1) there is a plastic deformation component at very low strain levels (< 200 μin./in.), (2) for strains less than 6×10^3 μin./in., the modulus of plate material is higher than that of the screen alone, and (3) the strength (stiffness) of the positive matrix is greater than that of the negative matrix.

The changes in mechanical properties of the plates as the result of sterilization and electrolyte solution saturation were determined. The positive plate is only slightly changed in the modulus of elasticity and yield strength, although the ultimate strength is significantly higher. The negative plate is changed much more; there are significant decreases in the modulus of elasticity and yield strength and only a slight reduction in ultimate strength.

In the measurements of the mechanical properties in compression loading it was shown that: (1) the matrix is the major load-bearing element up to the point of fracture, (2) the positive plates can withstand impact levels of 3700 g in pure dynamic compression (> 2600 psi) with no apparent damage, and (3) negative plates have a fracture load of 135 lb for the 2-in. width (2400 psi). The results of static and dynamic testing show the positive plate to be more capable of sustaining compressive loading than the negative plate.

Some cells, which were not designed for impact resistance, were impact tested to determine the failure modes. Two cell sizes of the prismatic design and a cylindrical cell were used. These were the observations:

(1) The prismatic cells failed in buckling of the electrodes. It is believed that insufficient lateral support was obtained from the cell case and that no failures would have occurred if thicker axial spacers and lateral restraining plates had been used.

(2) The cylindrical cell shorted due to electrode movement, but there was almost no evidence of the buckling mode of failure. The difference between the capabilities of prismatic and cylindrical cells to withstand impact thus appears to be due to inherent differences in structural characteristics of the cell case designs.

The continuation of this development has been prevented by the decision of Texas Instruments Inc. to withdraw from the Ni–Cd battery field. Under this contract, one hundred ten 25-A-h, nonimpact cells, of which 90 are cylindrical and 20 are prismatic, were fabricated and have been delivered to JPL. A final report has been issued.

In support of the development of high-impact-resistant cells, Dr. K. K. Gupta of JPL has completed an analysis and a computer program for nonlinear high-impact dynamic response. This program has been thoroughly checked out by running several test cases on the UNIVAC 1108 computer. As a consequence, the program IMAN may now be conveniently used for the analysis of impact on practicable battery structures.

2. JPL Contract With Eagle-Picher Industries

This development is for a heat-sterilizable, remotely activated Ag-Zn battery capable of 200 W-h capacity and of maintaining a 1200-W load for 10 min or a 500-W load for 24 min at 26 to 30 V dc. This work has been completed. Three batteries were fabricated and tested by activation and discharge after sterilization at 135°C for 120 h. During activation, the internal pressure increased to 40 psig, dropped rapidly to 5 psig, and then rose steadily, necessitating venting at 100 psig. During the discharge, the voltage remained above the 26-V dc minimum for both the 500- and 1200-W load. Thus the electrical goals of the development were met.

The conclusions from this effort are that:

(1) This type of battery can be heat-sterilized, activated, and discharged successfully.

(2) Sterilization is responsible for a 40% loss in capacity based on actual capacity comparison tests. The loss is caused by silver oxide reduction at the elevated temperature.

(3) The energy density of 15 W-h/lb, which was obtained in these tests, is by no means a maximum since several battery components were not at their minimum weight. For example, the electrolyte solution reservoir was made from elbows and straight sections rather than from the lighter die-shaped tubing.

(4) The major problem remaining is the pressure in the battery. The results of tests in which the pressure and temperature were monitored continuously during the discharge indicate that, while some of the pressure is the vapor pressure of the heated electrolyte solution, the major contribution must have come from gassing electrodes during the high rate discharge. Since a vent or a pressure vessel is unacceptable in a space capsule, further research into the area of gassing of electrodes at high discharge rates is needed if this system is to be developed to its maximum capability.

3. JPL Contract With the University of California at Berkeley

This research program, set up to study the permeability characteristics of membranes as a function of the application of different forces, includes a detailed theoretical application of steady-state thermodynamics to transport across membranes and experimental determinations of the derived relationships. An experimental technique, the concentration clamp method, has been developed for measurements of membrane potential, of streaming potential, and of the transport of salt, ions, and water across membranes with differences in concentration, electric potential, and pressure as driving forces.

In the study using an AMF C-103 membrane and NaCl solutions, these conclusions were derived:

(1) There is a strict linearity of transport with time.

(2) There is a strong dependence of salt diffusion and osmotic transport on pretreatments of the membrane, such as direct-current passage and stretching.

(3) Diffusional and electric transport of salt seems to be additive, but there is a moderate discrepancy for water fluxes.

Investigations using the SWRI-GX battery separator material, concentrated KOH solutions, and soluble Zn species are underway.

4. JPL Contract With the University of Pennsylvania

This program includes investigations of (1) the oxidation and reduction and the rate of dissolution of silver oxide crystals; (2) denditric growth and the oxidation and reduction of fresh Zn surfaces; (3) the frequency response of the Ag-Zn battery; and (4) the effects of pulse charging on the morphology of electrodes.

Single crystals of AgO, prepared by an electrolyte method, have been determined to be $Ag_7O_8NO_3$ by X-ray diffraction measurements. These crystals are very stable in alkaline solutions and are readily converted to AgO by treatment in H_2O at 110°C. The overpotentials for O_2 gassing on the AgO material were unexpectedly low, being 35 mV at 6.7 mA/cm^2 and 66 mV at 16.7 mA/cm^2 (at the Hg/HgO electrode.)

As part of the investigation of the effects of transient current distribution on dendritic growth, a system comprising a nonreacting Ni rotating disc electrode and a ferri-ferrocyanide solution are being used. The data for the transient overpotential vs time behavior have been shown to fit the theoretical prediction very well for current interruption (decay). The correspondence is poor for current switch-on (buildup). A review of the theoretical interpretation of the boundary condition at the disc surface during the buildup interval is underway.

Pulsed charging processes are being studied using a rotating disc electrode. A theoretical treatment has been developed, and the results have been used to fix the time intervals of the pulse cycle. It has been shown that if the pulse current is at least 25 times the limiting current in an interval limited to the time needed to deplete the reacting species at the electrode surface, charging occurs in less time than for continuous operation at the diffusion-limited current density. Hence, for the combined effects of convection and pulse charging, the charging time is reduced by more than 80% using pulse currents 10 times the steady-state diffusion limiting current.

VIII. Guidance and Control Analysis and Integration

GUIDANCE AND CONTROL DIVISION

A. *Mariner* Mars 1969 Approach Guidance Demonstration, *T. C. Duxbury and W. G. Breckenridge*

1. Introduction

The objectives of the *Mariner* Mars 1969 approach guidance demonstration (SPS 37-51, Vol. III, pp. 50–51) were to develop and demonstrate hardware and software capabilities required for producing and processing spacecraft-based navigation data. Specifically, these objectives were: (1) demonstration of the operational capability of a spacecraft-based optical-navigation measurement system and the associated data processing; (2) development of the hardware and software required by optical-approach navigation; (3) planning and timely execution of the ground processing to demonstrate that the optical-approach navigation can form the basis of practical, near-encounter maneuvers and operations; (4) performance analysis of the optical-approach navigation system, to be performed subsequent to encounter; (5) verification of the assumed error and performance models; and (6) demonstration, by ground-based computer simulation, of the feasibility of a self-contained, on-board, optical-approach navigation system.

Analysis showed that a significant increase in trajectory estimation accuracy could be obtained by combining spacecraft-based measurements of the Mars direction with earth-based radio tracking data. A planet tracker (SPS 37-52, Vol. III, pp. 49–52), which would measure precisely the direction to the optical center of Mars during a 10-day period before Mars encounter, was developed to yield the spacecraft-based data. The planet-tracker development was at a test-model stage when funding limitations required the cancellation of the flight-model development.

A study (Ref. 1) of existing science and engineering instruments aboard the *Mariner* spacecraft showed that the demonstration would still be possible, however, at the expense of degraded navigation performance. Mars direction was obtained by combining telemetered measurements from several instruments (not designed for navigation) which were located at various places on the spacecraft. (Originally, Mars direction was to be obtained by combining measurements from a smaller number of navigation instruments which were centrally located.) To accommodate the new spacecraft-based measurement system, the objectives were modified and the demonstration was placed on a minimum interference basis with the science and engineering instrument development and mission operations. The modified objectives of the experiment were: (1) obtain measurements from on-board optical instruments which can be used for estimating the spacecraft trajectory with respect to Mars, (2) develop software for processing these measurements and for estimating the spacecraft trajectory in near-real time, (3) make available to mission operations an estimate of the spacecraft trajectory based on a combination of radio and available optical measurements for optional use in encounter operations, and (4) make a post-encounter comparison of the accuracy of the estimated spacecraft trajectory based on the optical and radio data to that based on radio data alone. These objectives are essentially the original objectives, with the hardware development deleted.

2. Spacecraft Measurement System

Instruments aboard the *Mariner* spacecraft which were used to obtain navigation data included the narrow-angle TV camera, the far-encounter planet sensor (FEPS), the two degree-of-freedom scan platform, and the attitude-control sensors. The FEPS and attitude-control sensor error signals, the positions of the scan platform gimbals, and TV pictures of Mars were telemetered to earth during the approach to Mars.

The telemetered spacecraft data were used to determine the spacecraft-centered direction to Mars in a celestial reference system. The direction to the center of Mars with respect to the scan platform was determined from TV pictures of Mars, and independently from FEPS error signals, together with instrument mounting and calibration data. This direction was then referenced to a spacecraft-fixed coordinate system by using the scan platform gimbal position readout together with mounting and calibration data. Finally, Mars direction was transformed from the spacecraft-fixed system to a celestial reference system by using the attitude-control sensor error signals together with mounting and calibration data.

3. Mission Operations

The near-Mars phase of the *Mariner* Mars 1969 mission was divided into two phases: far encounter (FE), and near encounter (NE). The FE phase began a few days before Mars encounter and continued until a few hours before Mars encounter. Directly following FE was NE, which continued until one hour past encounter ($E + 1$ h). During FE, the scan platform pointing was controlled by the FEPS and a TV picture was recorded about every 40 min. Recorded pictures were played back to earth while the spacecraft was being tracked by the Deep Space Network station at Goldstone, California. FEPS, scan platform, and attitude-control measurements were telemetered to earth in real time as part of the spacecraft engineering data. The demonstration used data from FE.

Telemetered engineering data from *Mariner VI* were obtained at $E - 46$ h, $E - 36$ h, and $E - 20$ h. The TV pictures were available at $E - 25$ h. These data were processed on the mission computers at the scheduled times of $E - 44$ h, $E - 34$ h, and $E - 20$ h. Trajectory estimates were available within a short period after these times.

Telemetered engineering data from *Mariner VII* were obtained at $E - 70$ h, $E - 46$ h, and $E - 20$ h. The TV pictures were available at $E - 48$ h, $E - 25$ h, and $E - 20$ h. These data were processed on the mission computers at the scheduled times of $E - 68$ h, $E - 44$ h, and $E - 20$ h. Because of the success of the navigation demonstration on *Mariner VI*, the FE sequence of events was changed to allow the demonstration to obtain an additional 10 pictures during the period $E - 24$ h to $E - 22$ h, to help estimate the trajectory of *Mariner VII*.

4. Conclusions

All of the real-time objectives of the experiment were met. Spacecraft-based measurements were obtained from the *Mariner* spacecraft and processed by navigation software developed for the experiment. The data gathering and processing were performed in near-real time, and trajectory estimates were made available to mission operations for use in encounter operations. A detailed discussion of the numerical results is given in Ref. 2.

Post-encounter evaluation of the demonstration is continuing. The TV data processing capability has been improved (SPS 37-63, Vol. III, pp. 103–105) to increase the accuracy of determining the direction to Mars. Estimation sensitivity studies are being performed to determine the effect of error parameter values and uncertainties on the trajectory estimate. The capability to process natural satellite and star image data is being implemented into the software for a navigation demonstration during the approach and orbiting phases of *Mariner* Mars 1971.

References

1. Breckenridge, W. G., and Duxbury, T. C., "Investigation of Planetary Navigation Using Spacecraft-Based Measurements," paper presented at the ION National Space Meeting, NASA Manned Spacecraft Center, Houston, Texas, April 22–24, 1969.
2. Duxbury, T. C., and Breckenridge, W. G., "*Mariner* Mars 1969 Optical Navigation", *AAIA J.* Paper 70-70, January 1970.

IX. Spacecraft Control

GUIDANCE AND CONTROL DIVISION

A. TOPS Attitude-Control Single-Axis Simulator Command Telemetry Link, *L. S. Smith*

The TOPS single-axis simulator currently in the buildup stage uses a gas-bearing table which by necessity must have very low residual torque. Consequently, the digital attitude-control system located on the table should receive ground site commands via means producing no mechanical torque. This report presents the capacitive coupling technique being used to deliver digital commands to the table.

Figure 1 shows the gas bearing with the table platform removed. An aluminum-foil-backed tape is placed around the bearing plate, and a ground site plate is mounted on the bearing base opposite the foil. Effectively there are three capacitances formed: C_1, ground site plate to foil; C_2, foil to bearing plate; and C_3, bearing plate to bearing base. The approximate capacitance values are: 300 pF, 1500 pF, and 0.25 μF, respectively.

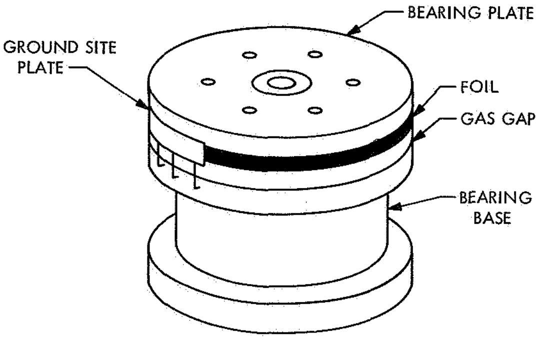

Fig. 1. Gas bearing

Figure 2 shows the equivalent circuit of the three capacitances when set up for transmission of commands from the console to the table. The input pulse, V_{in}, initially charges C_1 and C_3 through the parallel arrangement of C_2, R_1 and Z_1 causing a positive spike that is subsequently amplified by Z_1. When V_{in} returns to zero, C_1 and C_3 discharge via the same path causing a negative spike. These spikes are sensed to cause logical functions in the attitude-control electronics (ACE) system.

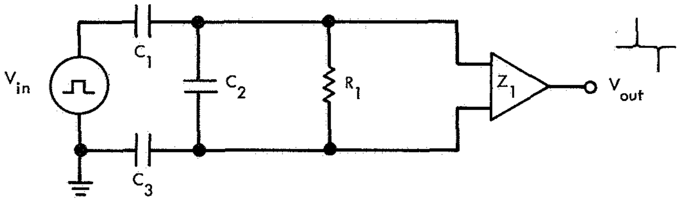

Fig. 2. Console to table linkage equivalent circuit

An alternate capacitance circuit configuration can be implemented to transmit data from the table to the console. The equivalent circuit is shown in Fig. 3. In this instance V_{in} charges and discharges C_1 and C_3 through R_1 and Z_1 in parallel. The foil-to-bearing-plate capacitance, C_2, does not contribute to the development of the signal path but must be considered in designing the V_{in} driver.

Both transmission paths can be operated on the same foil and ground site plate. Figure 4 shows the equivalent circuit for this two-way linkage. Statically, with no V_{in} or V'_{in} signals, switches S_1 and S_2 are set as shown. Thus the table-to-console linkage is established. The V'_{in} signal will then be generated by the table circuits and sensed by the console circuits concluding with a negative spike which will transfer S_1 and S_2. This transfer establishes a console-to-table linkage such that a V_{in} signal can be generated by the console and sensed by the table. This sequence concludes automatically with the return of S_1 and S_2 to their static state.

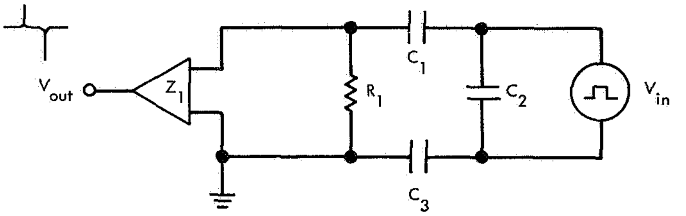

Fig. 3. Table to console linkage equivalent circuit

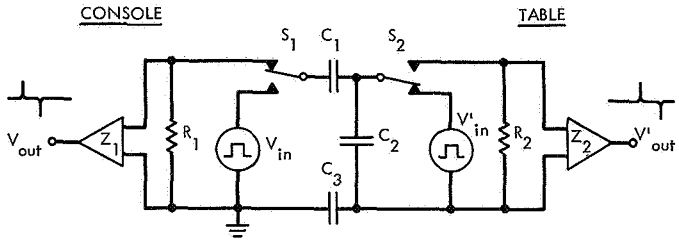

Fig. 4. Two-way linkage

B. Solar Electric Propulsion System Technology Project Thrust Vector Control Electronics,

W. E. Crawford

1. Introduction

The thrust vector control electronics hardware will be used to support the solar electric propulsion system technology (SEPST) effort, which is directed toward a system feasibility demonstration scheduled for calendar years 1970–1971. The goal of the feasibility demonstration is to conduct a ground test incorporating all equipment necessary to prove feasibility for a flight program. Part of the electronic hardware necessary to accomplish the ground test demonstration is the open-loop thrust vector control electronics. This report describes the electronic hardware in detail and also briefly describes the electric propulsion ion engine mechanical configuration.

2. Ion Engine Array

To better understand the operation of the open-loop electronics a brief description of the mechanical configuration of the ion engine array as well as a description of the electromechanical actuators that control the array will be helpful. Figure 1 is a sketch of the ion engine array showing the movement of the translator assembly and also the angular excursions of the four gimballed engines. Movement in the X and Y direction is controlled by the translator actuators while movement about the Z axis is controlled by the gimbal actuators. The actuators are electromechanical devices comprised of a stepper motor and a gear train coupled to an output shaft. The movement of

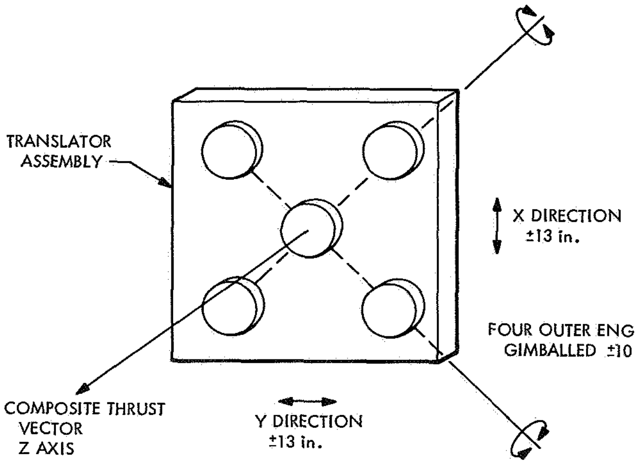

Fig. 1. Five-engine array

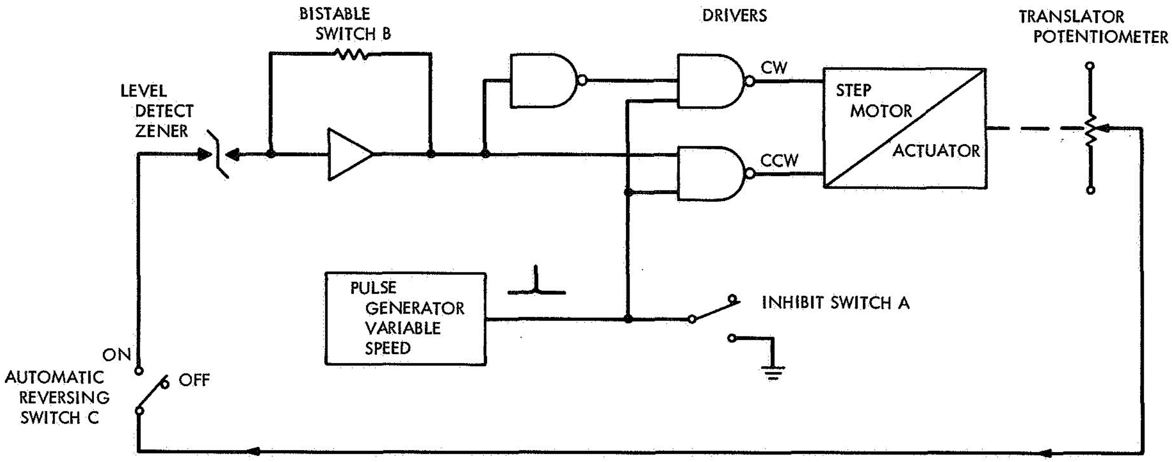

Fig. 2. Electric propulsion open-loop electronics

the translator is 2.2×10^{-4} ft for each actuation of the stepper motor. The gimbal actuator movement is 10^{-4} rad for each actuation of the stepper motor. The position of the translator is monitored by a potentiometer in the translator actuator. The gimbal position is determined by a linear motion transducer (LMT) located in the gimbal actuators. These two devices, the potentiometer or the LMT, are actively used in the electronic control of each axis.

3. Translator Control Electronics

Figure 2 is a block diagram of the translator control electronics. Two translator control systems are included in the open-loop control panel electronics. One system controls the X axis and one system controls the Y axis. The control electronics works in the following manner: the variable speed pulse generator signal is fed to both the clockwise and counterclockwise stepper motor drivers if the inhibit switch A is open. The bistable switch B determines which of the two drivers (clockwise or counterclockwise) will be enabled. The stepper motor is then driven in one direction until the voltage at the translator potentiometer wiper becomes large enough to exceed the threshold voltage of the level-detect zener. At this time the bistable switch is tripped to the opposite polarity and the circuit then causes the stepper motor to step in the opposite direction. This movement continues until the level-detect zener threshold is again exceeded. This causes the bistable switch to change polarity and again the direction of movement is reversed. The translator continues to move back and forth in a cyclic manner at a rate determined by the variable pulse generator. An additional feature in this circuit is the automatic reversing switch C. This is used to drive the translator assembly beyond the limits set by the level-detect zener and will be useful in the testing and alignment of the translator actuator assembly.

4. Gimbal Control Electronics

The gimbal control electronics is functionally similar to the translator control electronics shown in Fig. 2. In the place of the translator potentiometer, an LMT is substituted. Since the LMT is excited with a 6-kHz signal, the LMT output is an ac signal. This signal is demodulated and converted to direct current. The output voltage of the demodulator is proportional to gimbal angle and is used

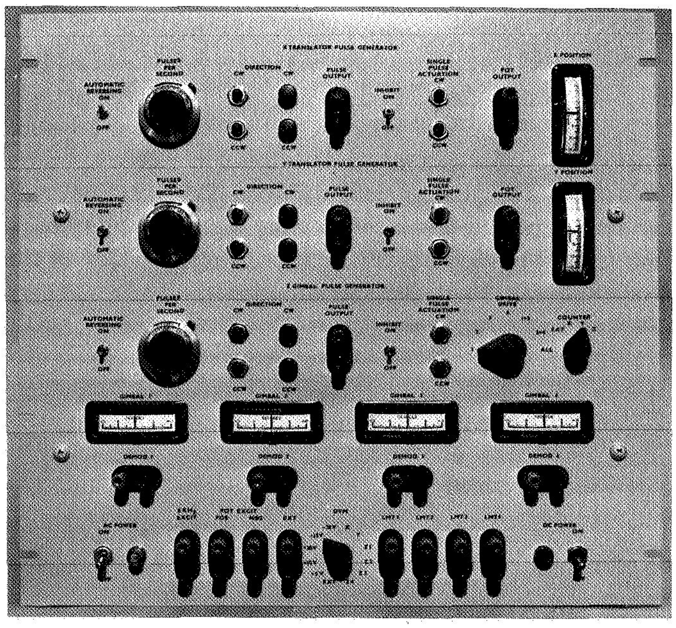

Fig. 3. Open-loop electronics control panel

to trip the bistable switch when the level-detect zener threshold voltage is reached. The gimbal control electronics causes the gimbal to cycle back and forth over its angular excursion of ±10 deg. As in the case of the translator electronics, the speed of movement of the gimbal can be controlled by the variable speed pulse generator.

5. Open-Loop Electronics Control Panel

The open-loop electronics control panel (Fig. 3) has many features not discussed in the previous paragraphs. Meters on the panel show the position of both the X and Y translator as well as the position of each of the four gimbal actuators. The clockwise and counter-clockwise lights give a visual indication of the direction of travel of each axis and the number of pulses per second. A potentiometer in each axis allows the pulse repetition rate to be varied from 3 to 100 pulses/s. Push button switches cause the translators or gimbals to change direction of travel. Listed below are the significant control features of the open-loop electronics control panel:

1. Automatic drive polarity reversal as the actuator approaches its stops (adjustable for each axis).
2. Individual control of each actuator being tested including start-and-stop and single-pulse actuation.
3. Meter indications to show the position of each actuator.
4. Provisions for digital voltmeter readout of both the potentiometer feedback and the linear motion transducer.

C. Digital Sun Sensor, *L. F. Schmidt*

1. Introduction

The sun sensor requirements for the thermoelectric outer planet spacecraft (TOPS) require sensor capabilities not developed for prior missions. These requirements and the resulting design approach are described in SPS 37-57, Vol. III, pp. 103–108.

The basic approach is to form a line image of the sun on a digital detector. The sensor output is the angle between its optical axis and the sun's position in terms of a Gray-coded digital word. The sensor signal processing logic stores the digital word in a storage/shift register where it is periodically sampled by the attitude control logic.

A single-axis breadboard sensor having a 6-deg field-of-view (FOV) has been constructed and tested. The output from this sensor is an 8-bit digital word.

2. Breadboard Testing

Testing of the breadboard sensor has been conducted, using a sun simulator for the radiation stimulus. The simulator provides a solar disk of various diameters and appropriate radiation intensities to approximate the conditions under which the sensor must operate while at different distances from the sun. An angle-setting device is used to position the sensor relative to the optical axis of the simulator. The precisely known angle between the sensor and simulator optical axes is compared to the digital output of the sensor in order to measure the sensor accuracy.

Testing under room ambient conditions have shown that the sensor performance meets the predicted resolution and accuracy described by Fig. 1. The sensor meets the predicted performance over the entire 6-deg FOV only when the best one of four available detectors is used. Each of

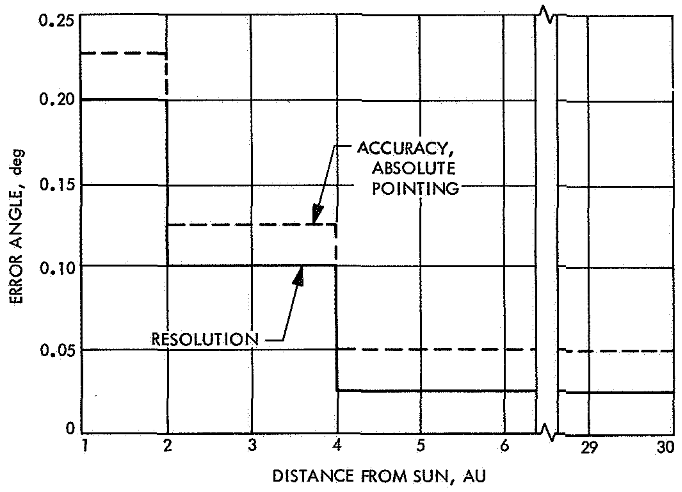

Fig. 1. Estimated accuracy versus distance from sun

the other detectors provide satisfactory operation over a portion of the total FOV. Over the rest of the FOV, one or more bits of the 8-bit output word are in error. This is a result of nonuniform detector characteristics over the entire sensitive area. Initial testing of the sensor resulted in satisfactory operation only with simulated sunlight equivalent to the illumination obtained at 20 to 30 times the earth's distance from the sun (20 to 30 AU) regardless of which detector was used. The cause for this degraded performance was straylight reflected from the detector window. The vendor replaced the defective windows with ones having the specified flatness and antireflection coating. This change greatly reduced the straylight as shown by the increased level of sensor performance.

A special test was conducted to evaluate operation under the conditions of 100 AU, in order to examine more thoroughly the sensors capability. Under the usual detector excitation of ±10 V, the sensor would not operate. Proper operation was obtained however, by raising the excitation to ±25 V. If an extended mission beyond 30 AU were desired, the excitation voltage could be programmed to achieve proper operation. It is estimated that the higher excitation voltage could not be used while the spacecraft was near the sun. Under this condition, the power dissipation within the detector would be excessive due to its low ohmic resistance.

3. Conclusions

The testing to date has shown that the sensors performance is extremely dependent on the detector characteristics. The test results do show that the desired detector characteristics are within the state of the art. Improved fabrication processes will be required to consistently produce detectors of satisfactory quality for flight hardware.

X. Materials

ENGINEERING MECHANICS DIVISION

A. Multilayer Insulation Testing, *J. R. Crosby*

The long-range objective of this task is to develop materials technology and fabrication processes necessary to optimize the performance characteristics of multilayer insulation thermal shield systems for use on spacecraft. Principal emphasis is placed on realistic fabrication and installation influences and on thermal shield predictability and reproducibility.

The calorimeter for measuring the thermal properties of multilayer insulation is in full operation. The calorimeter facility description was described in SPS 37-59, Vol. III, pp. 156–158, and detailed calibration and operation procedures were discussed in SPS 37-62, Vol. III, pp. 179–180.

Several project-oriented tests on various thermal shield configurations are complete. For these tests, the objective was to compare the relative thermal effectiveness of a *Mariner* Mars 1971 and a *Mariner* Mars 1969 thermal shield. In addition, for the *Mariner* Mars 1971 shield a determination was made of a practical amount of overlap to use at seams to minimize conductance without having to make the overlap excessively large.

The flight *Mariner* Mars 1971 thermal shield consists of 15 layers of doubly aluminized ⅛-mil Mylar using loose-knit nylon net spacers. A 1% vent area is attained by use of ¹⁄₁₆-in.-diam holes punched on 0.55-in. centers. The flight *Mariner* Mars 1969 thermal shield consisted of 20 layers of doubly aluminized ¼-mil Mylar using close-knit nylon net spacers. A 0.3% vent area was attained by use of ¼-in.-diam holes punched on 6-in. centers. For relative comparison purposes, the conductance tests were performed on 15-layer shields for both the *Mariner* Mars 1971

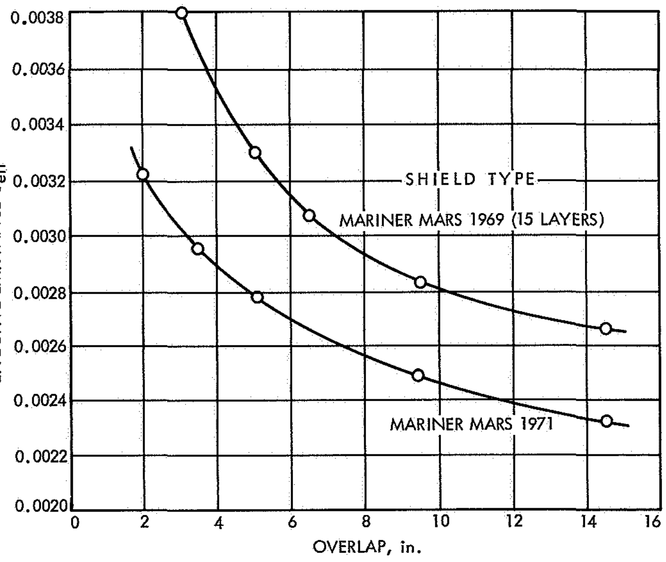

Fig. 1. Effective emittance vs overlap

and *Mariner* Mars 1969 types of insulation. The configuration of the shield during calorimeter testing is in the form of a cylindrical section 10 in. in diameter by 28 in. in length, with the seam located axially along the length of the cylinder. Since the actual test section length is 16 in. (allowing 6-in.-long guard sections on either end), the effective area of the shield in the test section is approximately 3.5 ft^2. During each test, conductance measurements were performed as the amount of circumferential overlap at the seam was varied from 2 in. to 14.5 in.

As expected, the change in conductance as a function of overlap is exponential, as shown in Fig. 1. Examination of the data shows the optimum amount of overlap for use on a *Mariner* Mars 1971 shield seam is about 5 to 6 in. This results in an effective emittance of 0.0027 to 0.0028 for the shield configuration and seam described above.

Regarding the optimum overlap, a similar observation for the *Mariner* Mars 1969 shield data is not valid since the configuration tested was 15 layers, instead of the 20-layer shield actually used on the spacecraft. However, a comparison of the two shields based on an equal number of layers does show that the effective emittance of the *Mariner* Mars 1971 shield is approximately 20% lower than that of the *Mariner* Mars 1969 shield. The reasons for this significant difference in conductance are currently being analyzed.

B. Improved Solar Cell Contact-Interconnect Feasibility Study, *M. Adams*

1. Introduction

The present state of the art of solar cell array fabrication encompasses costly, and, at times, unreliable techniques for the electrical contacting, interconnection, and structural support of diffused-silicon solar cells. The objective of this study was to demonstrate the feasibility of a new materials and design approach to the problems of interconnecting solar cells and mounting them on a structural panel, primarily to reduce fabrication costs.

The approach taken was that of using thick-film ink technology, a printed circuit interconnection scheme, and wraparound cell contacts to allow simultaneous interconnection and structural mounting of the cells. The possibility of using screenable, thick-film materials to achieve low-resistance, ohmic contact patterns on the N- and P-doped regions of silicon solar cells was investigated. The most promising thick-film contacting material and techniques were used in conjunction with a novel epoxy resin wraparound technology to demonstrate the feasibility of applying such materials and fabrication methods to the construction of a lower cost, more effective solar cell array (see Fig. 1). (Many of the problems encountered were left unsolved in an effort to demonstrate total feasibility of the entire solar cell array scheme.)

Several problems are immediately apparent when an attempt is made to use thick-film materials for such a purpose. First, commercially marketed thick-film materials are formulated to bond to ceramic materials (alumina, beryllia) and are, for the most part, designed to be fired at temperatures higher than those compatible with diffused-silicon technology. The formulations of the inks are proprietary. This lack of composition information complicates the problem of selecting inks most likely to be compatible with the diffused-silicon technology.

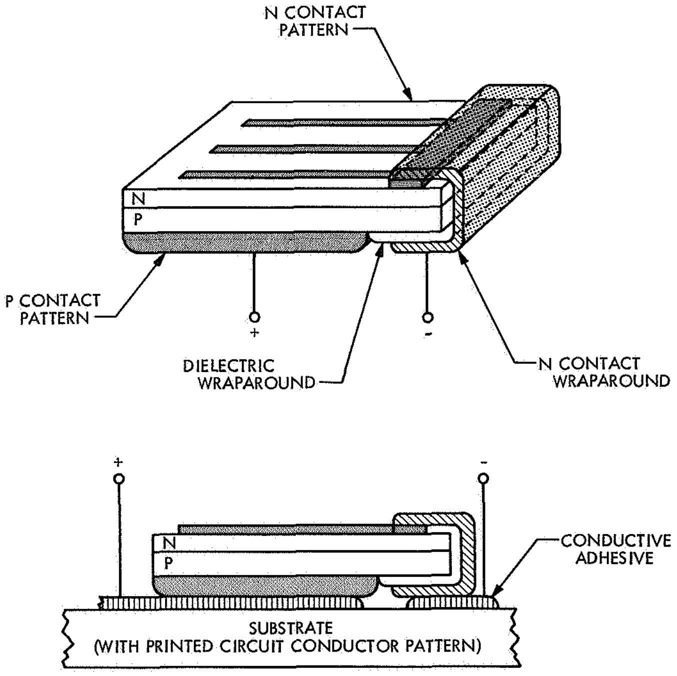

Fig. 1. Thick-film wraparound cell and interconnect structure

To achieve low-resistance, ohmic contact and good adhesion to the diffused silicon, an alloy or chemical bond must be formed between the film material and the doped silicon layer. The active depth of the N-layer (phosphorus-diffused layer) is somewhat less than 1 μm. Alloying or penetration of the contact film material by diffusion beyond this <1 μm depth (i.e., PN junction depth) results in a destruction of the photovoltaic properties of the cell's junction. Fast-diffusing elements from the contact material or contamination on the surface which can contribute holes, electrons, traps, or recombination centers in the junction area of the cell can degrade performance without destroying the junction.

The thick-film inks, as they are currently formulated, must be sintered or alloyed at elevated temperatures to produce continuous, adherent, conducting films on the silicon. This elevated temperature treatment must both alloy the contact material to the doped silicon regions and transform the powdered agglomerate of contact material on the surface into a continuous conducting sheet without causing excessive diffusion of foreign material into the silicon junction area. During sintering, the times or temperatures cannot be so great that the impurity profile of the N-type phosphorus layer or the boron doping is altered appreciably. The thick-film compositions and the heat-treating times, temperatures, and atmospheres must be carefully optimized to achieve this end.

2. Conductive Inks

A large variety of conductive thick-film inks are available which can be screen-printed and sintered to obtain the desired mechanical and conduction properties. Unfortunately, none of these inks have been designed to be compatible with diffused-silicon technology. The types of ink chosen for evaluation in this study, shown in Table 1, can be grouped into two categories.

Table 1. Thick-film contact coupon data

Run number	Contact material	Heat treatment		Cell side	Contact pad pattern[a]	Pad-to-pad resistance, Ω	Type of contact	Adhesion rating[b]
		Time, min	Temperature, °C					
1	Vacuum-evaporated 99.99% aluminum	10	260	N	I	16 (av)	Ohmic	(c)
				P	I	26 (av)	Ohmic	↓
2	↓	None		N	I	18 (av)	Ohmic	↓
				P	I	35 (av)	Ohmic	↓
3	Vacuum-evaporated 99.99% aluminum	15	445	N	I	14 (av)	Ohmic	↓
				P	I	32 (av)	Ohmic	(c)
4	DuPont Conductive Silver No. 7713	10	704	N	III	8	Ohmic	Excellent
				N	II	59	Ohmic	(c)
				P	—	10^2 (av)	Unstable	Excellent
5	DuPont Conductive Silver No. 7095	10	760	N	II	86	Ohmic	(c)
				N	III	25	Ohmic	(c)
				N	I	54	Ohmic	Bad
				P	—	10^3 (av)	Unstable	Bad

[a] See Figure 2.

[b] Excellent—no detectable removal of contact material.
Good—less than 5% removal of contact material.
Fair—less than 25% removal of contact material.
Poor—greater than 25% but less than 75% removal of contact material.
Bad—greater than 75% removal of contact material.
c—not tested for adhesion.

Table 1 (contd)

Run number	Contact material	Heat treatment		Cell side	Contact pad pattern[a]	Pad-to-pad resistance, Ω	Type of contact	Adhesion rating[b]
		Time, min	Temper-ature, °C					
6	Electro Materials Corp. of America (EMCA) Conductive Silver No. 92	30	566	N	III	7	Ohmic	(c)
				N	III	26	Unstable	Good
				N	II	44	Ohmic	(c)
				P	—	10^3 (av)	Unstable, nonohmic	Excellent
7	↓	20	566	N	—	38 (av)	Ohmic	Fair
				P	—	10^3 (av)	Unstable	Bad
8	↓	15	650	N	—	$10^2 \rightarrow 10$ (av)	Unstable	Excellent
				P	—	10^3 (av)	Unstable, nonohmic	(c)
9	↓	30	495	N	—	34 (av)	Nonohmic	Excellent
				P	—	10^3 (av)	Unstable, nonohmic	Excellent
10	Electro Materials Corp. of America (EMCA) Conductive Silver No. 92	20	495	N	—	31 (av)	Ohmic	Bad
				P	—	10^3 (av)	Unstable, nonohmic	Excellent
11	Electro Science Gold Conductor No. 8800B	6.2	755	N	I	200 (av)	Nonohmic	Excellent
				P	I	$10^3 \rightarrow 10$ (av)	Unstable, nonohmic	Excellent
12	EMCA unfluxed silver	10	640	N	III	13	Ohmic	(c)
				N	III	100	Ohmic	Bad
				P	III	10^3 (av)	Nonohmic	Bad
13	↓	1.9	841	N	III	10 (av)	Ohmic	Fair
				P	III	10^3 (av)	Nonohmic	Good
14	EMCA unfluxed silver	1.4	978	N	III	35	Ohmic	Good
				P	III	~700	Ohmic	Excellent
15	EMCA unfluxed aluminum	10	562	N	I	45	Ohmic	Bad
				P	I	33 (av)	Ohmic	Bad
16		2.5	585	N	—	17 (av)	Ohmic	Poor
				P	—	34 (av)	Ohmic	Poor
17	EMCA unfluxed aluminum	1	663	N	—	12 (av)	Ohmic	Fair
				P	—	34 (av)	Ohmic	Fair
18	EMCA unfluxed copper	10	502	N	I	10^2	Unstable, nonohmic	(c)
				N	II	10^2	Unstable, nonohmic	(c)
				N	I	88	Ohmic	Fair
				P	—	10^3 (av)	Unstable	Poor

Table 1 (contd)

Run number	Contact material	Heat treatment		Cell side	Contact pad pattern[a]	Pad-to-pad resistance, Ω	Type of contact	Adhesion rating[b]
		Time, min	Temperature, °C					
19	↓	10	700	N	I	108	Ohmic	(c)
				N	II	63	Ohmic	(c)
				N	I	67	Ohmic	Fair
				P	—	10^3	Unstable	Fair
20	EMCA unfluxed copper	2	900	N	I	10^2	Unstable	(c)
				N	II	93	Ohmic	(c)
				N	I	180	Ohmic	Excellent
				P	—	10^3 (av)	Unstable	Excellent
21	EMCA unfluxed nickel	10	482					No adherence
22	↓	5	652					↓
23	EMCA unfluxed nickel	1	980					↓
24	EMCA gold-silicon eutectic	5	368					↓
25	↓	2.5	384					↓
26	EMCA gold-silicon eutectic	1	425					No adherence
27	Hanovia gold metal resinate	15	302	N	I	10^3	Ohmic	(c)
				N	II	260	↓	↓
				N	I	500	↓	↓
				P	I	10^4 (av)	↓	↓
28	↓	5	501	N	I	70	↓	↓
				N	II	150	↓	↓
				N	I	65	↓	↓
				P	I	10^3 (av)	↓	↓
29	Hanovia gold metal resinate	5	502	N	I	120	↓	↓
				N	II	200	↓	↓
				N	I	110	Ohmic	↓
				P	I	103 (av)	Nonohmic	(c)

The first category chosen comprises those used by manufacturers of hybrid electronic circuits. These inks are normally screened onto ceramic substrates and fired to produce interconnection patterns of conductors, resistor networks, and dielectric films. The formulation of these inks is complex and proprietary. In general, they contain organic vehicles or solvents, organic binders, and mixtures, in varying proportions, of glass powders and metal powders. When fired, the organic solvents, vehicles, and binders pyrolitically decompose or burn off. A continuous conducting film is formed in these materials by a solid-state sintering and alloying mechanism occurring between the glass particles and the metal particles. Inks containing only metals and organic materials were evaluated, in addition to some containing organic material, metal, and glass particles.

The second category of inks evaluated consisted of special preparations which are termed organic metal resinates.[1] These materials are true organometallic compounds. The metal is chemically bonded to an organic molecule and, during heat treating of the compound, the organic constituents decompose, leaving atomic metal on the substrate. It is generally assumed that these inks require an oxidation process to break the metal–organic bond, which results in oxidation of the metal and a reduction in its conductivity. Attempts were made to avoid this problem by decomposing the metal resinate in a neutral or reducing atmosphere rather than an oxidizing one.

One advantage of the metal resinate inks is that known alloys may be mixed with them before firing. On firing, the organic constituents are removed and a metallic alloy of the desired composition is formed from the atomic metal. Attempts were made to produce two "alloy" mixtures of desirable compositions by this technique. The two alloys were a lead–tin composition and the gold–silicon eutectic composition.

3. Contact Coupon Test Program

To evaluate the electrical performance of the sintered thick-film contacts to the doped silicon and the physical and mechanical properties of the films, test coupons were used initially for all thick-film inks. The test coupons were fabricated by screening the thick-film materials onto diffused-silicon solar cell blanks supplied by Heliotek Corp.[2] The solar cell blanks supplied were 2 × 2-cm squares, 0.043 cm thick, consisting of 2Ω-cm boron-doped bulk silicon diffused with phosphorus at a surface concentration of $\sim 10^{20}$ atoms/cm^3 to form the P–N junction. Three different contact patterns shown in Fig. 2 were used to perform the evaluations. The coupons were heat-treated under carefully controlled conditions, the electrical properties of the film and film–silicon contacts were measured, and a tape test was performed on the contacts to measure mechanical adhesion. The contact patterns with a film thickness of 0.001 to 0.002 in. were screened onto cleaned silicon coupons using a Presco thick-film screen printer and masks made by conventional photolithographic techniques.

Two electrical measurements were made on the test coupons which included the pad-to-pad resistance of the contact structure and the sheet resistivity of the screened material. The pad-to-pad resistance measurement was made by probing the two contact pads with tungsten probe points and passing a constant, rectified current through the structure. The voltage drop was measured across the pads. A Model 351A Fluke dc power supply was used in conjunction with a Series X-2 Nonlinear Systems digital voltmeter to perform the measurements. This technique yielded an "order of magnitude" value and was used only as a gross screening procedure. The current polarity was reversed during the resistance determinations to establish whether the contacts were ohmic. A Tektronics curve tracer was also used later to verify the nature of the contact.

The sheet resistivity was measured with the same two-point probe apparatus. The resistance of a strip 0.39 in. long and 0.04 in. wide was measured. The resistance of a 0.20-in. length of the same strip was subtracted from this value to compensate for probe point contact resistance, and an order-of-magnitude approximation was obtained for the sheet resistivity. Mechanical adhesion of the contact pads were measured by pressing a length of Scotch No. 810 tape on the contact pad and attempting to peel off

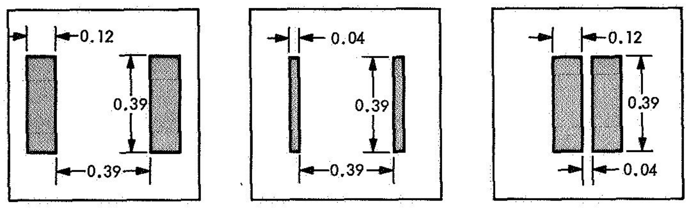

(a) PATTERN I (b) PATTERN II (c) PATTERN III

DIMENSIONS IN INCHES

Fig. 2. Contact coupon pad patterns

---

[1] Hanovia Liquid Gold Division, East Newark, N.J.

[2] Heliotek Corp., Sylmar, Calif.

the contact at a 90-deg angle. The electrical and adhesion data are reported in Table 1.

Since little information was available about the firing characteristics of the metal resinate materials, a less expensive coupon was chosen for evaluation of these materials. The metal resinates were screened in a ~0.650 × 0.650-in. pattern onto glass microscope slides. These were heat-treated under carefully controlled conditions, as shown in Table 2. The sheet resistivities of the films, measured with the two-point-probe technique, are reported in Table 2.

Table 2. Metal resinate data[a]

Heat Treatment		Atmosphere	Sheet Resistivity (Ω/square)		
Time, min	Temperature, °F		Gold	Nickel	Gold–silicon eutectic, 5.5 wt % Si, 94.5 wt % Au
3	1112	N_2	25	—	5×10^5
15	1120	N_2	3×10^4	—	3×10^5
20	662	Air	2	—	—
3	680	H_2	—	7×10^4	—
15	688	H_2	—	10^3	—
5	748	H_2	1.4	100	—
3	1106	H_2	10^3	10^4	10^4

[a] The following metal resinate films had measured resistance values greater than $10^6 \Omega$ for all heat treatments: silver, copper, zinc, lead–tin eutectic (18.2 wt % Sn, 81.8 wt % Pb).

4. Metal Resinate Test

The metal resinate heat treatments and electrical tests are reported in Table 2. The only metal resinate that produced a good conducting film was the gold. This material produced bright, low-sheet-resistance films when fired in air at 662°F, and the properties improved when the films were refired in H_2 at 784°F. All other films fired in atmospheres of N_2,H_2, or air showed visual evidence of organic decomposition products and oxidized metal remaining in the film. Considerably more work would be needed to establish the proper decomposition conditions for these inks.

5. Thick-Film-Contacted Solar Cell

The special prepared unfluxed aluminum ink[3] was chosen on the basis of the coupon data as the most promising candidate to be used for screening on the thick-film cell contacts. Screening was done on the Presco Screen Printer using 325-mesh stainless steel masks. Two mask geometries were used (see Fig. 3). The P side of the cell was screened first, and the volatile solvents were evaporated from the films by drying at 200°F for 20 min in air. A Mylar fixture was made to support and protect the P-side contact on the cell during the N-side screening. This procedure allowed the use of one heat treatment cycle to alloy both contacts. The heat treatment variables are reported in Table 3.

To evaluate the cells electrically, the short circuit current I_{sc} and the open circuit voltage V_{oc} were measured under a constant intensity source of illumination from a projector lamp. These values were compared with those measured in the same fashion for a Ti–Ag-contacted cell produced by Heliotek for the *Mariner* Mars 1969 Project.

The best cells measured produced a short-circuit current of 3 mA and an open-circuit voltage of 40–50 mV (Table 3).

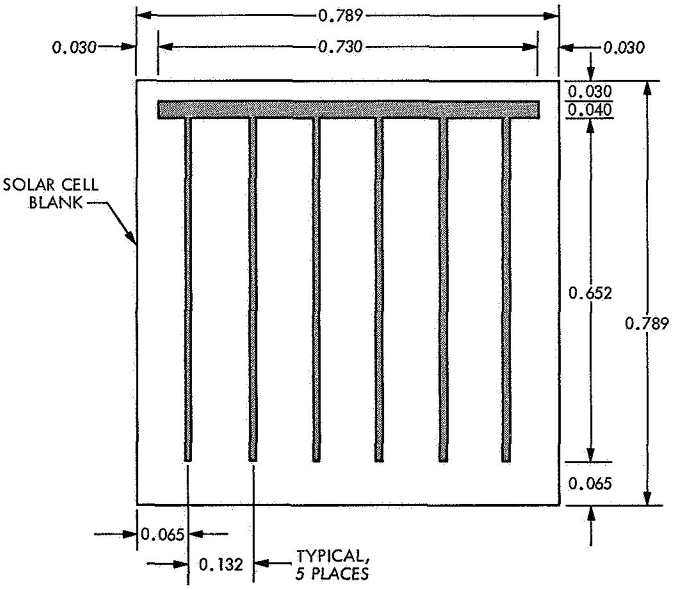

(a) FRONT CONTACT (N SIDE)

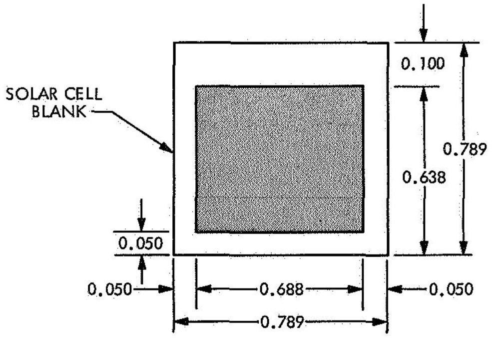

(b) BACK CONTACT (P SIDE)

Fig. 3. Front and back solar cell contact geometries

---

[3] Electro Materials Corporation of America, Mamaroneck, N.Y.

Table 3. EMCA unfluxed aluminum-contacted solar cell data

Cell Lot	Dry time at 200°F, min	Intermediate hold		Atmosphere	Heat Treatment		Contact adhesion	Short-circuit current, mA	Open-circuit voltage mV
		Time, min	Temperature, °F		Time, min	Temperature, °F			
1	20	7	600	N_2	1.25	1190	Poor	2.5 (max)	30
2	None	10	376	N_2	1.0	1009	Bad	—	—
3	None	5	600	N_2	1.0	1225	Poor	3.0	20–40
4	None	5	600	N_2	1.0	1225	Poor	3.0	20–40
5	20	5	600	N_2	2.0	1225	Fair	3.0	15–20
6	10	5	600	N_2	2.5	1090	Poor	~3	40–50
7	12.5	10	600	H_2	2.5	1085	Poor	<1	30
8	16.5	5	600	H_2	10	1044	Bad	—	—

The short circuit current value is approximately 1–2% of that measured for the *Mariner* Mars 1969 cells, and the open-circuit voltage is approximately 7% of the *Mariner* Mars 1969 cells under the same illumination. Curve tracer measurements indicated that the experimental cells did not have the desired diode characteristics of the P–N junction found in all *Mariner* Mars 1969 cells.

Metallographic sections of the N finger contacts made on the unfluxed aluminum-contacted cells revealed that the aluminum was most likely penetrating into the junction area of the cell when the heat treatment temperatures were high enough to bring about reasonable adhesion of the aluminum film to the silicon. Electron microprobe analysis indicated that in the area of the silicon diffused with the aluminum, the aluminum–silicon eutectic phase was present. This aluminum penetration into the junction area may be the reason that the diode characteristics were not observed for the PN junction in the aluminum-contacted cells.

The aluminum films fired at temperatures above the aluminum–silicon eutectic phase had a dull gray appearance as compared with the bright metallic appearance of the unfired films. An X-ray diffraction analysis to determine the composition of these fired films indicated that the only detectable material present was pure aluminum. No evidence of aluminum oxide was found in the diffractograms.

6. Wrap-Around Structure

A group of the unfluxed aluminum thick-film cells, selected on the basis of electrical and adhesion measurements, was used in the construction of wraparound cells employing epoxy dielectrics and silver-filled conductive epoxy resins. These cells were constructed as follows (see Fig. 1):

(1) A high-temperature epoxy dielectric coating (Emerson & Cuming TF-11)[4] was applied to one edge of the cell by dipping and was cured at 350°F for 20 min to form a coating for the junction to prevent shorting of the cell by the wraparound conductor.

(2) The silver-filled conductive epoxy (Emerson & Cuming Eccobond Solder V-91) wraparound structure was applied to the cells by dipping or brushing in the pattern shown in Fig. 1 and was cured at room temperature for 24 h.

The cells were again tested electrically. The short-circuit current outputs of the cells decreased slightly as compared with the values measured before the wraparound structure was applied, but the open-circuit voltage remained essentially unchanged. Some instability in the power output was observed. This was determined to be in the electrical interface between the silver-filled epoxy and the thick-film contacts.

7. Mock-Up of Prototype Submodule for Solar Array

To simulate the printed circuit interconnection scheme for the solar array, an adhesive-backed copper tape was bonded to a glass plate in the desired interconnection pattern. The wraparound cells were bonded in place to the copper interconnection stripes with Eccobond 57C solder, a silver-filled epoxy resin, and cured at room temperature. The submodule fabricated in this manner contained four cells, two groups of two cells in series, connected in parallel (see Fig. 4). The total power output from this submodule was no more than the output from one cell contained in the module.

---

[4] Emerson & Cuming, Inc., Canton, Mass.

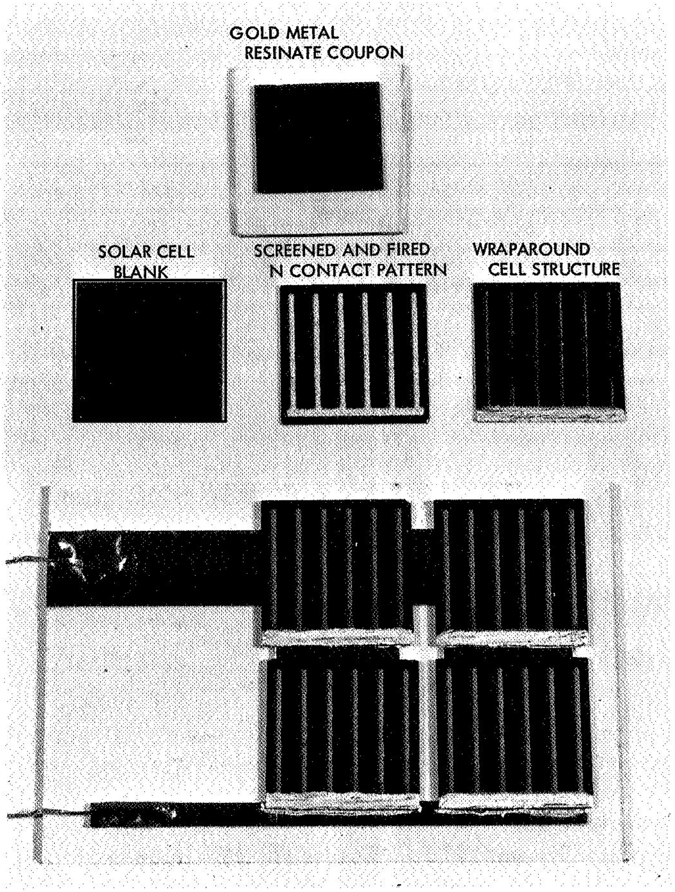

Fig. 4. Test coupons and mockup of prototype submodule of solar array

8. Conclusions

Of the screenable inks evaluated (Table 1), only the EMCA unfluxed aluminum appeared to have limited feasibility as a contact material. The sheet resistivity of the film as screened and fired in Run 17 (Table 1) was 0.012 Ω/square. The theoretical sheet resistivity for bulk aluminum of this geometry would be ~0.001 Ω/square. A stable, low-resistance, ohmic contact was not made to the P side of the cell with any other material tested. The inks containing glasses, such as the DuPont conductive silver preparations, were unstable when the level of current was changed during the electrical resistance measurements. Metallographic sections of the contact pads made with these inks indicate that some of the material in the film, identified as fast-diffusing alkali ions from the glass, diffused through the N-layer and into the P-bulk material to a depth of at least 0.002-0.003 in.

The concept of a wraparound cell structure utilizing printed circuit technology for mounting and interconnection appears feasible based on the limited amount of work done. However, the outputs of the two-by-two array fabricated were low. The low power output of the array was probably due to the low power conversion efficiency of the solar cells made with the thick-film aluminum contacts and also to the rather high contact resistance observed between the silver-filled epoxy and the fired-aluminum ink. Further work would be required to establish whether the power output of the array could be increased to usable values.

XI. Applied Mechanics

ENGINEERING MECHANICS DIVISION

A. Nuclear Radiation Mapping of Thermoelectric Outer Planet Spacecraft, *F. Wolf*

1. Introduction

Determination of the radiation environment of a spacecraft equipped with a radioisotope auxiliary power supply is a necessary step in the definition of the spacecraft configuration. During the design, maps of increasingly improved accuracy are required by systems design groups concerned with shielding problems and by environmental testing groups that prepare the qualification test program for the spacecraft components. Initial calculations of the three-dimensional gamma radiation field for the thermoelectric outer planet spacecraft (TOPS) were obtained by considering only the three tandem radioisotope thermoelectric generator (RTG) fuel capsules.[1] A more extensive Monte Carlo type radiation transport program is being used to map the geometrically complex case presented by the TOPS structure (Ref. 1).

2. Radiation Field Map

A simplified form of the spacecraft, which preserves the shape and mass of the bus and the antenna, formed the basic input together with as accurate a description of the material composition as could be obtained from the preliminary lay-out of the 12j version. The main spacecraft subsystems, electronics, propulsion compartment, and fuel were deprived of structural detail for the first computing runs and were represented by regions of homogeneous density. The multi-hundred-watt[2] (MHW) source was equipped with a simulated generator jacket containing typical thermoelectric materials uniformly distributed around the fuel cells.

The program described the 12j configuration by means of 55 surfaces and 60 regions. Twenty different locations for detecting the gamma and neutron flux were selected with emphasis on the most likely position of the payload. Some of the detector point locations are shown in Fig. 1.

The emission from the MHW source was monitored by five detection points in the vicinity of the RTG and extrapolated to larger distances to obtain an approximate map of the radiation field in the absence of any spacecraft structure for comparison purposes. This is shown in Fig. 1, with surfaces of constant gamma energy flux (solid lines) and constant neutron energy flux (broken lines), which are nearly symmetrical in respect to the main axis of the RTG.

---

[1] Dore, M., *Gamma Radiation Mapping for Three RTG's in Tandem*, May 8, 1969 (JPL internal document).

[2] The "multi hundred-watt" radioisotope thermoelectric generator developed by the General Electric Co., Space Division, King of Prussia, Pa., under AEC contract.

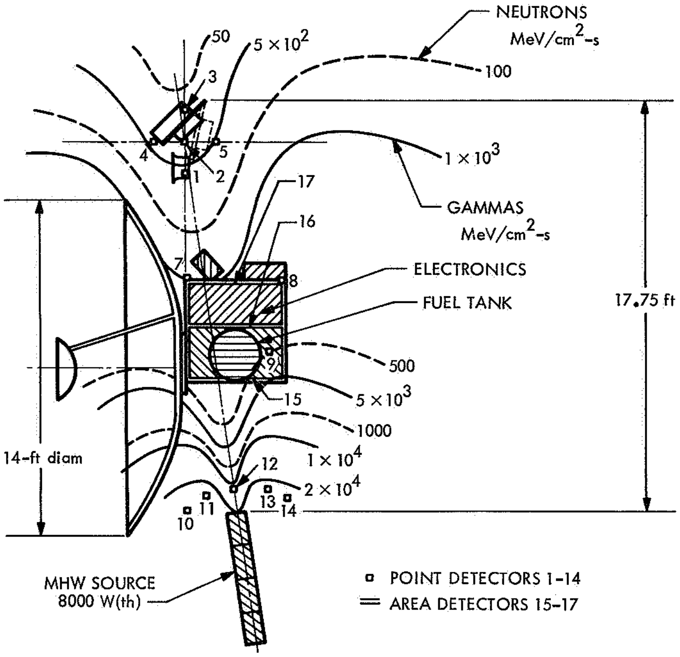

Fig. 1. Bare field radiation environment of RTG with simplified spacecraft superimposed

The presence of the massive spacecraft in this field causes large changes in the total radiation dose rates to which payload components and electronics will be exposed. The shielding effect of the central mass of the spacecraft can be seen by comparing the gamma flux calculated for detector points 1 to 6, which is presented in Table 1, with the unperturbed field shown in Fig. 1. This region covers approximately the main payload area (cameras A and B) and obtains a two order of magnitude reduction of the exposure dose rate.

A traverse along detector points 4, 2, and 5, which represents a tentative centerline of the payload volume, is shown in Fig. 2; this indicates higher gamma dose rates for the area that is closer to the antenna (point 4), compared to its symmetrical opposite across the MHW axis. Thus, the original aiming point of the axis, point 2, does not form a minimum dose as expected in the preliminary layout procedure. The most likely cause for this condition is the relatively large scattering from the antenna dish to the payload area. The contribution of antenna scatter to the scalar flux at point 2 is larger than 40% of the total, while in absolute amount point 4 receives the largest scattered flux due to its proximity to the antenna. Also marked in the figure are total gamma dose rates obtained at various stages of the computation, showing the improvement of results with an increased number of particle histories run in the program (a maximum of 1024).

Table 1. Gamma flux after 1024 packets (MHW fuel age, 5 yr)

Region	Detector point	Cumulative number flux, γ/cm^2-s	Energy flux, MeV/cm²-s	Response, rad/h
Payload	1	1.95 + 0	1.93 + 0	2.83 − 6
	2	1.63 + 0	1.63 + 0	2.39 − 6
	3	1.38 + 0	1.40 + 0	2.04 − 6
	4	2.24 + 0	2.61 + 0	3.74 − 6
	5	1.03 + 0	1.46 + 0	2.02 − 6
	6	1.73 + 0	1.66 + 0	2.45 − 6
Bus	7	1.78 + 0	2.40 + 0	3.32 − 6
	8	3.11 + 0	6.50 + 0	8.64 − 6
	9	9.83 + 2	5.47 + 2	8.76 − 4
Near RTG	10	2.78 + 4	3.12 + 4	4.44 − 2
	11	2.32 + 4	2.64 + 4	3.75 − 2
	12	9.83 + 3	1.10 + 4	1.57 − 2
	13	1.85 + 4	2.43 + 4	3.42 − 2
	14	2.23 + 4	2.75 + 4	3.90 − 2
Bus surfaces	15	2.50 + 4	3.25 + 4	4.58 − 2
	16	1.70 + 1	1.44 + 1	2.05 − 5
	17	1.35 + 0	2.73 + 0	3.65 − 6
Bus volumes	18	2.55 + 2	2.74 + 2	3.95 − 4
	19	1.10 + 2	1.02 + 2	1.51 − 4
	20	8.07 + 0	7.87 + 0	1.12 − 5

Another shielding effect of the spacecraft structure is apparent in comparing the total dose rates of detector points 4 and 7 in Table 1. Although in an empty field point 4 would receive one half of the dose of point 7, scattering from the sources in the electronics compartment and antenna increases the flux at point 4 to a 10% larger dose than the one in point 7. Thus, extreme closeness to a large number of scattering sources will prevent a detector from "seeing" these sources.

Antenna scatter is approximately one third of the total gamma dose in the payload area (Fig. 2), and its effect can also be observed in detector points 10 and 11 where the flux is larger than in the corresponding symmetrical

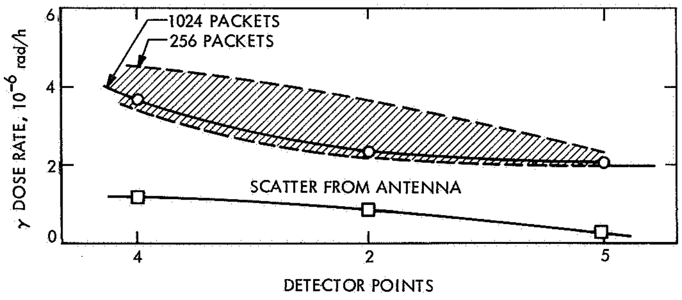

Fig. 2. Radiation environment in TOPS 12j main payload area

points 13 and 14. Therefore, the antenna dish could be viewed as forming a conducting link, bypassing the spacecraft central mass, and producing generally higher dose rates on the antenna side of the RTG midplane.

As a tentative first conclusion, from a shielding standpoint, it would be advantageous to line up the payload with the fuel tank and electronics midplane and also let the RTG axis coincide with it.

A radiation intensity profile across the spacecraft along the RTG axis is shown in Fig. 3. Average area gamma dose rates for the surfaces of the propulsion and electronics compartment (area detectors 15, 16, and 17) indicate several orders of magnitude decrease of the flux on traversing the bus in the direction towards the payload. The average intensity of radiation in the three compartments of the bus given by volume detectors is in good agreement with the intensity given by point detectors 7, 8, and 9, located immediately behind the bus and within the propulsion compartment. The shielding effect is apparent in planes 16 and 17 when the dose there is compared to the dose in an empty field along a ray from the RTG through detector points 12 and 13. In contrast, the total dose rate in the front face of the bus (area detector 15) is larger than the empty field value due to backscatter of radiation from the immediately adjoining large mass (fuel tank, propulsion, and electronics compartment). The main payload area, represented by point detectors 1, 2, and 3, falls well into line with the calculated area averages 15, 16, and 17.

Table 1 gives a preliminary survey of total gamma flux in the most important regions of the TOPS, based on a MHW source and 5-yr-old fuel. Detector points 1 to 6 describe the principal payload location, points 7 to 9 the bus, points 10 to 14 an RTG envelope, and surface detectors 15 to 17 and volume detectors 18 to 20 are also in the bus. Columns 2 and 3 give the cumulative number flux and energy flux, and column 4 gives the response dose rate in rad/h. The contribution to the total flux by scattering from the antenna is seen to be quite high, around 40% in the payload region, and very small in most other parts of the field. Thus, the location of the main payload relative to the antenna dish appears to have increased importance in spacecraft configuration studies.

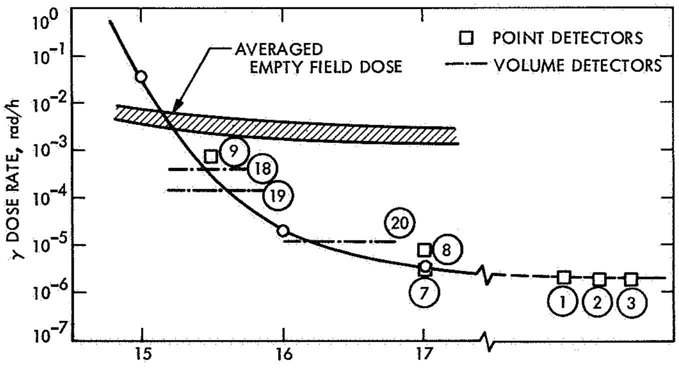

Fig. 3. TOPS 12j gamma dose rate

Convergence of the calculations for three point detectors can be seen in the cross-hatched area in Fig. 2; this covers the variance of dose rate after each one of four increments in the number of particle histories calculated, leading to a total of 1024 iterations. The final improvement in the results, or the decrease of statistical error, appears to be small such as to permit some reduction in number of histories and in required computer time for future runs without much loss in accuracy.

The neutron flux is shown in Fig. 4 for a traverse of the spacecraft along the axis of the RTG. Again, the shielding effect of the spacecraft bus appears in a reduction of neutron flux by two orders of magnitude. The contribution to the scalar flux in the payload area due to scatter from

Table 2. Neutron flux after 1024 packets (MHW fuel age, 5 yr)

Region	Detector point	Cumulative number flux, n/cm^2-s	Energy flux, MeV/cm^2-s	Response, rad/h
Payload	1	1.03 − 1	1.92 − 1	1.44 − 6
	2	8.25 − 2	1.56 − 1	1.16 − 6
	3	6.67 − 2	1.26 − 1	9.35 − 7
	4	1.07 − 1	2.07 − 1	1.52 − 6
	5	6.53 − 2	1.12 − 1	8.96 − 7
	6	1.02 − 1	1.90 − 1	1.43 − 6
Bus	7	1.87 − 1	3.04 − 1	2.33 − 6
	8	2.30 − 1	5.27 − 1	3.45 − 6
	9	1.26 + 2	2.24 + 2	1.76 − 3
Near RTG	10	1.80 + 3	3.62 + 3	2.55 − 2
	11	1.45 + 3	2.91 + 3	2.05 − 2
	12	7.93 + 2	1.54 + 3	1.11 − 2
	13	1.67 + 3	3.24 + 3	2.32 − 2
	14	1.99 + 3	3.88 + 3	2.77 − 2
Bus surfaces	15	2.11 + 3	4.19 + 3	2.97 − 2
	16	3.55 + 0	5.95 + 0	4.87 − 5
	17	2.82 + 0	5.96 + 0	4.15 − 5
Bus volumes	18	3.33 + 1	6.22 + 1	4.67 − 4
	19	6.43 + 0	7.34 + 0	6.47 − 5
	20	1.93 + 0	3.48 + 0	2.62 − 5

the antenna dish is two thirds of the total (Table 2), much larger than in the gamma radiation field.

At present, additional calculations are under way to improve the mapping of this spacecraft configuration. Later versions of the TOPS will require similar treatment.

Reference

1. Jordan, T. M., *FASTER, a Fortran Analytic Solution of the Transport Equation by Random Sampling*, WANL-PR-(LL)-010, Vol. 9, Contract NAS-8-20414. Westinghouse Astronuclear Laboratory, Pittsburgh, Pa., Jun. 1967.

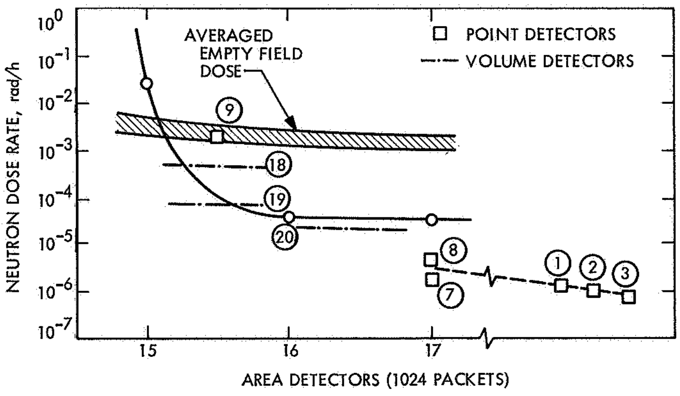

Fig. 4. TOPS 12j neutron dose rate

B. On the Maximum Dynamic Response of Structures and Proof Testing,

J.-N. Yang and E. Heer

1. Introduction

Flight data taken in a number of recent space flights show that the major spacecraft excitations during any one flight are not only highly transient but also associated with considerable statistical variation from one spacecraft or flight to another. An example of such excitation is given in Ref. 1. The theoretical approach, from the viewpoint of random vibration, was outlined in SPS 37-59, Vol. III, pp. 168–171, in which it is assumed that the available flight data are sufficient enough for the statistical characterization of nonstationary random inputs. Unfortunately, however, it is difficult to make a theoretical statement of whether the available information or finite flight measurements are sufficient for the statistical characterization of random input. Therefore, other possible approaches appear to be desirable and, in fact, such an attempt was made in SPS 37-61, Vol. III, pp. 179–183, in which a frequency domain analysis is employed to find the upper bound of the maximum dynamic response as well as the least favorable input. In this article, a similar approach is taken in the time domain analysis, which yields various upper bounds of the maximum dynamic response and the dynamic testing forcing function, which, in turn, will produce the expected upper bound of the maximum response. A rational design rule seems to be that the less information or data one has, the more conservative design one should take. Although a system with a single input is considered here, the extension of the present technique to a system with multi-excitations appears to be possible and will be investigated in the near future.

2. When the Total Energy and Maximum Duration of Inputs can be Specified

Let a structural system be characterized by a linear time invariant operator L which relates the structural response $Y(t)$ to the excitation $X(t)$ through the following form

$$L[Y(t)] = X(t) \tag{1}$$

From past experience (Ref. 1), the excitation to the spacecraft, or the booster–spacecraft interface acceleration, has a rather short duration, such as 1 to 2 s. Therefore, it is reasonable to assume that

$$X(t) = 0 \qquad \text{for } t < 0 \text{ or } t > T^* \tag{2}$$

in which T^* represents the maximum duration of $X(t)$.

The response $Y(t)$ can then be written as

$$Y(t) = \int_0^{T^*} h(t-\tau)\, X(\tau)\, d\tau \tag{3}$$

where $h(t)$ is the impulse response function of the system, i.e.,

$$L[h(t)] = \delta(t) \tag{4}$$

where $\delta(t)$ is the dirac delta function.

It is noted that $Y(t)$ and $X(t)$ can be displacement, acceleration, or stress, etc., and that they do not necessarily represent the same quantity.

It follows from Eq. (3) that

$$|Y(t)| \leqq \int_0^{T^*} |h(t-\tau)|\,|X(\tau)|\,d\tau \tag{5}$$

and because of the Schwarz inequality,

$$|Y(t)| \leqq \left[\int_0^{T^*} h^2(t-\tau)\,d\tau\right]^{1/2} \left[\int_0^{T^*} X^2(\tau)\,d\tau\right]^{1/2} \tag{6}$$

Since the right-hand side of Eq. (6) is a monotonically increasing function of t, one obtains

$$\max_t |Y(t)| \leqq \left[\int_0^{T^*} h^2(\tau)\,d\tau\right]^{1/2} \left[\int_0^{T^*} X^2(\tau)\,d\tau\right]^{1/2} \tag{7}$$

where

$$\max_t |Y(t)|$$

is the maximum absolute value of the response $Y(t)$ for $t < \infty$. The inequality of Eq. (7) was used in Ref. 2.

Consider a class of input excitations with the total energy less than or equal to M^2, i.e.,

$$\int_0^{T^*} X^2(t)\,dt \leqq M^2 \tag{8}$$

Then, it follows, from Eqs. (7) and (8), that an upper bound of a class of maximum absolute response produced by such a class of inputs is

$$\max_t |Y(t)| \leqq MN \tag{9}$$

where

$$N^2 = \int_0^{T^*} h^2(\tau)\,d\tau \tag{10}$$

The proof testing forcing function, denoted by $\overline{X}(t)$, which will produce the maximum response given in Eq. (9) follows from Eq. (3) as

$$\overline{X}(t) = \frac{M}{N} h(T^* - t) \tag{11}$$

Substituting $\overline{X}(t)$ in Eq. (11) into Eq. (3) for $X(t)$, one obtains

$$Y(t) = \frac{M}{N} \int_0^{T^*} h(t-\tau)\,h(T^*-\tau)\,d\tau \tag{12}$$

and hence $\max_t |Y(t)|$ occurs at $t = T^*$, i.e.,

$$\max_t |Y(t)| = Y(T^*) = MN \tag{13}$$

In conclusion, the upper bound of the maximum response is MN under a class of excitations with the total energy less than or equal to M and the maximum duration T^*. Note that the above development is not a straightforward Fourier transform of the result given in SPS 37-61, Vol. III. The upper bound MN in this article (Eqs. 8–10) is smaller than that given in SPS 37-61, Vol. III. The testing forcing function $\overline{X}(t)$ which produces such an upper bound of the response is the mirror image of the truncated impulse response function $h(t)$ for $t < T^*$, with respect to $t = 0$ and translating an amount of T^* to the right of the time axis, as given in Eq. (11).

3. When the Maximum Envelope of Inputs Can be Specified

It is clear that the above discussion is based on the assumption that the upper bound of the total energy of a class of excitation can be specified in some ways. Frequently, however, more information on excitations is available from past experience. Furthermore, it is also desirable to obtain not only the upper bound of the absolute maximum response

$$\max_t |Y(t)|$$

but also the upper bound of the response history. In this connection, the envelope function of a class of excitation may be of particular importance. Let $X_e(t)$ be the envelope function of a class of excitations. Then, replacing $X(t)$ in Eq. (5) by $X_e(t)$, one obtains an upper bound of the absolute value of the response history $Y(t)$ as follows:

$$|Y(t)| \leqq \int_0^{T^*} |h(t-\tau)|\,|X_e(\tau)\,d\tau = V(t) \tag{14}$$

From past experience (Ref. 1), the envelope function of the excitation to the spacecraft has the following form:

$$X_e(t) = A(e^{-\alpha t} - e^{-\beta t} - \gamma) \tag{15}$$

where A, α, β, and γ are some constants.

It is noted that $V(t)$ in Eq. (14) is the envelope of the upper bound of the absolute response history, which has some significance to design engineers, e.g., fatigue failure analysis. Since $V(t)$ can be computed and plotted numerically without any difficulty, the time at which $V(t)$ takes a maximum value, say t^*, can be determined, i.e.,

$$V(t^*) \geqq V(t) \tag{16}$$

The proof testing forcing function $\bar{X}(t)$ which will produce the maximum response $V(t^*)$ can be obtained from Eqs. (3) and (14) as

$$\bar{X}(t) = X_e(t)\frac{|h(t^* - t)|}{h(t^* - t)} \tag{17}$$

The fact that the maximum response

$$\max_t \; |Y(t)|$$

of $Y(t)$ produced by Eq. (17) is equal to $V(t^*)$ can be realized by substituting Eq. (17) into Eq. (3) to yield

$$Y(t) = \int_0^{T^*} h(t - \tau)\frac{|h(t^* - \tau)|}{h(t^* - \tau)} X_e(\tau)\, d\tau \tag{18}$$

and in a similar fashion as before, one can easily show that

$$\max_t \; |Y(t)| = Y(t^*) = V(t^*) \tag{19}$$

It is very interesting to note that the testing forcing function obtained in Eq. (17) has a general form. The term

$$\frac{|h(t^* - t)|}{h(t^* - t)}$$

takes either +1 or −1, depending on whether $h(t^* - t)$ is positive or negative and is independent of the magnitude of the structural characteristics $h(t)$. The magnitude of the testing forcing function $\bar{X}(t)$, however, depends only on the magnitude of the input envelope $X_e(t)$. This indicates that the magnitude of the testing forcing function is taken from the excitation envelope while its frequency is from the frequency content of the impulse response function $h(t)$.

When a multi-degree-of-freedom system with a single input is considered, the above discussions are still valid where $Y(t)$, $V(t)$, and $h(t)$ are the vectors.

When the structure is subjected to multi-inputs, it is usually very expensive and difficult to perform multidimensional proof testing and, hence, a single input (or a shaker) is sometimes preferable. In this connection, the testing forcing function derived in Eq. (17) appears to be useful. Suppose one can find the upper bound of the maximum response, say $\bar{M}$, in some way; then the single testing forcing function can be obtained from Eqs. (3) and (17) as

$$\bar{X}(t) = X_e \frac{|h(t^* - t)|}{h(t^* - t)} \frac{\bar{M}}{V(t^*)}$$

4. Numerical Example

As an illustrative example, consider a simple torsional vibratory system whose angular response $Y(t)$ relative to its base is related to the angular acceleration $X(t)$ at the base by

$$\ddot{Y}(t) + 2\zeta\omega_0 \dot{Y}(t) + \omega_0^2 Y(t) = X(t) \tag{20}$$

in which ζ and ω_0 are the damping coefficient and the natural frequency of the system, respectively. The impulse response function $h(t)$ of the system is

$$\left.\begin{aligned} h(t) &= \frac{e^{-\zeta\omega_0 t}}{\sqrt{1-\zeta^2}} \sin \sqrt{1-\zeta^2}\,\omega_0 t, \qquad t \geqq 0 \\ &= 0, \qquad t < 0 \end{aligned}\right\} \tag{21}$$

Furthermore, consider a class of excitations with $M = 1.21$ where the envelope function can be expressed as

$$X_e(t) = A(e^{-\alpha t} - e^{-\beta t}) \tag{22}$$

in which A, α, and β are some constants.

In this particular example, $\zeta = 0.02$, $\omega_0 = 20$ Hz, $\alpha = 2.0$, $\beta = 3.5$, $A = 10.0$, and $T^* = 2.0$ s.

From the numerical computation, it is found that $N = 0.3154$ and, hence, the upper bound of the maximum response based on the energy of inputs is $MN = 0.38$. The maximum $V(t^*)$ of the upper bound of the response history, based on the envelope function of inputs, occurs at $t^* = 0.77$ s and is equal to 0.373. To give some idea about the upper bounds computed above, a particular excitation $X(t)$ is chosen from a class of excitations stated above (Eq. 22),

$$X(t) = A(e^{-\alpha t} - e^{-\beta t})\sin\omega t \qquad (23)$$

with $\omega = 20$ Hz. This input $X(t)$ is plotted in Fig. 1. The response $Y(t)$ due to the excitation $X(t)$ and the upper bound $V(t)$ of the response history are plotted in Fig. 2. The testing forcing function $\bar{X}(t)$ given in Eq. (11) is plotted in Fig. 3, and the testing forcing function $\bar{X}(t)$ given in Eq. (17) is plotted in Fig. 4.

It can be observed from Fig. 2 that the maximum response due to the excitation $X(t)$ (Eq. 23), that is randomly selected from the class of excitations given in Eq. (22), is 0.295. The upper bounds $MN = 0.38$ and $V(t^*) = 0.373$ exceed 0.295 by about 28%. Therefore, if one has to design a structure to resist a class of inputs defined in Eq. (22), the upper bounds discussed above provide valuable information even if they are not used as design criteria. Furthermore, the testing forcing function derived in Eq. (17) appears to be of particular interest.

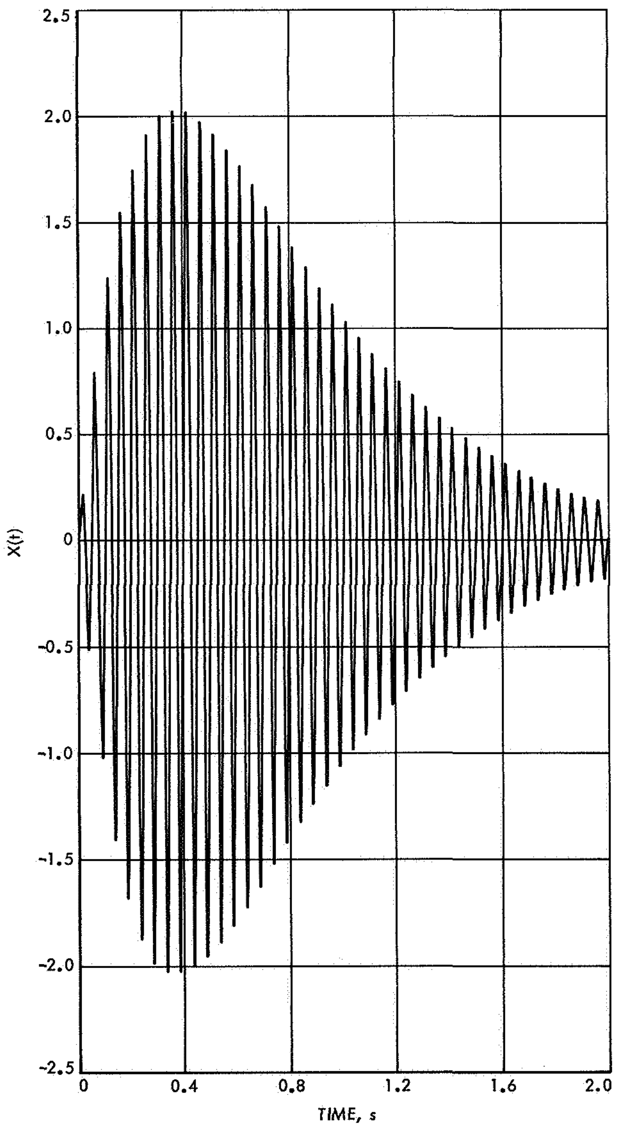

Fig. 1. Time history of excitation

References

1. Heer, E., and Trubert, M., *Analysis of Space Vehicle Structures Using the Transfer Function Concept*, Technical Report 32-1367. Jet Propulsion Laboratory, Pasadena, Calif., Apr. 1, 1969.
2. Drenick, R. F., *On the Model-Free Design of A Seismic Structure*, paper presented at ASCE National Meeting on Structural Engineering, Portland, Ore., Apr. 7–11, 1970.

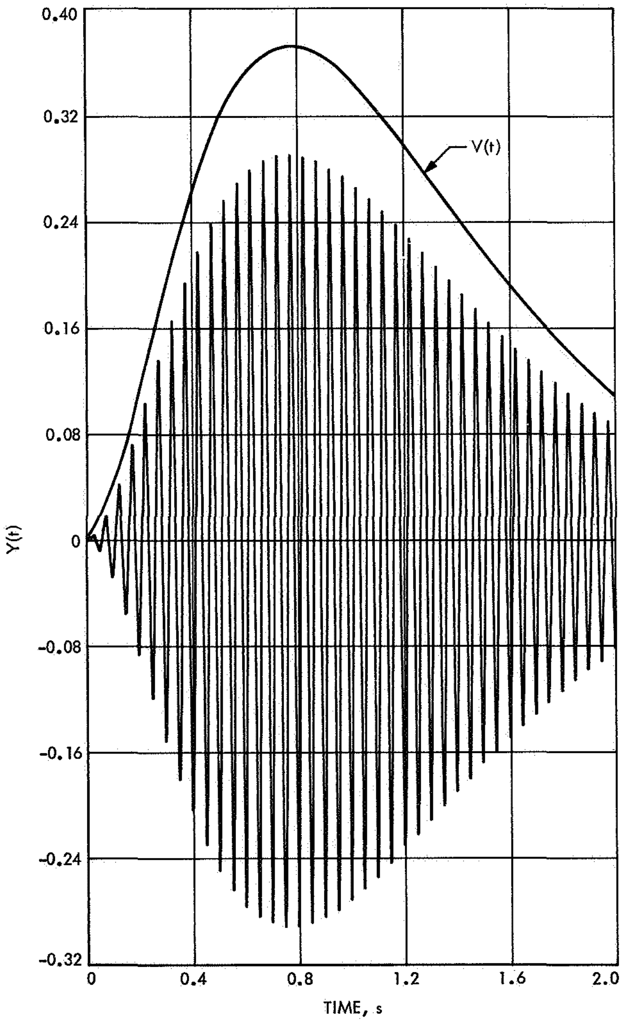

Fig. 2. Response and envelope of upper bound of absolute response history

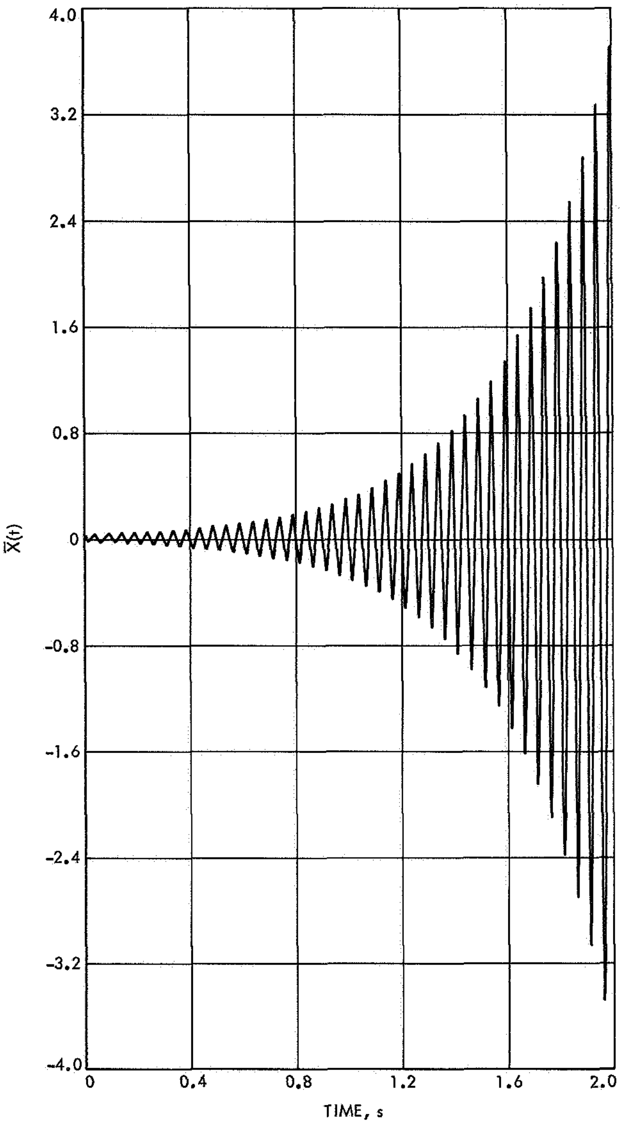

Fig. 3. Proof testing forcing function in Eq. (11)

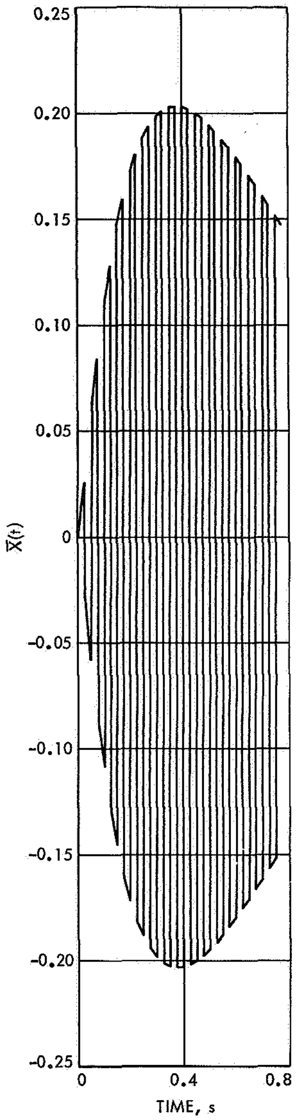

Fig. 4. Proof testing forcing function in Eq. (17)

C. Nonlinear Vibration of an Infinite Long Circular Cylinder, *J. C. Chen*

1. Introduction

When a flexural structural system, such as a large deep-space antenna, undergoes deployment-induced vibration, the governing equations of motion become nonlinear due to its large deformation. Although the response of the structural system can be calculated by the usual digital programming, some of the so-called "nonlinear phenomena" can only be predicted by a detailed study of the governing equations. A typical example is the multi-value response of a nonlinear structural system at a certain frequency. The stability analysis will then determine the true response at that frequency. To develop a general computer program to handle the large deformation flexural structural system, the nature of the nonlinear governing equations must be fully understood. A thin-walled infinite long circular cylindrical shell under periodic loading was chosen for this study because of its similarity with the large antenna in governing equations and because of its existing experimental data.

In SPS 37-62, Vol. III, pp. 182–187, the nonlinear equations of a vibrating infinite long circular cylinder were derived and reduced to a sequence of linear equations by the perturbation method. In this article, the linearized equations are solved and the stability analysis are performed. Finally, comparison is made with the existing test results.

2. Solutions of the Governing Equations

The solutions of the linearized governing differential equations are as follows:

$$\epsilon^0 \left\{ \begin{aligned} N_1 &= a\cos\tau\cos n\theta + b\sin\tau\sin n\theta && (1)\\ \bar{W}_0 &= \bar{a}\cos\tau\cos n\theta + \bar{b}\sin\tau\sin n\theta && (2) \end{aligned} \right.$$

$$\epsilon \left\{ \begin{aligned} N_2 &= \alpha_1\cos 2\tau + \alpha_2\cos 2n\theta + \alpha_3\cos 2\tau\cos 2n\theta + \alpha_4\sin 2\tau\sin 2n\theta && (3)\\ \bar{W}_1 &= \bar{\alpha}_1\cos 2\tau + \bar{\alpha}_2\cos 2n\theta + \bar{\alpha}_3\cos 2\tau\cos 2n\theta + \bar{\alpha}_4\sin 2\tau\sin 2n\theta \end{aligned} \right.$$

where

$$\left. \begin{aligned} \alpha_1 &= -\frac{1}{2}\frac{\lambda_0 n^2(\bar{a}^2-\bar{b}^2)}{(1-4\lambda_0)}\\ \bar{\alpha}_1 &= -\frac{1}{8}\frac{n^2(\bar{a}^2-\bar{b}^2)}{1-4\lambda_0}\\ \alpha_2 &= 0\\ \bar{\alpha}_2 &= \frac{1}{32}\frac{1}{n^2 r^2}(b\bar{b}-a\bar{a})\\ \alpha_3 &= -\frac{1}{2}n^2(a\bar{a}+b\bar{b}) + 4(\lambda_0-4n^4r^2)\,\bar{\alpha}_3\\ \bar{\alpha}^3 &= \frac{\lambda_0 n^2\left[2(a\bar{a}+b\bar{b})-\frac{1}{2}\,(\bar{a}^2+\bar{b}^2)\right]-2n^4(a\bar{a}+b\bar{b})}{16(\lambda_0-n^2)(\lambda_0-4n^4r^2)-4\lambda_0}\\ \alpha_4 &= -\frac{1}{2}n^2(a\bar{b}+\bar{a}b)+4(\lambda_0-4n^4r^2)\,\bar{\alpha}_4\\ \bar{\alpha}_4 &= \frac{\lambda_0 n^2[2(a\bar{b}+\bar{a}b)-\bar{a}\bar{b}]-2n^4(a\bar{b}+\bar{a}b)}{16(\lambda_0-n^2)(\lambda_0-4n^4r^2)-4\lambda_0} \end{aligned} \right\} \qquad (4)$$

In a similar manner, Eq. (22), SPS 37-62, Vol. III, p. 186, can be solved. Again the periodicity condition requires that the coefficients of terms $\cos\tau\cos n\theta$ and $\sin\tau\sin n\theta$ be zero to avoid secular solution. This leads to the relations

$$\left.\begin{aligned} (n^2+1)\lambda_2 + (P+Q)\bar{a}^2 + (S-P)\bar{b}^2 + \frac{n^2F}{\bar{a}} &= 0 \\ \bar{b}\left\{(n^2+1)\lambda_2 + (S-P)\bar{a}^2 + (P+Q)\bar{b}^2\right\} &= 0 \end{aligned}\right\} \quad (5)$$

where

$$\left.\begin{aligned} P &= \frac{1}{4}\frac{n^6\lambda_0}{1-4\lambda_0} \\ Q &= \frac{n^4\lambda_0}{16}\frac{(2n^4+10n^2+9)}{(n^2+1)(4n^2+5)} \\ S &= \frac{n^4\lambda_0}{16}\frac{(6n^4+14n^2+7)}{(n^2+1)(4n^2+5)} \end{aligned}\right\} \quad (6)$$

These are the equations that relate frequency and response and represent a special feature of nonlinear vibration.

Equation (5) can be rewritten as

$$\left.\begin{aligned} (n^2+1)\lambda_2 + (P+Q)\bar{a}^2 + (S-P)\bar{b}^2 + \frac{n^2F}{\bar{a}} &= 0 \\ \bar{b} &= 0 \end{aligned}\right\} \quad (7)$$

$$\left.\begin{aligned} (n^2+1)\lambda_2 + (P+Q)\bar{a}^2 + (S-P)\bar{b}^2 + \frac{n^2F}{\bar{a}} &= 0 \\ (n^2+1)\lambda_2 + (S-P)\bar{a}^2 + (P+Q)\bar{b}^2 &= 0 \end{aligned}\right\} \quad (8)$$

Equation (7) represents only the driven mode participating in vibration and Eq. (8) represents both driven mode and companion mode participating in vibration.

Figures 1 and 2 show the relations of driven mode $\bar{a}$ and frequency $\lambda/\lambda_0 = \Lambda$ as the results of Eqs. (7) and (8), respectively; the dotted lines indicate the effects of damping.

Equations (7) and (8) indicate that in the nonlinear vibration of a thin circular infinite cylinder the response is not only a function of the forcing function and frequency but also is multivalued. Since this cannot be true for the real physical system, some of the response obtained from Eqs. (7) and (8) must be unstable. This stability analysis is summarized in the following subsection.

3. Stability Analysis

In any consideration of stability of a given system, one fundamental difficulty is that of defining the notion of stability in a logical and reasonable manner without destroying the chances of applying the definition in a practical way. We take simply the following often used definition for stability, sometimes called infinitesimal stability: Let $\overline{W}(\theta,\tau) + \Phi(\theta,\tau)$ and $N(\theta,\tau)$ be the perturbed solutions of differential equations (given in SPS 37-62, Vol. III, p. 185)

$$\frac{\partial^2 N}{\partial\theta^2} - \frac{\omega^2}{\Omega^2}\frac{\partial^2 N}{\partial\tau^2} = -\epsilon\frac{\omega^2}{\Omega^2}\frac{\partial^2 W}{\partial\tau^2} - \frac{1}{2}\epsilon^2\frac{\omega^2}{\Omega^2}\frac{\partial^2}{\partial\tau^2}\left[\left(\frac{\partial W}{\partial\theta}\right)^2\right] \quad (9)$$

$$\epsilon r^2\frac{\partial^4 W}{\partial\theta^4} - \epsilon\frac{\partial}{\partial\theta}\left(N\frac{\partial W}{\partial\theta}\right) + \epsilon\frac{\omega^2}{\Omega^2}\frac{\partial^2 W}{\partial\tau^2} + N = \epsilon^3\bar{q} \quad (10)$$

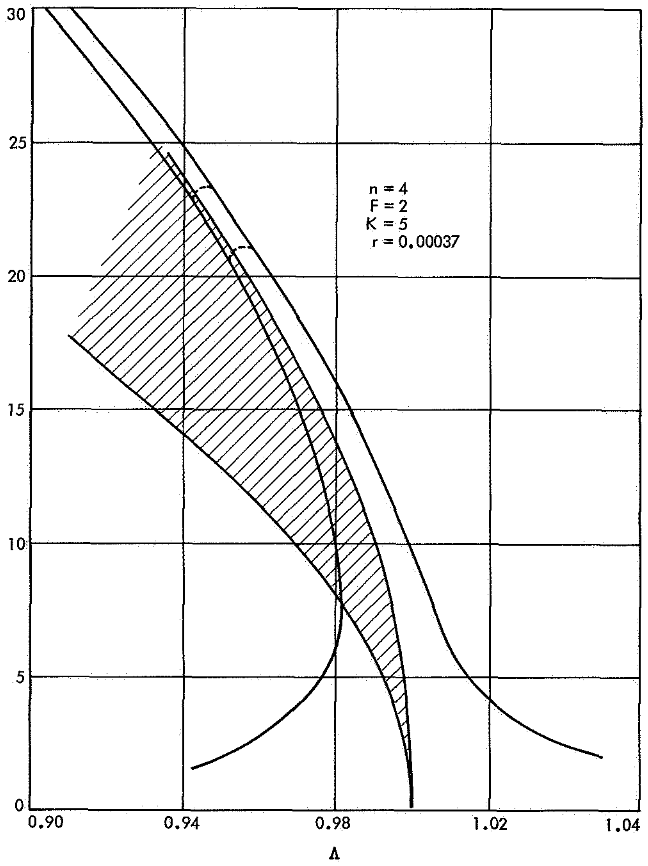

Fig. 1. Driven-mode response of one mode only

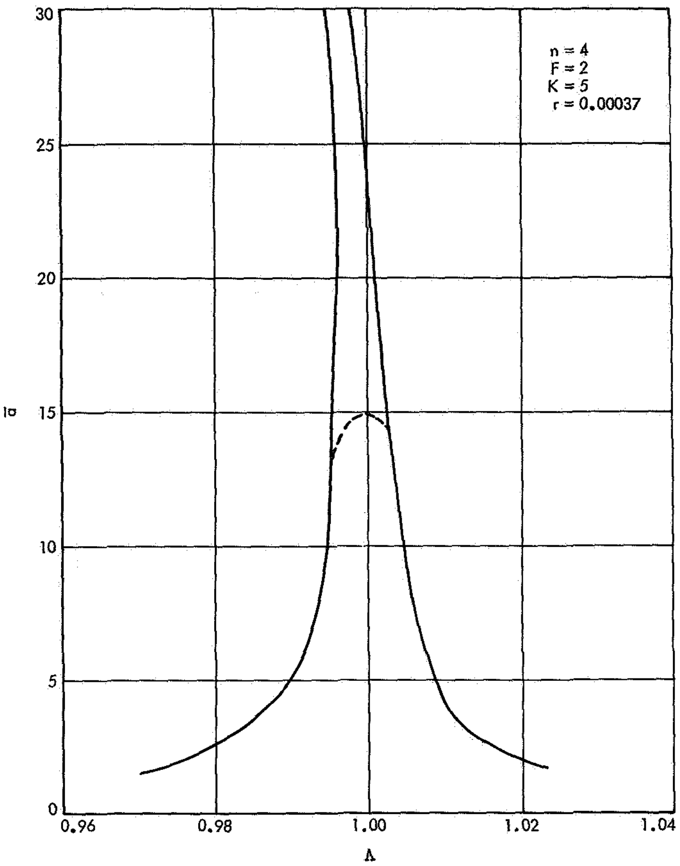

Fig. 2. Driven-mode response of two-mode consideration

If we insert $\overline{W}(\theta,\tau) + \Phi(\theta,\tau), N(\theta,\tau)$ in Eqs. (9) and (10) and neglect powers of $\Phi(\theta,\tau)$ above the first, we obtain the linear "variational" differential equations for $\Phi(\theta,\tau)$. If all solutions of $\Phi(\theta,\tau)$ of these equations are bounded, the $\Phi(\theta,\tau)$ is said to be stable; otherwise it is unstable.

Before performing the stability analysis in Eqs. (9) and (10), it is desirable to reduce these equations from partial differential equations to ordinary differential equations. We use Galerkin's procedure, as outlined in Ref. 1. The deflection $\overline{W}$ is assumed according to the previous perturbation solution:

$$\overline{W}(\theta,\tau) = -\frac{\epsilon n^2}{4}\left[A^2(\tau) + B^2(\tau)\right] + A(\tau)\cos n\theta + B(\tau)\sin n\theta \tag{11}$$

where the first term in the expression is required to satisfy the circumferential periodicity condition, and N is assumed to be zero for approximation. It should be noted that $A(\tau)$ is associated with the driven mode and $B(\tau)$ is associated with the companion mode. To apply Galerkin's procedure, Eq. (11) is substituted for $\overline{W}$ in Eq. (10). The resulting expression is then multiplied by a weighting function associated with $A(\tau)$ and integrated with respect to θ from 0 to 2π. This procedure yields an ordinary differential equation involving primarily $A(\tau)$. An equation for $B(\tau)$ is obtained in a similar fashion. The weighting functions used are

$$\frac{\partial \overline{W}}{\partial A} = -\frac{\epsilon}{2} n^2 A(\tau) + \cos n\theta \tag{12}$$

and

$$\frac{\partial \overline{W}}{\partial B} = -\frac{\epsilon}{2} n^2 B(\tau) + \sin n\theta \tag{13}$$

respectively. Performing the operations just indicated yields the following equations:

$$\lambda \frac{d^2A}{d\tau^2} + n^4 r^2 A + \frac{1}{4}\epsilon^2 n^4 \lambda \left(\frac{d^2 A^2}{d\tau^2} + \frac{d^2 B^2}{d\tau^2}\right) A = \epsilon^2 F \cos\tau \tag{14}$$

$$\lambda \frac{d^2B}{d\tau^2} + n^4 r^2 B + \frac{1}{4}\epsilon^2 n^4 \lambda \left(\frac{d^2 A^2}{d\tau^2} + \frac{d^2 B^2}{d\tau^2}\right) B = 0 \tag{15}$$

a. Stability of driven-mode response. To investigate the stability of the driven-mode response, we perturb the term associated with driven mode in the steady-state solution. Hence,

$$A(\tau) = A_0(\tau) + \Phi(\tau) \tag{16}$$

Since the companion mode is not participating in the vibration, we let $B = 0$. Upon substitution of Eq. (16) into Eq. (14), subtracting out the steady-state equation and neglecting higher order terms, one obtains

$$(1 + \mu_1 \cos^2\tau)\frac{d^2\Phi}{d\tau^2} - \mu_1 \sin 2\tau \frac{d\Phi}{d\tau} + \left[\frac{1}{\Lambda^2} - \mu_1(\sin^2\tau - 2\cos^2\tau)\right]\Phi = 0 \tag{17}$$

where

$$\mu_1 = \frac{1}{2}\epsilon^2 n^4 \bar{a}^2, \qquad \Lambda^2 = \frac{\lambda}{\lambda_0}$$

It will be noted that Eq. (17) is an ordinary differential equation with coefficients that are periodic in time. Such equations arise frequently in stability analyses; they are typified by the Mathieu's equation, which has been studied extensively (Ref. 2).

The first instability region of Eq. (17) can be estimated from the known results of Mathieu's equation. In terms of μ_1 and Λ, the one-mode response is unstable within the area bounded by

$$1 - \frac{3}{8}\epsilon^2 n^4 \bar{a}^2 < \Lambda < 1 - \frac{1}{8}\epsilon^2 n^4 \bar{a}^2 \tag{18}$$

The shaded region in Fig. 1 indicates the unstable region in the μ, Λ plane.

b. Stability of the companion-mode response. The relation between the driven mode and the companion mode can be obtained by Eq. (8) as

$$\bar{b}^2 = \bar{a}^2 + \frac{1}{2P + Q - S} \cdot \frac{n^2 F}{\bar{a}} \tag{19}$$

Since a could be either positive or negative, for a real b to exist, the following condition must be true.

$$\bar{a}^2 \geqq \frac{1}{2P + Q - S} \frac{n^2 F}{|\bar{a}|} \tag{20}$$

Physically, this can be considered as a critical amplitude of driven mode for which the companion mode could be excited if the driven mode is greater than the critical amplitude.

Now to investigate the stability of the companion-mode response, we associate the perturbed value with the companion mode; hence,

$$B(\tau) = B_0(\tau) + x(\tau) = \bar{b} \sin \tau + x(\tau) \tag{21}$$

$$A(\tau) = A_0(\tau) = \bar{a} \cos \tau \tag{22}$$

Performing similar previous operations, one obtains the stability equation

$$\frac{d^2 x}{d\tau^2} + \left[\frac{1}{\Lambda^2} - \frac{1}{2}\epsilon^2 n^4 (\bar{a}^2 - \bar{b}^2) \cos 2\tau\right] x = 0 \tag{23}$$

From the known results of Mathieu's equation, the instability region can be established as

$$\left.\begin{aligned} \Lambda &< 1 - \frac{1}{8}\epsilon^2 n^4 \frac{\frac{n^2 F}{|\bar{a}|}}{2P + Q - S} \\ \Lambda &> 1 + \frac{1}{8}\epsilon^2 n^4 \frac{\frac{n^2 F}{|\bar{a}|}}{2P + Q - S} \end{aligned}\right\} \tag{24}$$

The second term on the right-hand side of the inequalities is very small, especially for $\bar{a}$ greater than the critical amplitude. Therefore, there is a very narrow region adjacent to $\Lambda = 1$ in which the companion mode response is stable.

Although the stability analysis just performed is by no means accurate and exact, it provides adequate information to determine the correct response among the possible multivalues. Figure 3 shows the stable response as function of the frequency. The dashed line indicates that the companion mode is participating in the vibration. For the companion mode to participate in the vibration, not only the driven mode must exceed its critical amplitude but also the frequency must be in a limited narrow region. Also, a softening-type jump phenomenon is clearly shown in the plot. These phenomena have been observed in the experiments. When the amplitude of the companion mode reaches that of the driven mode ($\bar{a} = \bar{b}$), the total response becomes

$$\begin{aligned} \overline{W}(\theta, \tau) &= \bar{a} \cos \tau \cos n\theta + \bar{b} \sin \tau \sin n\theta \\ &= \bar{a} \cos (\tau - n\theta) \end{aligned} \tag{25}$$

This is a traveling wave in the circumferential direction. Since this can only occur at large amplitudes (larger than critical amplitude), this is strictly a nonlinear phenomenon. This traveling wave has also been observed in the experiments.

Figure 4 is a response frequency relation of a thin circular ring vibration taken from Ref. 1. The comparison of Figs. 3 and 4 is surprisingly similar.

4. Conclusion

The nonlinear flexural vibrations of thin-walled circular cylinders of infinite length were analyzed by the perturbation method. The stability of the solutions was investigated by using the results of Mathieu's equation. Although only one mode was directly driven by the forcing function, it was necessary to include two vibration modes in the calculations. Two modes were required because under certain conditions nonlinear coupling caused the companion mode to respond and participate in the motion.

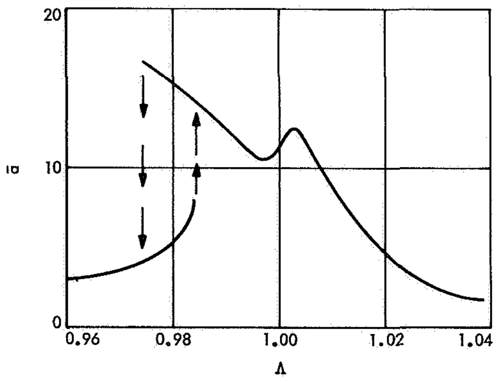

Fig. 3. Stable driven-mode response

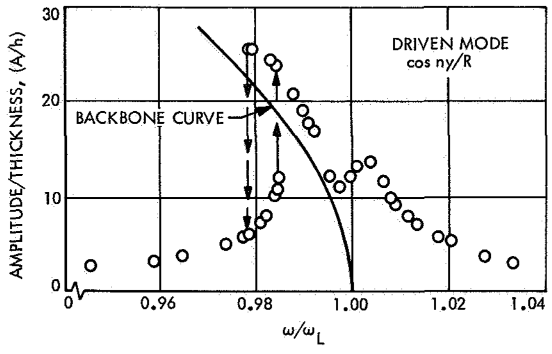

Fig. 4. Response curve from experiment ($n = 4$)

The results of this analysis demonstrate that nonlinear phenomenon in a large amplitude vibration (such as a jump phenomenon) traveling wave condition can be predicted by the analysis; the results compare well with existing experimental results. Furthermore, this analysis provides a systematic approach to a nonlinear analysis. This is of importance for more complicated problems for which the automation of analysis by digital computers becomes necessary.

However, due to the multivalued response frequency relation, stability analysis has to be performed to determine the true response at various frequency regions. In general, more complicated problems yield the stability equation as a coupled Mathieu's equation for which the solution becomes very complicated. This is an area which needs more attention to obtain a general systematic approach that can be automated.

In conclusion, the large amplitude vibration of a flexural structural system can be analyzed and the true response can be determined by its stability analysis. The perturbation method presented in this article provides a systematic approach which can be automated to a more complicated flexural structural system, such as the deep space large antenna. Work is currently under study in this area.

References

1. Evensen, D. A., *A Theoretical and Experimental Study of the Nonlinear Flexural Vibrations of Thin Circular Rings,* NASA TR R-227. National Aeronautics and Space Administration, Washington, D.C., 1965.

2. McLachlan, N. W., *Theory and Application of Mathieu Function.* Dover Publications, Inc., New York, N.Y., 1964.

D. Holography Application Study to Pressure Vessel Flaw Detection, *G. Morse, A. Knoell, and R. Badin*

1. Introduction

If a flaw or crack in the wall of a spacecraft pressure vessel or its associated tubing were to result in a leak during flight, this could result in failure of the entire mission. For this reason, inspection techniques are applied in an attempt to discover and reject any tank which has a flaw of sufficient size to be detrimental. Non-destructive inspection methods currently being used include visual inspection, X-ray examination, dye penetration, and microscopic examination. It would be desirable to have a method of detecting smaller sub-surface flaws than any of these methods are capable of locating. Double-exposure holography is useful for flaw detection, so a preliminary attempt was made to apply this technique to a pressurized thick-walled tube. Although the attempt was unsuccessful due to the nature of the problem, it indicated the need for an analytic study to examine under what circumstances holography is useful in pressure vessel flaw detection. This study is currently underway.

2. Holographic Technique

The holographic technique to be used in this application involves generation of a double-exposure hologram (Ref. 1 and SPS 37-61, Vol. III, pp. 187–190). In this technique, two exposures are made, the second with the object perturbed slightly. Upon development and reconstruction, the hologram shows an interference fringe pattern between the two different wavefronts that emanated from the object. If the hologram subject does not contain flaws, the fringe pattern is characteristic of the object shape, and the fringe density can be determined from the magnitude of the deformation. If the object contains flaws, the fringes may be distorted, and the distortions will contain information about the flaws.

The usefulness of this technique for detecting small flaws depends partly on the fringe density, since, for a flaw to distort the fringes, the fringe spacing cannot greatly exceed the size of the flaw. The fringe density is a function of the characteristics of the object being perturbed and the magnitude of the perturbation.

3. Analytic Approach

The vessels being studied include both thin- and thick-walled cylinders and spheres. It is assumed that the object is flawless, and it is perturbed by a change in internal pressure. The results will yield a fringe density for a given shape as a function of pressure change, material constants, and laser wave-length. An attempt will be made to evaluate the dependence of fringe distortion on flaw size, shape, and orientation.

4. Experimental Approach

A series of holograms will be made to test the validity of the analytic results of fringe density as a function of pressure. Then the effects of known flaws in various types of objects will be recorded holographically. This information will test the analytic results and provide a means of developing vessel acceptance standards.

Reference

1. Wolf, E., Editor, *Progress in Optics*, p. 40, Vol. VI. John Wiley & Sons, Inc., New York, 1967.

E. Holographic Interferometry Application to Shell Structures, *J. C. Chen and R. Badin*

1. Introduction

A thin-walled circular cylindrical shell is a commonly used element of an aerospace structure. Often in the course of structural development, the vibration mode shapes of a thin-walled circular cylindrical shell are determined experimentally. Due to the thinness of the shell structure, the mode shape has to be measured by non-contact means, and holographic interferometry provides a new technique for this type of measurement.

Reported experimental studies of buckling loads of thin-walled circular cylindrical shells under axial compression show that, when compared with the results predicted by the linearized small deflection theories, the experimental values are much lower and the data has a larger scatter band. For the past 30 yr, considerable effort has been made to find an explanation for the great discrepancy between theoretical and experimental results and for the large scatter of experimental results. In the past few years, the initial geometrical imperfections of the shell have come to be accepted as the main degrading factor. Investigations show that in some cases an imperfection of a mere 10% of the shell wall thickness would result in a 40% reduction of the load-carrying capacity of the shell (Ref. 1). Therefore, the growth of the initial imperfections during the loading process, prior to buckling, provides the mechanism by which the initial geometric imperfections reduce the buckling load. Since most laboratory experiments have used very thin shells, an accurate small imperfection growth measurement of the shell wall requires that the measurement must be made by non-contact means. Holographic interferometry is an ideal technique for this task. In addition to serving as a non-contact experimental technique, holography also allows the entire surface to be mapped at one time. A conventional point measurement device would have to sweep the entire surface to obtain a surface measurement mapping.

2. Experimental Approach

The holography techniques used in the vibration and shell buckling studies are described in SPS 37-61, Vol. III, pp. 187–190. The holographic process is one of recording the object's wavefront and at a later time reconstructing that wavefront with the use of coherent illumination. Both double-exposure and time-average holographic techniques depend upon the geometry of the optical system. The techniques of holographic interferometry for vibration analysis and static deformation measurements are described in Refs. 2 and 3.

The holographic arrangement in both studies is shown in Fig. 1. Major components include a 4- × 8-ft vibration isolation optical table, a 15-mW helium–neon gas laser, and a precision plate holder. To record a hologram, the laser beam is split by a beamsplitter. One, called the reference beam, is used to illuminate the photographic plate while the second, called the object beam, illuminates the object. The object beam reflects off the cylindrical shell to the photographic plate where it can interfere with the reference beam to form the hologram.

3. Results

The pre-buckling imperfection growth of a thin-walled circular cylindrical shell under axial compression is shown in Fig. 2. Double-exposure holography was used with a small change in compression between exposures. Therefore, the hologram reconstructs two different wavefronts of the cylindrical shell and the fringe patterns represent the interference between the different wavefronts. It is of interest to notice the fine detail in the vicinity of the boundary, keeping in mind the extremely small deformations taking place. Although the initial imperfections are of a random nature throughout the shell, the pre-buckling imperfection growth can be seen as a certain wave pattern.

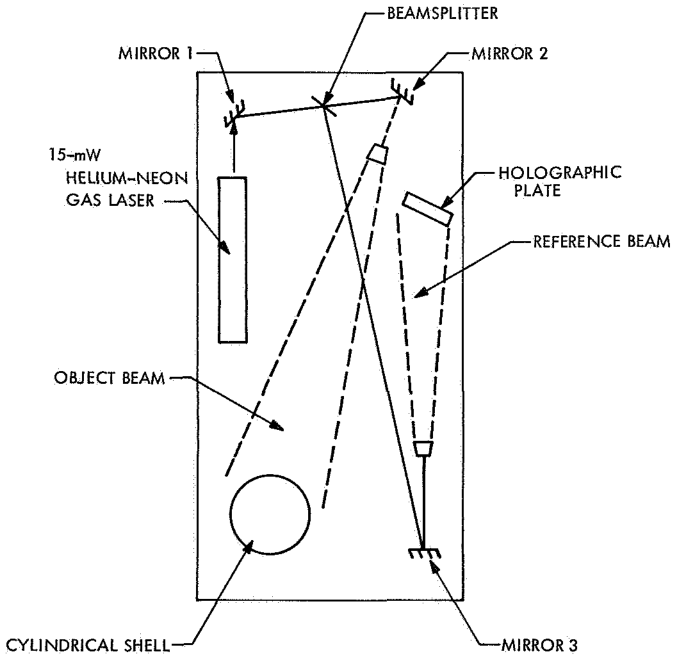

Fig. 1. Holographic arrangement

The vibration mode shapes of a thin-walled circular cylindrical shell are shown in Fig. 3. The agreement of mode shapes between holographic mapping and theoretical results can be seen by comparing Figs. 3c and 4. The number of axial waves and circumferential waves and the corresponding resonant frequency are in agreement with the theoretical results from the linear shell theory, as shown in Fig. 5 (Ref. 4). The time-average holography was used to record the mode shapes while real-time holography was used to find the resonant frequencies. A small light-weight accelerometer (2 g) was attached to the inside of the shell to monitor the frequency. The effects of the small mass can be seen in Fig. 3d. Here, the vibrational amplitude at the top of the shell is much greater than the lower section. Also, the fringe pattern has been altered by the accelerometer's mass in the top right section. Figures 3a–c include only low frequencies, which show fairly uniform mode shapes. As the frequency increases, the initial imperfections of the shell affect the mode shape, as shown in Fig. 3e. Figure 3f shows the mode shape at a high resonant frequency.

4. Conclusions

Holographic interferometry has been applied to study the vibration and pre-buckling imperfection growth of a thin-walled circular cylindrical shell. The vibration studies resulted in the determination of mode shapes at the resonant frequencies predicted by the theory. The circumferential and axial standing waves can be clearly observed and their magnitude can be estimated by counting the fringes. It is interesting to note that in some cases the effects of a light-weight accelerometer attached to the shell wall can be observed. In the buckling studies, the pre-buckling imperfection growth patterns were obtained for the entire surface. The growth pattern indicates that the shell deforms in a certain fashion, depending upon the initial imperfections; this is in contrast to the linear shell theory, which states that the shell does not deform prior to buckling. Also, the pre-buckling deformation in the vicinity of the boundary indicates the boundary effects of the buckling problem.

Due to its extremely accurate measurements and visible graphic patterns, holographic interferometry is a powerful new tool for vibration and buckling analysis. However, it does have some limitations. The experiments must be

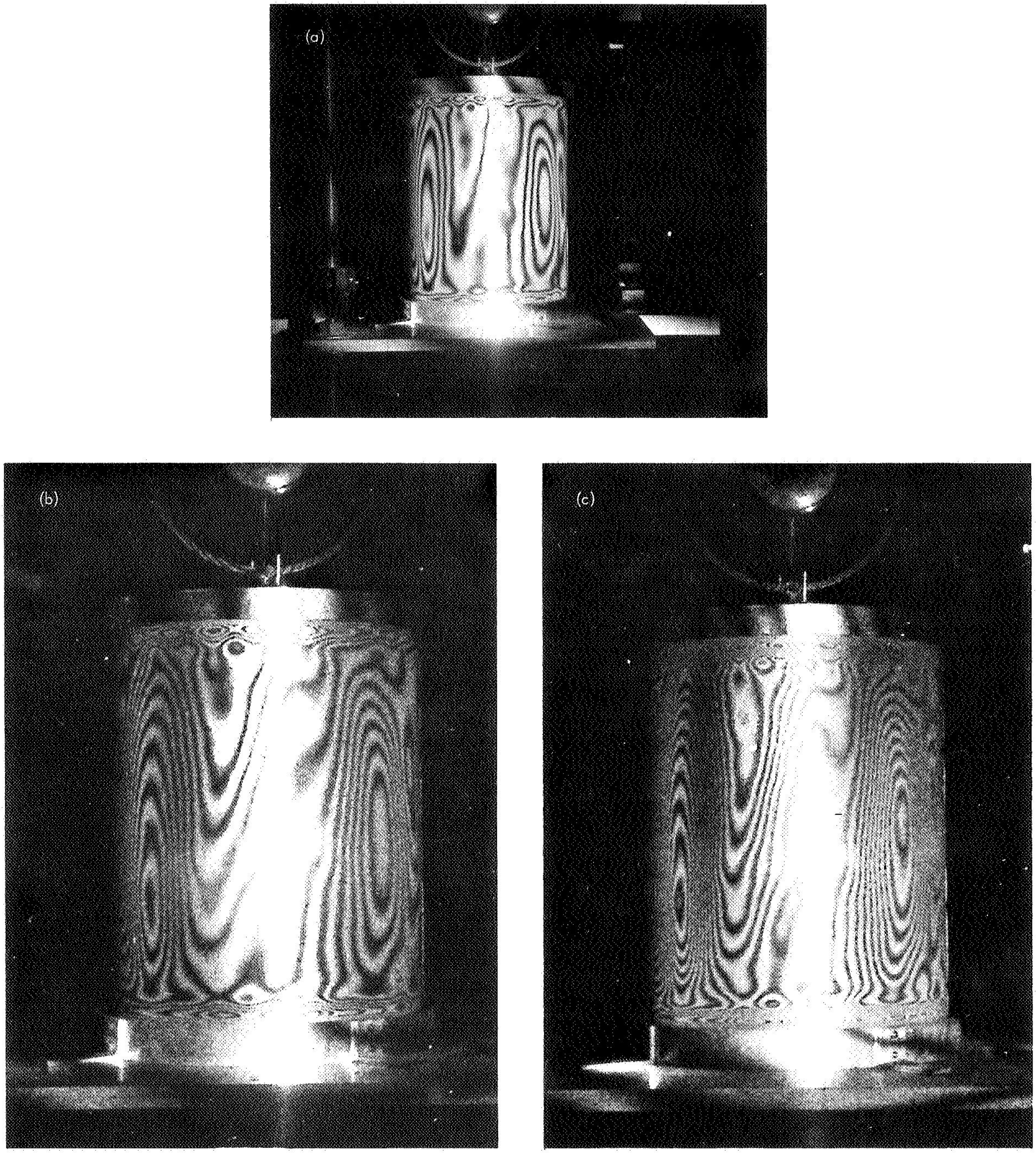

Fig. 2. Pre-buckling imperfection growth at: (a) 72 % of buckling load with change of 0.5 %, (b) 77 % of buckling load with change of 6.5 %, (c) 83.5 % of buckling load with change of 9.7 %

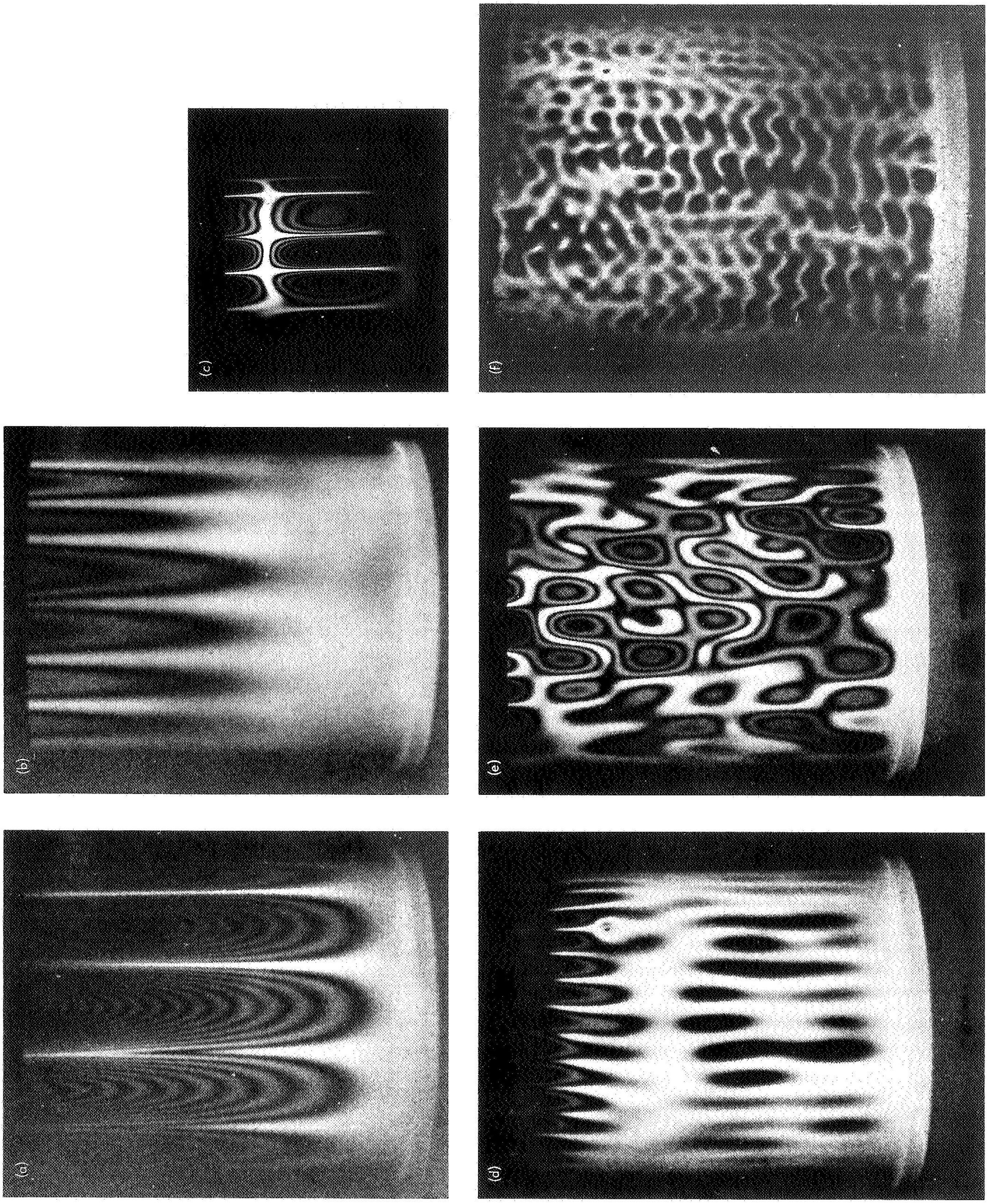

Fig. 3. Vibration mode shapes at frequencies: (a) 154.4, (b) 304, (c) 491, (d) 1385, (e) 1465, (f) 5846 Hz

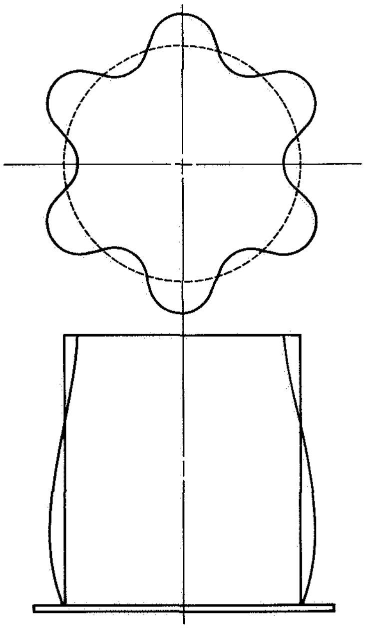

Fig. 4. Theoretical deformation of the shell at 491 Hz (Ref. 4)

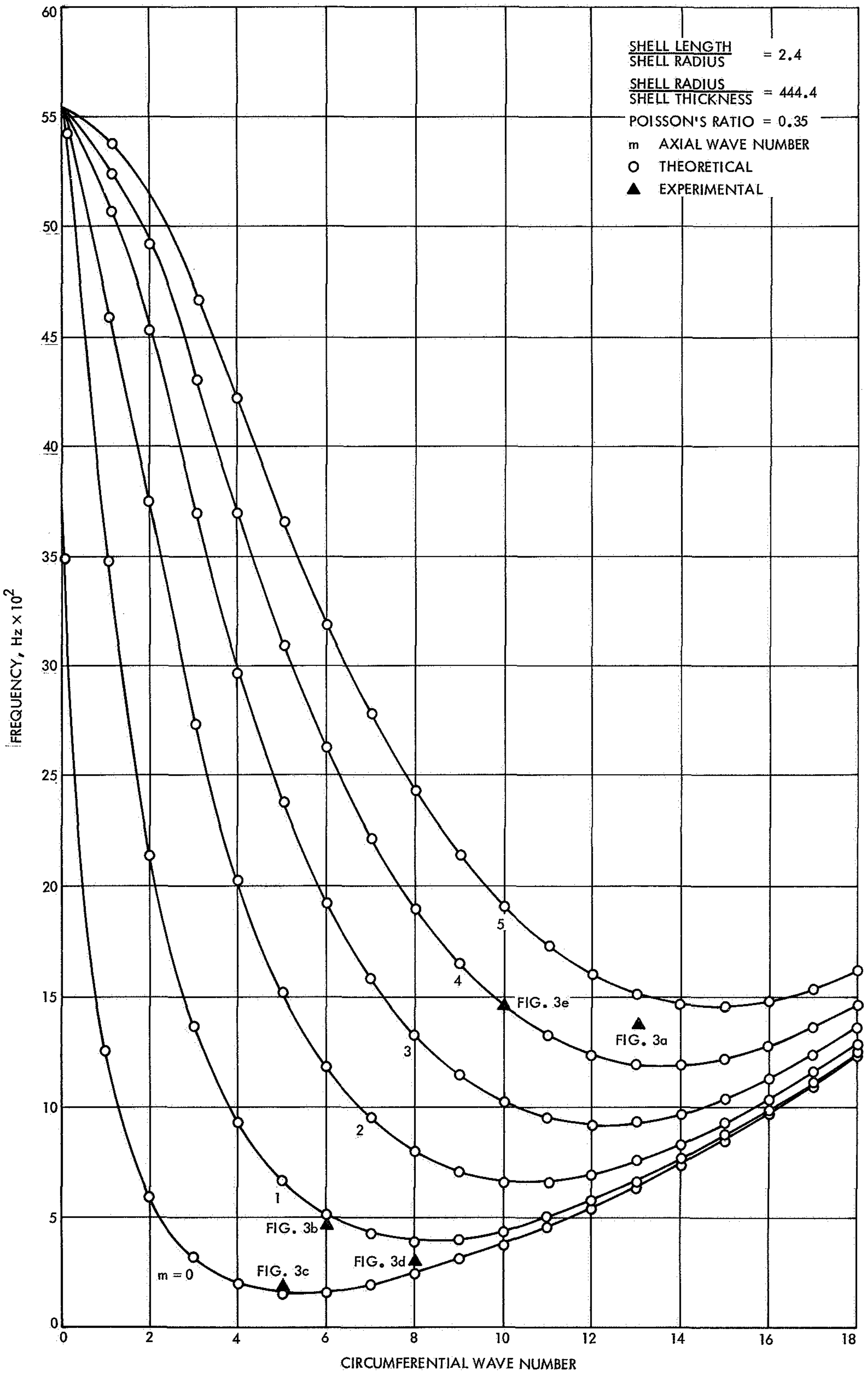

Fig. 5. Frequency plot

made on the shock-isolated table, and the deformations must be small to prevent the crowding of fringes. Work is currently underway to map the vibration modes of a *Mariner* spacecraft high-gain antenna.

References

1. Arbocz, J., and Babcock, C., "The Effect of General Imperfections on the Buckling of Cylindrical Shells," *Trans. ASME, Ser. E: J. Appl. Mech.*, Mar. 1969.
2. Powell, R. L., and Stetson, K. A., "Interferometric Vibration Analysis by Wavefront Reconstruction," *J. Opt. Soc. Am.*, Vol. 55, pp. 1593–1598, Dec. 1965.
3. Haines, K. A., and Hildebrand, B. P., "Surface-Deformation Measurement Using the Wavefront Reconstruction Technique," *Appl. Opt.*, Vol. 5, No. 4, Apr. 1966.
4. El Raheb, M., *Some Approximations in the Dynamic Shell Equations*, PhD. Thesis. California Institute of Technology, Pasadena, Calif., Dec. 1969.

F. Fiber-Reinforced Composite Materials for Spacecraft Antenna Structures, *C. Zweben*

Outer planetary missions will require substantial increases in communications capability. Antennas with higher gain than those used on *Mariner* spacecraft will be required. Thermal distortions potentially impose a severe limitation on gain improvement. For example, Fig. 1 (taken from SPS 37-61, Vol. III, pp. 171–177) shows that, based on data from current aluminum antennas, the maximum gain that can be achieved with an antenna uncorrected for thermal distortions, regardless of antenna size, is about 60 dB.

One way of reducing thermal distortions, and therefore raising antenna gain, is by the use of materials with lower coefficients of thermal expansion than that of aluminum. The problem is to find materials whose density is low enough to permit their use in spacecraft structures. Low expansion materials, such as Invar and the family of silicates, have densities that are about three times as great as aluminum, without a compensating increase in stiffness or strength. Recently developed advanced filamentary composite materials are generally characterized by low thermal expansion coefficients in combination with high stiffness-to-density and strength-to-density ratios, making them attractive candidates for antenna structures and for spacecraft applications in general.

Advanced filamentary composite materials consist of high-modulus, high-strength fibers such as boron and graphite, imbedded in matrix materials like epoxy and aluminum. Table 1 presents typical axial properties for unidirectional composites containing parallel continuous fibers, along with data for more common materials. α is the coefficient of thermal expansion and E/ρ and σ/ρ are the stiffness-to-density and strength-to-density ratios, respectively.

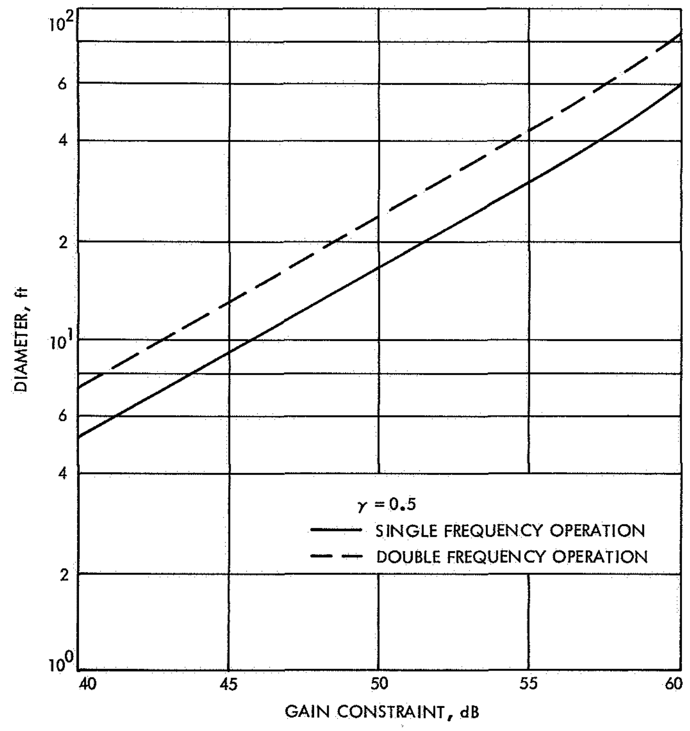

Fig. 1. Optimum antenna diameter vs gain constraint

Table 1. Thermomechanical properties of advanced filamentary composites and other materials

Material	α_1, in./in./°F $\times 10^{-6}$	E/ρ, in.$^{-1} \times 10^{-6}$	σ/ρ, in.$^{-1} \times 10^{-6}$
Boron/epoxy	2.5	442	2.500
Boron/aluminum	4.0	320	1.850
Graphite/epoxy	−0.6 to 0.4	400 to 500	3.300 to 7.500
Aluminum	13.2	100	0.450
Beryllium	6.4	657	0.440
Titanium	4.6	95	1.000

One of the significant advantages of composite materials is that material properties can be tailored to fit the particular requirements of the situation by appropriate choice of constituents and geometric arrangement. This permits the design of materials that have a desired coefficient of thermal expansion, even zero or negative, in at least one direction. The objective of this program is to evaluate the various approaches to obtain controlled thermal expansion materials for spacecraft antenna structures. These concepts are now discussed.

Table 1 shows that unidirectional composite materials are attractive for application to linear structural elements such as ribs and struts. Since the transverse strength and modulus properties of unidirectional materials are significantly lower than those in the fiber direction, it is often necessary to fabricate structural items by laminating unidirectional materials with the fibers in various directions, as is done with plywood. Since antenna structures are generally lightly loaded, it may be possible to use unidirectional materials without lamination in struts and ribs to obtain low thermal deformations and high axial stiffness and strength. It is possible to vary the expansion properties to a small degree by changing the volume fraction of the fibers and the matrix thermal expansion and stiffness properties.

However, by laminating unidirectional materials, it is possible to achieve a wider range of thermal expansion properties. For example, consider a laminate that consists of layers of tungsten carbide filaments in a polyester matrix arranged symmetrically about a reference axis. That is, the fiber directions of the layers make angles of $\pm\theta$ with the 1-axis, as shown in Fig. 2. Figure 3, taken from Ref. 1, shows the variation of the coefficient of expansion in the 1-direction, α_1, normalized with respect to the fiber coefficient of variation, as a function of θ. It has been verified, experimentally, that it is indeed possible to obtain the zero and negative values predicted by the theory.

The reduction in α, as θ increases from zero, is the result of a "scissoring" action caused by the large coefficient of expansion of the matrix in conjunction with the low coefficient of expansion and high stiffness of the fibers. To

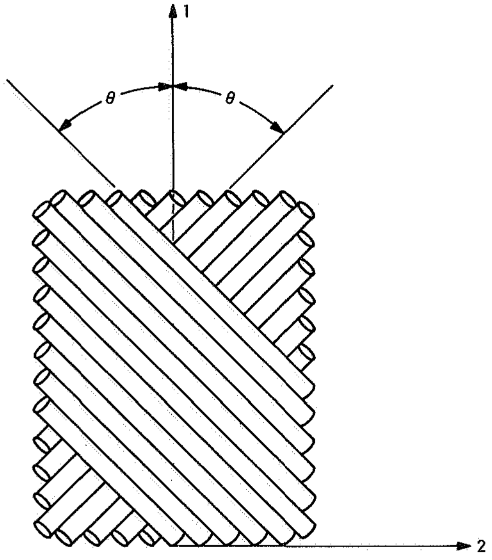

Fig. 2. Laminate and fiber geometry

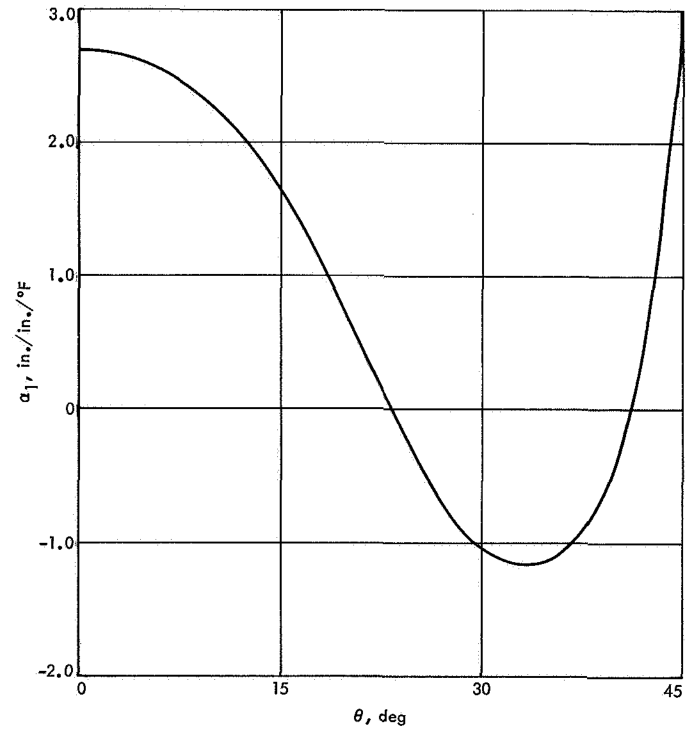

Fig. 3. Coefficient of thermal expansion as a function of fiber angle for tungsten carbide/polyester

permit a greater flexibility in the choice of fibers and matrices for controlling thermal expansion, it was decided to study the effect of adding fibers parallel to the 2-axis of materials that are different than those in the $\pm\theta$ directions. Figure 4 shows the influence of adding aluminum and Mg–Li fibers at 90 deg to the reference angle. The addition of aluminum fibers raises the minimum value of α, so that it never reaches zero. On the other hand, because of its high coefficient of expansion, Mg–Li reduces α for values of θ greater than 20 deg.

The results of this study indicate that transverse fibers can significantly effect the thermal expansion characteristics of $\pm\theta$ laminates, thus providing greater flexibility in the design of composite materials.

The extremely low coefficients of expansion of graphite/epoxy composites (Table 1) in conjunction with their high stiffness-to-density and strength-to-density ratios make these materials particularly attractive for antenna structures. Using these materials, it is possible to construct thin sheets that have low coefficients of thermal expansion and are isotropic with regard to elastic and thermal properties in the plane of the material. These properties make graphite/epoxy composites ideal candidates for such applications as rigid antenna dishes. However, the low thermal expansions are accompanied by relatively high internal stresses. These stresses were studied as part of this program. It was found that for a 0-deg, ±60-deg laminate, transverse internal stresses increase by about 20 psi for each degree of temperature change. This may possibly result in creep and/or cracking if such a material is subjected to large temperature variations. This problem is being studied.

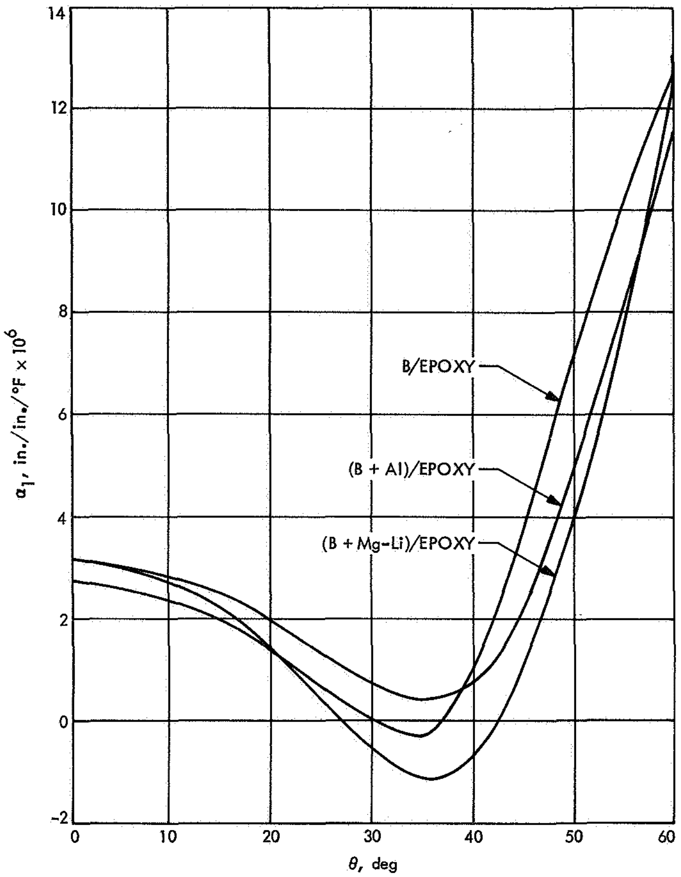

Fig. 4. Coefficient of thermal expansion as a function of fiber angle for various fiber/matrix systems

Reference

1. Dow, N. F., and Rosen, B. W., "Zero Thermal Expansion Composites of High Strength and Stiffness," Final Report, NASA Contract NAS 1-7659, General Electric Co., Sept. 1968.

G. Results of *Apollo* Gamma Ray Spectrometer Thermal Model Tests, *S. W. Petrick*

1. Introduction

This development test was run to study the thermal response of the flight configuration *Apollo* gamma ray spectrometer (AGRS) temperature control system under simulated normal and worst-case conditions. A thermal model (TM) of the AGRS was exposed to thermal conditions similar to those expected during a normal mission and thermal conditions more severe than those of a normal mission. Briefly, a normal mission consists of the AGRS being

(1) contained in the *Apollo* command–service module scientific instrument module (SIM) during launch, translunar coast, and the first part of the lunar orbit; (2) deployed on a 25-ft boom during the latter part of the lunar orbit; (3) restowed into the SIM during transearth injection; and (4) deployed again during transearth coast. The detector assembly must be maintained at 59 ±1.8°F during operation and at no time must it be exposed to temperatures below −4°F, above 120°F, or to a temperature transient greater than 20°F/h. Based on the thermal performance of the TM, the design of the temperature control system was to be evaluated and altered, if necessary.

The major components of the AGRS are shown in Fig. 1. While the AGRS is exposed to the space environment, the thermal control point pattern produces a fluctuating temperature profile in the detector assembly. The maximum temperature points of this profile are slightly below the desired operating temperature range (59 ±1.8°F). A temperature control circuit, triggered by a thermistor, applies power to the heater to maintain the temperature of the detector assembly at the desired level. Thermal isolators at the mounting pads and boom attachment interface protect the AGRS from the temperature extremes and transients of the SIM structure.

2. Test Descriptions

The test objective was to determine the thermal response and temperature histories of the TM under simulated and extreme mission conditions. A description of the initial tests performed on only the detector assembly of the AGRS is contained in SPS 37-60, Vol. III, pp. 166–173. A brief description of the tests run to accomplish the test objective follows. The analytical computer model was used to estimate some of the test procedure parameters (such as heater power levels, cooldown times, etc.).

Test 1 (temperature control circuit (TCC) stability test). The purpose of this test was to evaluate the performance of the temperature control and sensing system that activates the internal heater. Previous testing (SPS 37-60, Vol. III) indicated a shifting of the temperature control range with the changing of thermal environment. It was conjectured that this apparent "instability" was the result of using two sensing thermistors. It was decided to test the TCC with both one and two sensing thermistors. The TCC with one sensing thermistor was to be run first and the TCC with two sensing thermistors was to be run only if the first test was not satisfactory.

The temperature control point of the TCC was approached from higher temperatures by cooling the heated TM, and the temperature control point was approached from cold temperatures by heating the cooled TM. After the TCC was activated in each case, the TM was maintained with the TCC controlling it to determine if the steady-state control point was different than the initial control point. External thermal environment was varied while the TCC was controlling the TM in an attempt to duplicate the instability observed in the previous testing.

Test 2 (lunar orbit simulation). The test heater was cycled every 2 h to simulate the solar and lunar heating that AGRS would experience while in lunar orbit. TCC control capability, thermal response of the AGRS, and heater performance were determined from this test.

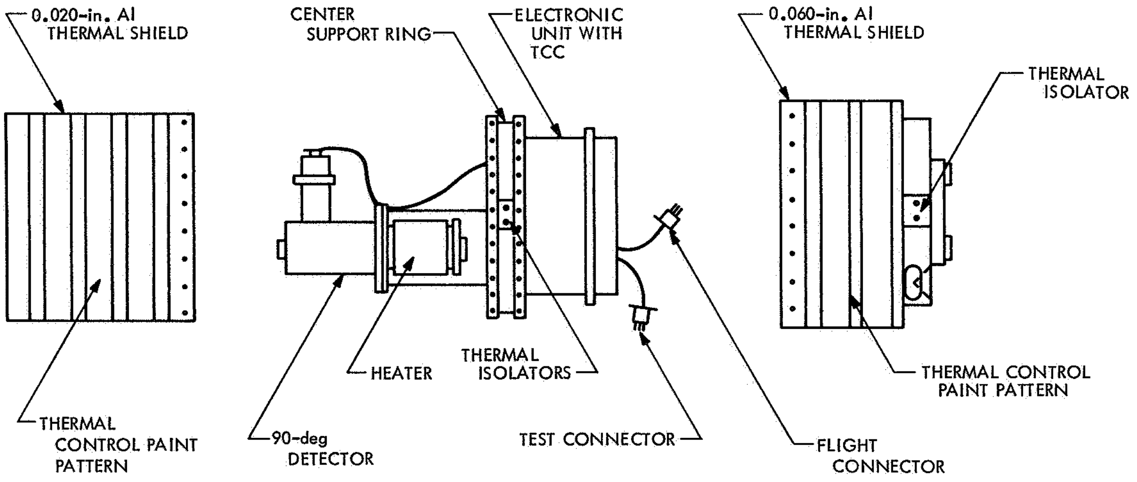

Fig. 1. *Apollo* gamma ray spectrometer (exploded view)

Test 3 (simulated scientific instrument module). The chamber wall and the manifold temperatures were cycled to simulate the highest temperatures and most severe temperature transients expected in the *Apollo* service module SIM at the time of testing. This test and the following two tests were performed to study the thermal response of the AGRS under extreme SIM conditions and the effects of the thermal isolators.

Test 4 (simulated transearth SIM temperatures). The walls and manifold temperatures were cycled to simulate the expected SIM transearth temperatures. The test was started with the TM at room temperature.

Test 5 (steady-state simulated transearth SIM temperatures). This test was exactly the same as Test 4 except that the TM start temperature was the average of the temperature excursions of the walls and manifold.

Test 6 (solar simulation). The TM was installed into the 10-ft-diam solar simulator with the largest projected area exposed to the solar beam. The solar beam impinged on the thermal shield 180 deg from where the test heaters were installed. Equilibrium temperatures were obtained for 1-sun and for ½-sun intensities. This test provided data from which the absorptance of the thermal shield was computed.

Test 7 (deep space cooldown). The TM achieved thermal equilibrium while installed inside a LN_2-cooled vacuum chamber with the internal heater as its only heat source. This test simulated the coldest possible temperature extreme the AGRS could experience. The cooldown rate with heaters in deep space, the emittance, and the lowest possible AGRS temperature were determined.

Test 8 (TCC stability test). This test is identical to Test 1. After Test 1 was completed, a design change was made that reduced the controlling range of the TCC from ±9 to ±1.8°F. The test was rerun to verify that the design change would accomplish its purpose and that this change did not affect the overall stability of the TCC.

Test 9 (simulated solar simulation). Heat, calculated to be that incident on the TM during solar simulation, was applied to the TM by the test heaters. This test was run as a further check on the absorptances and emittances of the thermal shield.

Test 10 (margin test). This test was run to determine the thermal margin above the temperature limitations imposed on the AGRS. The lower specified temperature of −4°F, the upper specified limit of +120°F, and the time–temperature gradient of 20°F/h were purposely exceeded. During this test, the detector assembly was lowered to −40°F, raised to 140°F, and exposed to a time–temperature gradient of 70°F/h.

3. Test Setup

The TM was built to flight drawings and flight hardware was utilized as much as possible. Certain changes had to be made to the TM to facilitate testing, but the changes were designed and incorporated in such a way that they are considered to have a negligible effect on the overall thermal performance of the TM; i.e. the AGRS should respond like the TM to a given thermal environment.

A block diagram of the test setup and the instrumentation used is shown in Fig. 2. All tests were run under vacuum conditions with appropriate heater and cooling devices attached. Thermocouple millivolt readings were printed on paper tapes by a Datex unit. The millivolt readings were then punched on computer cards from the paper tapes. The CINDA[1] computer program converted the millivolt readings to temperatures and plotted these temperatures.

4. Test Results

A summary of the gross thermal parameters of each test is presented in Table 1. Test results follow.

Tests 3, 4, and 5. Although the TM was exposed to a SIM thermal environment more severe than that predicted by the spacecraft designer (North American Rockwell Corp., Downey, Calif.), the detector assembly temperature remained within acceptable limits.

Tests 1 and 8. These tests demonstrated that the TCC, using one temperature sensor, maintained the detector temperature to within ±2°F of the set point consistently without any of the previously noted instabilities.

Tests 2, 6, and 9. During simulated lunar orbit heating conditions, the detector temperatures were within the desired controlling range. The solar simulation test indicated that the thermal properties of the shield would maintain the AGRS within desirable temperature limits.

---

[1] CINDA = Chrysler improved numerical differencing analyzer.

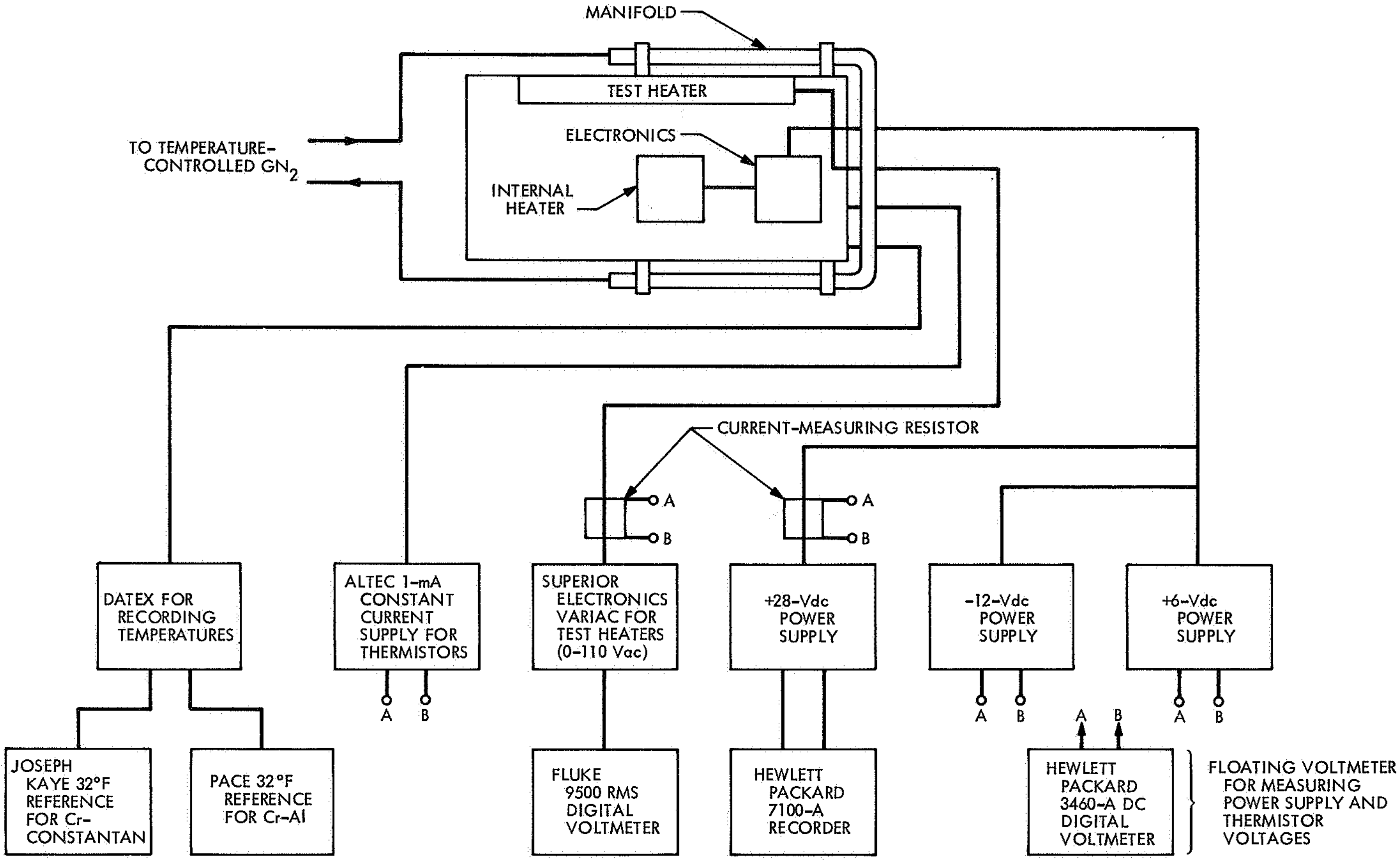

Fig. 2. Schematic of AGRS thermal model test setup

Tests 7 and 10. Test 7 was an extreme test, not representative of actual mission conditions, to determine the ultimate lower limit of the AGRS. During Test 10, critical parts of the detector assembly were exposed to test temperature extremes greater than those of the specified temperature limitations. Upon disassembly, no changes or damage to any of the components could be detected.

5. Conclusions

The AGRS thermal model tests indicate that:

(1) The temperature transients caused by the 20-W heater are not detrimental to the detector.

(2) The fiberglass isolators provide sufficient protection from the expected temperature transients of the SIM during the planned mission.

(3) The TCC appears to be stable with satisfactory temperature control and response.

(4) The thermal system performs satisfactorily under simulated lunar orbit conditions.

(5) The detector assembly exhibits a 20°F margin above the upper temperature of 120°F, a 30°F margin below the lower limit of -4°F, and a 50°F/h temperature–time gradient margin above the 20°F/h limit imposed on the detector assembly.

(6) The AGRS detector temperature, under worst possible mission thermal environment conditions (direct sunlight or shade for extended time periods), cannot go above 73°F or below -36°F as long as power is supplied to the unit. Under normal expected mission thermal operating conditions, the unit should maintain a detector temperature within 2°F of the TCC set temperature.

(7) The thermal radiation properties of the thermal shield appear to be sufficient to insure satisfactory thermal performance.

Table 1. Test parameter summary

Test number	Detector crystal				Detector plastic scintillator		Detector photomultiplier tubes		Electronic unit		Thermal shield		Boundary		Heater duty cycle, %
	Temperature, °F		Cooling Gradient, °F/h	Heating Gradient, °F/h	Temperature, °F		Temperature, °F		Temperature, °F		Temperature, °F		Temperature, °F		
	Min	Max			Min	Max	Min	Max	Min	Max	Min	Max	Min	Max	
1	−35	115	26	28	−35	121	−50	145	−50	125	−70	256	−305	0	60
2	51	61	10	13	46	58	40	68	25	54	7	120	−305	—	59
3	13	139	23	26	18	138	10	140	10	143	5	148	−15	160	—
4	74	98	—	7	74	96	74	100	74	100	74	110	74	134	—
5	100	108	—	—	101	107	99	108	100	108	95	114	70	134	—
6	46	68	—	—	43	68	33	68	26	68	12	66	−310	—	—
7	2	75	6	—	0	75	−14	75	−34	75	−43	75	−305	—	100
8	−30	118	30	28	−18	125	−30	145	−38	125	−55	210	−305	0	61
9	−6	75	26	—	−9	75	−6	75	−10	75	−32	75	−305	—	—
10	−35	135	31	70	−35	140	−35	190	−46	166	−55	320	−305	—	—

XII. Advanced Projects Development

ENGINEERING MECHANICS DIVISION

A. TOPS Thermomechanical Pump, *E. Sabelman*

1. Introduction

The Thermoelectric Outer Planet Spacecraft (TOPS) has a requirement for 125 W of active temperature control power. Only 25 electrical watts are available for temperature control; hence, alternatives to electric resistance heating are under consideration, such as a fluid loop transferring waste heat from the radioisotope thermoelectric generators to the science instruments. Power estimates for electric pumps for circulating this fluid range from 15 W down to 6 W. The thermomechanical pump study described herein was initiated to consider elimination or augmentation of the electric pump motor by a heat engine driven by the 200 to 300°F temperature difference between the incoming warm temperature-control fluid and the science instrument package.

2. Multivibrator Pump Design

The design resulting from this effort is a two-cylinder piston pump with provision for diverting all or part of the warm temperature-control fluid to operate a heat-to-displacement conversion mechanism which drives the pistons. Each cylinder is equipped with a temperature-control fluid chamber, a thermally insulating piston, a piston return spring (which, with the aid of the loop pressure, drives the piston during the downstroke), a chamber containing an evaporative fluid such as Freon-12, a copper tube heat exchanger coupled to the temperature-control fluid input of the other cylinder, and a heat sink surface (Fig. 1). Each cylinder requires three check valves and constricting valves to set the ratios of direct to diverted fluid.

The operation of the pump is analogous to an electronic astable multivibrator. When Freon vapor in one cylinder is condensing, that cylinder's piston moves down, drawing in warm temperature-control fluid through the heat exchanger of the second cylinder. Freon liquid in the second cylinder then evaporates, causing that piston to rise and expel temperature-control fluid into the loop. When the first piston reaches bottom, it stops drawing fluid through the second exchanger, allowing the exchanger to cool and the Freon to recondense. The distributed timing capacitance determining the cycle period comprises the thermal

(a) CYLINDER A INTAKE (FREON VAPOR CONDENSING) AND CYLINDER B EXHAUST (FREON LIQUID EVAPORATING):

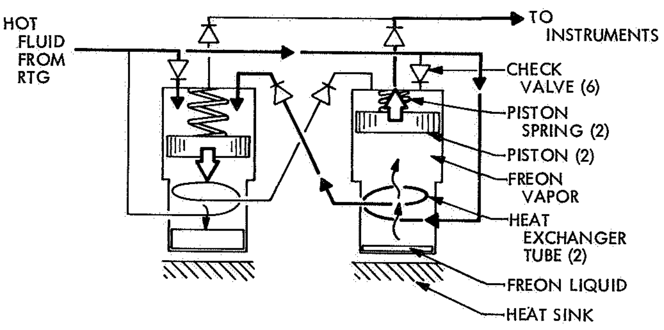

(b) BEGINNING OF CYLINDER B INTAKE AND CYLINDER A EXHAUST

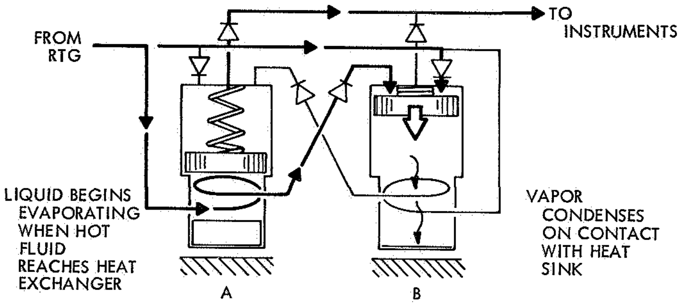

Fig. 1. Thermomechanical pump schematic, showing operating cycle

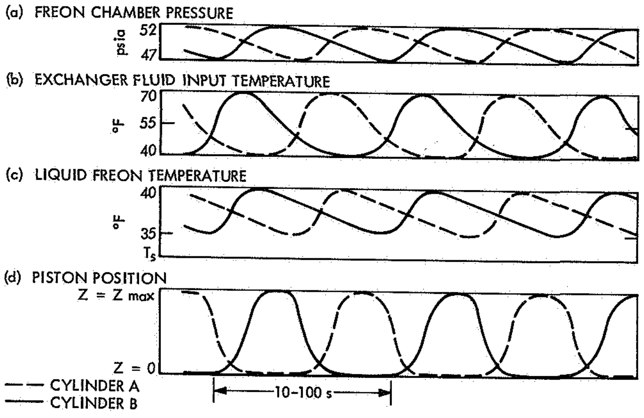

Fig. 2. Typical proposed operating cycle conditions

capacities of the cylinder wall, liquid Freon, and heat exchanger, while the timing resistance is expressed by the heat transfer coefficients from the exchanger to the liquid, liquid to vapor, and liquid to heat sink. The piston return spring serves to adjust the rise/fall time ratio and the spring preload plus loop pressure sets the evaporation pressure range.

Before the hardware design was begun, an analog model was constructed to estimate cycle characteristics. The model showed that for a nominal 2-in.-diam cylinder and a 1-in. stroke, half cycles in the desired 10- to 100-s range were achievable but were sensitive to heat leakage through the piston as well as to variations in heat transfer and capacity parameters. A typical operating regime such as that shown in Fig. 2 was selected, with a heat sink temperature T_s of about 32°F, the desired temperature of the science instruments, allowing waste heat from the pump to be used in temperature control of the instruments.

3. Thermodynamic Model

The thermomechanical pump is essentially a Rankine vapor cycle engine, with minimal subcooling or superheating of the working fluid to avoid piston dwell at the ends of the stroke. Excess of liquid Freon at the end of the evaporation part of the cycle is also to be avoided for the same reason. Rankine efficiency for a 10°F range of working fluid is on the order of 2% of a 40-W heat input. This work output is sufficient to overcome temperature-control fluid friction in the loop, but apparently is not enough to compensate for excessive piston friction losses.

The energy balance equation for one cylinder equates the work output, heat rejected to the sink, and change in internal energy of the working fluid to the sum of the heat inputs through the exchanger and the piston (Table 1):

$$W_P + q_{FS} + \Delta U + \text{LOSSES} = q_H + q_P$$

A term for piston friction, check valve, and fluid heat losses is also included. The heat input during the expansion part of the cycle (q_H) must be sufficient to overcome the continuous source q_P and sink q_{FS}:

$$q_{FS} = \frac{\Delta T_{F-S} A_{\text{sink}}}{\dfrac{1}{h_{FVS}} + \dfrac{Z_F}{k_F}}$$

The heat input can be expressed either as the heat lost by the temperature-control fluid moving through the exchanger, or as the integrated flux through the exchanger tube wall:

$$q_H = \sum_{N_{HTR}, L_{HTR}} \frac{\Delta T_{H-F}|_L}{\dfrac{1}{h_{HE} A_{E,ID}} + \dfrac{1}{h_{EF} A_{E,OD}}}$$

The internal energy U is the sum of the heat gained by the Freon liquid and that used to vaporize the liquid:

$$\Delta U = q_{FV} + q_F \begin{cases} q_{FV} = \lambda_{FV} \Delta M_V \\ q_F = c_{P_F} m_F \Delta T_F \end{cases}$$

Table 1. Nomenclature

$A_{E,ID}$	internal area/unit length of exchanger tube
$A_{E,OD}$	external area/unit length, corrected for fin efficiency
c_{p_F}	specific heat of liquid Freon
h_{HE}	film coefficient, temperature-control fluid to exchanger tube, function of temperature-control fluid laminar Nusselt number
h_{EF}	evaporating film coefficient, exchanger to liquid Freon, function of Freon Prandtl and Grashof numbers
h_{FVS}	condensing film coefficient, Freon to heat sink
k_F	liquid Freon conductivity
L_{HTR}	exchanger tube length
m_F	mass of liquid Freon at time t
N_{HTR}	number of parallel exchanger tubes
q_H	heat transferred from temperature-control fluid to liquid Freon/unit time
q_F	heat absorbed/released by liquid Freon
q_{FV}	heat involved in Freon evaporation/condensation
q_{FS}	heat transferred from Freon to sink
q_P	heat leakage by conduction through piston
T_F	temperature of liquid Freon, function of position along exchanger tube L and time t
T_s	heat sink temperature
W_P	available pump work output
Z	height of piston above its low point
Z_F	depth of liquid Freon
ΔT_{H-F}	log mean differential temperature, temperature-control fluid to liquid Freon
ΔT_{F-S}	log mean differential temperature, Freon to sink
ΔU	change in internal energy of Freon liquid/vapor system
λ_{FV}	latent heat of vaporization of Freon
ΔM_V	mass of Freon vaporized/unit time

The term q_{FV} determines the mass of Freon vaporized, and hence the volume output of the cylinder at a particular operating pressure. The change in internal energy must be zero over a full cycle for continuing operation at the same conditions. A digital computer simulation program is presently being prepared to solve this system of equations using temperature-dependent fluid properties and data derived experimentally.

4. Prototype History

a. Experimental test setup. In testing working models, equipment was needed for simulating the radioisotope thermoelectric generator (RTG), the science platform (heat sink), and the intervening length of fluid loop (Fig. 3). The hot temperature-control fluid source was a 1-liter sealed reservoir, pressurized with nitrogen and heated with a 500-W immersion element. The heat sink was a copper plate clamped to the base of the pump through which dry-ice-cooled alcohol or chilled water was circulated. A fine needle valve was used as a dummy head loss load in the temperature-control fluid loop, with other valves being required for pump priming and Freon injection and purging. Monitoring equipment included four to ten copper-constantan thermocouples, two Freon pressure transducers, two piston position transducers (in the second model), and an eight-channel chart recorder. The temperature-control fluid for all tests was Coolanol 45, a silicate ester, the primary candidate for the TOPS fluid loop.

b. Preliminary model (model 1). Because of the scarcity of literature on small cyclic heat exchangers and small heat engines in general, construction of a feasibility test model was undertaken on an empirical basis. Visual observations of piston movement, valve operation, Freon liquid level, and mode of evaporation were major design criteria. Cylinder walls were therefore made of 1.75-in. precision-bore glass tubing, and valves and exchanger manifolds, of transparent polycarbonate. Both these materials caused difficulties in sealing, later solved by shrouding the glass cylinders in a view-ported Micarta block to absorb gasket loads and by replacing the exchanger manifold with Micarta to allow epoxy tube joints. The exchanger itself was a single 11-in. length of ⅛-in.-OD copper tubing. Stainless steel tubing was used for the exchanger supply and return ducts, and Teflon rod for the pistons, with circumferential grooves to prevent leakage. Each cylinder had a 1½-in.-diam return spring with adjustable preload and a rate of about 1 lb/in. One cylinder was equipped with an electric starter heater (a ceramic-cased Nichrome wire immersed in the Freon liquid) which required 20 W for 3 to 10 s for full piston displacement.

The preliminary model was tested with nominal 200°F temperature-control fluid, alcohol-cooled sink (−10 to 0°F), and 12- to 18-psig loop pressure, in a series of seven tests. Early in the series it was apparent that cycle periods would be nearer the 100-s limit than the 10-s time desired for the optimum volume output. The major factors contributing to this cycle lengthening were: (1) the cooling of

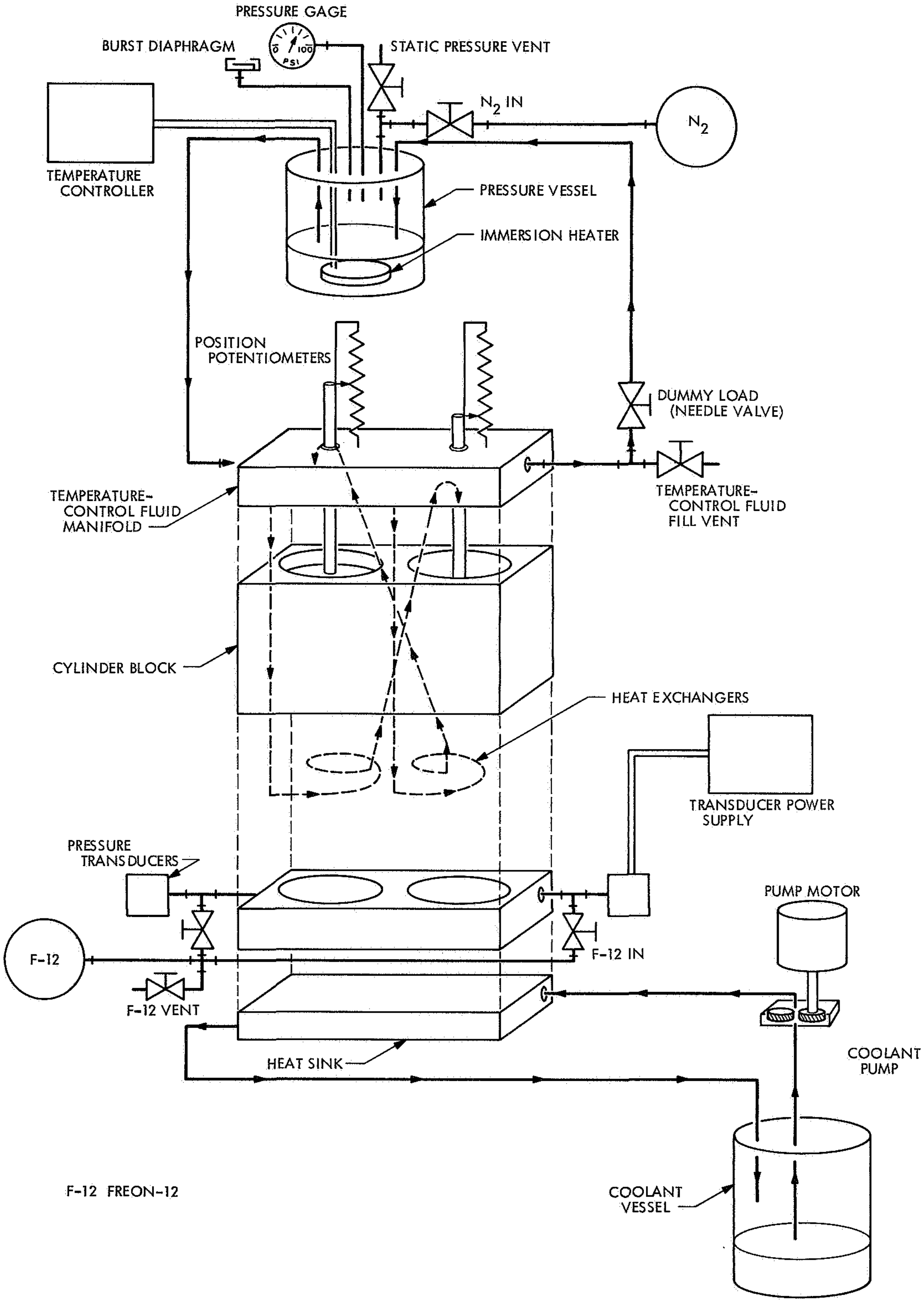

Fig. 3. Test setup for thermal pump (model II)

the temperature-control fluid in the lines leading to the heat exchanger, (2) the large thermal inertia of the thick-wall exchanger tube and enclosed fluid, and (3) contamination of the heat sink surface by temperature-control fluid leaking past the pistons. The longest self-powered oscillation produced by this model was seven cycles, averaging 82 s (Fig. 4).

c. Second prototype (model II). A second model was constructed to minimize the difficulties encountered in the first, especially in gaskets and seals. The pump body and manifolds were a laminate of Micarta sheets with temperature-control fluid channels milled in the laminae, which were then epoxied together. Leakage was positively prevented by 2-in.-diam Bellofram[1] rolling diaphragms on both ends of the piston (Fig. 5). Piston position indication was provided by ⅛-in. shafts through the upper manifold, also used for manual piston starting. Heat exchanger reaction time was improved by fabricating a 0.005-in.-wall finned tube, with six parallel tubes per cylinder. The heat sink surface was milled with fins fitting into the spaces between the exchanger tubes (Fig. 5, inset).

Six tests with an alcohol-cooled sink and two with water cooling have been performed, with largely inconclusive results. The rolling diaphragms apparently consume an excessive proportion of the pump work output in flexing the rubber-fabric sheet during piston motion. A comparison of typical output recordings (Fig. 6) shows that a gradient of at least 3 psi is required before spontaneous piston motion begins. Heat exchanger lag has been considerably reduced (Fig. 6b, cylinder A) with the finned tubes; the long cool-down time for cylinder B in this instance is due to insufficient liquid Freon to wet the exchanger tube. This has been a recurrent difficulty, as Freon quantities have had to be calculated from temperature and pressure data on the read-out chart. Overriding of the heat exchanger by heat conduction through the piston and from the supply tubes in the wall is evident in the low range of liquid Freon temperatures. This model has achieved piston half-cycles of 38 s at downstroke/upstroke velocity ratios of 78%.

5. Conclusion

The experiments conducted to date indicate that a thermomechanical pump can operate in the desired temperature range. Requirements remaining to be fulfilled are:

---

[1] Bellofram Corp., Burlington, Mass.

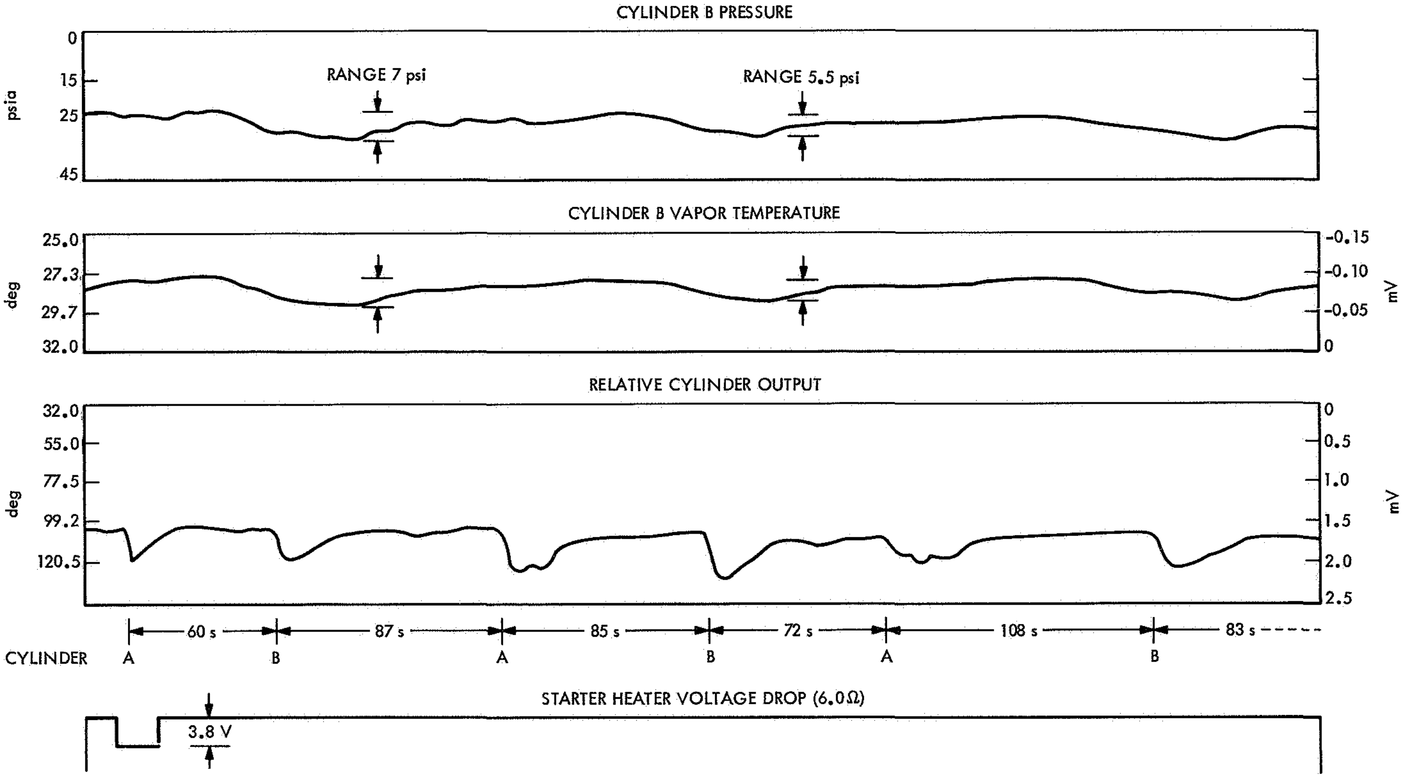

Fig. 4. Tracing of model I recorder output

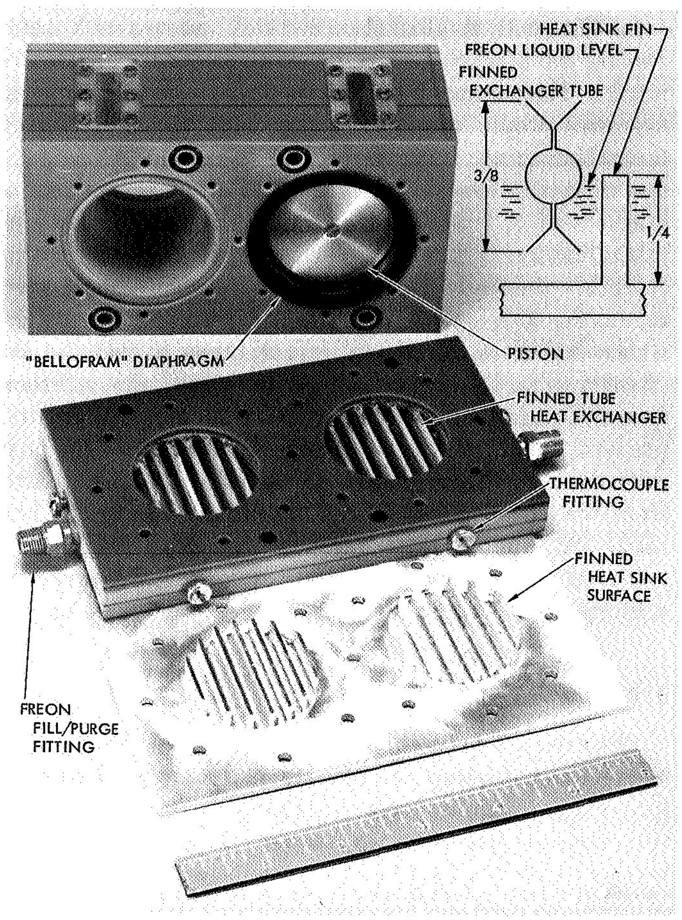

Fig. 5. Thermal pump, model II

(1) finding a piston sealing system with hermetic sealing and minimum hysteresis and thermal conduction; (2) optimizing the trade-off between maximum exchanger and heat sink areas and minimum vapor volume for a shorter cycle; (3) deciding on the optimum series, parallel, or combined heat exchanger configuration; and (4) obtaining a quantitative measure of Freon masses in the cylinders, rather than simply assuring equal mass by cross-connecting the Freon chambers, as at present.

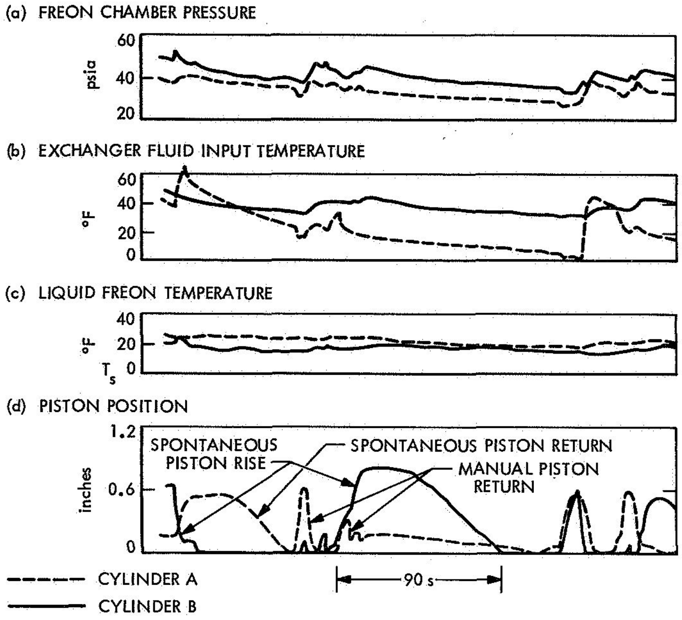

Fig. 6. Typical actual half-cycle operating conditions

It is unlikely that any reciprocating device would be able to meet the demands of an operating life of more than 40 million cycles that is required for continuous operation on the TOPS mission; however, augmentation of an electric pump during peak power demand remains a possibility. Similarly, completely cyclic operation ($\Delta U = 0$) is not a necessity, since the pump can be "kicked" with the starter heater at intervals and still provide a power consumption advantage over an electric pump.

Because of a lessening need (lower power estimates for an electric pump), further test model construction is not anticipated. The computer simulation and data reduction of cyclic heat exchanger calorimetry experiments are presently near completion. In addition to the experience gained in cyclic thermal mechanisms, this study has demonstrated the capability of Freon-evaporative devices to perform single-actuation force amplification functions.

XIII. Spacecraft Data Systems

ASTRIONICS DIVISION

A. Evaluation of Recording Tapes for Use in Spacecraft Magnetic Tape Recorders,

J. K. Hoffman, S. H. Kalfayan,[1] and R. H. Silver[1]

The second phase of an investigation of the characteristics of magnetic recording tape and the tape-to-head interface in the spacecraft environment was performed under direction of the JPL Spacecraft Data Systems Section. The results of this work are discussed in detail in *Chapter XIV-E* (the JPL Propulsion Division provided personnel and facilities employed in this effort). Phase I is described in SPS 37-63, Vol. III, pp. 209–214.

The experiments were designed to determine: (1) the effect of periods of tape recorder non-operation on the tape-to-head interface, (2) more details on the effect of operating speed and environmental temperature, (3) the potential of precluding tape-to-head sticking by pretreatment (degassing) of the tape, and (4) the behavior of the tape base material (oxide–binder removed) when in contact with the head surface.

The knowledge obtained from this program has been instrumental in understanding and solving the tape-to-head interface problems encountered in development of the *Mariner* Mars 1971 data storage subsystem. Particularly significant from these latest results is confirmation of the value of degassing the magnetic tape, or of providing areas stripped of oxide and binder, as means of reducing the tendency of the tape to stick to the heads during non-operating periods and environmental extremes.

Further tests investigating additional parameters are in process.

---

[1] Polymer Research Section, Propulsion Division.

B. Linear *m*-ary Feedback Shift Registers,

M. Perlman

1. Introduction

A diagram of a linear m-ary feedback shift register (FSR) is shown in Fig. 1. The behavior of the FSR can be described by the linear recurrence relation

$$a_k = \gamma + \sum_{i=1}^{r} c_i \, a_{k-i} \qquad \bmod m \tag{1}$$

The state of the ith stage at clock pulse interval (CPI) k is denoted by a_{k-i}. Each of the r-stages is capable of assuming any one of m distinct states $0, 1, \cdots, m-1$. The state of the ith state at CPI k becomes the state of the $(i+1)$th stage at CPI $k+1$. That is,

$$a_{(k+1)-(i+1)} = a_{k-i}$$

accounts for the effect of shifting that occurs upon the application of a clock pulse.

The output of the modulo m summer at CPI k is denoted by a_k. As shown in Eq. (1), $c_i a_{k-i}$ is the contribution of the ith stage to the input of the modulo m summer where c_i is a constant multiplier. The state-value of c_i and γ (a constant input to the modulo m summer) is $0, 1, \cdots$, or $m-1$. An FSR of length r requires that $c_r \neq 0$. The state-value of the feedback at CPI k (i.e., a_k) becomes the state of the first stage at CPI $k+1$.

The recurrence relation provides information about the cycle (of states) structure. The periodicity of $\{a_k\}$ for a given initial state $a_{-1} \, a_{-2}, \cdots, a_{-r}$ can be determined from the generating function of $\{a_k\}$.

$$G_\gamma(x) = \sum_{k=0}^{\infty} a_k x^k = \sum_{k=0}^{\infty} \left(\gamma + \sum_{i=1}^{r} c_i \, a_{k-i} \right) x^i$$

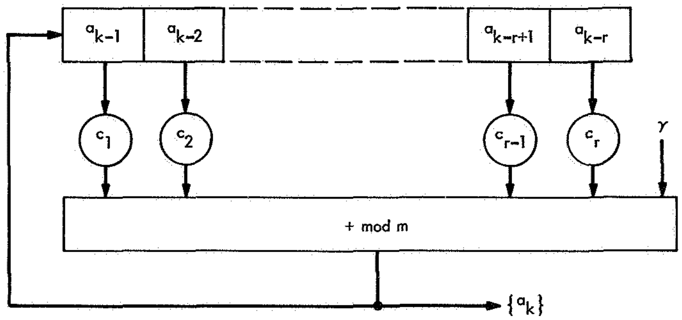

Fig. 1. Linear *m*-ary FSR

Expressed in closed form (Refs. 1 and 2)

$$G_\gamma(x) = \frac{\gamma + (1-x)\, g(x)}{(1-x)\, f(x)} \tag{2}$$

where

$$g(x) = \sum_{i=1}^{r} c_i \, x^i \left(a_{-i} x^{-i} + a_{-i+1} x^{-i+1} + \cdots + a_{-1} x^{-1} \right)$$

and

$$f(x) = 1 - \sum_{i=1}^{r} c_i \, x^i$$

The generating function $G_\gamma(x)$ is a ratio of two polynomials whose coefficients are $0, 1, \cdots$, or $m-1$. When performing the division, all arithmetic operations are reduced modulo m, and the coefficients of the ascending powers of x correspond to the sequence $\{a_k\}$, which is periodic or ultimately becomes periodic.

The polynomial $g(x)$ is of degree $r-1$ or less and is a function of the initial state and $c_1, c_2, \cdots, c_r$, the feedback configuration. The characteristic polynomial $f(x)$ is of degree r and is a function of the feedback configuration only.

Throughout the remainder of this article, theorems will be stated without an accompanying proof. Examples will be given to illustrate an assertion.

2. Cycle Structure and Periodicity

Theorem 1. *Given an r-stage linear m-ary FSR. Distinct states will have distinct successor states if and only if* $(c_r, m) = 1$.

Example 1. The state diagram for

$$a_k = a_{k-1} + 2a_{k-2} \qquad \bmod 4$$

appears in Fig. 2a. Since $c_2 = 2$ and 4 are not relatively prime, there are states that have more than one predecessor state. The generating function for a_k is

$$G_0(x) = \frac{g(x)}{f(x)} = \frac{(a_{-1} + 2a_{-2}) + 2a_{-1} x}{1 - x - 2x^2}$$

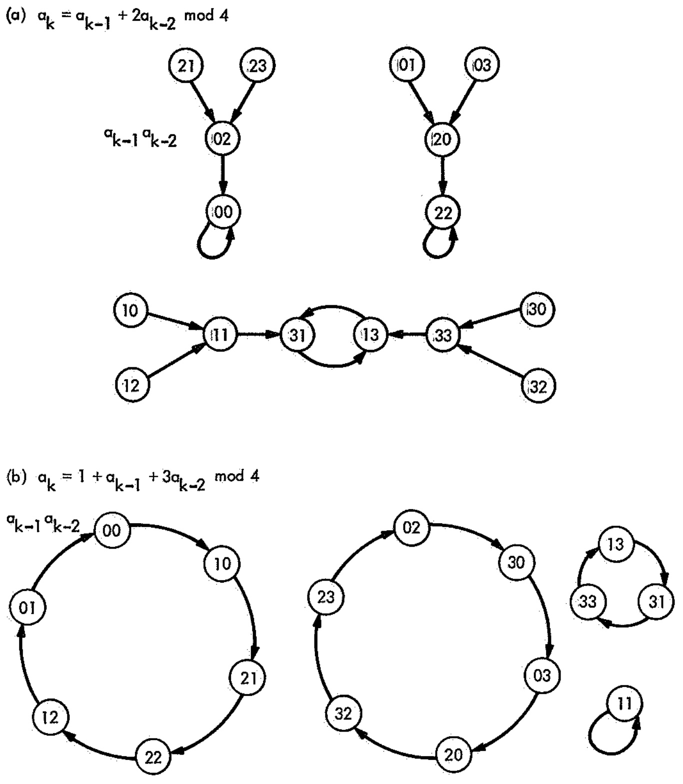

Fig. 2. State diagrams

For $a_{-1} = 1$ and $a_{-2} = 0$

$$G_0(x) = \frac{1-2x}{1-x-2x^2}$$

$$= \frac{1}{1+x} = 1 + 3x + x^2 + 3x^3 + \cdots +$$

Example 2. The state diagram for

$$a_k = 1 + a_{k-1} + 3a_{k-2} \qquad \text{mod}\,4$$

appears in Fig. 2b. Since $(3, 4) = 1$, the cycles are branchless. The generating function for a_k is

$$G_1(x) = \frac{(1 + a_{-2} + 3a_{-2}) + (2a_{-1} + a_{-2})x + a_{-1}x^2}{(1-x)(1-x-3x^2)}$$

For $a_{-1} = a_{-2} = 0$

$$G_1(x) = \frac{1}{1 + 2x + 2x^2 + 3x^3}$$

$$= 1 + 2x + 2x^2 + x^3 + 0x^4 + 0x^5 + \cdots +$$

Branchless cycles correspond to FSR sequences that are periodic for every possible initial state. In general, cycles with branches will correspond to a periodic sequence preceded by a "transient" sequence if the initial state is on a branch. (*Example 1* is an exception.)

Hereafter, only linear *m-ary FSR sequences* with *branchless cycles* will be considered.

Theorem 2. *The length of the longest cycle(s) characterized by $G_0(x)$ is ℓ where ℓ is the least integer for which*

$$f(x) \,|\, 1 - x^\ell \qquad \text{mod}\, m$$

and the state $00 \cdots 01$ is always contained in a cycle of longest length.

Theorem 3. *The length of the longest cycle(s) characterized by $G_\gamma(x)$, where $(\gamma, m) = 1$, is ℓ where ℓ is the least integer for which*

$$(1-x)f(x) \,|\, 1 - x^\ell \qquad \text{mod}\, m$$

The state $00 \cdots 0$ is always contained in a cycle of longest length.

Theorem 4. *The length of each cycle generated by a linear m-ary FSR divides the length of the longest cycle(s).*

In example 2,

$$(1-x)(1-x-3x^2) \,|\, 1 - x^\ell \qquad \text{mod}\,4$$

for ℓ having a least integer value of 6. The disjoint cycles are of length 6, 6, 3, and 1.

3. Decomposition of the Linear *m*-ary FSR into Parallel *p*-ary FSRs

The behavior of linear *p*-ary (where $m = p$ a prime) FSRs is well understood (Refs. 1 and 3). $G_\gamma(x)$ is the ratio of polynomials over $GF(p)$ (Galois field characteristic p) (Refs. 3 and 4). Let

$$\phi(x) = (1-x)f(x) = [\phi_1(x)]^{s_1}[\phi_2(x)]^{s_2}, \cdots, [\phi_t(x)]^{s_t} \tag{3}$$

over $GF(p)$. The roots of an irreducible factor, say $\phi_1(x)$ of degree n_1, are

$$\alpha, \alpha^p, \alpha^{p^2}, \cdots, \alpha^{p^{n_1-1}}$$

Each of the n_1 roots has the same multiplicative order. The *period* of $\phi_1(x)$ over $GF(p)$ is ℓ_1 the order of its roots where $\ell_1 \mid p^{n_1} - 1$. Equivalently, the period of $\phi_1(x)$ is the least integer ℓ_1 for which $\phi_1(x) \mid 1 - x^{\ell_1}$. Whenever a root of $\phi_1(x)$ is a primitive element of the extension field $GF(p^{n_1})$, $\phi_1(x)$ is defined as a primitive polynomial over $GF(p)$ and has order $\ell_1 = p^{n_1} - 1$.

The repeated factor $[\phi_1(x)]^{s_1}$ has a period of $p^{j_1}\ell_1$ where $p^{j_1-1} < s_1 \leqq p^{j_1}$. The period of $\phi(x)$ is

$$\ell = \text{LCM}\,[p^{j_1}\ell_1, p^{j_2}\ell_2, \cdots, p^{j_t}\ell_t] \qquad (4)$$

where LCM is the least-common multiple. The generating function $G_\gamma(x)$ with $\phi(x) = (1-x)f(x)$ as its denominator (Eq. 3) characterizes a linear p-ary FSR. The number of stages is equal to the degree of $f(x)$. The factor $1 - x$ appears when $\gamma \neq 0$ (Eq. 2). The length of the longest cycle(s) is ℓ (Eq. 4) and ℓ is the least integer for which $\phi(x) \mid 1 - x^{\ell}$.

Note that $\phi(x)$ over a field has a unique factorization of products of powers of irreducible polynomials. In the m-ary case, the coefficients of $\phi(x)$ are taken from a *ring* and $\phi(x)$ *cannot be factored uniquely.*

Example 3. The factorization of $1 - x^4$ over the ring $\{0, 1, 2, 3\}$ (addition and multiplication of the coefficients are reduced mod 4) can be done in the following ways:

$$1 - x^4 = (1-x)(1+x)(1+x^2) \qquad \text{mod } 4$$

$$1 - x^4 = (1-x)^2(1+2x-x^2) \qquad \text{mod } 4$$

Corresponding to an m-ary linear recurrence relation where

$$m = p_1^{e_1} p_2^{e_2}, \cdots, p_s^{e_s}$$

are s simultaneous p-ary linear recurrence relations. Information about the length of an m-ary FSR cycle containing a given initial state can be determined from the LCM of the periods of the s p-ary FSRs. Each of the p-ary FSRs will contain an initial state corresponding to the initial state of the m-ary FSR.

Theorem 5. *A linear m-ary FSR is described by the linear recurrence relation*

$$a_k = \gamma + \sum_{i=1}^{r} c_i\, a_{k-i} \qquad \textit{mod } m$$

where

$$m = p_1^{e_1} p_2^{e_2}, \cdots, p_s^{e_s}, \qquad (c_r, m) = 1$$

and $\gamma = 0$ *or* $(\gamma, m) = 1$. *The length of the cycle containing the initial state* $a_{-1}a_{-2}, \cdots, a_{-r}$ divides *the LCM of the periods of the generating functions*

$$G_\gamma^j(x) = \frac{\gamma + (1-x)\,g(x)}{(1-x)\left[1 - \sum_{i=1}^{r} (c_i \textit{ mod } p_j)\, x^i\right]^{p_j^{e_j-1}}} \qquad (5)$$

for $j = 1, 2, \cdots, s$, *and an initial state*

$$a_{-1} \textit{ mod } p_j, a_{-2} \textit{ mod } p_j, \cdots, a_{-r} \textit{ mod } p_j$$

Note that all arithmetic operations are reduced mod p_j.

In determining the period of $G_\gamma^j(x)$, $G_\gamma^j(x)$ *is first reduced to its lowest terms. An initial state that results in a numerator for* $G_\gamma^j(x)$ *that is relatively prime to its denominator will be contained in a longest* p_j*-ary cycle.*

Example 4. (See Ref. 5 for an application.) Given

$$a_k = a_{k-1} + a_{k-2} \qquad \text{mod } 10 \qquad (6)$$

the longest cycle will contain $a_{-1}a_{-2} = 01$ as an initial state.

$$G_0(x) = \frac{1}{1 + 9x + 9x^2} \qquad \text{mod } 10$$

$$G_0^2(x) = \frac{1}{1 + x + x^2} \qquad \text{mod } 2$$

$$G_0^5(x) = \frac{1}{(1+2x)^2} \qquad \text{mod } 5$$

Since $1 + x + x^2$ over $GF(2)$ is primitive, it has period

$$k_2 = 2^2 - 1 = 3$$

The factor $1 + 2x$ over $GF(5)$ is primitive and has period $5^1 - 1$ or 4. Since

$$5^0 < 2 < 5^1$$

the period of $(1 + 2x)^2$ is

$$k_5 = 5 \times 4 = 20$$

The length of the longest cycle divides k where

$$k = \mathrm{LCM}\,[k_2, k_5] = 60$$

The reader may verify that the longest cycle actually equals 60.

Let $\{b_k\}$ be associated with $G_0^2(x)$ and $\{d_k\}$ with $G_0^5(x)$. Then

$$G_0(x) = \frac{(a_{-1} + a_{-2}) + a_{-1}x}{1 + 9x + 9x^2} \qquad \mathrm{mod}\ 10$$

$$G_0^2(x) = \frac{(b_{-1} + b_{-2}) + b_{-1}x}{1 + x + x^2} \qquad \mathrm{mod}\ 2$$

$$G_0^5(x) = \frac{(d_{-1} + d_{-2}) + d_{-1}x}{(1 + 2x)^2} \qquad \mathrm{mod}\ 5$$

where

$$b_{-1} \equiv a_{-1} \bmod 2, \qquad b_{-2} \equiv a_{-2} \bmod 2,$$

$$d_{-1} \equiv a_{-1} \bmod 5, \qquad d_{-2} \equiv a_{-2} \bmod 5$$

and

$$(d_{-1} + d_{-2}) + d_{-1}x = 1 + 2x$$

when $d_{-1} = 2$ and $d_{-2} = 4$.

Therefore, an initial state $a_{-1} = 2$ and $a_{-2} = 4$ results in

$$G_0^2(x) = \frac{0}{1 + x + x^2} \qquad \mathrm{mod}\ 2$$

$$G_0^5(x) = \frac{1}{1 + 2x} \qquad \mathrm{mod}\ 5$$

with periods of 1 and 4, respectively. Therefore, a_k of Eq. (6), where $a_{-1} = 2$ and $a_{-2} = 4$, has a period that divides $k = 1 \times 4$ or 4. The following state table shows the period to be 4:

k	a_{k-1}	a_{k-2}	a_k
0	2	4	6
1	6	2	8
2	8	6	4
3	4	8	2

Example 5. Given

$$a_k = 1 + a_k + 3a_{k-1} \qquad \mathrm{mod}\ 8 \qquad (7)$$

The initial state $a_{-1}\,a_{-2} = 00$ lies in a cycle of longest length described by

$$G_1(x) = \frac{1}{(1 - x)(1 + 7x + 5x^2)} \qquad \mathrm{mod}\ 8$$

$$G_1^2(x) = \frac{1}{(1 - x)(1 + x + x^2)^4} \qquad \mathrm{mod}\ 2$$

The period associated with $G_1^2(x)$ is 12 whereas a_k of Eq. (7), with $a_{-1}\,a_{-2} = 00$, has a period of 6 (a divisor of 12 as asserted in Theorem 5) as shown in the following state table:

k	a_{k-1}	a_{k-2}	a_k
0	0	0	1
1	1	0	2
2	2	1	6
3	6	2	5
4	5	6	0
5	0	5	0

4. Conclusions

A linear m-ary feedback shift register can be decomposed into parallel linear p-ary FSRs where each p is a distinct prime factor of the integer m.

The behavior of a linear p-ary FSR is determined from the divisibility properties of $\phi(x)$ over $GF(p)$ where $\phi(x)$ is the denominator of its generating function.

An initial state of a linear m-ary FSR is shown to be on a cycle whose length divides the LCM of the periods of p-ary FSRs with corresponding initial states.

Applications and implementations with binary devices of m-ary FSRs will be subjects for future work.

References

1. Golomb, S. W., *Shift Register Sequences,* Holden-Day, Inc., San Francisco, Calif., 1967.
2. Perlman, M., *Pseudo-noise Sequence Generation with Three-Tap Linear Feedback Shift Registers,* Technical Report 32-1432. Jet Propulsion Laboratory, Pasadena, Calif., Nov. 15, 1969.
3. Peterson, W. W., *Error-Correcting Codes,* MIT Press, Cambridge, Mass., 1961.
4. van der Waerden, B. L., *Modern Algebra,* Frederick Ungar Publishing Co., New York, 1953.
5. Rubin, D., and Deo, N., "An Additive Pseudorandom Number Generator with Semi-infinite Sequence Length", Proceedings of the Second Hawaii International Conference on System Sciences, University of Hawaii, Honolulu, Ha., 1969.

XIV. Polymer Research

PROPULSION DIVISION

A. Long-Term Aging of Elastomers: Kinetics of Oxidation of SBR by Infrared Spectroscopy,

R. Rakutis, R. H. Silver, and S. H. Kalfayan

1. Introduction

Infrared spectroscopy has proven to be a useful tool in thermal oxidation studies of polyethylene (Refs. 1 and 2), polypropylene (Refs. 3 and 4), natural rubber (Refs. 5, 6, and 7), and other elastomers (Ref. 8). Both qualitative and quantitative information were obtained from these studies.

Preliminary examinations using infrared spectroscopy to follow the oxidation of styrene–butadiene rubber (SBR) indicated that the new functional groups formed during oxidation could be measured quantitatively (SPS 37-57, Vol. III, pp. 166–169, and SPS 37-61, Vol. III, pp. 237–241).

The present study involves the determination of energies of activation for the oxidation processes taking place in SBR and an examination of the reactions that could be taking place in the rubber network.

2. Experimental Method

a. Materials. SBR (Lot 386, type 1500) was obtained from the National Bureau of Standards. The raw gum was extracted with acetone to remove the antioxidant and other nonrubber ingredients.

b. Procedure. Films 0.04- to 0.06-mm thick were cast on NaCl discs from a 2 to 3% benzene solution of the extracted rubber. Infrared spectra were continuously recorded on a Perkin-Elmer model 421 spectrophotometer. The NaCl disc supporting the film layer was placed in a specially constructed oxidation cell. The cell temperature was controlled by means of a thermocouple inserted directly into the NaCl disc and connected to a Honeywell (type R7161 B) temperature controller. The temperatures used during the oxidation reaction ranged from 110 to 150°C, accurate within ±1°C. Air or O_2 was passed through the reaction chamber at a flow rate of 100 ml/min.

As the chamber was heated to the desired temperature, a constant flow of N_2 was maintained through the cell. At the desired temperature, the NaCl disc was quickly inserted into the cell and the spectrum was recorded immediately. The N_2 was now replaced by air or O_2 and the spectra were recorded periodically, the frequency of the recording depending on the temperature of the particular run. Exposure time was determined from that instant when the appropriate gas was introduced into the cell. Experiments were terminated when there was no further change in either the hydroxyl or the carbonyl region of the spectrum.

An example of an infrared spectrum of a typical run is shown in Fig. 1. The total areas of the absorption band in the hydroxyl and the band in the carbonyl region were measured by means of a planimeter. Curves were obtained by plotting the total hydroxyl and the total carbonyl areas versus exposure time in order to obtain rate data. Maximum rates of formation were determined by drawing maximum tangents to these curves. This technique has been used in other investigations (Refs. 4 and 5).

The induction time t_i was determined by examining the rate curves (Figs. 2 and 3). Arrhenius plots (Figs. 4 and 5) from the maximum rates and reciprocals of the induction periods were obtained by using a least squares computer program.

c. Chemical analysis of functional groups. Films of the oxidized SBR were tested chemically for functional groups resulting from oxidation. The hydroperoxide test with sodium iodide in isopropanol was positive. A slight reddish precipitate was also obtained with 2,4-dinitrophenylhydrazine, indicating the presence of aldehydes and/or ketones. The ferric hydroxamate test for esters and the ferric chloride test for alcohols were both negative.

Bubbling NH_3 gas for 15 min at room temperature onto the surface of an oxidized SBR film caused the disappearance of the peak at 1690 cm^{-1}, indicating the formation of the ammonium salt from the carboxylic acid. A similar experiment for testing the presence of a hydroperoxide group by bubbling SO_2 gas on the oxidized film gave negative results.

To obtain better solubility of the oxidation products for chemical analysis, a sample of liquid SBR, known by the trade name Flosprene VLV (American Synthetic Rubber Corp.) was oxidized in oxygen after extraction with acetone to remove the chain transfer agent. Similar chemical tests were carried out on the oxidized VLV. Only trace amounts of hydroperoxides, carboxyl (titration with alcoholic KOH), and carbonyl groups were found.

3. Results and Discussion

a. Energy of activation of autoxidation. The effect of temperature on the rates of total hydroxyl and carbonyl formation in oxygen and air is shown in Figs. 2 and 3, respectively. Maximum rates of formation v_m were determined from these curves. The values obtained for maximum rates are listed in Table 1 along with reaction temperatures and induction times for air and oxygen atmospheres.

As shown in Figs. 2 and 3, the rate curves for the formation of —OH and $>C{=}O$ groups had the same shape whether the oxidation was carried out in air or in 100% oxygen. Increase in reaction temperature decreased the induction period and increased the reaction rate, as

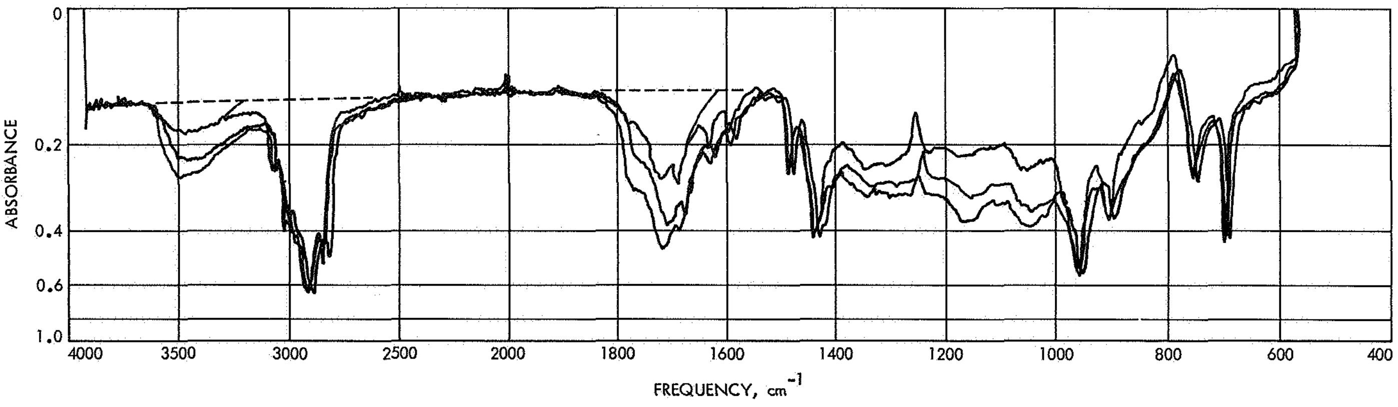

Fig. 1. Infrared spectra of SBR rubber oxidized at 119°C in air (area limits used in measuring hydroxyl and carbonyl content)

Table 1. Maximum slopes and induction periods of oxidation rate curves for —OH and $>$C=O formation in air and oxygen

Temperature, °C	$1/T \times 10^3$, °K	Maximum slope, cm^2/min				Reciprocal of induction period $1/t_i$, min			
		—OH		$>$C=O		—OH		$>$C=O	
		Air	Oxygen	Air	Oxygen	Air	Oxygen	Air	Oxygen
107	2.632	—	—	0.78	—	0.0044	—	0.0050	—
119	2.551	0.46	1.83	1.26	2.10	0.0163	0.0107	0.0105	0.0107
131	2.475	0.74	2.90	1.57	4.00	0.0259	0.0370	0.0256	0.0357
143	2.404	1.15	5.33	3.50	6.36	0.0500	0.0667	0.0476	0.0689
154	2.342	1.97	7.77	5.25	11.00	0.0909	0.1250	0.0869	0.1050

expected. The induction periods in pure oxygen were shorter and the rates of formation of oxygenated products were higher than in air.

Both the hydroxyl and carbonyl rate curves leveled off at the end of the reaction. No relationship was observed between the thickness (or weight) of the SBR film and the area at which the leveling off was observed. The phenomenon of leveling off may be caused by crosslinking, at the surface leading to skin formation, which reduces the permeability of the film to air or oxygen.

In general, it was found that measurements based on the absorption bands in the carbonyl region gave more consistent results than those in the hydroxyl region.

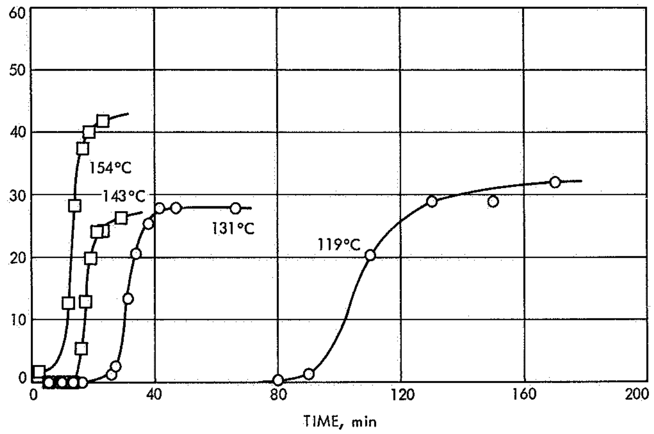

Fig. 2. Hydroxyl (—OH) content of styrene–butadiene during oxidation in oxygen

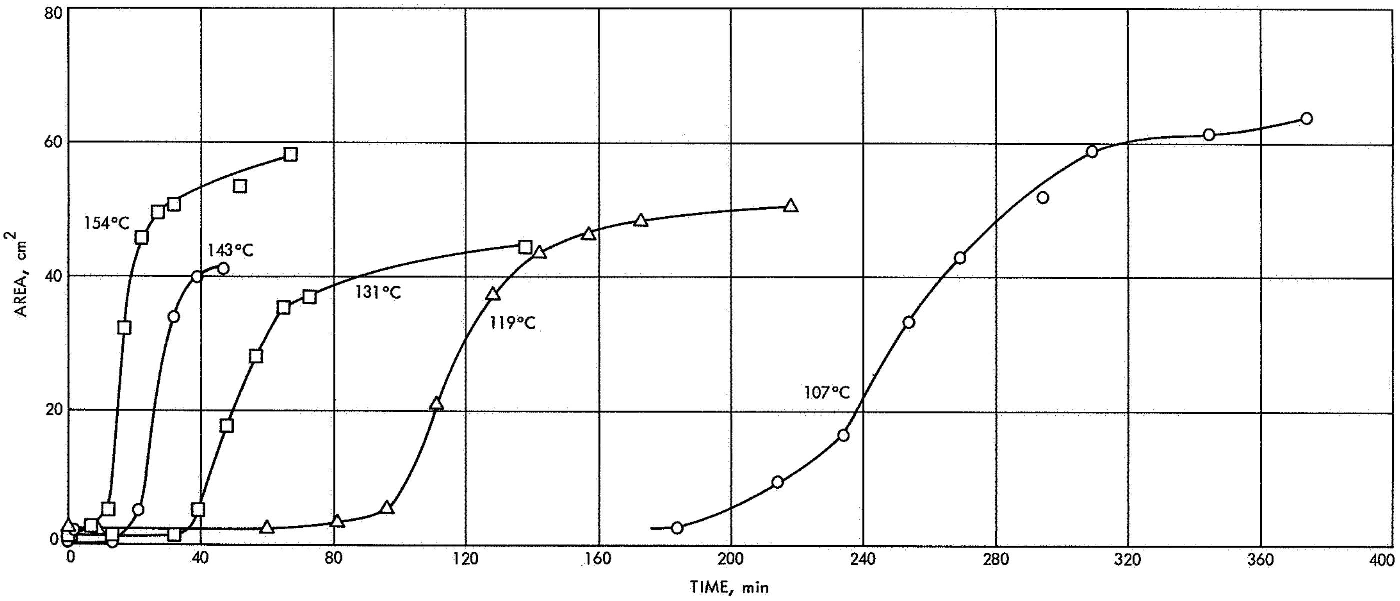

Fig. 3. Carbonyl ($>$C=O) content of styrene–butadiene during oxidation in air

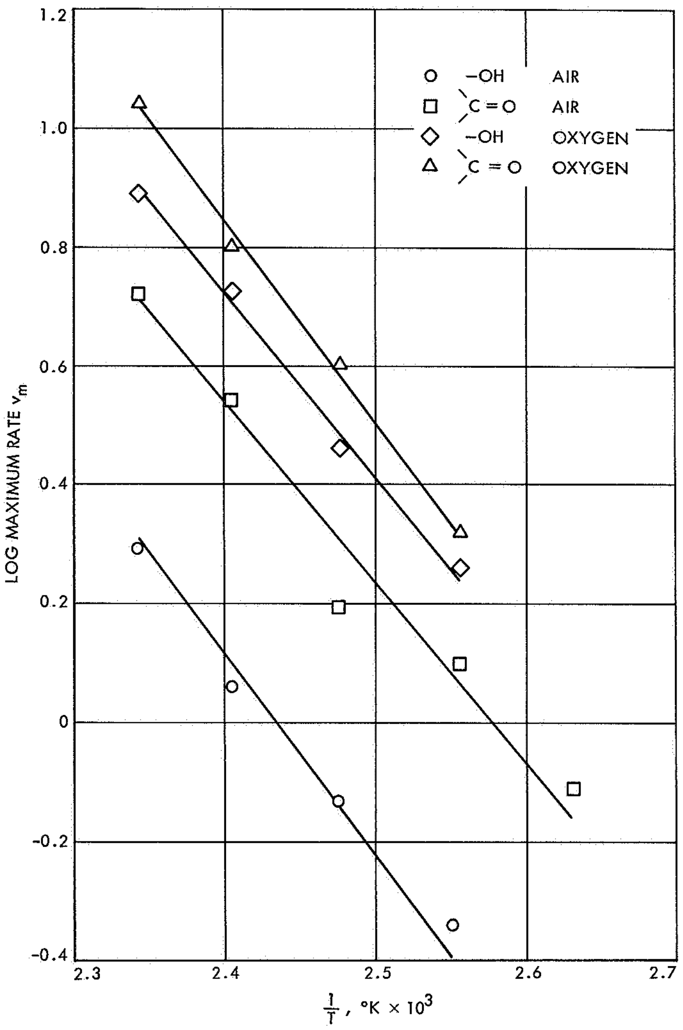

Fig. 4. Relationship of maximum rates v_m of hydroxyl and carbonyl formation to temperature

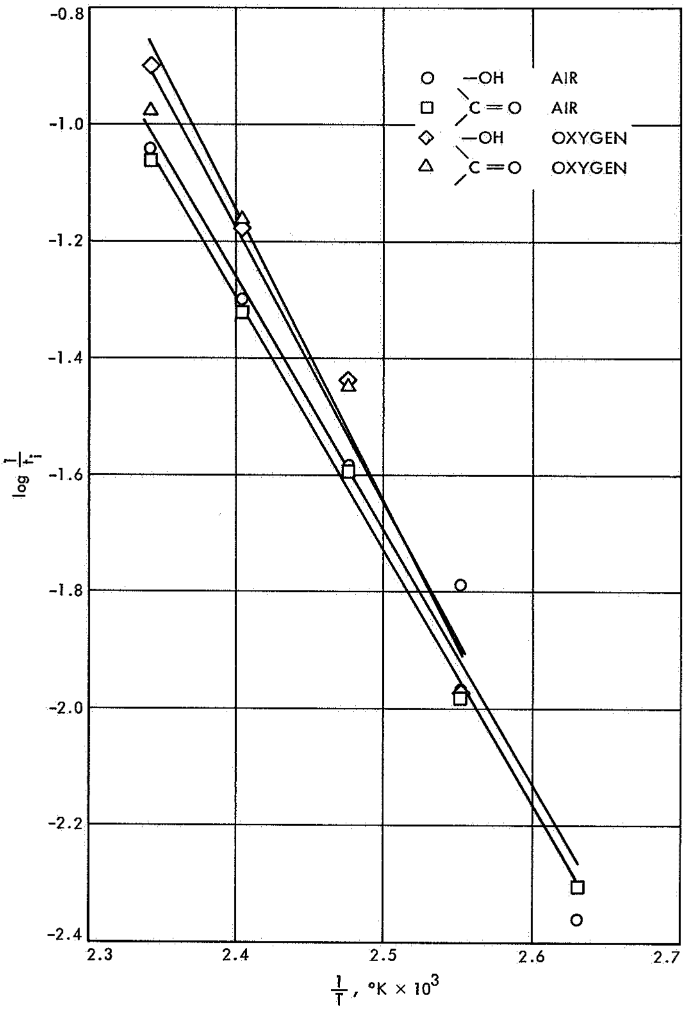

Fig. 5. Relationship of reciprocal induction period $1/t_i$ to temperature

Plots of maximum rates v_m versus $1/T$ (°K) showed good linearity (Fig. 4). Reasonably linear plots were also obtained when the reciprocals of the induction periods $1/t_i$ were plotted versus $1/T$ (Fig. 5). The energies of activation ΔH calculated from these curves are listed in Table 2. The values for ΔH from maximum rates were 14.8 ± 1 and 14.2 ± 1 kcal for hydroxyl and carbonyl groups, respectively. The values obtained from the induction periods were 21.2 ± 1 kcal for hydroxyl and 20.5 ± 1 kcal for carbonyl group formation. The higher value from periods of induction, also observed by other workers (Ref. 4), is probably due to the fact that the two methods of determining the energies of activation are controlled by different reactions in the autoxidation scheme. The following sequence of steps has been proposed for autoxidation (Ref. 9):

Table 2. Activation energies

Functional group	ΔH maximum rates v_m, kcal	ΔH induction periods $1/t_i$, kcal
OH (air) OH (O_2)	15.5 14.1	19.7 22.7
>C=O (air) >C=O (O_2)	13.1 15.4	19.7 21.4

Initiation
$$2ROOH \xrightarrow{k_1} RO_2^{\bullet} + RO^{\bullet} + H_2O \qquad (1)$$
$$(2RO^{\bullet} \longrightarrow 2R^{\bullet} + O_2)$$
$$R^{\bullet} + O_2 \xrightarrow{k_2} RO_2 \qquad (2)$$

Propagation
$$RO_2^{\bullet} + RH \xrightarrow{k_3} ROOH + R^{\bullet} \qquad (3)$$
$$R^{\bullet} + R^{\bullet} \xrightarrow{k_4} RR \qquad (4)$$

Termination $R^\bullet + RO_2 \xrightarrow{k_5} ROOR$ (5)

$$RO_2^\bullet + RO_2 \xrightarrow{k_6} ROOR + O_2 \qquad (6)$$

The induction period is controlled by the activation energy for Reaction (1), i.e., the initiation step (Ref. 9). The value of 21 kcal reported here agrees well with the value of 21.3 kcal reported for natural rubber (Ref. 5), also obtained by infrared spectroscopy. Other reported values range from 22–26 kcal (Ref. 4).

The energies from maximum rates, on the other hand, probably represent Reaction (3), the propagation step (Ref. 9). In this step, the activation energy is partially dependent on the stability of the free radical $R^\bullet$ formed after hydrogen abstraction. In SBR, there are many possibilities for stabilized free radicals to form, and hence, the lower activation energy. From oxygen absorption studies (Ref. 10), 15 kcal have been reported for Na-butadiene rubber and, likewise, 15 kcal for natural rubber (Ref. 11).

The energies of activation obtained from stress relaxation measurements (SPS 37-59, Vol. III, pp. 194–198) for SBR are about 27.5 kcal, somewhat higher than those from this study. Stress relaxation measures mostly the scission taking place in the network; infrared spectroscopy includes both scission and crosslinking. A higher amount of energy would be necessary for bond scission than for crosslinking (i.e., free radical addition to double bonds) and, consequently, a larger ΔH value would be expected for the stress relaxation process.

b. Analysis of infrared spectra. In the carbonyl region of absorption, three main band heads were distinguishable at 1690, 1720, and 1770 cm^{-1} (Fig. 1). Identical oxidized spectra were obtained regardless of whether the oxidation was carried out in air or oxygen. The peak at 1690 cm^{-1} was assigned to peresters, although there is only limited knowledge of the exact frequencies at which peresters (and peracids) absorb (Ref. 2).

The broad absorption centered at 3450 cm^{-1} was attributed to hydrogen-bonded —OH groups, i.e., alcohol and hydroperoxide (Ref. 12). The sharp band at 3555 cm^{-1}, characteristic of hydroperoxides, was not observed in the oxidized spectra of SBR. However, since positive chemical tests were obtained for peroxides, some of the absorption at 3450 cm^{-1} must be caused by peroxidic groups.

The double bond region at 1640 cm^{-1} was obscured by the broad absorption of the carbonyl peaks. Thus, the change in unsaturation could not be estimated. It has been reported (Refs. 2, 5, and 12) that there was either no change or only a very slight increase at the ethylenic band at 1640 cm^{-1} upon oxidation of other polymeric films. Although a significant decrease would be expected in the amount of unsaturation as a result of a direct attack at the double bonds during oxidation, chain scission in the network could offset this change. Consequently, the total concentration of double bonds would not necessarily be affected.

There was general absorption between 1350 and 1000 cm^{-1} with two broad peaks at 1050 and 1070 cm^{-1} (Fig. 1). Similar results have been reported in infrared studies of the oxidation of SBR (Ref. 8) and polyethylene (Ref. 2). The absorption in this region is due to a composite of the various alcoholic components and ether linkages (C—O—C) formed among the oxidation products.

During oxidation in air, the —OH peak appeared slightly later than the $>C=O$ peak. In oxygen, the two peaks formed approximately at the same time. It has been noted (Ref. 8) that the minimum amounts of —OH and $>C=O$ groups detectable by infrared are 0.5 and 0.1%, respectively. Consequently, —OH groups are being formed at the same time or, in oxygen, before the $>C=O$ groups are formed. Alcohols can result from the decomposition of hydroperoxides formed by oxidation of secondary carbons.

In the carbonyl absorption area, the carboxylic acid peak (1690 cm^{-1}) and the ketonic peak (1720 cm^{-1}) appeared at the same time; at the half way stage of the oxidation, the ketonic peak began to increase more rapidly and envelop the acid peak. The perester band at 1790 cm^{-1} was observed after the appearance of the —OH and $>C=O$ peaks.

Since the extinction coefficient of acid groups is significantly higher than that of aldehydes and ketones (Ref. 12), there are apparently large amounts of ketonic and aldehydic groups formed even in the early stages of oxidation. It is interesting to note that carboxylic groups are formed also at the start of the oxidative reactions. Acids can be formed either by further oxidation of aldehydes and ketones (Ref. 1) or by direct attack at the double bond (Ref. 13). Since there is a high degree of unsaturation in SBR, the latter method appears to be more likely for the formation of acid groups during these oxidative conditions.

References

1. Beachell, H. C., and Tarbett, G. W., "The Oxidative Degradation of Polyethylene," *J. Polym. Sci.*, Vol. 45, p. 451, 1960.
2. Luongo, J. P., "Infrared Study of Oxygenated Groups Formed in Polyethylene During Oxidation," *J. Polym. Sci.*, Vol. 42, p. 139, 1960.
3. Chien, J. C. W., Vandenberg, E. J., and Jabloner, H., "Polymer Reactions. III. Structure of Polypropylene Hydroperoxide," *J. Polym. Sci.*, Vol. 6, p. 381, 1968.
4. Stivala, S. S., Reich, L., and Kelleher, P. G., "Kinetics of the Thermal Oxidation of Isostatic Polypropylene by Infrared Spectroscopy," *Makromol. Chem.*, Vol. 59, p. 28, 1963.
5. Kello, V., Tkac, A., and Hrivikova, J., "A Study of the Aging of Natural Rubber by Means of Infrared Spectroscopy. V. Aging Accelerated by Heat," *Rubber Chem. Technol.*, Vol. 29, p. 1245, 1956.
6. D'Or, L., and Kossler, I., "An Infrared Spectrometric Study of the Oxidation of Natural Rubber," *Rubber Chem. Technol.*, Vol. 25, p. 251, 1952.
7. Solomon, G., and Van der Schee, A. C., "Infrared Analysis of Isomerized, Vulcanized and Oxidized Natural Rubber," *J. Polym. Sci.*, Vol. 19, p. 503, 1954.
8. Field, J. E., Woodford, D. E., and Gehman, J. D., "Infrared Study of Oxidation of Elastomers," *J. Polym. Sci.*, Vol. 15, p. 51, 1955.
9. Mesrobian, R. B., and Tobolsky, A. V., *Autoxidation and Antioxidants*, Vol. I, p. 107. Edited by W. O. Sundberg. Interscience Publishers, New York, 1961.
10. Augert, L. G., and Kuzminskii, "Oxidation Mechanism of Rubbers in the Presence of Inhibitors," *J. Polym. Sci.*, Vol. 32, p. 1, 1958.
11. Tobolsky, A. V., Metz, D. J., and Mesrobian, R. B., "Low Temperature Autoxidation of Hydrocarbons: the Phenomenon of Maximum Rates," *J. Am. Chem. Soc.*, Vol. 72, p. 1942, 1950.
12. Carlsson, D. J., and Wiles, D. M., "The Photodegradation of Polypropylene Films. II. Photolysis of Ketonic Oxidation Products," *Macromol.*, Vol. 2, p. 587, 1969.
13. Bevilacqua, E. M., *Autoxidation and Antioxidants*, Vol. II, p. 857. Edited by W. O. Sundberg. Interscience Publishers, New York, 1961.

B. The Molecular-Sieve Catalyzed Polymerization of Isobutylene, *R. A. Rhein*

1. Introduction

This effort was initiated when J. A. Miller (SPS 37-58, Vol. III, pp. 194–199) discussed the preparation of polymers of isobutylene with higher-than-unity unsaturation/mole by catalysis with a 5Å molecular sieve. The objective of this effort was the preparation of poly(isobutylene) α,ω-diols having number-average molecular weights in the range 1000–2000. The reason for choosing this objective is that solid propellant prepolymers must exhibit minimum reactivity with propellant oxidizers, be of maximum molecular weight (yet of low bulk viscosity), and yield cured solid propellants with minimal temperature dependence of mechanical properties. The polymer must be terminally difunctional so that it can be chain-extended after the oxidizer is incorporated. Poly(isobutylene) α,ω-diol apparently satisfies the above requirements, but it has been difficult to prepare.

Poly(isobutylene) α,ω-diol of number-average molecular weight 2850 was prepared (Refs. 1 and 2) by the ozonolysis (and subsequent reduction) of butyl rubber containing 2 mol % isoprene. Evidence for the preparation of the terminal poly(isobutylene) diene by the $VOCl_3$-naphalene catalyzed polymerization of isobutylene was presented by Yamada, Shimada, and Hayashi (Ref. 3). However, further investigation by J. D. Ingham[1] indicated that although there was evidence for higher-than-unity unsaturation, it could not be conclusively shown that the poly(isobutylene) diene was prepared. However, Miller (Ref. 1) reported the preparation of the terminal poly(isobutylene) diene by the molecular-sieve (5A) catalyzed polymerization of isobutylene at ambient temperature and at 0°C, and for reaction time from 1 to 11 days.

There are only two other reports of molecular-sieve catalyzed polymerization of isobutylene. Norton (Ref. 4)

---

[1] SPS 37-45, Vol. IV, pp. 113–115 and SPS 37-52, Vol. III, pp. 97–98.

stated that isobutylene polymerized more readily than did propylene of ethylene, and that the order of sieve reactivities toward propylene polymerization was

$$10X > 13X > 5A > 4A > 3A = 0$$

but there was no discussion of the isobutylene polymerization products. Gensheimer and Brown (Ref. 5) reported that a molecular sieve of 5A (and also 4A, 10X, and 13X) pore size could polymerize isobutylene to di(isobutylene) and higher polymers. However, if the sieve was preheated in an inert oxygen-free gas, it would polymerize isobutylene to di(isobutylene) to the extent of 1–3%.

In this work, a variety of molecular sieves and conditions of temperature and reaction time were employed for isobutylene polymerization catalysis. The products were primarily low-boiling telomers, but polymers were formed in nearly every case. The pore diameters of the most common commercially available molecular sieves used in this work are type 3A, 3Å; type 4A, 4.2Å; 5A, 5Å; 10X, 8Å, and 13X, 10Å.

Other molecular sieves used as catalysts (Linde Division of Union Carbide Corp.) were SK45, a potassium-exchanged type L; SK100, decationized type Y with 0.5% Pd; SK110, partly decationized type Y with 5.2% MnO and 0.5% Pd; SK200, calcium-exchanged type Y with 0.5% Pt; SK310, calcium-exchanged type Y with 0.5% Pd; SK400, sodium-exchanged type Y with 1.0% Ni; SK410, sodium-exchanged type Y with 1.0% Ni; and SK500, type Y with 35% cations, 15% Na_2O, and 50% mixed rare-earth oxides.

2. Experimental

Although a variety of experimental methods and approaches were employed, there were features common to all of the experiments. In all cases, 75 ml of isobutylene are added to 25 g of molecular sieve (pretreated by heating to 100–300°C and evacuating to $\leqq 10^{-3}$ torr for $\geqq 1$ day) in a 250-ml bulb. With only one exception (0°C), the reaction temperature was ambient (generally around 25°C).

After the reaction period, the reaction bulb was then opened to a cooled graduated tube, in which nonreacted isobutylene was collected and its volume measured. The products in the reaction bulb were washed with several portions of *n*-pentane. Then the mixture of pentane and reaction products, in either a 500-ml beaker or a 500-ml Ehrlenmeyer flask, was opened to the atmosphere for a period of 1–4 days to permit the pentane to evaporate. There was also some loss of volatile reaction products, but this was taken into account.[2]

The resulting liquid product was then heated to approximately 150°C and evacuated to approximately 50 μm for a period of 1–3 days; the distillates were collected, either in a trap cooled to −196°C or in a series of two traps, and one was cooled to 0°C and the other to −196°C. For the volatile distillate mixtures, the index of refraction and infrared spectrum were obtained and the mixtures then analyzed by gas chromatography for isobutylene telomers.

For the polymer residue, the index of refraction, the infrared spectrum, and the gel permeation chromatogram were obtained.

The volatile reaction products also were determined by gas chromatography. The chromatograph consisted of a Consolidated Electrodynamics Corp. 26-014 analyzer and 26-002 control unit. The column used was aluminum tubing 5 ft in length by ¼ in. in diameter and contained 10% SE-30 on 60/80 mesh Chromasorb-W. The carrier gas was helium at a flow rate of 40 ml/min. To calibrate the chromatograph, di(isobutylene) 1:4 isomer mixture (terminal/chain alkene), tri(isobutylene), and tetra(isobutylene) were used. In several gas chromatography analyses, a peak beyond that for tetra(isobutylene) was observed; this peak was attributed to penta(isobutylene). The optimum column temperature was found to be 235°C for separation of the isobutylene telomers.

3. Results

The experimental reaction conditions and results are shown in Table 1. The polymers were characterized by the gel-permeation chromatogram and infrared spectrum. The number-average molecular weights, the weight-average molecular weights, and also the peak molecular weight(s) were obtained from the gel-permeation chromatogram. The peak molecular weights, corresponding to peaks in the gel-permeation chromatogram, are represented by the maxima in the molecular weight versus weight-percent distribution.

---

[2] It was generally found that the sum of the reaction products and unreacted isobutylene was less than that of the initial isobutylene. The difference was assumed to be di(isobutylene) that evaporated along with the pentane. A brief experiment indicated that tri(isobutylene) evaporated at approximately 1/10 the rate of di(isobutylene); since generally only a few grams of di(isobutylene) evaporated, the evaporation of tri(isobutylene) and higher homologues was not considered.

Table 1. Experimental conditions and results

Molecular sieve type and size	Reaction time, days	Stirring	Unreacted isobutylene	Percent yield of polymer	Number-average molecular weight M_n	Weight average molecular weight M_w	Peak molecular weights	$M_n \times A(6.1\ \mu m)$
3A, 1/16 Pellets	7	No	100	0				
4A, 100/120 Mesh	7	No	100	0				
5A, 1/16 Pellets	10	No	0	22.7	555	1325	305, 1186	28
5A, 40/50 Mesh	4	Yes	0	54.3	350	[b]	250, 1310	32
5A, 40/50 Mesh	4	Yes	0	52.6	322	1032	250, 1600	31
5A, 40/50 Mesh	10	No	0	18.9	515	1264	291, 1302	24
5A, 80/90 Mesh	10	No	0	43.6	469	1397	277, 1302	29
5A, 120/130 Mesh	4	Yes	0	56.3	526	1641	250, 1680	35
5A, 160/170 Mesh	10	No	0	48.7	663	1963	302, 1725	33
5A, 160/170 Mesh	1	Yes	0	9.6	1241	3669	535, 1985	45
5A, 160/170 Mesh[a]	1	Yes	0	8.0	1229	3438	487, 2888	36
5A Powder, 1-4 μm	10	No	0	0				
10X, 100/120 Mesh	7	No	0	4.5	300	480	290	23
10X, 100/120 Mesh	9	Yes	0	3.9	575	1390	345	39
13X, 100/110 Mesh	7	No	50	7.8	2569	5989	4836	48
13X, 100/110 Mesh	9	Yes	13.3	10.9	1140	4896	320, 4050	87
SK45 Powder, 1–4 μm	5	Yes	[b]	[b]	839	2566	385, 3027	155
SK45 Powder, 1–4 μm	9	Yes	76.0	0.2	1417	3292	3151	139
SK100 1/16 Pellets	5	Yes	[b]	[b]	315	365	291	12
SK100	9	Yes	0	5.6	639	1830	367	26
SK110	3	Yes	[b]	[b]	982	2164	535	31
SK110	9	Yes	0	4.4	832	1950	462	16
SK200	3	Yes	[b]	[b]	781	1232	560	35
SK200	9	Yes	0	0.5	564	1124	440	22
SK310	3	Yes	0	1.2	457	761	351	27
SK400	3	Yes	60	2.2	448	2114	240, 3027	87
SK400	9	Yes	66.6	2.5	1233	3807	464, 3800	52
SK410	3	Yes	80	0				
SK500	3	Yes	0	2.0	610	1608	404	21

[a] Polymerized at 0°C. All others polymerized at room temperature.

[b] Not determined.

From the infrared absorbances at wavelengths very near 6.1, 11, and 12 μm, an estimation of the type of unsaturation, i.e., terminal, (1-olefin), or internal (2-methyl-2-olefin), and a qualitative notion of the degree of unsaturation were obtained. The data for the polymers presented in Table 1 include the number-average, weight-average, and peak molecular weight, the parameter $M_n \times A\,(6.1\ \mu\mathrm{m})$, which is approximately proportional to the degree of unsaturation, the weight-percent polymer yield (based upon the initial monomer weight), the number-average molecular weight of the polymer, and the percent monomer that reacted.

4. Discussion

From the experimental conditions, the character of the molecular sieves and the nature of the reaction products (Table 1) comparative relationships between the experimental variables and the reaction products were obtained. The dependent variables considered were the degree of unsaturation, the weight percent polymer yield, the number-average molecular weight of the polymer, and the percent monomer that reacted.

The following were regarded as independent variables: pore diameter (of the molecular sieve), the exchanged cation, the type of molecular sieve, the metal catalyst on the molecular sieve, the particle size of the molecular sieve, the polymerization temperature, the reaction time, the effect of stirring the reactants, and the effects of various methods of processing the molecular sieve prior to its use as catalyst. Table 2 presents the qualitative relationship between each of the dependent variables to each of the independent variables in this work. The information presented in Table 2 can only be regarded as tentative; in many cases, further effort is required to establish these relationships to a reasonable certainty.

a. Type of molecular sieve. Four types of molecular sieves, A, X, Y, and L were used, representing three types of crystal structures. Types X and Y have the same skeletal structure, but type Y has more cation vacancies. It is difficult to assign the characteristics of the reaction products to the type of molecular sieve, due to the influence of other factors, such as pore diameter.

Apparently the highest polymer yields, as well as complete conversion of isobutylene to telomers and polymers, are produced by the use of 5A molecular sieve, although 3A and 4A sieves induce no reaction at all. Although rather low yields resulted from the use of type L molecular sieve, the polymers that resulted apparently had the highest degree of unsaturation and high polymer molecular weights.

b. Pore diameter. The pore diameters for the molecular sieves for types 3A, 4A, 5A, 10X, and 13X molecular sieves are 3, 4.2, 5, 8, and 10Å, respectively. SK45, the potassium cation form of type L, has a pore diameter of 9.1Å. The molecular sieves of SK designation are type Y, which may have a pore diameter of about 10Å. It was observed that no reaction occurs with pore diameter $<$5Å. The maximum polymer yield is obtained at 5Å. Polymer was produced with pore size $>$5Å. The degree of unsaturation, and the polymer molecular weight apparently increase with increasing pore diameters. Consequently, the polymerization reaction presumably takes place or is initiated within the cavity of the molecular sieve.

c. Nature of cation. Since isobutylene reportedly only polymerizes by a cationic mechanism (Ref. 7), it is assumed here that isobutylene is polymerized by cationic sites within the molecular sieve cavity. It was found that the percent polymer yield, and the percent isobutylene reacted were greatest for the molecular sieves with cationic exchanged sites and least for the sodium and potassium forms. However, the sodium and potassium forms produced the highest degree of unsaturation. Also, reasonable yields were obtained by the use of 13X molecular sieve (a sodium form). The monovalent metal cationic forms of types X and Y, however, tend to promote radical-type reaction intermediates. Hence the interesting speculation arises as to what effect radical processes may have on producing a higher degree of unsaturation in the polymer.

d. Effect of metal catalyst. For increase in polymer yield and isobutylene reacted, the effect of palladium was found to be greater than that of platinum, and that of nickel greater than of copper, when these metals were loaded in type Y molecular sieves. However, the use of platinum resulted in a higher polymer molecular weight than did palladium. Platinum and palladium had about the same effect on the degree of unsaturation.

e. Effects of reaction temperature, reaction time, and molecular sieve particle size. These parameters were not investigated thoroughly, so many of the observations must be regarded as tentative. It was noted that with decreasing particle size, an increase was observed in the degree of unsaturation and polymer molecular weight.

Table 2. Parameters influencing the characteristics of the reaction products from the molecular-sieve-catalyzed polymerization of isobutylene

Independent variable	Dependent variable			
	Degree of unsaturation	Percent polymer yield	Polymer molecular wt M_n	Percent isobutylene reacted
Pore diameter	Increasing with increasing pore diameter	No yield $\leqq$ 4.2Å maximum at 5Å	Increasing with increasing pore diameter	None $\leqq$ 4.2Å; maximum 5–8Å, above 8A decreasing yield with increasing pore size
Exchanged cation	Apparently $K_2O > Na_2O > CaO >$ cations $>$ rare earths	Generally cations $>$ cations $+ MnO > Na_2O > (Na_2O +$ cations rare earth oxides$) > CaO$	Generally (cations $+ MnO) \sim Na_2O > CaO >$ (cations $+ Na_2O +$ rare earth oxides) $>$ cations	Generally (cations) $\sim$ (cations $+ MaO) \sim CaO \sim (Na_2O +$ cations $+$ rare earth oxides) $> Na_2O$
Type of sieve	Generally $L > X > A > Y$	$A > X > Y > L$	$L > Y$, $L > A$, otherwise indeterminate	$A \geqq Y \geqq X > L$
Catalyst on sieve	$Pt \sim Pd$	$Pd > Pt, Ni > Cu$	$Pt > Pd$	$Pt = Pd, Ni > Cu$
Particle size	Increasing with decreasing particle size	Irregular trend toward increasing yield for decreasing size	Irregular trend toward increasing Mn for decreasing particle size	Indeterminate
Temperature	Indeterminate	Indeterminate	Indeterminate	Indeterminate
Time of reaction	Can increase or decrease, depending upon other variables	Generally increasing with increasing reaction time	Generally increasing, but can decrease under some conditions	Evidence for increasing for increasing time
Effect of stirring	Ambiguous, but apparently increases unsaturation	Stirring apparently increases polymer yield	Somewhat indeterminate, but stirring can increase Mn	Apparently stirring increases the percent C_{48} that reacts
Effect of the processing of the molecular sieve	Indication that slightly higher unsaturation with higher processing temperature	Indication of slightly greater polymer yield with higher processing temperature	Indication of somewhat higher mol. wt. with increasing processing temperature	Insufficient data

An increase in reaction time generally resulted in an increased yield of polymer, a higher polymer molecular weight and an increasing conversion of isobutylene to telomers and polymers. These results indicate that the polymerization reaction was very slow, and in all probability none of the polymerizations went to completion. Finally, it was observed that a variety of preliminary processing methods for the molecular sieves did not result in appreciable changes in the catalytic properties, so evidently all of the methods resulted in satisfactory dehydration and/or degassing of the molecular sieves.

f. Discussion of unsaturation. The presence of unsaturation can be determined from the absorption bands observed at 6.1 μm ($C{=}C$ stretch), at 11.00–11.30 μm (C—H bending vibrations of the pendant vinyl group, ($C{=}H_2$), and at 12.05 μm (C—H bending of the 2-methyl-2-ene terminal groups (Ref. 8, pp. 370, 378–379, and Ref. 9, pp. 33, 154–155).

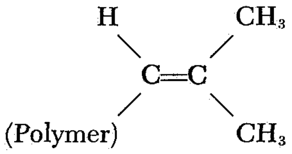

Attempts by the author to correlate the unsaturation/mole, for a wide variety of alkenes and nonconjugated dienes, to be absorbences at 6.1, 11, and 12 μm (0.025-mm cell) met with rather limited success. Consequently, rather than tabulating the estimated unsaturation/mole, the parameters $M_n \times A$ (6.1 μm) (the number-average molecular weight multiplied by the absorbence at 6.1 μm) were tabulated. This parameter is approximately proportional to the unsaturation/mole. To get some notion as the "expected" values of $M_n \times A$ (6.1 μm), these parameters were computed for a series of commercially available poly(isobutylene) "polybutenes" (Chevron Chemical Co.). The commercial polybutenes are mono-unsaturated.[3] Although the nature of the terminal unsaturation of the polybutenes is somewhat different from that of poly(isobutylene); since these were prepared in the presence of 1-butene, comparisons can be made between the parameter $M_n \times A$ (6.1 μm), for the commercial polymers and for the polymers produced in this work. For commercial polymers, this parameter ranged from 11 to 27, averaging 17.5. However, virtually all the polymers produced by molecular sieve catalysis had values for that parameter exceeding 17.5. From SK45 the values obtained were 155, 139; from 13X they were 48, 87; and from SK400 they were 87, 52. Consequently, there is definite indication of higher than unity unsaturation of isobutylene polymers produced from monocation molecular sieves.

5. Conclusions

Types A, X, Y, and L molecular sieves have served as catalysts for the polymerization of isobutylene. In all cases, the polymerization reaction was relatively slow. Divalent cation exchanged and decationized molecular sieves produced higher yields of polymer than did monovalent cation sieves, but the latter produced polymers with higher degrees of unsaturation. No polymerization was observed for 3A and 4A molecular sieves, implying that a minimum pore size (approximately 5Å) is required for polymerization. Hence, the polymerization evidently occurs within the cavities of the molecular sieve structure.

A comparison of the olefinic infrared absorbence of the polymers produced by molecular sieve catalysis with that of commercially available polymers provided evidence that a higher than unity unsaturation was achieved. Further work will be carried out to obtain polymers with high unsaturation at reasonable yields for endgroup modification, chain extension, and crosslinking.

References

1. Jones, E. B., and Marvel, C. S., "α,ω-Glycols From Isobutylene and Some Derived Block Copolymers," *J. Polymer Science*, Vol. A2, pp. 5313–5318, 1964.
2. Shubbs, W. H., Gore, C. R., and Marvel, C. S., "α,ω-Glycols From Polyisobutylene," *J. Polymer Sci.*, Part A1, Vol. 4, p. 447, 1966.
3. Yamada, N., Shimada, K., and Hayashi, T., *J. Polymer Sci.*, Series B, Vol. 4, pp. 447–480, 1966.
4. Norton, C. J., "Olefin Polymerization Over Synthetic Molecular Sieve," *I. and E. C. Process Design and Development*, Vol. 3, No. 3, pp. 230–236, July 1964.
5. Gensheimer, D. E., and Brown, E. C., "Isobutylene Purification Using a Pre-Treated Zeolitic Molecular Sieve." U. S. Patent 3,061,654 issued to the Esso Corp., Oct. 20, 1962.
6. "Linde Molecular Sieves," Technical Bulletin F-1979B. Union Carbide Corp., Linde Division.
7. Schildknecht, C. E., "Vinyl and Related Polymers," Chapt. 10. John Wiley and Sons, Inc., New York, 1952.
8. West, W., *Technique of Organic Chemistry, Vol. IX. Chemical Applications of Spectroscopy*, Interscience Publishers, Inc., New York, 1956.
9. Haslem, J., and Willis, H. A., "Identification and Analysis of Plastics," D. Van Nostrand and Co., Princeton, N. J., 1965.

---

[3] Detert, F. L., Chevron Chemical Co., personal communication.

C. Investigation of Sterilizable Battery Separator Membranes, *E. F. Cuddihy, D. E. Walmsley, and J. Moacanin*

1. Introduction

Thin films of polyethylene unto which has been grafted poly(potassium acrylate) are being employed as battery separator membranes in sterilizable silver–zinc batteries. Studies of the chemical and physical properties of these films have been previously reported (SPS 37-50, -52, -54, -56, -59, and -61, Vol. III). Current investigations are concerned with the stability of these films to battery electrolyte and soluble silver; this article provides an update of our studies in this area.

2. Background

Silver–zinc batteries employ as an electrolyte a solution of 40% KOH in water which becomes strongly oxidative by the presence of silver ion, which dissolves (40–50 mg Ag^+/liter) from the silver electrode. The stability studies are concerned with the influence of this electrolyte on the films which acts to limit their lifetime as battery separators.

So far, previous work (SPS 37-59, -61, Vol. III) has demonstrated that exposure of the separator to this strongly oxidative–caustic environment results in a loss of poly(potassium acrylate) PKA from the films, along with a corresponding accumulation of deposits of metallic silver and silver oxide. Total PKA losses have been observed to occur by two mechanisms, one a portion extractable by KOH and the remainder from oxidative degrafting, which also results in the accumulation of the reduced metallic silver. Silver oxide deposition is not completely explained, but appears to be related to the level of unsaturation in polyethylene.

Studies are continuing in efforts to identify additional interaction and problem areas between the film and electrolyte. Kinetic studies on the known interaction have been initiated (SPS 37-59, -60, Vol. III) and are continuing. These studies are intended to explain the mechanism of interaction and provide direction for minimizing or eliminating these problem areas. Additionally, the kinetic studies will permit an estimate of the service lifetime of these separators, which is limited by either a critical loss of PKA or sufficient deposition of silver products to render the films electrically conducting.

3. Update on Kinetic Studies

The interaction between the separators and the electrolyte is being monitored by following the PKA loss as a function of time, from both sterilized and unsterilized separator samples exposed at 50, 65, 80, and 95°C to 45% KOH electrolyte and silver-oxide-saturated 45% KOH solutions. For exposure to the latter solution, the amounts of deposited silver and silver oxide are also being monitored.

Table 1 and Fig. 1 present the results to date for exposure at 95°C to 45% KOH solution. After 3712 h, an unsterilized separator has lost 24 wt % of its initial PKA, with the curve in Fig. 1 indicating that complete removal of the KOH-extractable PKA has not yet been achieved. Data for a sterilized sample is also given. Sterilization of the membranes by exposure to 45% KOH for 120 h at 135°C results in extraction of approximately 19 wt % PKA. The data shown are for subsequent PKA losses at the lower

Table 1. Loss of potassium acrylate from GX-152 membranes exposed at 95°C to a 45% KOH solution

Unsterilized		Sterilized[a]	
Time, h	Loss of initial PKA, %	Time, h	Loss of initial PKA, %
21	3	272	2
162	12	679	5
812	17	1296	7
1796	20		
2695	22		
3712	24		

[a] Sterilized by exposure to 45% KOH solution at 135°C for 120 h, which resulted in a loss of 19 wt % of initial potassium acrylate. Values shown are subsequent losses from the continued exposure at the lower temperature of 95°C. Actual total losses from the combined exposures are the values shown plus 19%.

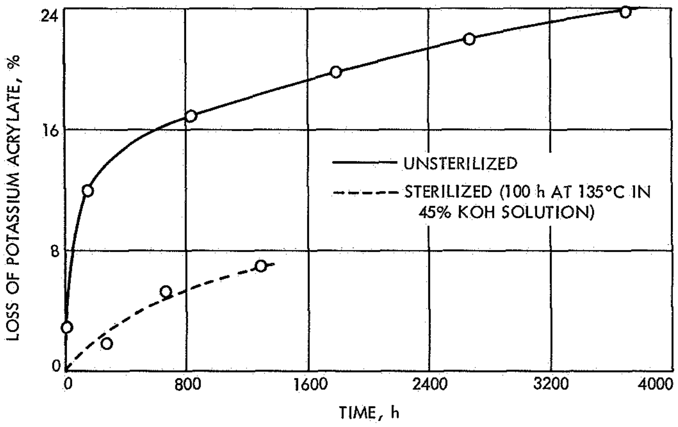

Fig. 1. Loss of potassium acrylate from GX-152 membranes exposed at 95°C to a 45% KOH solution

Table 2. Results of exposure of GX-152 membranes to silver-oxide-saturated 45% KOH solution at 95°C

Item	Sterilized membranes							Unsterilized membranes				
Exposure time, h	20	57	69	316	800	1728	3150	69	316	336	1460	3476
Loss of initial potassium acrylate, %	20	22	15	22	35	52	60	22	33	41	44	46
Total gain of deposited silver products initial potassium acrylate, wt %	14	16	21	104	57	68	185	27	49	50	93	142
Ag^0, %	72	92	66	95	83	92	94	68	92	85	86	91
Ag^+, %	28	8	34	5	17	8	6	32	8	15	14	9
Potassium acrylate lost/Ag^0 deposited, equivalence ratio	0.62	1.5	1.0	0.21	0.61	0.62	0.35	1.2	0.74	1.0	0.53	0.34

temperature of 95°C. After 1296 h, the separator loses an additional 7 wt % PKA for a total of 26 wt % loss from both sterilization and continued exposure at 95°C. Again the curve for PKA loss from the sterilized separator (Fig. 1) indicates that complete removal of the KOH-extractable PKA has not yet been achieved.

PKA losses from sterilized and unsterilized separator samples exposed at 95°C to silver-oxide-saturated 45% KOH solutions are given in Table 2, with Fig. 2 being a plot of the PKA losses from the sterilized samples. The PKA losses given for the sterilized samples are percentages based on the PKA remaining after sterilization. The intent is that, since sterilization removes the bulk of the KOH-extractable PKA, these percentages should reflect only the PKA loss by the oxidation reaction with the silver ion. The semi-log plot in Fig. 2 suggests a first-order kinetic oxidation reaction between silver and PKA, with the curvature most likely attributable to some continued removal of extractable PKA.

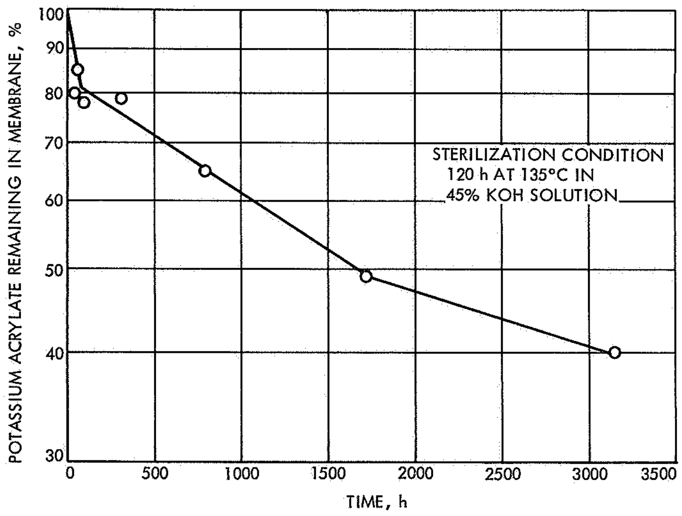

Fig. 2. Loss of potassium acrylate from sterilized membranes exposed to a silver-oxide-saturated 45% KOH solution at 95°C

For the unsterilized samples, the initial rates of PKA loss (up to 316 h) are predictably higher (SPS 37-61, Vol. III) than those of the sterilized samples by an amount corresponding to the additional KOH-extractable PKA present in the unsterilized samples. Above 316 h, the rate of PKA loss from the unsterilized sample slows significantly as compared to the sterilized sample, an effect not yet explained.

Information on silver products deposition is also given in Table 2, where it is seen that the amounts of deposit increase as expected with increasing exposure time. Metallic silver accounts for more than 70% of the deposits in the initial stages of exposure and climbs to in excess of 90% as exposure continues.

Some preliminary data on exposure of unsterilized membranes to silver-oxide-saturated 45% KOH solution at 80 and 65°C are given in Table 3. The rate of PKA lost decreases as expected with decreasing temperature. An

Table 3. Results of exposure of unsterilized GX-152 membrane to silver-oxide-saturated 45% KOH solution at 80 and 65°C

Item	80°C		65°C	
Exposure time, h	263	1224	912	1643
Loss of initial potassium acrylate, %	25	39	1.4	26
Total gain of deposited silver products				
Initial potassium acrylate, wt %	20	31	24	19
Ag^0, %	69	77	57	50
Ag^+, %	31	23	43	50
Potassium acrylate loss/Ag^0 deposited, equivalence ratio	1.8	1.6	0.09	2.8

interesting observation is that the percentage of deposits occurring as metallic silver decreases with decreasing temperatures, but this just may be an artifact resulting from a slower oxidation reaction between silver ion and PKA.

Kinetic studies to longer times plus additional information on KOH extraction at temperatures below 95°C are in progress.

4. Cell Resistance

In service, the membranes are positioned between the silver and zinc electrodes, with their primary function intended to prevent soluble silver from reaching the zinc electrode while permitting ready permeation of the KOH. Because of their placement directly between the electrodes, these films can have a direct effect on cell performance by altering the internal cell resistance as a result of losses of PKA or accumulation of deposits.

Cell resistance is the resistance in ohms measured across a silver and zinc electrode while immersed in standard 40% KOH battery electrolyte. Increases in cell resistance are observed when a battery separator is positioned between the two electrodes, with the differential increase in resistance above the separator-free cell being considered the separator cell resistance. Values of separator cell resistance in $\Omega/\text{in.}^2$ are given in Table 4 for an unsterilized and sterilized membrane, and for a membrane after 200-h exposure at 95°C in silver-oxide-saturated 45% KOH solution. For this latter sample, all of the deposited silver was removed so the separator cell resistance would reflect only the effect of the decrease in the PKA content.

Table 4. Cell resistivities of GX-152 membranes

Sample	Area resistance, $\Omega/\text{in.}^2$
Unsterilized	0.01
Sterilized	0.03
Exposed 200 h at 95°C in silver-oxide-saturated 45% KOH solution	0.18

The unsterilized sample having a PKA content near 40 wt % has a separator cell resistance of 0.01 $\Omega/\text{in.}^2$, which after sterilization increased to 0.03 $\Omega/\text{in.}^2$. Sterilization removes about 19 wt % of KOH-extractable PKA. For the third sample, nearly 30 wt % of initial PKA was removed and the separator cell resistance increased to 0.18 $\Omega/\text{in.}^2$, an eighteen-fold increase above the initial membrane.

These results clearly show the increase in cell resistance and therefore determination of cell performance, which results from decreasing PKA content. Studies of the effects of filler from silver deposit are in progress.

5. Future Work

Continued studies on separator membranes will include microscopic examination of the film. This approach will provide fundamental information on the distribution of poly (potassium acrylate) across the polyethylene film as well as monitoring the changes in distribution as a function of exposure time to battery electrolyte. Such information will provide the clues for identifying the sites of PKA degrafting and extraction, and the extent of silver penetration in the chemical oxidation reaction. These studies should provide the framework for a logical modification of the system intended to minimize or eliminate some of the basic and critical problem areas.

D. Functionality of Isobutylene Prepolymers,

J. D. Ingham

1. Introduction

In previous articles, the preparation of isobutylene prepolymers for solid propellant applications and significance of the degree of functionality have been widely discussed (SPS 37-45, Vol. IV, pp. 113–115; SPS 37-52, Vol. IV, pp 97–98; SPS 37-58, Vol. III, pp. 194–199). The purpose of this article is to attempt to interpret available infrared-molecular weight data to arrive at more reliable estimates of the concentration of unsaturation and thus determine whether or not any of the poly(isobutylenes) prepared to date approach difunctionality with respect to unsaturation.

2. Discussion

The intensity of infrared absorption for $>C{=}C<$ stretch at 1630 cm^{-1} is extremely dependent on the types of groups attached to the carbon atoms. The intensity decreases drastically with increased molecular symmetry. For example, the intensity ratios for the model compounds 2, 4, 4-trimethyl-1-pentene (I), 2, 4, 4-trimethyl-1-2-pentene (II), and 2,3,4-trimethyl-2-pentene (III) are 1: 0.35: 0.14 (Ref. 1).

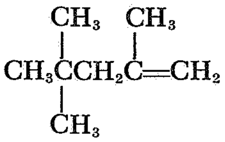

$$\underset{CH_3}{\overset{CH_3}{CH_3C}}CH_2\overset{CH_3}{C}{=}CH_2$$

I

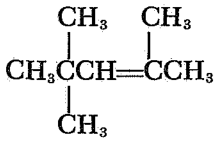

$$\underset{CH_3}{\overset{CH_3}{CH_3C}}CH{=}\overset{CH_3}{C}CH_3$$

II

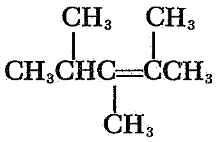

$$\overset{CH_3}{CH_3CH}\underset{CH_3}{\overset{CH_3}{C}}{=}CCH_3$$

III

Furthermore, ethylene (IV) and trans-dichloroethylene (V) are symmetrical and exhibit no infrared absorption near 1630 cm^{-1}.

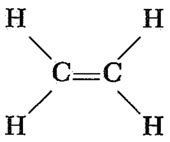

IV

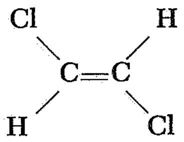

V

Therefore, unless the molecular structure in the vicinity of the double bonds is known, unsaturation determinations by infrared will not be accurate. However, it has been found empirically that there is a good correlation between unsaturation in poly(isobutylenes) determined by hydrogenation and by infrared at 1630 cm^{-1}. The infrared absorbance was used to calculate the concentration of unsaturation by applying the relationship between the known concentration and absorbance for a poly(butadiene) containing 34% 1, 2-vinyl, 38% 1, 4-trans, and 28% 1, 4-cis unsaturation. Also, determinations of unsaturation type and concentration have been effectively carried out by nuclear magnetic resonance (NMR) measurements (SPS 37-58, Vol. III, pp. 194–199).

Some typical data obtained in recent work is shown in Fig. 1, in which absorbance versus $(1/M_n)10^3$ is plotted. Line A is based on the absorbance: unsaturation concentration relationship for poly(butadiene), calculated to correspond to the absorbancies that should be observed for the reciprocal number average molecular weights (or concentration of unsaturation) for monofunctional isobutylene polymers. Line B was calculated similarly with the absorbancies increased by a factor of two to correspond to

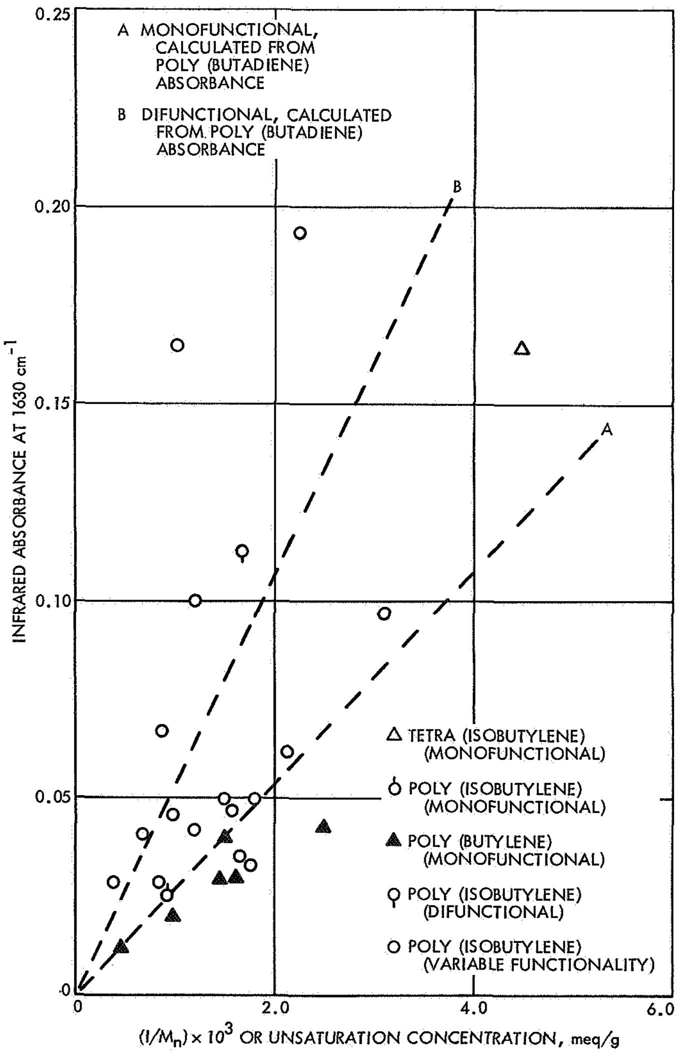

Fig. 1. Absorbance versus reciprocal number average molecular weight M_n for butylene polymers

a difunctional polymer. It can be seen that poly(isobutylene) that was monofunctional by hydrogenation measurements (SPS 37-52, Vol. IV, pp. 97–98) falls on line A and a polymer that was determined to be difunctional by NMR (SPS 37-58, Vol. III, pp. 194–199) is slightly above line B. Also, tetraisobutylene and poly(butenes) that are monofunctional are near line A. The open circles are for poly(isobutylenes) prepared under different conditions by molecular sieve catalysis by R. A. Rhein (see Chapter XIV-B.) It appears that sufficient data on polymers of isobutylene of known functionality might give nonlinear reciprocal molecular weight–absorbance relationships, particularly at low molecular weights. In any case, poly(isobutylenes) with molecular weights between 600 and 2000 that fall above line B are likely to have functionalities of two or more. Therefore, polymers above line B that can be prepared readily in good yield, such as the one at absorbance 0.164, and $1/M_n$ of 0.99×10^{-3}, are good candidates for studies of chain extension. For the purposes of this work, chain extension capability is the best criterion for determining adequate difunctionality, although it appears that infrared is the best method available for screening and selecting potentially useful poly(isobutylene) prepolymers. Careful hydrogenation and NMR methods are reliable for determinations of unsaturation; however, both of these are time-consuming and not suitable for routine measurements at the present time.

Reference

1. Bellamy, L. J., *The Infrared Spectra of Complex Molecules*, p. 39. John Wiley & Sons, Inc., New York, 1960.

E. Evaluation of Spacecraft Magnetic Recording Tapes, *S. H. Kalfayan, R. H. Silver, and J. K. Hoffman*[1]

1. Introduction

The study of magnetic tape to head interactions is continued. Data were reported previously (SPS 37-63, Vol. III, pp. 209–214) for the dynamic frictional behavior of three different tapes under various conditions. These three tapes, namely 3M 990, 3M 20250, and CEC W-4 were evaluated at 25 and 55°C and 0.133 and 0.333 ips speeds, under dry and humid conditions. Results of these experiments, Series A, showed, among other things, that the CEC W-4 tape was much more susceptible to environmental changes than the other two. Of the remaining two, 3M 20250 showed marginal advantages over 3M 990. Based upon these findings, 3M 20250 tape was selected for further study. The present experiments, Series B, were carried out by means of a similar setup as in Series A, with the difference that *two* magnetic heads were used instead of five. The outstanding consequence of this change was that the $\mu\beta$ values (coefficient of friction μ, x angle, β) dropped considerably.

The Series B experiments were performed with the following objectives: (1) to establish an adequate "wait" or static contact period for type approval (TA) testing, and studying the relationship of the static contact to "sticking" of tape to magnetic head; and (2) to understand the effects of temperature and crosshead speed on the frictional and various other types of tape behavior. The two parameters, temperature and crosshead speed, were considered in Series A. Wider ranges of both parameters were used this time to establish more definite relationships. Also studied were the effects of tape degassing, a comparison of the Mylar side of the tape to the oxide-binder side relative to their "sticking" and frictional behavior, and the effect of the removal of oxide–binder on "postwait" sticking.

The type of response obtained from measurements of frictional forces when a tape is in dynamic contact with magnetic head is shown in Fig. 1. The ruggedness of these curves varies with such factors as temperature and the state of the tape, namely, new or used. The exact causes of this jaggedness is not understood, but the possibility that it may be a manifestation of the stick–slip phenomenon is not excluded. The instantaneous velocity of the tape would change because of stick–slip. It would be higher at slip and lower at near stick. This would change the output of the load cell, causing the peaks and valleys or the ruggedness in the force curve. Determining the instantaneous tape-to-head velocity would be very helpful in understanding the causes of this rugged pattern and possibly shed more light on the stick–slip phenomenon.

---

[1] Spacecraft Data Systems Section, Astrionics Division.

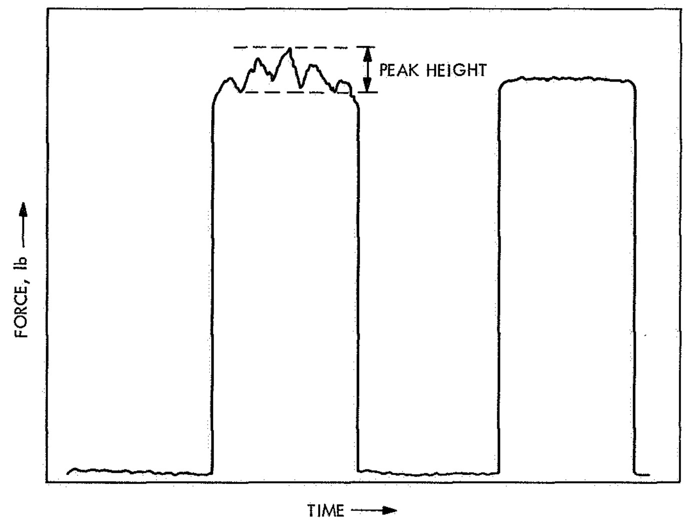

Fig. 1. Examples of rugged and smooth patterns from Instron graphs

2. Experimental Methods

The test method used for the determination of the coefficient of friction μ was based on ASTM D 1894-63, entitled "Coefficient of Friction of Plastic Films." This method was modified to take into account the tape contact or "wrap" angle. The equation for flexible band friction may be expressed as follows:

$$\log \frac{T_2}{T_1} = 0.434\,\mu\beta \qquad (1)$$

where

T_2 = force necessary to sustain motion

T_1 = supported weight (110 g)

μ = coefficient of sliding friction

β = angle of contact, or "wrap" angle, in radians

a. Test apparatus and procedure. The test apparatus used was described previously in SPS 37-63, Vol. III. This time, however, most of the tape samples were passed 100 times over 2 magnetic heads placed in a semicircular configuration. The dynamic tests were performed in dry argon, whereas the static tests were carried out in dry nitrogen, because the duration of such tests, up to 4–6 days, prohibited the use of the expensive argon. The size and shape of the tape samples and the make of the magnetic heads were the same as previously.

b. Gaseous atmosphere. No change in procedure for flushing the chamber with argon or nitrogen was made during the Series B experiments. All tests were carried out under dry conditions.

c. Degassing. Several tape samples were degassed at 65°C and 3×10^{-7} torr for 24 h to remove low molecular weight polymer fractions, plasticizers, etc., termed collectively volatile condensible materials. These tapes were then stored in sealed glass tubes, to be opened at the time of testing.

3. Results and Discussion

Except for one experiment where the effect of change of crosshead speed on μ was studied, all tests were carried out at 0.133 ips (8 ipm).

a. Effect of static contact of sticking, and determination of adequate "wait" period for TA testing. There were indications from previous tests that, when tapes were kept in contact with magnetic heads, adhesion sometimes occurred. This phenomenon could be easily detected with the instrument used, which is sensitive enough to measure the small force necessary to "peel" the adhering tape from the head. This force is over and above the normal dynamic frictional force.

For TA testing, the initial "wait" period prescribed was 12 days at 55°C. This length of time severely limited the number of tests. Establishing a shorter and yet still adequate "wait" period was considered. Consequently, samples of unused 3M 20250 tape were first passed a hundred times over the two magnetic heads in an atmosphere of argon at 55°C, and then kept in nitrogen at the same temperature for "wait" periods of 4, 24, 72, 96 and 144 h. The results are plotted in Fig. 2. $\Delta(\mu\beta)$ is the difference between the first $\mu\beta$ value obtained after the "wait" period and the last $\mu\beta$ value obtained before the "wait" period. As shown, these values were all positive, except for the 4-h wait period, which was zero. It was also observed that $\Delta(\mu\beta)$ was maximum after the 96-h "wait". Thus, a 12-day wait period was considered unnecessary, since after 96 h there was a leveling off of the $\Delta(\mu\beta)$ value.

Similar tests were also carried out at 25°C, with wait periods of 4, 8, 16, 24, 48, and 72 h. In all these cases, $\Delta(\mu\beta)$ values were negative, indicating that "waiting" in dry nitrogen at 25°C did not aggravate the "sticking" problem, as it did at 55°C. The results are shown in curve B of Fig. 2.

It must be pointed out that, although $\Delta(\mu\beta)$ values at 25°C were negative, the $\mu\beta$ of the first pass after the wait

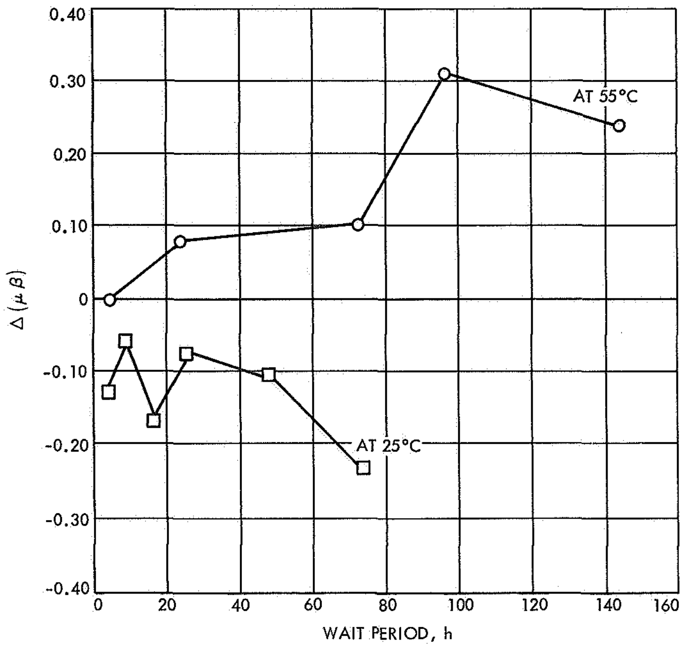

Fig. 2. Relationship of "wait" period to $\Delta(\mu\beta)$

period was still larger than the $\mu\beta$ values of the initial 8–10 passes of the "prewait" period. This might indicate that the tape is recovering, while resting at 25°C, from whatever damage it had undergone while passing over the magnetic heads a hundred times, but not recovering completely. It is shown in Fig. 3 that at 25°C the "postwait" $\mu\beta$ values increase gradually back to where they were just before the "wait". In the case of the runs at 55°C, the postwait $\mu\beta$ values start higher, decrease gradually to where they were just before "waiting," and then show signs of increasing. Curve envelopes are used instead of points in illustrating these to avoid the confusion that may be caused by crowding the figure with numerous points and curves.

The behavior of 3M 20250 new tape resting at 55°C suggests pronounced adhesion to the heads, probably due to the binder becoming tacky at points of contact with the magnetic heads. The tacky material probably is reduced by a wiping action as the tape is set into motion to explain the fact that $\mu\beta$ values decrease gradually before leveling, after the wait period.

b. Effect of temperature. Figure 3 shows the plots of $\mu\beta$ versus the number of passes, data that was obtained for the study discussed under *Subsection 3-a.* Instead of a multitude of curves, shaded areas are shown again. The upper band represents 6 runs (six curves) carried out at 25°C. The lower band represents 5 runs at 55°C. The extent of data scatter is estimable from the width of each band. It is obvious that data scatter was worse at 55°C.

These results confirm the previous finding that the coefficient of friction of new 3M 20250 is lower when tested at 55°C in argon, than at 25°C. One suggested explanation for this phenomenon is the increase of lubricity at the higher temperature, resulting in lower friction.

It would have been of interest to test used 3M 20250 tape, but because of limited supply, used 3M 990 tape was tested instead. Results of experiments carried out at 0, 30, and 55°C are given in Fig. 4a. It is seen that $\mu\beta$ increased with temperature for this kind of tape, again confirming what was indicated in Series A tests.

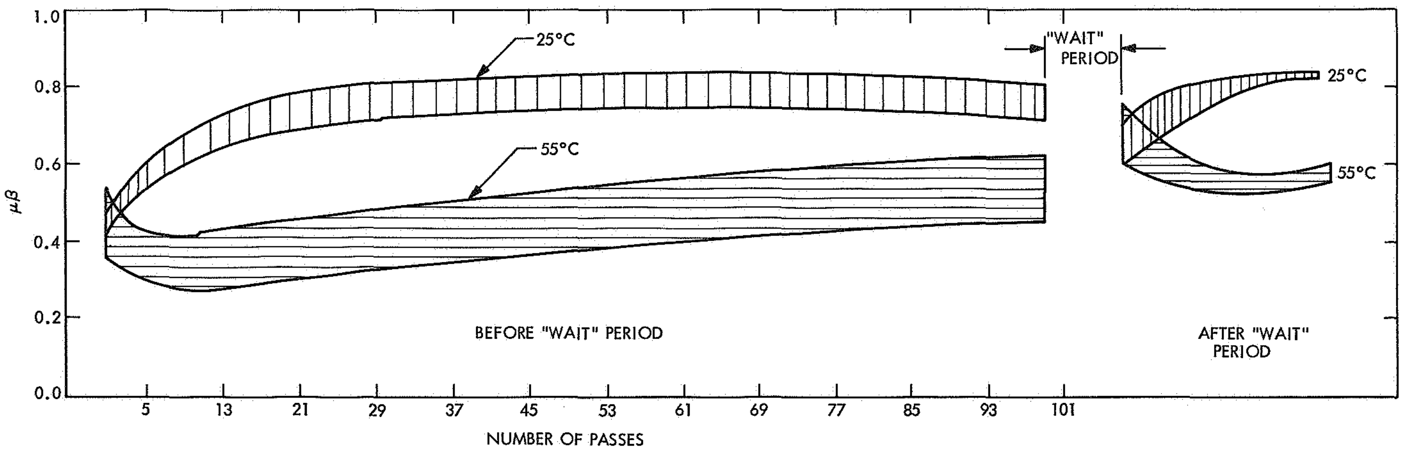

Fig. 3. Behavior of new 3M 20250 tape at 25 and 55°C, before and after "wait" period

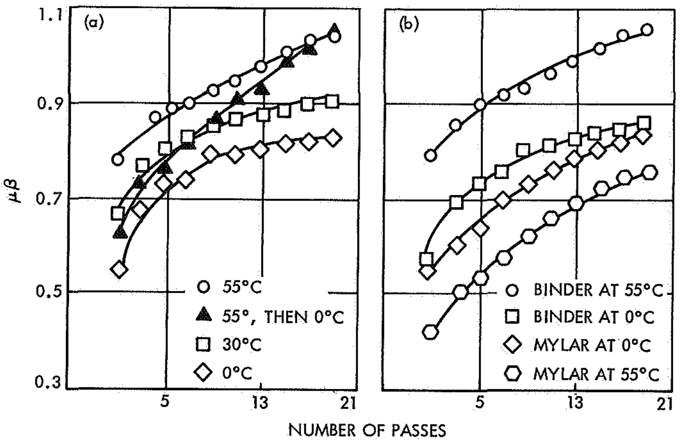

Fig. 4. Behavior of 3M 990 used tape: (a) temperature effect on $\mu\beta$; (b) comparison of mylar and binder sides

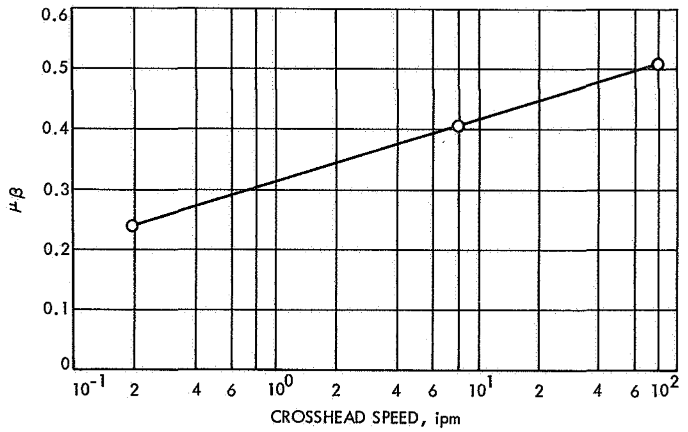

Fig. 5. Relationship of crosshead speed to coefficient of friction

An interesting observation was made when used 3M 990 tape that had undergone 20 passes at 55°C was rerun at 0°C. While $\mu\beta$ values started intermediate to values obtained at 0 and 30°C (Fig. 4), they increased to the same magnitude as obtained at 55°C. This indicates that a permanent change had occurred when the tape was run at 55°C.

c. Effect of crosshead speed. It was observed during Series A experiments that the effect of crosshead speed on new 3M 20250 was negligible when speeds varied from 0.133 to 0.333 ips (8 and 20 ipm). The effect of speed was studied again using a wider range: 0.0033, 0.133, and 1.33 ips (0.2, 8, and 80 ipm, respectively). When $\mu\beta$ values obtained were plotted against the logarithms of crosshead speeds, the straight line shown in Fig. 5 was obtained. Each of the $\mu\beta$ values plotted are averages of at least 5 values obtained from consecutive passes. These values were also corrected for the increase in $\mu\beta$ that would have been experienced normally. Thus, it is shown that μ increases with speed and the relationship is exponential.

d. Effect of degassing on performance. One sample of tape degassed for 24 h at 65°C and 3×10^{-7} torr was tested at 55°C. After the usual 100 passes, it was let stand 96 h. Figure 6 shows the results. The $\mu\beta$ curve showed the same pattern and values as undegassed samples, but unlike these, the $\Delta(\mu\beta)$ value was negative, showing that the degassed sample did not stick as badly as the undegassed samples. Its behavior, in this respect, was similar to samples run at 25°C.

e. Effect of removal of binder and oxide. Since results indicated strongly that adhesion of some sort occurred at 55°C between the binder–oxide side and the heads, tests were conducted with specimens of new tape from which the oxide and binder were removed in a 2-in. space where the magnetic heads rested during the "wait" period. Two specimens, one run at 25°C and the other at 55°C, showed negative $\Delta(\mu\beta)$ after 96-h "wait" periods. Results are shown in Fig. 6. This supported the contention that the binder–oxide combination was responsible for adhesion and in actual use a prelocated "window" would alleviate sticking. Instron graphs showed unusual ruggedness for specimens with windows, especially the sample tested at 55°C. Also, higher $\mu\beta$ values were obtained with these samples compared to standard ones, particularly near the end of the runs. A microscopic examination revealed excessive wear in the form of numerous tracks on the tape surface. It is quite possible that these tracks were caused by binder–oxide particles formed when "windows" were prepared by using solvents. The same particles could have roughened the tape or magnetic head surface, resulting in higher $\mu\beta$ values. Thus, although part of the tape in dynamic contact with the magnetic heads was bare Mylar and lower friction was expected, the opposite effect was observed because of the reason just cited.

f. Phenomenon of ruggedness in graphs. Ruggedness is estimated by measuring the peak heights on the graphs (Fig. 1). Since this height represents force and can be converted to $\mu\beta$ units, $\Delta_r(\mu\beta)$ represents ruggedness:

$$\Delta_r(\mu\beta) = (\mu\beta)_{\max} - (\mu\beta)_{\min}$$

Average ruggedness is estimated by subtracting the arithmetic average of all minimum points from those of all maximum points:

$$\Delta_r(\mu\beta)_{\text{av}} = (\mu\beta)_{\max\ \text{av}} - (\mu\beta)_{\min\ \text{av}}$$

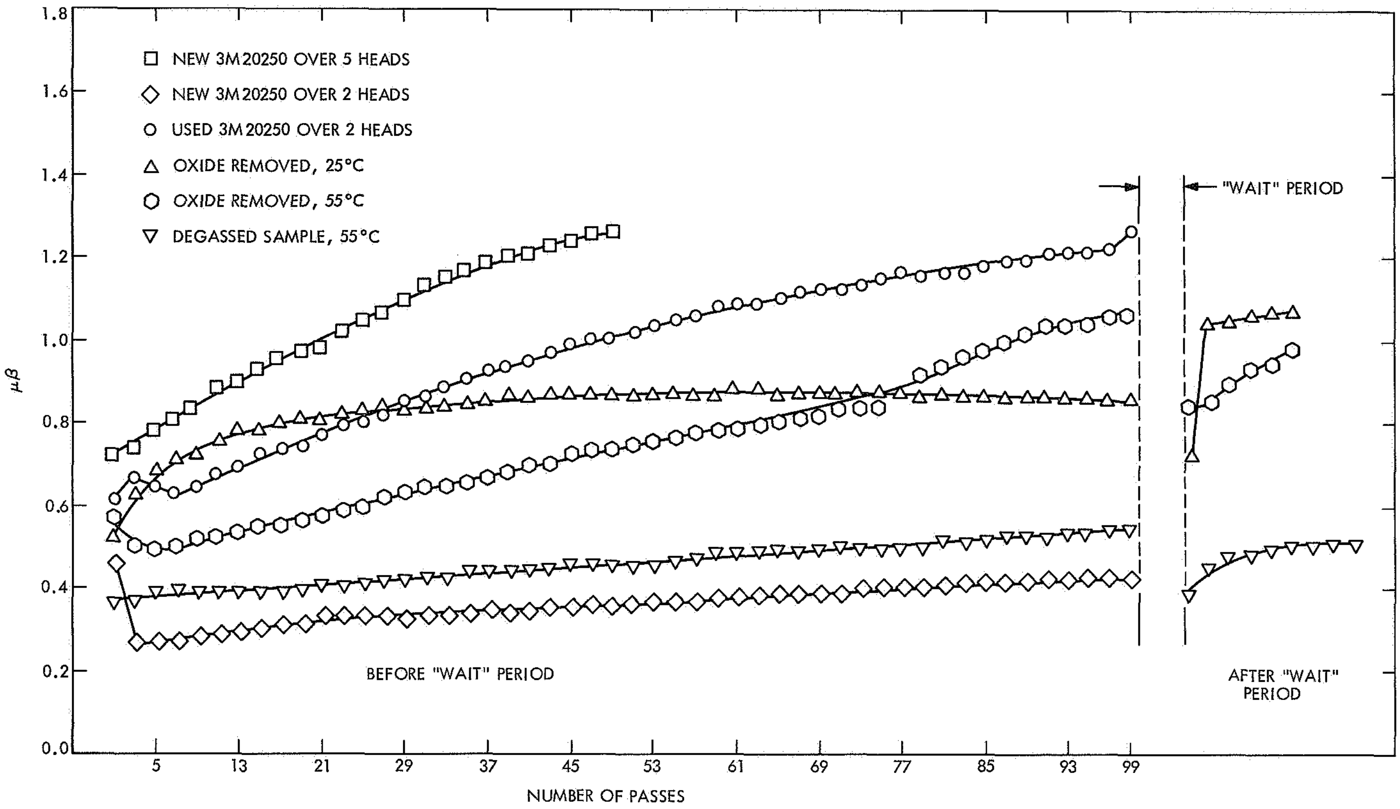

Fig. 6. Behavior of 3M 20250 tape under various conditions, before and after "wait" period

Examination of the graphs allows the following conclusions:

(1) For used 3M 990 tape, $\Delta_r(\mu\beta)_{av}$ increases with temperature. Tested at 0, 30, and 55°C, calculated $\Delta_r(\mu\beta)_{av}$ values were 0.041, 0.065, and 0.85, respectively.

(2) For new 3M 20250 tape on which "windows" were opened by removal of binder–oxide, calculated $\Delta_r(\mu\beta)_{av}$ values were 0.115 and 0.151 at 25 and 55°C, respectively. Thus, ruggedness was worse in this case than it was in the case of used 3M 990 tape. Again $\Delta_r(\mu\beta)_{av}$ increased with temperature.

(3) Comparison of new 3M 20250 with used tape gave the following $\Delta_r(\mu\beta)_{av}$ values, both kinds being tested at 55°C—used tape = 0.113, new tape = 0.040—showing that ruggedness was much more pronounced with the used tape.

(4) In the case of degassed new 3M 20250 samples, the temperature effect was reversed. At 25°C, $\Delta_r(\mu\beta)_{av}$ was 0.058 and, at 55°C, it was 0.031.

(5) With untreated new 3M 20250 samples, the temperature effect was similar to that of the degassed samples, i.e., $\Delta_r(\mu\beta)_{av}$ at 25°C tending to be higher than that at 55°C, but the differences were not as great.

g. Comparison of frictional behavior of binder side with Mylar side. Figure 4b shows the results obtained when the bare Mylar side of used 3M 990 tape, as well as its binder–oxide side, were tested at 0 and 55°C. Examination of the curves show that the Mylar side has lower $\mu\beta$ values than the binder side at both temperatures. This is not unexpected and the difference between $\mu\beta$'s of the two sides at 55°C is much more pronounced than at 0°C. Also notable is the fact that, whereas the binder at 0°C shows lower $\mu\beta$ values than at 55°C, the Mylar side shows the opposite behavior, registering lower $\mu\beta$ values at 55°C than at 0°C.

h. Used versus unused 3M 20250. Figure 6 shows the difference between the frictional behavior of used and new 3M 20250, tested at 55°C. The fact that used tape shows higher μ at 55°C than new tape confirms the previous findings.

i. Effect of number of magnetic heads. Figure 6 also shows the much larger $\mu\beta$ values obtained, when five magnetic heads are used instead of two. Both curves represent tests conducted at the same speed and temperature, i.e., 0.133 ips and 55°C.

4. Conclusions

The present experiments have shown the following:

(1) Elevated temperature (55°C) aggravates the sticking problem of 3M 20250, when the tape is at rest in contact with the magnetic heads. The degree of sticking levels off after about 4 days.

(2) Reducing the number of magnetic heads in contact with 3M 20250 tape from 5 to 2, reduces $\mu\beta$ values 2 to 3 times.

(3) Part of the changes (damage) induced into the tape when it is run over the magnetic heads is permanent, but part is recoverable.

(4) $\mu\beta$ increases with crosshead speed and the relationship is exponential.

(5) Degassing reduces the sticking of the tape to the head, in static contact, but does not affect the $\mu\beta$ values significantly.

(6) Exposing bare Mylar "windows" to the magnetic heads reduces sticking, but tape samples with such windows show a ragged pattern and higher $\mu\beta$ values, probably because of dislocation of iron oxide–binder particles during the preparation of windows, which rub against the binder surface and roughen it.

(7) The phenomenon of ruggedness in the Instron graphs is given attention. It is thought that this may be a manifestation of the stick–slip problem. Experiments are being planned to verify this.

(8) Results obtained in this series of experiments confirmed and supported previous findings reported in SPS 37-63, Vol. III.

(9) The dependence of μ on the number of passes with the Mylar in contact with the heads shows that flexing of the binder–oxide material may contribute to the change in $\mu\beta$.

XV. Research and Advanced Concepts

PROPULSION DIVISION

A. Ion Thruster Hollow Cathode Studies,

E. V. Pawlik and D. J. Fitzgerald

1. Introduction

An experimental evaluation of solar-electric primary propulsion is currently in process (Ref. 1).[1] These tests employ a hollow cathode as the electron source to ionize mercury propellant by electron bombardment (SPS 37-48, Vol. III, pp. 119–125). The cathode has been operated extensively with the thruster without any significant cathode erosion being observed during short-interval testing (SPS 37-49, Vol. III, pp. 207–211). The present study is directed towards determining the cathode operating temperature and investigating the effects of cathode orifice geometry changes on both temperature and thruster operation.

2. Apparatus

The nominal operating level for the 20-cm-diam ion thruster used in the program (Fig. 1) is 1000 to 2000 W (0.5 to 1.0 A beam current at 2000 V) of throttleable output beam power at a constant specific impulse near 4000 s. (Details of thruster performance can be found in Ref. 1.) The thruster is operated in a 3 × 7-ft vacuum tank while maintaining pressures on the order of 2 to 8×10^{-6} torr.

The hollow cathode and the mounting arrangement within the thruster are shown in Fig. 2. Three cathode orifice sizes (0.063, 0.075, and 0.100 cm-diam) were investigated. The hollow cathode is essentially a plasma device, supplied with gaseous mercury from a vaporizer, that consists of a hollow tube with a small orifice and a keeper electrode. Cathode interior pressure is on the order of 1.0 torr during operation. The cathode contains a heating element and an internal insert impregnated with barium carbonate. The cathode discharge is initiated by heating the cathode until the low work function material begins emitting electrons. These electrons are electrostatically attracted to the keeper and, at sufficient flowrates, will ionize the mercury, thus creating a plasma discharge. A modified enclosed keeper structure of the type first reported in Ref. 2 was used.

The power to heat the cathode was measured with a tungsten/tungsten–rhenium thermocouple. (The temperature-to-power relationship is presented in Fig. 3.) The cathode operating temperature is a function of both the

---

[1] Also discussed by T. D. Masek in "Solar Electric Propulsion System Technology," a paper proposed for presentation at the Eighth Electric Propulsion Conference at Stanford University, Calif., during August 1970.

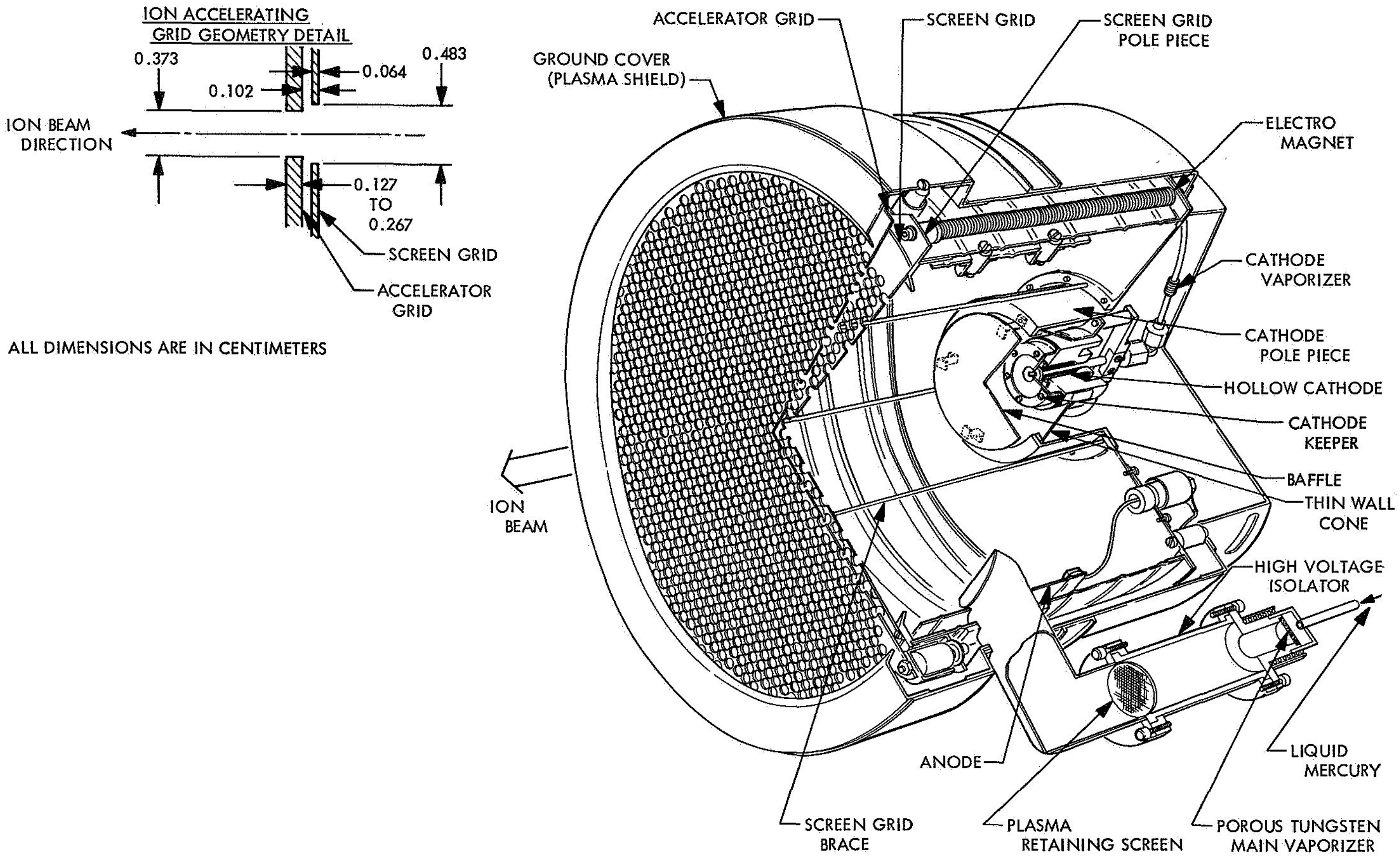

Fig. 1. 20-cm-diam ion thruster

method of mounting and the surrounding thermal environment. Heating data are presented for both a hot and cold thruster, where a cold thruster is one that has been cooled by radiation to a liquid-nitrogen cold surface (mercury condenser within the vacuum tank) for several hours and a hot thruster is a unit immediately after operation (on the order of 250°C).

The cathode mounting was designed to minimize heat conduction to the thruster. This was accomplished by using a cone of thin stainless steel to support the boron nitride in which the cathode is held. This approach thermally isolates the cathode, providing rapid heat-up and minimizing mercury condensation during initial operation.

3. Results and Discussion

Thermocouple data was obtained for the three cathode orifice sizes as the thruster was operated at low output power (0.5 A ion beam). The cathode was self-heated during thruster operation by the discharge plasma; no power was supplied to the cathode heater. The cathode temperatures, presented in Fig. 4a, were observed to increase with the cathode emission current (approximately the sum of the keeper and anode currents). The magnetic field and flowrate through the cathode were maintained nearly constant for each cathode investigated, which left arc voltage as an independent parameter that would increase with arc current (Fig. 4b).

The temperature of the cathode face for the 0.063-cm-diam orifice was found to be extremely high, presenting the possibility of evaporation of the barium carbonate over long-term tests. It was also observed that the arc discharge may supply in excess of 30 W of heating to the cathode during thruster operation, which can represent about 25% of the power supplied to the arc chamber.

As the orifice diameter was increased, both the operating temperature and internal pressure of the cathode were reduced significantly. The reduced temperature is believed to be due to reduction of ion bombardment of the cathode from the internal plasma, which would be directly proportional to the pressure.

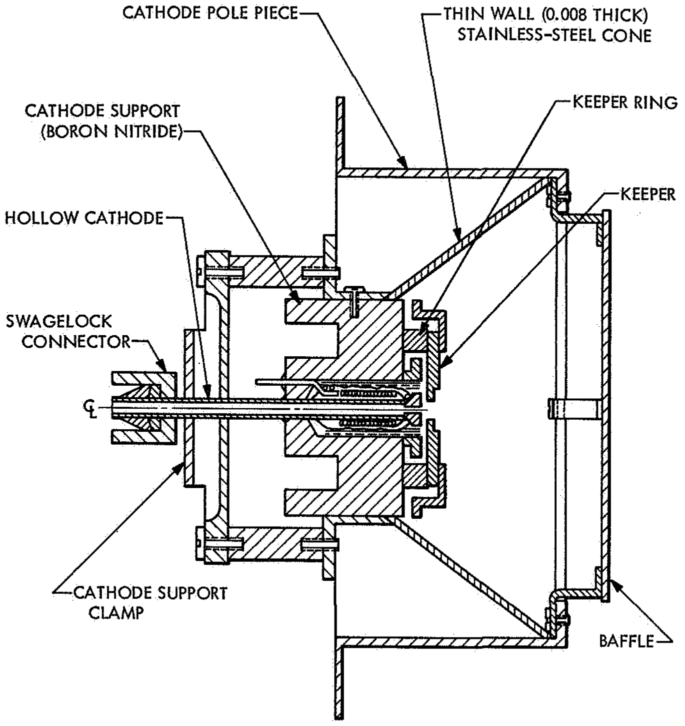

POLE PIECE AND CATHODE MOUNTING DETAIL

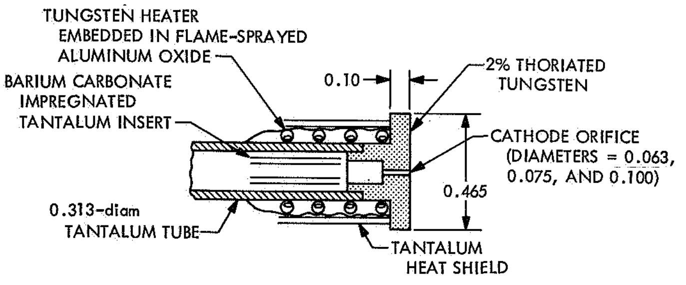

CATHODE DETAIL

ALL DIMENSIONS ARE IN CENTIMETERS

Fig. 2. Cathode design and mounting

Lower cathode operating temperatures are desirable inasmuch as they reduce the loss of barium carbonate by vaporization, which serves to retain cathode restarting abilities; however, the actual emission process is not well understood at this time. All of the cathode emission mechanisms (Auger, field, Schotky, photo, and thermionic) are enhanced by lowering the work function; therefore, retention of barium carbonate may also be desirable for optimum cathode operation.

One drawback observed as lower cathode operating temperatures were obtained was a dependence on an increasing level of keeper current in order to maintain a stable discharge. Operation of the two smaller orifices could be maintained above an emission current of 4 A

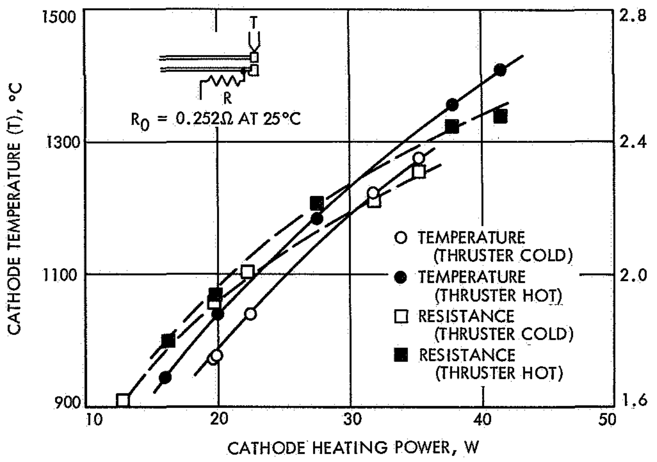

Fig. 3. Cathode face temperature vs cathode heater power

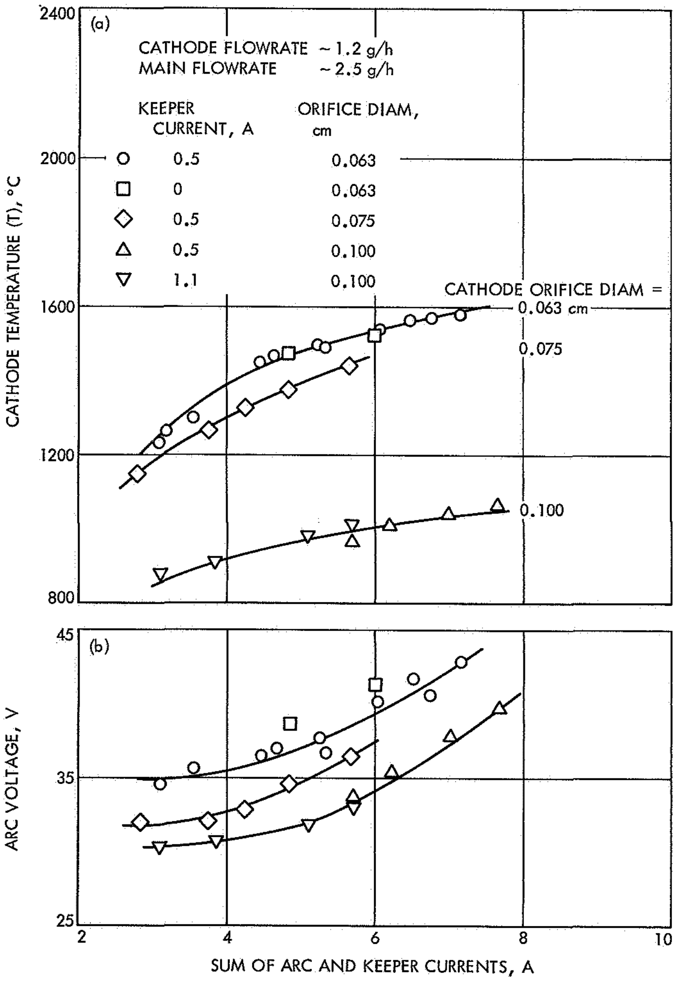

Fig. 4. Effects of cathode orifice size on (a) cathode temperature and (b) arc voltage during thruster operation

without keeper current, but the largest orifice required keeper current at all emission currents investigated to maintain a discharge. The level had to be increased to 1.1 A at low cathode emission levels.

Thruster operation in terms of arc chamber losses and mercury propellant utilization are presented in Fig. 5 for the maximum and minimum cathode orifices. The lower temperature cathode operation was reflected in slightly lower arc chamber losses.

Overall thruster performance was improved over that presented in Ref. 1 by the solid cone-shaped surface used in place of a plasma retaining screen. This is probably due to an insufficient mesh size or a smaller plasma Debye distance than anticipated within the pole piece region that defeated the purpose of the plasma retaining screen. Similar thruster performance improvements have been reported in Ref. 3 where a solid surface was used to reduce surface recombination losses within the cathode pole piece.

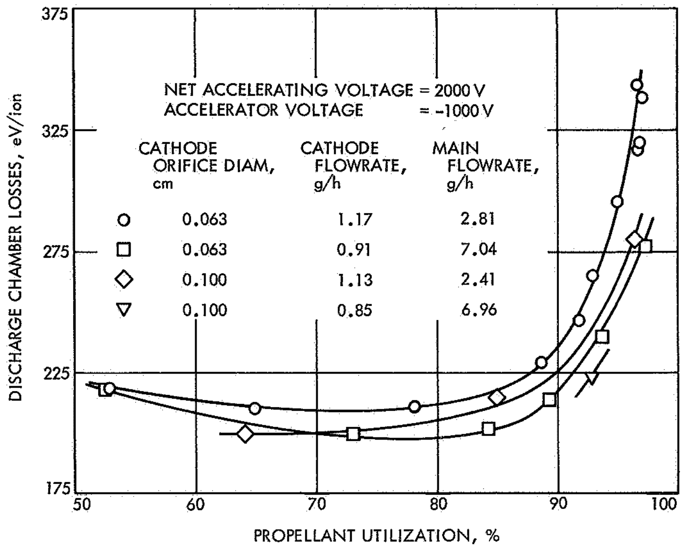

Fig. 5. Effect of propellant flowrate on discharge losses for two cathode orifice sizes

References

1. Pawlik, E. V., Costogue, E. N., and Schaefer, W. C., "Operation of a Lightweight Power Conditioner with a Hollow Cathode Ion Thruster," AIAA Paper No. 70-648, AIAA 6th Propulsion Joint Specialist Conference, San Diego, California, June 1970.
2. Kemp, R. F., and Hall, D. F., "Ion Beam Diagnostics and Neutralization," Final Report, NASA Contract NAS3-7937, TRW, Redondo Beach, California, September 1967.
3. "Research on Hollow Cathodes in Mercury Ion Thrusters," Semi-Annual Report, JPL Contract 952685, Colorado State University, Fort Collins, Colorado, March 1970.

B. Performance of a Supersonic Nozzle with a 75-deg Convergent Half-Angle and a Small Throat Radius of Curvature,

R. F. Cuffel and P. F. Massier

1. Introduction

This article presents the experimental results of tests conducted with a supersonic nozzle having a steep inlet half-angle of 75 deg and a comparatively small ratio of throat radius of curvature to throat radius r_c/r_{th} of 0.25. (Definitions of symbols used in this article are given in Table 1.) The divergent half-angle of the nozzle was 15 deg, the inlet area ratio was 9.8, the expansion area ratio was 2.3, and the throat diameter was 1.6 in. The specific impulse, the longitudinal distribution of thrust as determined from wall pressure measurements, and the experimental flow coefficient were evaluated using air flow at approximately room temperature.

Nozzles with steep convergent sections and small r_c/r_{th} are presently being considered for rocket engine applications since such nozzles are shorter, weigh less, have a smaller surface area and, hence, a lower total heat load than conventional nozzles. In addition, the heat conduction path between the throat and the upstream chamber is less. Also, a substantial reduction in heat transfer rates below those typical of turbulent boundary layers can occur along the convergent section and in the throat region. This heat

Table 1. Nomenclature

A	local cross-sectional area
C_D	flow coefficient
C_F	thrust coefficient
F	thrust
$f(\gamma)$	function of γ (Eq. 5)
I	specific impulse
$\dot{m}$	mass flow rate
p	static pressure
p_t	total pressure
R	gas constant
r	wall radius
r_c	throat radius of curvature
T_t	total temperature
V	velocity in the axial direction
z	axial distance
γ	specific heat ratio
Subscripts	
i	inlet of nozzle
e	exit of nozzle, or local limit of integration
t	local stagnation condition
th	at the throat
1-D	one-dimensional

transfer rate reduction occurs, under certain conditions, due to laminarization of a turbulent boundary layer because of acceleration of the flow (Refs. 1–3).

The desirability of actually using such nozzles in engines, however, will depend to a large extent on performance. Consequently, tests are being conducted in which compressed air at room temperature is being used to evaluate (primarily) the thrust and flow coefficient of several nozzle configurations.

2. Test Apparatus and Test Conditions

The tests were conducted in the auxiliary flow channel of the JPL hypersonic wind tunnel (Ref. 4). The air flowed through a venturi meter, a plenum chamber, a contraction section, a constant-diameter duct, and then through the nozzle from which it exhausted into an evacuated chamber. The boundary layer in the 5-in. constant-diameter duct at a distance of 1 in. upstream of the nozzle inlet was found to be turbulent. This boundary layer extended to about 12% of the duct radius as indicated by measurements with a 0.005-in. high, flattened-tip pitot probe. Tests were conducted over a stagnation pressure range from 24 to 86 psia at a stagnation temperature of about 530°R. Fifty 0.005-in.-diam wall pressure taps, connected to either mercury or oil manometer boards, were spaced along the nozzle. The axial and radial locations of the taps were measured to within 0.001 in.

3. Experimental Results

The wall contour of the nozzle and the measured wall static pressures for one test are shown in Fig. 1. The dashed curve represents the pressure distribution for one-dimensional flow ($\gamma = 1.4$). It is evident that the small value of r_c/r_{th} for this nozzle had a significant influence on the wall pressure distribution in the throat region. The

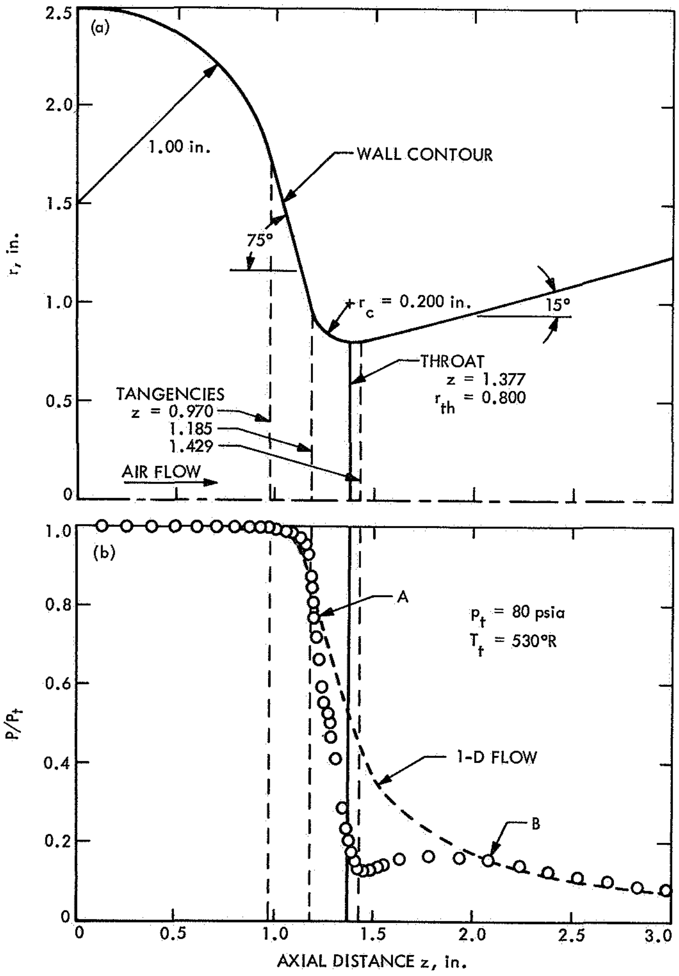

Fig. 1. Wall contour and wall pressure distribution

adverse pressure gradient downstream of the tangency of the circular arc throat and the divergent conical section is associated with a compressive turning of the flow; the subsequent formation of a weak shock wave as has been verified in another nozzle (Ref. 5).

The flow coefficient is defined as the ratio of the actual mass flow rate to the computed value for one-dimensional isentropic flow. Thus,

$$C_D = \frac{\dot{m}}{\dot{m}_{1\text{-}D}} = \frac{\dot{m}}{p_t A_{th}\left[\frac{\gamma}{RT_t}\left(\frac{2}{\gamma+1}\right)^{(\gamma+1)/(\gamma-1)}\right]^{1/2}} \tag{1}$$

The actual mass flow rate was determined by use of a venturi meter. The flow coefficient obtained in this manner was 0.951 ± 0.005.

A normalized thrust coefficient was evaluated from the wall pressure measurements. Hence, the pressure surrounding the outside of the nozzle was not taken into account. The thrust coefficient for a rocket motor operating in a vacuum is defined as

$$C_F \equiv \frac{F}{p_t A_{th}} \tag{2}$$

It may be shown that the thrust coefficient, neglecting the wall shear term, can be expressed in terms of the wall pressure distribution and the inlet conditions as

$$C_F = \frac{A_i}{A_{th}}\frac{p_i}{p_t} + \frac{\dot{m}V_i}{p_t A_{th}} + \int_i^e \left(\frac{p}{p_t}\right) d\left(\frac{A}{A_{th}}\right) \tag{3}$$

By combining Eqs. (1) and (3), and assuming the upstream flow to be isentropic and parallel to the axis, the thrust coefficient can be expressed as

$$C_F = \frac{A_i}{A_{th}}\frac{p_i}{p_t} + C_D f(\gamma)\left[1-\left(\frac{p_i}{p_t}\right)^{(\gamma-1)/\gamma}\right]^{1/2} + \int_i^e \left(\frac{p}{p_t}\right) d\left(\frac{A}{A_{th}}\right) \tag{4}$$

where

$$f(\gamma) = \frac{\gamma}{\left(\frac{\gamma-1}{2}\right)^{1/2}\left(\frac{\gamma+1}{2}\right)^{(\gamma+1)/2(\gamma-1)}} \tag{5}$$

For one-dimensional flow ($C_D = 1$), Eq. (4) reduces to

$$C_{F_{1\text{-}D}} = f(\gamma)\left[1-\left(\frac{p_{1\text{-}D}}{p_t}\right)_e^{(\gamma-1)/\gamma}\right]^{1/2} + \frac{A_e}{A_{th}}\left(\frac{p_{1\text{-}D}}{p_t}\right)_e \tag{6}$$

By adding and subtracting $C_{F_{1\text{-}D}}$ from Eq. (4), for convenience and for accuracy of evaluating the integral, the thrust coefficient becomes

$$C_F = C_{F_{1\text{-}D}} + \int_i^e \left(\frac{p}{p_t} - \frac{p_{1\text{-}D}}{p_t}\right) d\left(\frac{A}{A_{th}}\right) + \frac{A_i}{A_{th}}\left(\frac{p}{p_t} - \frac{p_{1\text{-}D}}{p_t}\right)_i + f(\gamma)\left\{C_D\left[1-\left(\frac{p_i}{p_t}\right)^{(\gamma-1)/\gamma}\right]^{1/2} - \left[1-\left(\frac{p_{1\text{-}D}}{p_t}\right)_i^{(\gamma-1)/\gamma}\right]^{1/2}\right\} \tag{7}$$

A short distance upstream of the nozzle, the experimental wall pressure ratio was found to be equal to the one-dimensional value; hence, these values were set equal to each other. This thrust coefficient (Eq. 7) is then normalized with the one-dimensional value (Eq. 6)

$$\frac{C_F}{C_{F_{1\text{-}D}}} = \frac{F}{F_{1\text{-}D}} \tag{8}$$

Figure 2 presents values of the thrust ratio calculated by evaluating Eqs. (6) and (7) at the local rather than at the exit condition. The major portion of the decrement in the thrust ratio occurs in the conical part of the convergent section where the wall pressures are higher than the one-dimensional values. A local minimum in the thrust ratio occurs in the circular-arc region of the throat because the wall pressures go below the one-dimensional values (location A, Figs. 1b and 2). A spike occurs at the throat where the derivative of the area ratio $d(A/A_{th})$ changes sign. Farther downstream, the lowest value occurs where the experimental and the one-dimensional pressures cross (location B, Figs. 1b and 2). This lowest value is somewhat lower than those obtained for conventional nozzles (Ref. 6). The thrust ratio then continues to rise since the wall pressures are higher than the one-dimensional pressures.

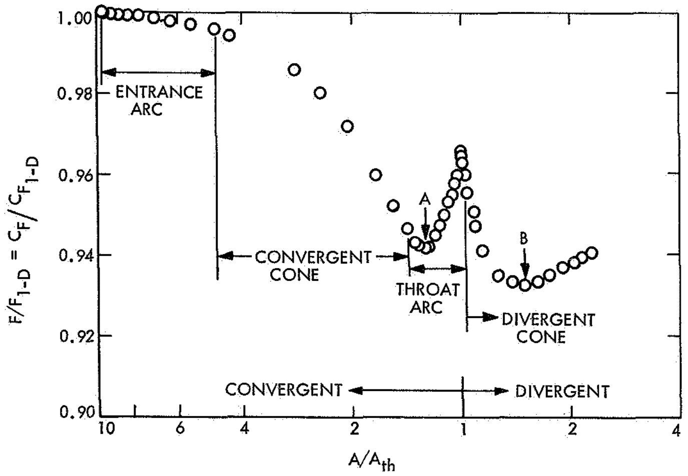

Fig. 2. Thrust ratio vs area ratio

Another performance indicator is the specific impulse ratio, $I/I_{1\text{-}D}$, which is the ratio of $F/F_{1\text{-}D}$ to the flow coefficient. Thus, $I/I_{1\text{-}D}$, which is not shown, varies with the divergent area ratio just as does the thrust ratio. At the exit of the nozzle ($A/A_e = 2.3$) the value of $I/I_{1\text{-}D}$ equals 0.99. This agrees well with results obtained using conventional nozzles with 15-deg divergent conical sections (Ref. 6).

4. Summary and Conclusions

Thrust, flow coefficient, and specific impulse were evaluated experimentally for a nozzle with a convergent half-angle of 75 deg, a divergent half-angle of 15 deg, and a r_c/r_{th} of 0.25. The throat diameter was 1.6 in. The flow coefficient was found to be 0.951 and at the exit of the nozzle ($A_e/A_{th} = 2.3$), $I/I_{1\text{-}D}$ was 0.99. This value of $I/I_{1\text{-}D}$ agrees well with those obtained for conventional nozzles with 15-deg divergent cones.

The thrust ratio $F/F_{1\text{-}D}$, was evaluated along the nozzle by integrating the wall static pressure measurements. In the convergent section, the thrust ratio decreased along the flow direction until a minimum of 0.942 was reached in the circular-arc throat region. However, a spike of 0.966 occurred at the throat; then the lowest value, 0.933, occurred farther downstream in the conical divergent part before it began to increase again to a value of 0.941 at the exit.

References

1. Back, L. H., Cuffel, R. F., and Massier, P. F., "Laminarization of a Turbulent Boundary Layer in Nozzle Flow—Boundary Layer and Heat Transfer Measurements with Wall Cooling," Paper 69-HT-56, presented at the ASME–AIChE Heat Transfer Conference, Minneapolis, Minn., Aug. 3–6, 1969. (To be published in the *ASME J. Heat Trans.*)

2. Back, L. H., Cuffel, R. F., and Massier, P. F., "Laminarization of a Turbulent Boundary Layer in Nozzle Flow," *AIAA J.*, Vol. 7, No. 4, pp. 730–733, April 1969.

3. Back, L. H., Massier, P. F., and Cuffel, R. F., "Some Observations on Reduction of Turbulent Boundary-Layer Heat Transfer in Nozzles," *AIAA J.*, Vol. 4, pp. 2226–2229, 1966.

4. Strand, L., Newton, J., and Herrera, J., *Initial Performance of a New Nozzle Gas-Dynamics Test Facility*, Technical Memorandum 33-310. Jet Propulsion Laboratory, Pasadena, Calif., Nov. 15, 1966.

5. Back, L. H., and Cuffel, R. F., "Detection of Oblique Shocks in a Conical Nozzle with a Circular-Arc Throat," *AIAA J.*, Vol. 4, No. 12, pp. 2219–2221, Dec. 1966.

6. Back, L. H., Massier, P. F., and Gier, H. L., "Comparison of Measured and Predicted Flows through Conical Supersonic Nozzles, with Emphasis on the Transonic Region," *AIAA J.*, Vol. 3, pp. 1606–1614, 1965.

XVI. Liquid Propulsion

PROPULSION DIVISION

A. TOPS Trajectory Correction Engine Testing,

G. Heidenreich

1. Introduction

The upcoming flyby missions to the outer planets will require extended and multiple firings of a trajectory correction engine for midcourse maneuvers. The JPL Liquid Propulsion Section is conducting advanced development of a 25-lbf thrust monopropellant engine to meet the mission requirements. The most severe duty cycle for such an engine, in terms of number of cold (40–70°F) starts and firing duration would be a mission designed to fly-by all five outer planets. Some preliminary test results were presented in SPS 37-63, Vol. III, pp. 227–235. The work discussed in this article is a series of tests on an existing flight-weight, space-qualified, catalytic monopropellant hydrazine engine. This engine was the transtage attitude control system (ACS) hydrazine engine developed for the *Titan IIIC* (Ref. 1). An engine module with 380-s accumulated burn time (consisting of qualification tests) was obtained on loan from the Martin Marietta Corporation. The objective was to determine the performance of a flight-qualified engine in a simulated Thermoelectric Outer-Planet Spacecraft (TOPS) mission duty cycle.

2. Apparatus and Test Procedure

The reaction engine module (REM) consists of two reaction engine assemblies (REAs), each with a series-redundant thrust chamber valve (Moog Model 50-315 AA) assembled to a mounting plate.

The motor used for the tests was S/N 0110, designated the "upstream engine" of transtage module P/Y REM 0000009. (See Ref. 2 for detailed information regarding this motor.) The tests were conducted at the JPL Pit J test facility. Figure 1 is a picture of the module on the test stand. Figure 2 shows a schematic of the test setup. Prior to each run, the fuel line from the Moog fire valve to the isolation valve V1 was evacuated to about 28 in. Hg by means of a water aspirator. The lines were then filled under gravity feed to the Moog fire valve, which was close-coupled to the thruster as seen in Fig. 1. Upon completion of a test, the shutdown signal was sent to the Marotta isolation valve V2 rather than to the Moog valve. Simultaneously, the purge valve V3 was opened, allowing gaseous nitrogen (regulated to 120 psig) to purge the remaining fuel through the Moog valve and the catalyst bed.

The propellant was neat hydrazine. Analysis determined the impurities to be 0.3% ammonia, 0.3% aniline, and 0.7% water (by weight), well within specifications (MIL-P-26536B).

The engines were mounted to fire vertically downward into ambient back pressure at the nozzle exit. The propellant was delivered from a nitrogen-pressurized facility tank. As the gaseous nitrogen was locked up in the tank prior to the start of the run, the pressure in the tank decayed as fuel was forced from the tank. This, then, approximated the dynamic conditions that will be encountered in the non-regulated blowdown mode selected for the TOPS propulsion system. A heat-exchanger coil immersed in a tank containing ice water conditioned the incoming propellant to temperatures of 50 ± 5°F.

The flight engines had provisions for only one chamber pressure tap. Accordingly, in the experimental setup, the line from the engine was split with one line going to a Taber pressure transducer and one to a high-response Photocon transducer. Three chromel–alumel thermocouples were tack-welded on the outside of the engine (1) at the midpoint of the feed tube connecting the valve to the injector inlet manifold, (2) midway down the cylindrical portion of the thrust chamber (under the insulation), and (3) at the nozzle throat. In addition, facility instrumentation included tank and line pressures, temperatures, and flows. The instrumentation signals were recorded both on oscillograph recorders running at 25 in./s and on a digital data acquisition system.

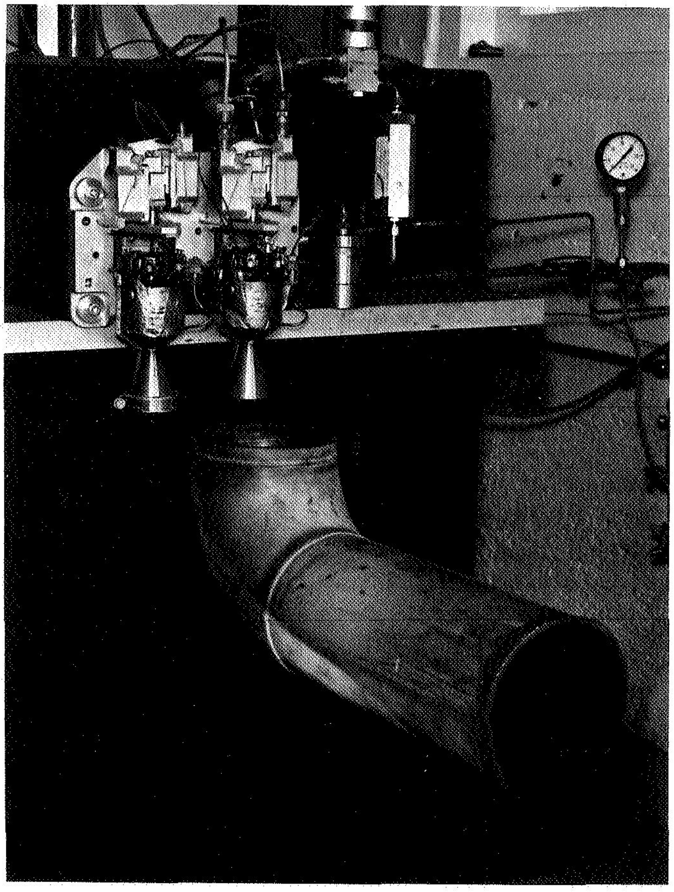

Fig. 1. Engine mounted on test stand

3. Test Results

A summary of the test results is presented in Table 1. A total of seven tests and 1270-s burn time were accumulated on the one engine (S/N 0110). The duty cycle was simply a series of steady-state burns ranging from 16 to 753 s. Ignition delay is defined here as the time from the electrical signal to the Moog fire valve to the time when chamber pressure has reached 2% of its final steady-state value. The characteristic velocity c^* values shown in Table 1 were taken at 10-s into each run and just before shutdown. The throat area was corrected for thermal growth by using the thermocouple reading at the throat (see Fig. VI-91 in Ref. 2).

As seen in Table 1, the ignition delay generally increased with the accumulated number of starts. The ignition delay for Run 1 was 64 ms; by Run 7, this delay had increased to 160 ms. Ignition delays longer than 100 ms resulted in transient overpressurization of the chamber. Maximum transient chamber pressures ranged between 200 and 250 psia, except for Run 4, where the pressures went off scale and the best estimate is that a pressure spike of over 700 psi occurred. Note that in Run 4, the fuel and catalyst bed temperatures were initially lower than those in all other tests except Run 1. The desired initial fuel temperature was about 50°F. The value given in Table 1 is that for the fuel in the lines at the start of the run. After 2–3 s of firing, the temperature of the fuel dropped as the fuel chilled in the heat exchanger reached the engine. Due to a misfire on a previous attempted firing, the initial bed temperature for Run 2 was 125°F. During the misfire, the facility isolation valve V2 did not actuate due to a broken electrical lead, and when the fire valve was actuated for Run 2, a small amount of hydrazine drained into the chamber under gravity and reacted with the catalyst, leaving the bed warm for Run 2.

The maximum chamber pressure roughness (defined as peak-to-peak chamber pressure change within 0.050 s divided by two times the average chamber pressure) became relatively large especially during Runs 6 and 7. Figure 3 shows the chamber pressure roughness during Run 1. The peak-to-peak pressure variation measured by transducer PC1 was ±3 psid or ±1.8% of the average chamber pressure. By Run 6, the peak-to-peak variation had risen to ±23 psi, or ±23% of average chamber pressure, as shown in Fig. 4. At the lower chamber pressure of Run 7, the roughness grew to ±29 psi or ±30% of the

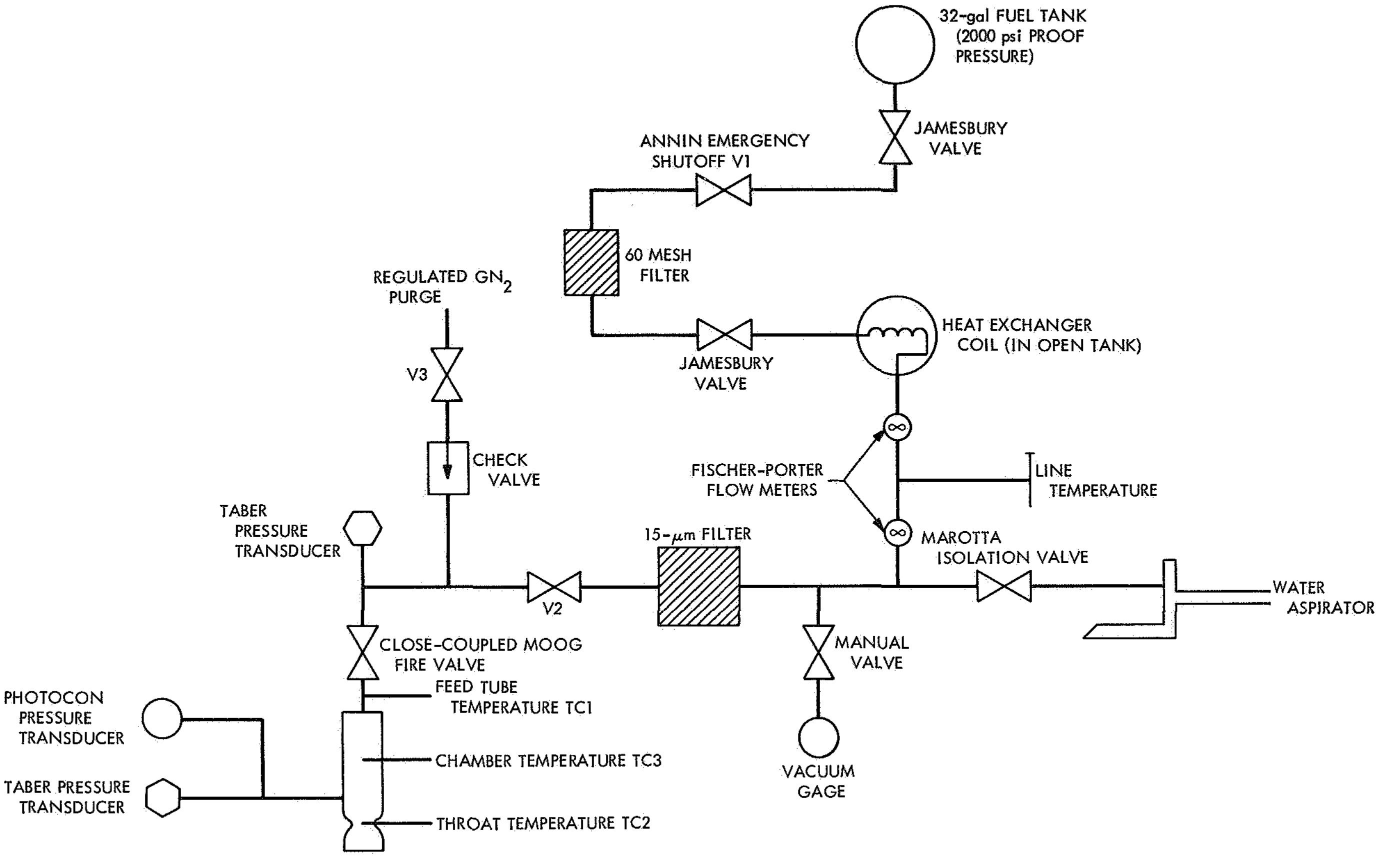

Fig. 2. Test setup schematic

average chamber pressure, as shown in Fig. 5. Since this is the maximum allowable pressure roughness for life duration (Ref. 2), testing was terminated. Up to this point, the engine had accumulated a total of 1650 s burn time (including the original 380 s). Mean state performance remained essentially constant. At the end of Run 7, the c^* value was still 4218 ft/s, a decrease of only 1.3% compared to Run 1, over a tank pressure blowdown ratio of 2:1.

4. Discussion of Results

The increased ignition delay with number of starts is an indication of catalyst bed deterioration. Since further testing may be done, the catalyst bed has not been examined; therefore, the exact state of the catalyst is unknown at this time. In general, pressure overpressures occur at long ignition delays (Ref. 3), but the magnitude of the maximum pressure cannot be predicted with any great accuracy (Ref. 4). The increase in chamber pressure roughness, particularly in Runs 6 and 7, indicates that catalyst attrition has occurred, creating voids in the bed. These voids allow an instability in the reaction rate and, thus, roughness to occur. Catalyst bed deterioration seems to be inevitable with present state-of-the-art catalysts and efforts at catalyst improvement have not been too successful to date. However, because of the increasing need for longer-life catalyst beds, work is continuing, e.g., Rocket Research Corporation, under JPL contract, is investigating a monolithic catalyst consisting of a foamed metal substrate.

To arrive at a reference norm, no attempt was made to cool the catalyst bed below ambient temperature. However, the startup performance of a hydrazine catalytic chamber has been shown to be quite sensitive to both propellant and catalyst bed temperature (Ref. 3). Further investigation of this temperature sensitivity is planned for the future.

5. Conclusions

In general, the results offer some verification of the contention that a state-of-the-art neat hydrazine engine suitable for application to outer-planet missions is available. Performance remained virtually constant, and 1650 s of total burn-time duration were accumulated without exceeding any previously established user limit values.

Table 1. Summary of test results on transtage motor S/N 0110

Run	Ignition delay,[a] ms	Initial fuel temperature, °F	Initial bed temperature, °F	Maximum pressure roughness, ±psi/±% P_c[b]	Initial tank pressure, psig	c^* at + 10 s, ft/s	c^* at shutdown, ft/s	Run duration, s
1	64	54	59	3/1.8	400	4238	4274	16
2	60	60	125[c]	12/7.5	400	4145	4246	100
3	128	60	70	6/3.9	378	4161	4223	25
4	136	57	70	10/7.9	370	4152	4182	49.5
5	142	63	86	4/3	365	4173	4243	57
6	130	66	81	23/23	360	4167	4268	753
7	160	64	79	29/30	260	4146	4218	270

[a] From fire valve electrical signal to 2% of chamber pressure.

[b] P_c = chamber pressure.

[c] High bed temperature due to dribble from reaction engine module manifold on a preceding aborted burn.

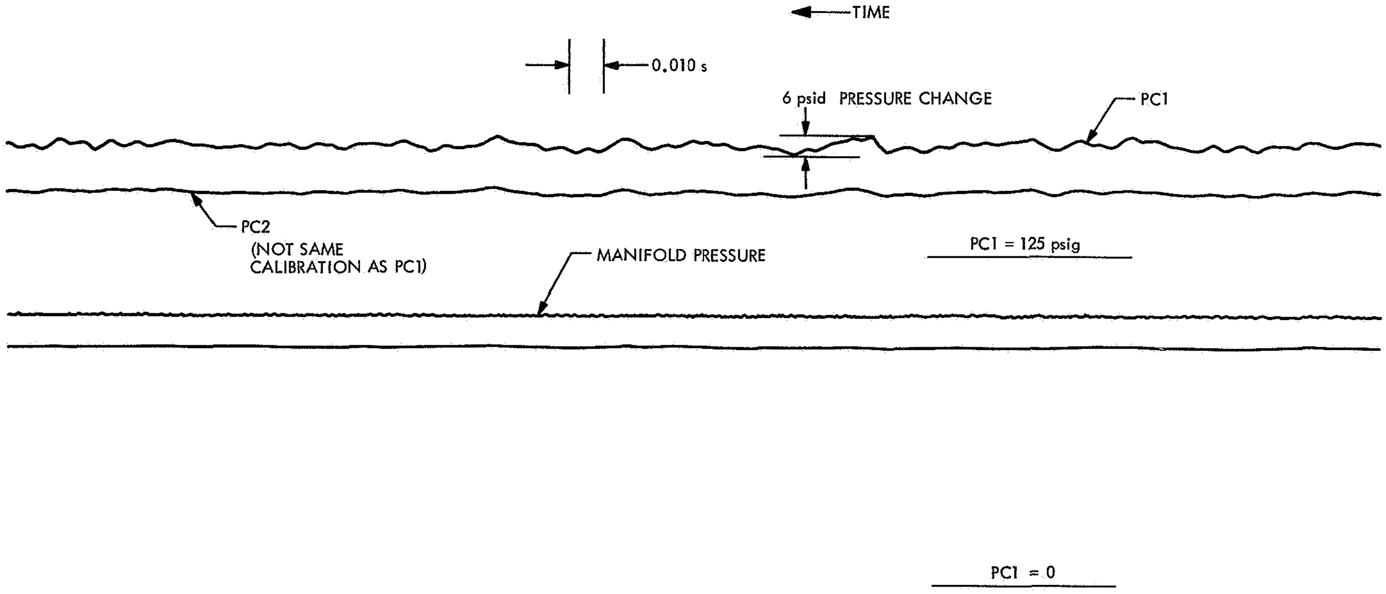

Fig. 3. Run 1 pressure roughness

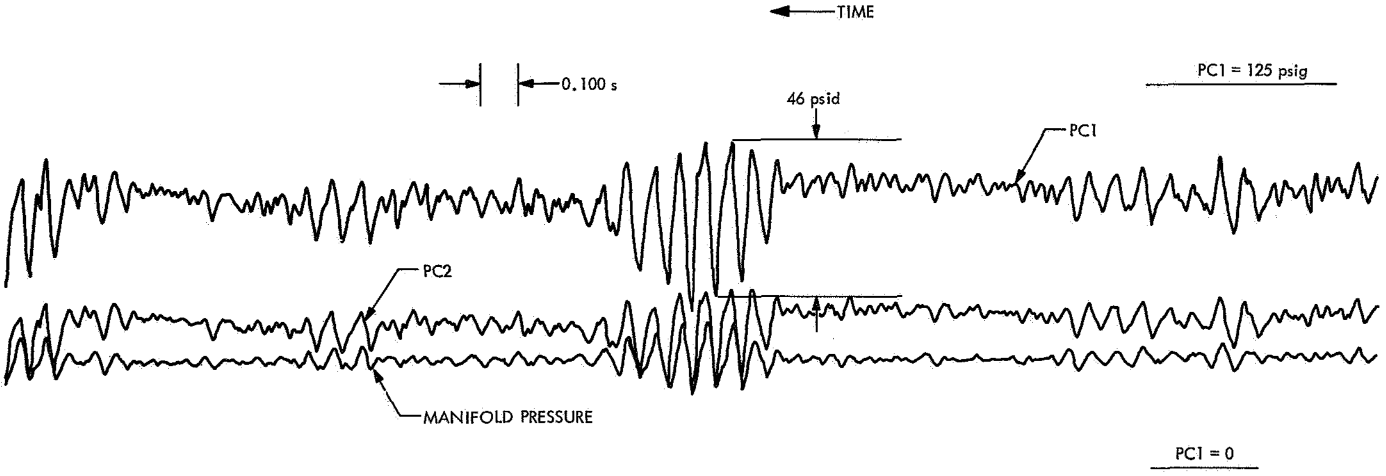

Fig. 4. Run 6 pressure roughness

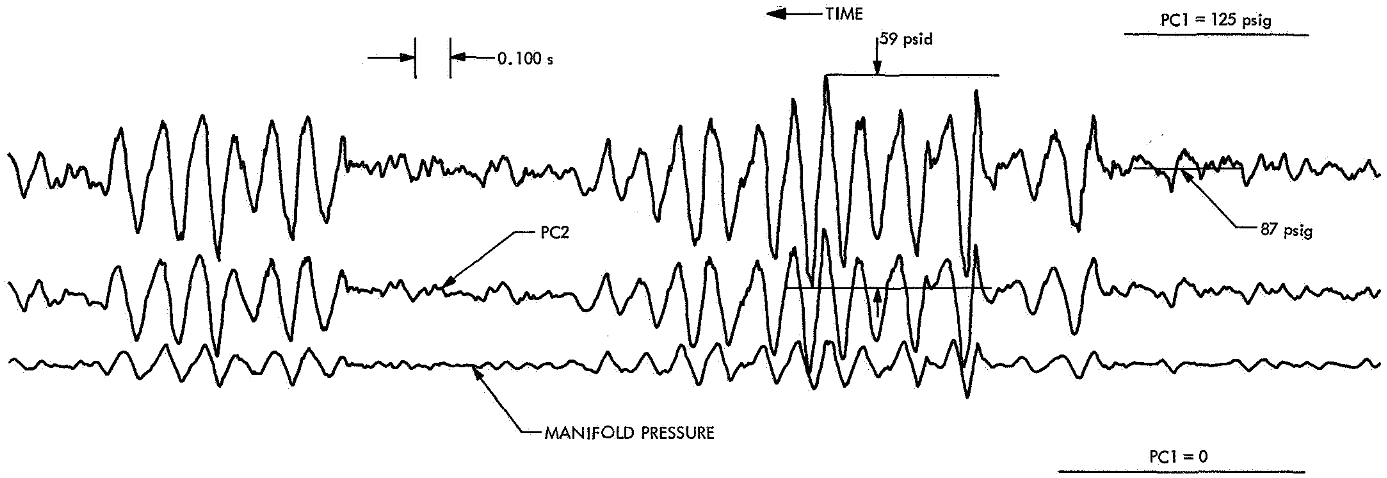

Fig. 5. Run 7 pressure roughness

However, the starts were not deep-vacuum starts, and the initial catalyst bed temperature could be lower during a deep-space mission. Therefore, additional low-temperature tests should be made to foster more complete confidence in, and to determine the ultimate capability and limits of, such a catalytic reactor.

References

1. Morrisey, D. C., et al., "Development of the *Titan III* Transtage ACS Hydrazine Monopropellant Rocket Engine Modules," Paper 69-422, presented at the Fifth AIAA Propulsion Joint Specialist Conference, U.S. Air Force Academy, Colo., June 9–13, 1969.
2. Steele, R. D., et. al., *Titian IIIC Hydrazine Attitude Control System Users' Manual,* Martin Marietta Corp., Denver, Colo. Nov. 1969.
3. Greer, H., "Vacuum Startup of Reactors for Catalytic Decomposition of Hydrazine," *J. Spacecraft Rockets,* Vol. 7, No. 5, May 1970.
4. Sangiovanni, J., and Kesten, A., *Study of Hydrazine Reactor Vacuum Start Characteristics,* First Annual Report (Contract NAS7-696), United Aircraft Research Laboratories, East Hartford, Conn., Dec. 1969.

B. Advanced Combustion Device Development,

R. W. Riebling

1. Introduction

A number of research programs are being conducted by the JPL Liquid Propulsion Section to evolve injector and thrust-chamber design criteria applicable to the development of rocket engines for unmanned spacecraft, using the space-storable propellant combination of oxygen difluoride (OF_2) and diborane (B_2H_6). One objective of the present program, "Advanced Combustion Device Development," is the application of these criteria to the development of a prototype OF_2/B_2H_6 flight propulsion rocket engine. The adopted technical approach emphasizes the application of existing technology, rather than the generation of new technology, with the intent of exposing any problems encountered in an actual application. These will be solved as they arise, or made the subject of additional new technology programs, as appropriate. Another program objective is the demonstration of the basic soundness of currently accepted design concepts in terms of performance and stability levels, durability, and inherent reliability.

The thrust-chamber design criteria evolved to date have been based on the concept of a passively cooled chamber, combined with an injector having a controlled gradient in mixture ratio. That is, the injector includes a central core region containing a large fraction of the total mass flow and operating at, or slightly above, the mixture ratio for maximum performance and an outer, or "barrier," zone containing a smaller proportion of the total mass flow and operating at a much-reduced mixture ratio. The fuel-rich conditions prevailing in this barrier zone should reduce both the adiabatic wall temperature and the concentrations of chemically undesirable species in the region immediately adjacent to the walls, thus helping to maintain the chamber's structural integrity. Nickel has emerged as the most durable injector material with the use of fluorinated oxidizers such as OF_2. Carbonaceous or graphitic materials have been reported to be the most promising candidates for use as chamber liners and throat inserts in chambers thermally insulated by ablative or other materials.

Accordingly, the technical approach adopted to develop a flight-prototype OF_2/B_2H_6 rocket engine has been based on a passively cooled chamber with a carbonaceous or graphitic inner liner and an injector made of nickel that incorporates some degree of barrier zone protection. In the event that the rocket engine must be "buried" within a spacecraft, its outside wall temperature and heat flux per unit area may not be permitted to exceed certain values. Therefore, an additional requirement imposed upon the engines currently being developed is that they be adequately thermally insulated.

Presently, four competing versions of this general design concept are being evaluated. Three of these have been described in SPS 37-57, Vol. III, pp. 187–192 and SPS 37-59, Vol. III, pp. 234–248. A fourth will be the subject of a future discussion.

Two self-impinging doublet injectors with different amounts of fuel-rich barrier protection were fabricated for evaluation with the four thrust chamber concepts (SPS 37-59, Vol. III). This article will present and discuss the results of a preliminary series of experiments in which these injectors were fired with $FLOX/B_2H_6$ propellants to determine their performance and solid deposition characteristics.

2. Injectors

The element arrangements of the two injectors, designated Mods I and II, are shown in Fig. 1. Both designs are quite conservative in that they provide a very high fraction of the total fuel flow to the barrier zone in an effort to guarantee maximum protection of the chamber and nozzle walls from the oxidizer-rich core combustion gases. The Mod I injector, for example, introduces 68% of the total fuel flow through its outer ring of 24 fuel doublets. With a low (1.23) overall design mixture ratio, it is designed to provide a greater degree of barrier protection than the Mod II version. The latter has only 41% of the total fuel flow in its outer ring, and a higher (2.27) overall design mixture ratio. The maximum possible core mixture ratio for both injectors (assuming no mixing between the core and the fuel from the outer ring) is 3.85 at their overall design mixture ratios. This value should maximize core characteristic velocity c^* at a chamber pressure of 100 psia. The "barrier zone" will be formed by the interaction of the oxidizer-rich core sprays and the fuel sprays from the outer ring. Since it is not possible to predict the degree of this interaction under combustion conditions, it would be fictitious to assign an average mixture ratio to the barrier region; in all probability, however, a mixture-ratio gradient will exist across the barrier zone, from a value of approximately 3.85 at its boundary with the core, to one approaching zero at the chamber walls.

The Mod I injector consists primarily of alternating rings of fuel and oxidizer doublets, while the Mod II injector contains alternating fuel and oxidizer doublets within each ring. Thus, the Mod I design maximizes the spacing between the long axes of the elliptical cross-sections of fuel and oxidizer spray fans, but the Mod II concept minimizes (reduces to zero) this spacing. It has been shown that fan spacing is a key variable affecting the degree of mixing in self-impinging doublet injectors, so the Mod II injector would be expected to provide better mixing and higher combustion efficiency in its core region than the Mod I injector. This is borne out by the values of the combustion efficiency η_{c^*} given in Table 1. These attributes of barrier protection and core performance should combine in such a way as to make the chamber and nozzle heat fluxes expected from the Mod II injector considerably higher than those from the Mod I injector. The Mod II should provide higher combustion efficiencies and a more severe chamber environment than the Mod I, thus providing comparative information which will hopefully lead to an optimized injector pattern for the subsequent 1000-lbf thrust chamber assemblies.

3. Test Conditions

The primary purpose of the test-firings was to screen the two injector designs for performance and solid deposition characteristics prior to their use in attempted long-duration (approximately 1000 s) firings with the carbonaceous and graphitic thrust chambers discussed above. The intent was to vary mixture ratios around the nominal design values of 1.23 (for Mod I) and 2.27 (for Mod II) to determine the sensitivity of performance to mixture ratio and the overall mixture ratio that would maximize combustion efficiency (expressed as η_{c^*}) for each injector. The test series for each injector was started at a mixture ratio of 3.0, or greater, and mixture ratios were progressively reduced in subsequent firings. A mixture ratio of 3.0 is of interest because it corresponds to equal propel-

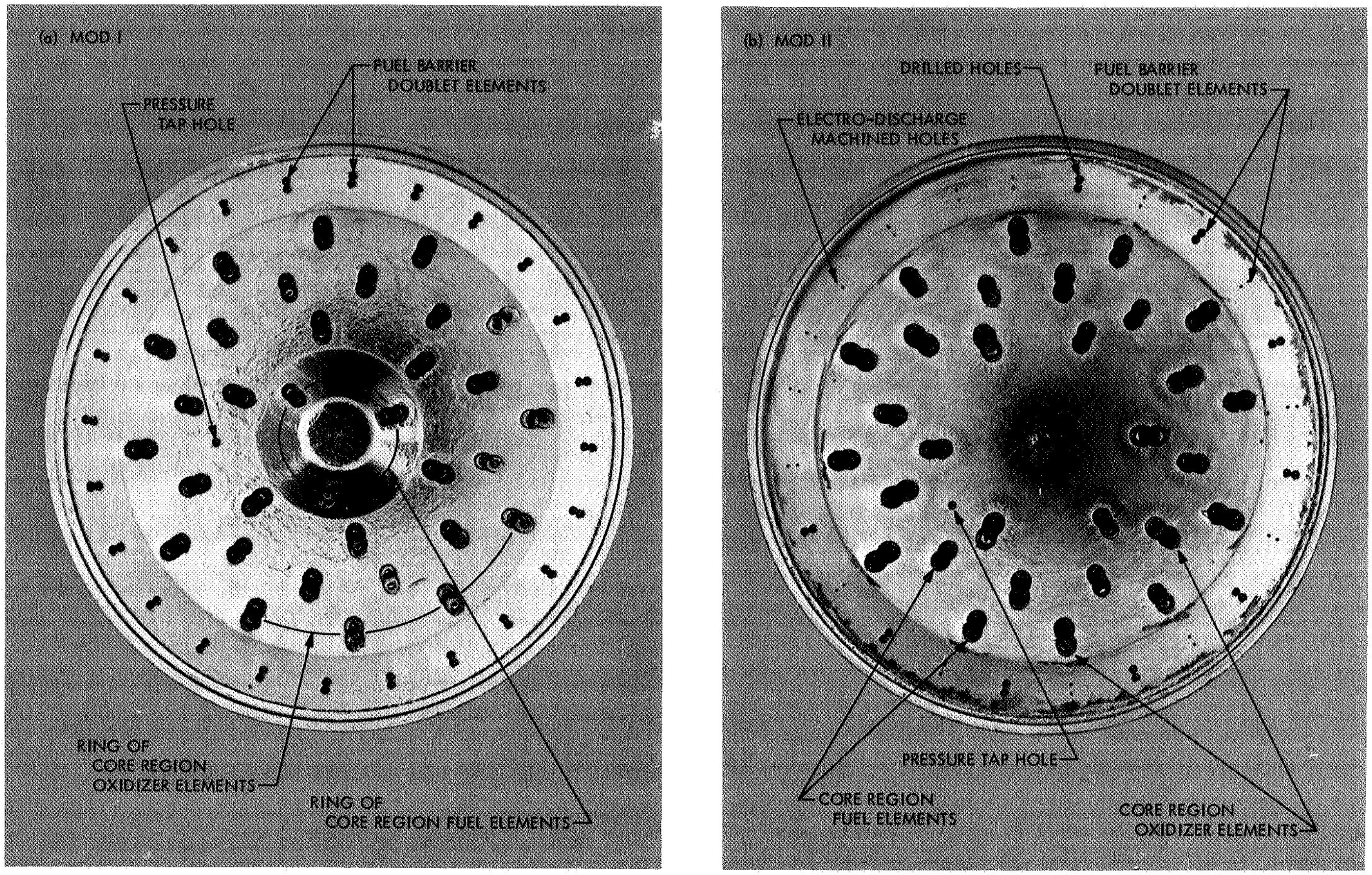

Fig. 1. Element arrangements of 200-lbf impinging-jet injectors

lant tank volumes for OF_2/B_2H_6 at their space storage temperatures. However, because of general performance levels and the degree of solids deposition encountered, the test series was terminated before the design value for the Mod I injector was reached.

A secondary objective was to determine the effect of B_2H_6 temperature on combustion efficiency.

Two test firings were conducted with the Mod I injector and three with the Mod II injector on C-stand at the Edwards Test Station (ETS). A 70 wt% F_2 FLOX mixture was used to simulate the more expensive OF_2 oxidizer. A thick-walled, uncooled, copper thrust chamber with a 5.0 contraction ratio ϵ_c and a 20-in. characteristic length L^* was employed. This chamber expanded the gases to ETS ambient pressure, and was not thermally instrumented. Steady-state test durations were nominally 4 s at a nominal stagnation chamber pressure P_c of 105 psia. Overall mixture ratios $\bar{r}$ were varied between 2.2 and 3.3 at essentially constant chamber pressure and total propellant flow rate. The FLOX oxidizer was conditioned to a nominal engine inlet temperature of −300°F, while the B_2H_6 fuel temperature was varied from −96 to −192°F.

4. Results and Discussion

The experimental conditions and performance results are summarized in Table 1. Only the overall mixture ratio is given since it is not possible to predict the degree of core–barrier mixing interaction under combustion conditions. (Therefore, it would be fictitious to calculate core or barrier mixture ratios.) The chamber pressures reported have been corrected to stagnation values. The thrust and specific impulse I_{sp} values are for ground-level expansion at ETS ambient pressure. Neither I_{sp} nor c^* have been corrected for heat losses to the thick-walled copper chamber since accurate heat flux measurements, which are essential to such corrections, were not made. Thus, the values of η_{c^*} tabulated are probably several percentage points too low. Rough estimates made with typical heat losses (measured with similar injectors and chambers in the past) indicate that η_{c^*} is probably on the order of 90% for tests 1 and 5. Accordingly, in this case, the relative

Table 1. Summary of test conditions and results

Test	Mod	Duration, s	Propellant flow rates, lbm/s			$\bar{r}$	P_c, psia	Propellant temperature, °F		Thrust, lbf	I_{sp}, lbf-s/lbm	c^*, ft/s	η_{c^*}, % [a]
			Oxidizer	Fuel	Total			Oxidizer	Fuel				
1	I	4.2	0.41	0.19	0.59	2.2	107	−297	−178	128	217	6020	87.5
2	I	4.2	0.42	0.14	0.57	2.9	104	−297	−178	125	215	6100	85.5
3	II	4.2	0.41	0.17	0.58	2.4	105	−303	−192	123	213	6120	88.0
4	II	4.3	0.44	0.13	0.57	3.3	103	−302	−96	123	215	6120	86.2
5	II	4.3	0.40	0.18	0.57	2.3	104	−300	−97	127	221	6100	88.4

[a] Based on theoretical shifting equilibrium value at measured stagnation P_c and measured $\bar{r}$ (uncorrected for heat or other losses).

changes in η_{c^*} are of greater interest than its absolute magnitude.

Figure 2 shows combustion efficiency (based on the *overall* mixture ratio) plotted versus overall mixture ratio. A consistent trend toward higher efficiencies at lower mixture ratios is noted for each injector. This is reasonable since the optimum core mixture ratio of 3.85 is approached as the overall mixture ratio decreases. The Mod II injector exhibits higher combustion efficiencies than the Mod I design. This is not surprising since its core region features edgewise impingement of the like doublet elements, and since only about 41% of the total fuel is introduced into the barrier zone. This relative ranking of the two injectors, attributed primarily to their *mixing* characteristics, was predicted in SPS 37-59, Vol. III based on cold-flow measurements of the degree of mixing attained in their nonreactive sprays. It is not possible, based on the results of these firings, to isolate the two effects (core element arrangement and core–barrier stratification ratio) or estimate their relative contributions.

Because of the relatively large L^* (20 in.), it seems unlikely that the low overall performance levels are attributable to incomplete propellant vaporization. Indeed, no correlation could be found between η_{c^*} and the atomization parameter $(d/\bar{v})^{1/2}$ for either oxidizer or fuel, and warming the B_2H_6 a full 82°F (Table 1 and Fig. 2) had no appreciable effect on η_{c^*}.

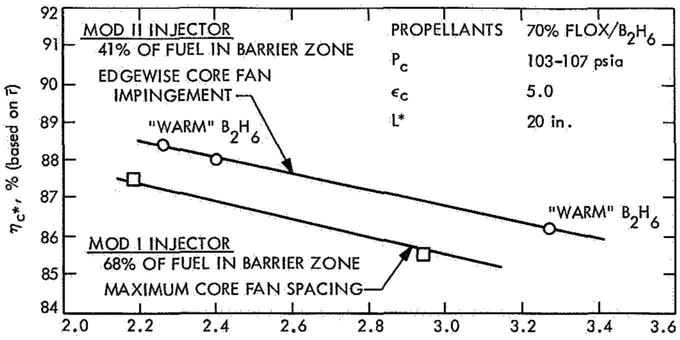

Fig. 2. Effect of overall mixture ratio and barrier stratification on combustion efficiency

Profuse quantities of solid deposits were found after each of the short-duration firings. Detailed chemical analysis revealed no distinct variations in the composition of these deposits from one injector to the other, or with position across the face of a given injector. However, elemental boron was the predominant component, with compositions ranging from 60 to 90 wt%. B_2O_3 concentrations were minimal, ranging only from 3 to 6 wt%. Less than 0.5 wt% BF_4^- was present after each test.

As shown in the representative photographs of Fig. 3, somewhat heavier deposits were sustained by the Mod I injector. This is logical, since that injector afforded less complete mixing in the core and a greater flow of B_2H_6 in the peripheral barrier. Both these effects would be expected to produce greater quantities of solid elemental boron according to the combustion and pyrolysis reactions discussed in Ref. 1. However, the quantities of solids produced by *both* injectors after such short firing durations are deemed unacceptable. It seems reasonable to imagine that the progressive encroachment of such deposits over the fuel doublet barrier orifices would rapidly destroy much of the intended barrier protection. Such effects have been postulated (Ref. 2) to explain the excessive throat erosion encountered when injectors of this type were fired into graphite-lined thrust chambers.

5. Evaluation of Results

These preliminary injector screening tests were useful in several respects. They indicated both that the performance of the two injectors is primarily mixing-limited, and that their design is probably too conservative with respect to the excessive quantities of fuel introduced into the barrier zone. The tests also revealed a severe solids deposition problem that, if not corrected, would almost certainly compromise the durability of even the most

(a) MOD I INJECTOR AFTER TEST 2

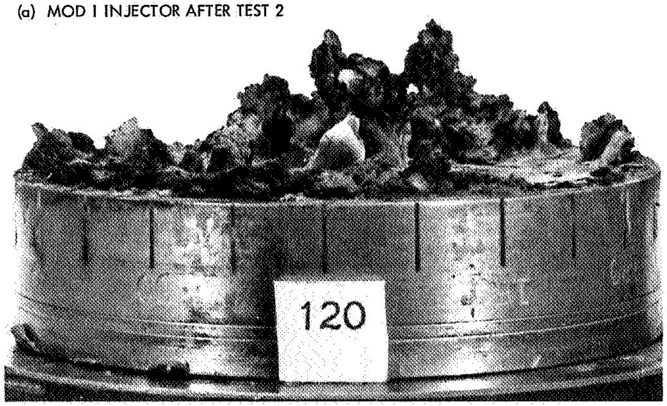

(b) MOD II INJECTOR AFTER TEST 3

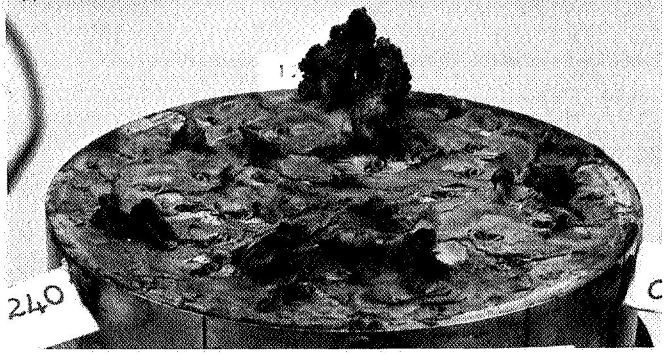

Fig. 3. Typical post-test appearance of injectors

advanced graphitic materials. These deposits, which are concentrated in the barrier region of the injector, may well be related to the copious quantities of barrier coolant employed.

Reference 2 indicates that introduction of the B_2H_6 barrier coolant in the form of a swirling liquid film is just as effective as a means of reducing wall heat flux as is mixture ratio stratification, but results in virtually no deposits at the injector–chamber peripheral interface. Accordingly, the two injectors will be modified to (1) reduce the amount of fuel boundary coolant, and (2) introduce that coolant as a swirling liquid film. Since the injectors were designed with the possibility of such eventual modifications in mind, the incorporation of a swirl film cooling ring is quite straightforward, as can be seen from the sectional views shown in Fig. 4.

References

1. Riebling, R. W. et al., "A Survey of the Current Status of Thrust Chamber Technology for Oxygen Difluoride/Diborane Propellants", Paper 70-717 presented at the Sixth AIAA Propulsion Joint Specialists Conference, San Diego, California, June 15–19, 1970.

2. *Chamber Technology for Space-Storable Propellants, Fourth Interim Report,* Contract NAS7-304, Report R-7985. Rocketdyne, Canoga Park, Calif., Sept. 1969.

(a) MOD I

(b) MOD II

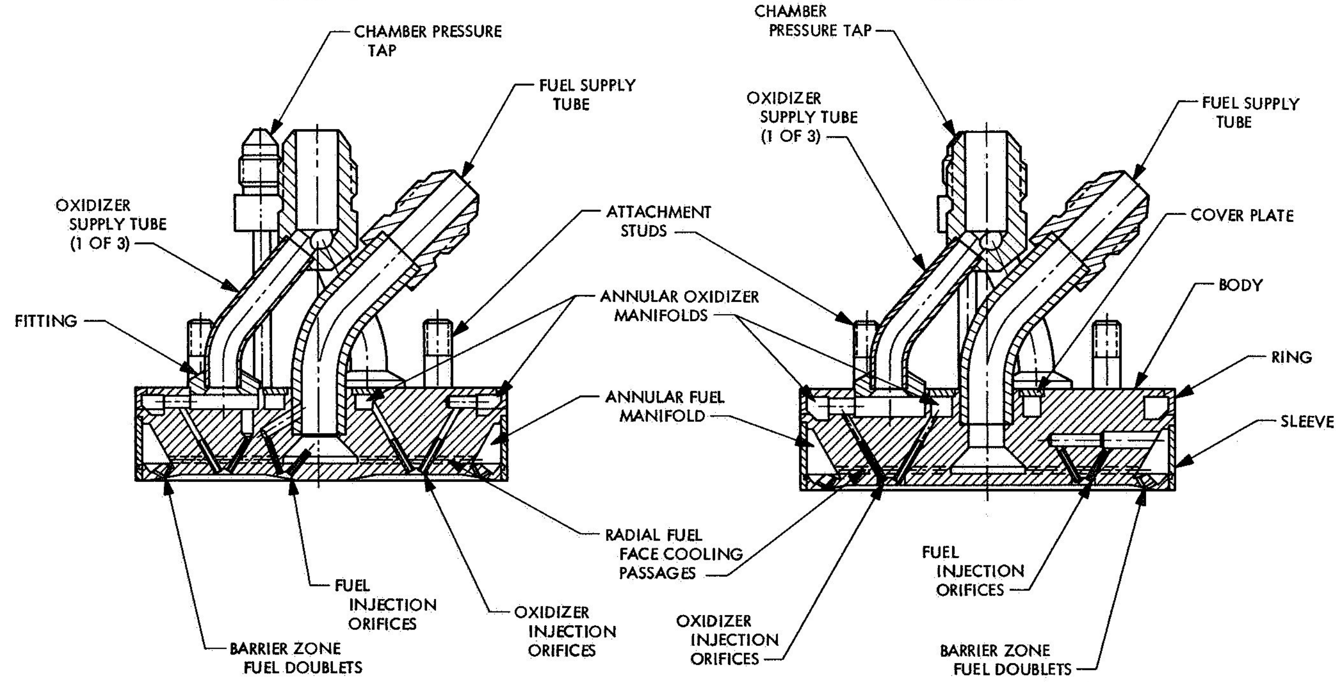

Fig. 4. Manifolding of 200-lbf impinging-jet injectors

XVII. Tracking and Orbit Determination

MISSION ANALYSIS DIVISION

A. Analytic Expressions for the Partial Derivatives of Observables with Respect to the Robertson's Relativistic Parameters, *R. M. Georgevic*

1. Introduction

The geocentric position vector of the spacecraft is given by

$$\boldsymbol{\rho} = \mathbf{r} - \mathbf{R}_E \tag{1}$$

where $\mathbf{r}$ and $\mathbf{R}_E$ are heliocentric position vectors of the spacecraft and Earth, respectively. If α, β, and γ are the three parameters in the Robertson general isotropic line element, and α is assumed to be equal to unity (Ref. 1), the partial derivatives of $\boldsymbol{\rho}$ with respect to β and γ will be

$$\frac{\partial \boldsymbol{\rho}}{\partial \beta, \gamma} = \frac{\partial \mathbf{r}}{\partial \beta, \gamma} - \frac{\partial \mathbf{R}_E}{\partial \beta, \gamma} \tag{2}$$

A differentiation of Eq. (1) gives

$$\dot{\boldsymbol{\rho}} = \mathbf{v} - \mathbf{V}_E \tag{3}$$

where $\mathbf{v}$ and $\mathbf{V}_E$ are velocity vectors of the spacecraft and the Earth, respectively. From Eq. (3) we can write

$$\frac{\partial \dot{\boldsymbol{\rho}}}{\partial \beta, \gamma} = \frac{\partial \mathbf{v}}{\partial \beta, \gamma} - \frac{\partial \mathbf{V}_E}{\partial \beta, \gamma} \tag{4}$$

From $\rho^2 = \boldsymbol{\rho} \cdot \boldsymbol{\rho}$ and $\rho\dot{\rho} = \boldsymbol{\rho} \cdot \dot{\boldsymbol{\rho}}$, it follows that

$$\left.\begin{aligned} \frac{\partial \rho}{\partial \beta, \gamma} &= \frac{\boldsymbol{\rho}}{\rho} \cdot \left(\frac{\partial \mathbf{r}}{\partial \beta, \gamma} - \frac{\partial \mathbf{R}_E}{\partial \beta, \gamma} \right) \\ \frac{\partial \dot{\rho}}{\partial \beta, \gamma} &= \frac{\mathbf{R}}{\rho} \cdot \left(\frac{\partial \mathbf{r}}{\partial \beta, \gamma} - \frac{\partial \mathbf{R}_E}{\partial \beta, \gamma} \right) + \frac{\boldsymbol{\rho}}{\rho} \cdot \left(\frac{\partial \mathbf{v}}{\partial \beta, \gamma} - \frac{\partial \mathbf{V}_E}{\partial \beta, \gamma} \right) \end{aligned}\right\} \tag{5}$$

where

$$\mathbf{R} = \dot{\boldsymbol{\rho}} - \frac{\dot{\rho}}{\rho} \boldsymbol{\rho} \tag{6}$$

Now let X, Y, Z and X_E, Y_E, Z_E be the heliocentric inertial equatorial rectangular coordinates of the spacecraft and of the Earth, respectively, and x and y be the coordinates of the spacecraft in the orbital plane

$$x = r \cos \theta, \qquad y = r \sin \theta \tag{7}$$

where

$$\theta = f + \omega \tag{8}$$

is its true orbital longitude. Here, f is the true anomaly and ω is the argument of periapsis of the instantaneous osculating conic.

Let **S** and **T** be the two unit vectors in the orbital plane, **S** directed toward the ascending node of the plane and **T** forming a right-oriented triad with **S** and the angular momentum vector. Then

$$\begin{bmatrix} X \\ Y \\ Z \end{bmatrix} = \begin{bmatrix} S_X & T_X \\ S_Y & T_Y \\ S_Z & T_Z \end{bmatrix} \begin{bmatrix} x \\ y \end{bmatrix} = [A] \begin{bmatrix} x \\ y \end{bmatrix} \tag{9}$$

where, if i is the inclination of the orbital plane to the equatorial plane and Ω the right ascension of the ascending node, we have

$$\begin{aligned} S_X &= \cos\Omega & T_X &= \sin\Omega \\ S_Y &= -\sin\Omega\cos i & T_Y &= \cos\Omega\cos i \\ S_Z &= 0 & T_Z &= \sin i \end{aligned}$$

Denoting by ξ, η, ζ the geocentric equatorial rectangular coordinates of the spacecraft,

$$\xi = X - X_E, \qquad \eta = Y - Y_E, \qquad \zeta = Z - Z_E$$

we can write from Eq. (5),

$$\frac{\partial\rho}{\partial\beta,\gamma} = \frac{1}{\rho}[\xi \;\; \eta \;\; \zeta] \begin{bmatrix} \dfrac{\partial X}{\partial\beta,\gamma} - \dfrac{\partial X_E}{\partial\beta,\gamma} \\[2ex] \dfrac{\partial Y}{\partial\beta,\gamma} - \dfrac{\partial Y_E}{\partial\beta,\gamma} \\[2ex] \dfrac{\partial Z}{\partial\beta,\gamma} - \dfrac{\partial Z_E}{\partial\beta,\gamma} \end{bmatrix} \tag{10a}$$

$$\frac{\partial\dot\rho}{\partial\beta,\gamma} = \frac{1}{\rho}\left\{[\xi_1 \;\; \eta_1 \;\; \zeta_1] \begin{bmatrix} \dfrac{\partial X}{\partial\beta,\gamma} - \dfrac{\partial X_E}{\partial\beta,\gamma} \\[2ex] \dfrac{\partial Y}{\partial\beta,\gamma} - \dfrac{\partial Y_E}{\partial\beta,\gamma} \\[2ex] \dfrac{\partial Z}{\partial\beta,\gamma} - \dfrac{\partial Z_E}{\partial\beta,\gamma} \end{bmatrix} + [\xi \;\; \eta \;\; \zeta] \begin{bmatrix} \dfrac{\partial \dot X}{\partial\beta,\gamma} - \dfrac{\partial \dot X_E}{\partial\beta,\gamma} \\[2ex] \dfrac{\partial \dot Y}{\partial\beta,\gamma} - \dfrac{\partial \dot Y_E}{\partial\beta,\gamma} \\[2ex] \dfrac{\partial \dot Z}{\partial\beta,\gamma} - \dfrac{\partial \dot Z_E}{\partial\beta,\gamma} \end{bmatrix}\right\} \tag{10b}$$

where

$$\xi_1 = \dot\xi - \frac{\dot\rho}{\rho}\xi, \qquad \eta_1 = \dot\eta - \frac{\dot\rho}{\rho}\eta, \qquad \zeta_1 = \dot\zeta - \frac{\dot\rho}{\rho}\zeta \tag{11}$$

2. Partial Derivatives of Equatorial Coordinates

Since the motion of the spacecraft is planar, the unit vectors **S** and **T** do not change. Therefore, from Eq. (9) and

$$\begin{bmatrix} \dot X \\ \dot Y \\ \dot Z \end{bmatrix} = \begin{bmatrix} S_X & T_X \\ S_Y & T_Y \\ S_Z & T_Z \end{bmatrix} \begin{bmatrix} \dot x \\ \dot y \end{bmatrix} = [A] \begin{bmatrix} \dot x \\ \dot y \end{bmatrix} \tag{12}$$

we can derive, by differentiation

$$\begin{bmatrix} \dfrac{\partial X}{\partial\beta,\gamma} \\[2ex] \dfrac{\partial Y}{\partial\beta,\gamma} \\[2ex] \dfrac{\partial Z}{\partial\beta,\gamma} \end{bmatrix} = [A] \begin{bmatrix} \dfrac{\partial x}{\partial\beta,\gamma} \\[2ex] \dfrac{\partial y}{\partial\beta,\gamma} \end{bmatrix}, \qquad \begin{bmatrix} \dfrac{\partial \dot X}{\partial\beta,\gamma} \\[2ex] \dfrac{\partial \dot Y}{\partial\beta,\gamma} \\[2ex] \dfrac{\partial \dot Z}{\partial\beta,\gamma} \end{bmatrix} = [A] \begin{bmatrix} \dfrac{\partial \dot x}{\partial\beta,\gamma} \\[2ex] \dfrac{\partial \dot y}{\partial\beta,\gamma} \end{bmatrix} \tag{13}$$

for the spacecraft, and

$$\begin{bmatrix} \dfrac{\partial X_E}{\partial\beta,\gamma} \\[2ex] \dfrac{\partial Y_E}{\partial\beta,\gamma} \\[2ex] \dfrac{\partial Z_E}{\partial\beta,\gamma} \end{bmatrix} = [A_E] \begin{bmatrix} \dfrac{\partial x_E}{\partial\beta,\gamma} \\[2ex] \dfrac{\partial y_E}{\partial\beta,\gamma} \end{bmatrix}, \qquad \begin{bmatrix} \dfrac{\partial \dot X_E}{\partial\beta,\gamma} \\[2ex] \dfrac{\partial \dot Y_E}{\partial\beta,\gamma} \\[2ex] \dfrac{\partial \dot Z_E}{\partial\beta,\gamma} \end{bmatrix} = [A_E] \begin{bmatrix} \dfrac{\partial \dot x_E}{\partial\beta,\gamma} \\[2ex] \dfrac{\partial \dot y_E}{\partial\beta,\gamma} \end{bmatrix} \tag{14}$$

for the Earth, where, because of $i_E = \epsilon$ (obliquity of the ecliptic), and $\Omega_E = 0$, the transformation matrix becomes

$$[A_E] = \begin{bmatrix} 1 & 0 \\ 0 & \cos\epsilon \\ 0 & \sin\epsilon \end{bmatrix} \tag{15}$$

From Eq. (7) and

$$\dot x = \dot r\cos\theta - r\dot\theta\sin\theta, \qquad \dot y = \dot r\sin\theta + r\dot\theta\cos\theta \tag{16}$$

we obtain, by differentiation with respect to β and γ,

$$\begin{bmatrix} \dfrac{\partial x}{\partial \beta, \gamma} \\[2ex] \dfrac{\partial y}{\partial \beta, \gamma} \end{bmatrix} = [T] \begin{bmatrix} \dfrac{\partial r}{\partial \beta, \gamma} \\[2ex] r \dfrac{\partial \theta}{\partial \beta, \gamma} \end{bmatrix}, \qquad \begin{bmatrix} \dfrac{\partial \dot{x}}{\partial \beta, \gamma} \\[2ex] \dfrac{\partial \dot{y}}{\partial \beta, \gamma} \end{bmatrix} = [T] \begin{bmatrix} \dfrac{\partial \dot{r}}{\partial \beta, \gamma} - r\dot{\theta} \dfrac{\partial \theta}{\partial \beta, \gamma} \\[2ex] \dot{r} \dfrac{\partial \theta}{\partial \beta, \gamma} + \dfrac{\partial (r\dot{\theta})}{\partial \beta, \gamma} \end{bmatrix} \tag{17}$$

for the spacecraft, and

$$\begin{bmatrix} \dfrac{\partial x_E}{\partial \beta, \gamma} \\[2ex] \dfrac{\partial y_E}{\partial \beta, \gamma} \end{bmatrix} = [T_E] \begin{bmatrix} \dfrac{\partial r_E}{\partial \beta, \gamma} \\[2ex] r_E \dfrac{\partial \theta_E}{\partial \beta, \gamma} \end{bmatrix}, \qquad \begin{bmatrix} \dfrac{\partial \dot{x}_E}{\partial \beta, \gamma} \\[2ex] \dfrac{\partial \dot{y}_E}{\partial \beta, \gamma} \end{bmatrix} = [T_E] \begin{bmatrix} \dfrac{\partial \dot{r}_E}{\partial \beta, \gamma} - r_E\dot{\theta}_E \dfrac{\partial \theta_E}{\partial \beta, \gamma} \\[2ex] \dot{r}_E \dfrac{\partial \theta_E}{\partial \beta, \gamma} + \dfrac{\partial (r_E\dot{\theta}_E)}{\partial \beta, \gamma} \end{bmatrix} \tag{18}$$

for the Earth, where

$$[T] = \begin{bmatrix} \cos\theta & -\sin\theta \\ \sin\theta & \cos\theta \end{bmatrix}, \qquad [T_E] = \begin{bmatrix} \cos\theta_E & -\sin\theta_E \\ \sin\theta_E & \cos\theta_E \end{bmatrix} \tag{19}$$

Here, $\theta_E = f_E + \omega_E$ is the true orbital longitude of the Earth.

The expressions for the relativistic effects on the radial distance and true orbital longitude of the spacecraft and their derivatives are[1]

$$\left.\begin{aligned} \delta r &= \frac{r}{a}\,\delta a - a\cos f\,\delta e + \frac{a^2 e}{b}\sin f\,\delta M \\ \delta\theta &= \frac{a}{p}\left(1 + \frac{p}{r}\right)\sin f\,\delta e + \frac{ab}{r^2}\,\delta M + \delta\omega \\ \delta\dot{r} &= -\frac{nae}{2b}\sin f\,\delta a + nb\left(\frac{a}{r}\right)^2 \sin f\,\delta e + nae\left(\frac{a}{r}\right)^2 \cos f\,\delta M \\ \delta\dot{\theta} &= -\frac{3nb}{2r^2}\,\delta a + \frac{na^3}{r^2 b}\left(2\frac{p}{r}\cos f - e\right)\delta e - 2ne\left(\frac{a}{r}\right)^3 \sin f\,\delta M \end{aligned}\right\} \tag{20}$$

where b is the semiminor axis of the osculating conic. Here $\delta r = r - r^*$; $\delta\theta = \theta - \theta^*$; $\delta\dot{r} = \dot{r} - \dot{r}^*$; $\delta\dot{\theta} = \dot{\theta} - \dot{\theta}^*$; $\delta a = a - a_0$; $\delta e = e - e_0$; $\delta M = M - M^*$; $\delta\omega = \omega - \omega_0$; r^*, θ^*, and M^* are the heliocentric distance, true orbital longitude, and mean anomaly of the position in the initial osculating conic at any arbitrary time t, and a_0, e_0, ω_0 are the remaining three orbital parameters of the same initial osculating conic. Since r^*, θ^* and their derivitives do not depend on either

---

[1] Georgevic, R. M., *Relativistic Effects in the Heliocentric Distance, Radial Velocity and Orbital Longitude of a Spacecraft Moving in the Gravitational Field of the Sun,* Nov. 25, 1969 (JPL internal document).

β or γ (as is also the case for a_0, e_0, and ω_0), we can write

$$\left.\begin{aligned}
\frac{\partial r}{\partial \beta, \gamma} &= \frac{r}{a} \frac{\partial (\delta a)}{\partial \beta, \gamma} - a \cos f \frac{\partial (\delta e)}{\partial \beta, \gamma} + \frac{a^2 e}{b} \sin f \frac{\partial (\delta M)}{\partial \beta, \gamma} \\
\frac{\partial \theta}{\partial \beta, \gamma} &= \frac{a}{p} \left(1 + \frac{p}{r}\right) \sin f \frac{\partial (\delta e)}{\partial \beta, \gamma} + \frac{ab}{r^2} \frac{\partial (\delta M)}{\partial \beta, \gamma} + \frac{\partial (\delta \omega)}{\partial \beta, \gamma} \\
\frac{\partial \dot{r}}{\partial \beta, \gamma} &= -\frac{nae}{2b} \sin f \frac{\partial (\delta a)}{\partial \beta, \gamma} + nb \left(\frac{a}{r}\right)^2 \sin f \frac{\partial (\delta e)}{\partial \beta, \gamma} + nae \left(\frac{a}{r}\right)^2 \cos f \frac{\partial (\delta M)}{\partial \beta, \gamma} \\
\frac{\partial \dot{\theta}}{\partial \beta, \gamma} &= -\frac{3nb}{2r^2} \frac{\partial (\delta a)}{\partial \beta, \gamma} + \frac{na^3}{r^2 b} \left(2 \frac{p}{r} \cos f - e\right) \frac{\partial (\delta e)}{\partial \beta, \gamma} - 2ne \left(\frac{a}{r}\right)^3 \sin f \frac{\partial (\delta M)}{\partial \beta, \gamma}
\end{aligned}\right\} \tag{21}$$

where n is the mean motion in the osculating conic.

Time variations of the instantaneous osculating orbital parameters, δa, δe, δM and $\delta \omega$ for the Robertson's relativistic line element, were derived in SPS 37-56, Vol. III.[2] They are

$$\delta a = -2m \frac{a^2 e}{p} \{[2(1 + e^2) + 2\beta + (3 + e^2)\gamma] \Delta (\cos f) + (2 + \beta + 2\gamma) \Delta (\cos^2 f)\}$$

$$\delta e = -\frac{m}{p} \{[4e^2 + 2\beta + (1 + 3e^2)\gamma] \Delta (\cos f) + (2 + \beta + 2\gamma) \Delta (\cos^2 f)\}$$

$$\delta \omega = \frac{m}{p} \left[(2 - \beta + 2\gamma) \Delta f - \frac{2\beta + (1 - e^2)\gamma}{e} \Delta (\sin f) - (2 + \beta + 2\gamma) \Delta (\sin f \cos f) \right]$$

$$\begin{aligned}
\delta M = -\frac{3ma}{p^2} \Big\{ & 2e^2 + \beta + (1 + e^2)\gamma + [2(1 + e^2) + 2\beta + (3 + e^2)\gamma] e \cos f_0 \\
& + (2 + \beta + 2\gamma) \frac{e^2}{2} \cos^2 f_0 \Big\} \Delta M - \frac{m}{a} (2 + \gamma) \Delta E \\
& + \frac{m}{b} \left[\frac{4e^2 + 2\beta + (1 + 3e^2)\gamma}{e} \Delta (\sin f) + (2 + \beta + 2\gamma) \Delta (\sin f \cos f) \right]
\end{aligned}$$

where E is the eccentric anomaly $m = GS/c^2$ and $\Delta M = M - M_0$, $\Delta f = f - f_0$, $\Delta E = E - E_0$, $\Delta (\sin f) = \sin f - \sin f_0$, $\Delta (\cos f) = \cos f - \cos f_0$, $\Delta (\sin f \cos f) = \sin f \cos f - \sin f_0 \cos f_0$, $\Delta (\cos^2 f) = \cos^2 f - \cos^2 f_0$

---

[2] Georgevic, R. M., *Relativistic Effects on the Motion of a Spacecraft in the Gravitational Field of the Sun*, SPS 37-56, Vol. III, pp. 8–15. Jet Propulsion Laboratory, Pasadena, Calif., Apr. 30, 1969.

The partial derivatives with respect to β and γ are then

$$\left.\begin{aligned}
\frac{\partial(\delta a)}{\partial\beta} &= (DAB) = -2me\left(\frac{a}{p}\right)^2 F_1 \\
\frac{\partial(\delta e)}{\partial\beta} &= (DEB) = -\frac{m}{p}F_1 \\
\frac{\partial(\delta\omega)}{\partial\beta} &= (DWB) = -\frac{m}{p}\left(\Delta f + \frac{F_2}{e}\right) \\
\frac{\partial(\delta M)}{\partial\beta} &= (DMB) = -3\frac{ma}{p^2}H\Delta M + \frac{m}{b}\frac{F_2}{e} \\
\frac{\partial(\delta a)}{\partial\gamma} &= (DAG) = -2me\frac{a}{p}\left[\frac{a}{p}G_1 + 2\Delta(\cos f)\right] \\
\frac{\partial(\delta e)}{\partial\gamma} &= (DEG) = -\frac{m}{p}G_1 \\
\frac{\partial(\delta\omega)}{\partial\gamma} &= (DWG) = \frac{m}{p}\left[2\Delta f - \frac{G_2}{e} + 4e\Delta(\sin f)\right] \\
\frac{\partial(\delta M)}{\partial\gamma} &= (DMG) = -3\frac{ma}{p^2}K\Delta M - \frac{m}{a}\Delta E + \frac{m}{b}\frac{G_2}{e}
\end{aligned}\right\} \tag{22}$$

where

$$H = 1 + 2e\cos f_0 + \frac{e^2}{2}\cos^2 f_0$$

$$K = 1 + e^2 + (3 + e^2)\,e\cos f_0 + e^2\cos^2 f_0$$

$$F_1 = 2\Delta(\cos f) + e\Delta(\cos^2 f)$$

$$F_2 = 2\Delta(\sin f) + e\Delta(\sin f\cos f)$$

$$G_1 = (1 + 3e^2)\,\Delta(\cos f) + 2e\Delta(\cos^2 f)$$

$$G_2 = (1 + 3e^2)\,\Delta(\sin f) + 2e\Delta(\sin f\cos f)$$

The formulae for the partial derivatives of the Earth's motion with respect to β and γ are given by Eq. (22), but with the orbital parameters a, e, ω, and M replaced by the values for the earth's orbit a_E, e_E, ω_E, and M_E. Denote these partials by

$$\frac{\partial(\delta a_E)}{\partial\beta} = (DABE), \frac{\partial(\delta e_E)}{\partial\beta} = (DEBE), \frac{\partial(\delta\omega_E)}{\partial\beta} = (DWBE), \frac{\partial(\delta M_E)}{\partial\beta} = (DMBE),$$

$$\frac{\partial(\delta a_E)}{\partial\gamma} = (DAGE), \frac{\partial(\delta e_E)}{\partial\gamma} = (DEGE), \frac{\partial(\delta\omega_E)}{\partial\gamma} = (DWGE), \frac{\partial(\delta M_E)}{\partial\gamma} = (DMGE)$$

Using Eq. (21), we can write

$$\left.\begin{aligned} \frac{\partial \dot{r}}{\partial \beta, \gamma} - r\dot{\theta}\frac{\partial \theta}{\partial \beta, \gamma} &= -\frac{nae}{2b}\sin f\frac{\partial(\delta a)}{\partial \beta, \gamma} - \frac{na^3}{br}\sin f\frac{\partial(\delta e)}{\partial \beta, \gamma} - \frac{na^3}{r^2}\frac{\partial(\delta M)}{\partial \beta, \gamma} - \frac{nab}{r}\frac{\partial(\delta\omega)}{\partial \beta, \gamma} \\ \dot{r}\frac{\partial \theta}{\partial \beta, \gamma} + \frac{\partial(r\dot{\theta})}{\partial \beta, \gamma} &= -\frac{nb}{2r}\frac{\partial(\delta a)}{\partial \beta, \gamma} + \frac{na^2b}{p^2}(e + \cos f)\frac{\partial(\delta e)}{\partial \beta, \gamma} + \frac{na^2e}{b}\sin f\frac{\partial(\delta\omega)}{\partial \beta, \gamma} \end{aligned}\right\} \tag{23}$$

and, similarly, two expressions for the Earth. Denoting by

$$[\Phi] = [\phi_{ij}], \qquad [\Psi] = [\psi_{ij}] \tag{24}$$

where

$$\left.\begin{aligned} &\phi_{11} = \frac{r}{a}, \phi_{12} = -a\cos f, \phi_{13} = 0, \phi_{14} = \frac{a^2e}{b}\sin f, \\ &\phi_{21} = 0, \phi_{22} = a\left(1 + \frac{r}{p}\right)\sin f, \phi_{23} = r, \phi_{24} = \frac{ab}{r}, \\ &\psi_{11} = -\frac{nae}{2b}\sin f, \psi_{12} = -\frac{na^3}{br}\sin f, \psi_{13} = -\frac{nab}{r}, \psi_{14} = -\frac{na^3}{r^2}, \\ &\psi_{21} = -\frac{nb}{2r}, \psi_{22} = \frac{na^2b}{p^2}(e + \cos f), \psi_{23} = \frac{na^2e}{b}\sin f, \psi_{24} = 0 \end{aligned}\right\} \tag{25}$$

Eqs. (17) and (18) become

$$\begin{bmatrix} \dfrac{\partial x}{\partial \beta} \\[2ex] \dfrac{\partial y}{\partial \beta} \end{bmatrix} = [T]\,[\Phi]\begin{bmatrix} (DAB) \\ (DEB) \\ (DWB) \\ (DMB) \end{bmatrix}, \qquad \begin{bmatrix} \dfrac{\partial x}{\partial \gamma} \\[2ex] \dfrac{\partial y}{\partial \gamma} \end{bmatrix} = [T]\,[\Phi]\begin{bmatrix} (DAG) \\ (DEG) \\ (DWG) \\ (DMG) \end{bmatrix},$$

$$\begin{bmatrix} \dfrac{\partial x_E}{\partial \beta} \\[2ex] \dfrac{\partial y_E}{\partial \beta} \end{bmatrix} = [T_E]\,[\Phi_E]\begin{bmatrix} (DABE) \\ (DEBE) \\ (DWBE) \\ (DMBE) \end{bmatrix}, \qquad \begin{bmatrix} \dfrac{\partial x_E}{\partial \gamma} \\[2ex] \dfrac{\partial y_E}{\partial \gamma} \end{bmatrix} = [T_E]\,[\Phi_E]\begin{bmatrix} (DAGE) \\ (DEGE) \\ (DWGE) \\ (DMGE) \end{bmatrix},$$

$$\begin{bmatrix} \dfrac{\partial \dot{x}}{\partial \beta} \\[2ex] \dfrac{\partial \dot{y}}{\partial \beta} \end{bmatrix} = [T]\,[\Psi]\begin{bmatrix} (DAB) \\ (DEB) \\ (DWB) \\ (DMB) \end{bmatrix}, \qquad \begin{bmatrix} \dfrac{\partial \dot{x}}{\partial \gamma} \\[2ex] \dfrac{\partial \dot{y}}{\partial \gamma} \end{bmatrix} = [T]\,[\Psi]\begin{bmatrix} (DAG) \\ (DEG) \\ (DWG) \\ (DMG) \end{bmatrix},$$

$$\begin{bmatrix} \dfrac{\partial \dot{x}_E}{\partial \beta} \\[2ex] \dfrac{\partial \dot{y}_E}{\partial \beta} \end{bmatrix} = [T_E]\,[\Psi_E]\begin{bmatrix} (DABE) \\ (DEBE) \\ (DWBE) \\ (DMBE) \end{bmatrix}, \qquad \begin{bmatrix} \dfrac{\partial \dot{x}_E}{\partial \gamma} \\[2ex] \dfrac{\partial \dot{y}_E}{\partial \gamma} \end{bmatrix} = [T_E]\,[\Psi_E]\begin{bmatrix} (DAGE) \\ (DEGE) \\ (DWGE) \\ (DMGE) \end{bmatrix}$$

Here $[\Phi_E]$ and $[\Psi_E]$ are matrices corresponding to Eq. (24), for the Earth, and can be obtained by substituting a_E, e_E, b_E, p_E, n_E, R_E and f_E into Eq. (25), instead of the values a, e, b, p, n, r and f of the spacecraft's motion.

Finally, we find

$$\left.\begin{aligned} \begin{bmatrix} \dfrac{\partial X}{\partial\beta,\gamma} \\[2mm] \dfrac{\partial Y}{\partial\beta,\gamma} \\[2mm] \dfrac{\partial Z}{\partial\beta,\gamma} \end{bmatrix} &= [A]\,[T]\,[\Phi] \begin{bmatrix} (DAB,G) \\ (DEB,G) \\ (DWB,G) \\ (DMB,G) \end{bmatrix} \\[4mm] \begin{bmatrix} \dfrac{\partial \dot{X}}{\partial\beta,\gamma} \\[2mm] \dfrac{\partial \dot{Y}}{\partial\beta,\gamma} \\[2mm] \dfrac{\partial \dot{Z}}{\partial\beta,\gamma} \end{bmatrix} &= [A]\,[T]\,[\Psi] \begin{bmatrix} (DAB,G) \\ (DEB,G) \\ (DWB,G) \\ (DMB,G) \end{bmatrix} \end{aligned}\right\} \tag{26}$$

and similarly, for the Earth

$$\left.\begin{aligned} \begin{bmatrix} \dfrac{\partial X_E}{\partial\beta,\gamma} \\[2mm] \dfrac{\partial Y_E}{\partial\beta,\gamma} \\[2mm] \dfrac{\partial Z_E}{\partial\beta,\gamma} \end{bmatrix} &= [A_E]\,[T_E]\,[\Phi_E] \begin{bmatrix} (DABE,GE) \\ (DEBE,GE) \\ (DWBE,GE) \\ (DMBE,GE) \end{bmatrix} \\[4mm] \begin{bmatrix} \dfrac{\partial \dot{X}_E}{\partial\beta,\gamma} \\[2mm] \dfrac{\partial \dot{Y}_E}{\partial\beta,\gamma} \\[2mm] \dfrac{\partial \dot{Z}_E}{\partial\beta,\gamma} \end{bmatrix} &= [A_E]\,[T_E]\,[\Psi_E] \begin{bmatrix} (DABE,GE) \\ (DEBE,GE) \\ (DWBE,GE) \\ (DMBE,GE) \end{bmatrix} \end{aligned}\right\} \tag{27}$$

3. Partial Derivatives of Two-Way Range and Doppler

The expression giving the two-way range is[3]

$$c\Delta t = 2\rho + 2m\,(1+\gamma)\ln\left(\frac{r+R_E+\rho}{r+R_E-\rho}\right) \tag{28}$$

The partials of this quantity with respect to β and γ are

$$\left.\begin{aligned} \frac{\partial\,(c\Delta t)}{\partial\beta} &= 2\,\frac{\partial\rho}{\partial\beta} \\ \frac{\partial\,(c\Delta t)}{\partial\gamma} &= 2\,\frac{\partial\rho}{\partial\gamma} + 2m\ln\left(\frac{r+R_E+\rho}{r+R_E-\rho}\right) \end{aligned}\right\} \tag{29}$$

where $\partial\rho/\partial\beta$ and $\partial\rho/\partial\gamma$ are given by Eq. (10a). Equation (28) was originally derived from

$$c\Delta t = 2\rho + 2m(1+\gamma)\int_0^\rho \frac{d\rho}{r}$$

and the differentiation of this expression gives the two-way doppler

$$\frac{d\,(c\Delta t)}{dt} = D = 2\dot{\rho} + 2m\,(1+\gamma)\,\frac{\dot{\rho}}{r}$$

so that the partials of D with respect to β and γ are

$$\left.\begin{aligned} \frac{\partial D}{\partial\beta} &= 2\,\frac{\partial\dot{\rho}}{\partial\beta} \\ \frac{\partial D}{\partial\gamma} &= 2\left(\frac{\partial\dot{\rho}}{\partial\gamma} + m\,\frac{\dot{\rho}}{r}\right) \end{aligned}\right\} \tag{30}$$

where $\partial\dot{\rho}/\partial\beta$ and $\partial\dot{\rho}/\partial\gamma$ are given by Eq. (10b), and

$$\dot{\rho} = \frac{1}{\rho}\,(\mathbf{r}-\mathbf{R}_E)\cdot(\mathbf{v}-\mathbf{V}_E).$$

Reference

1. Robertson, H. P., *Relativity and Cosmology, Space Age Astronomy.* p. 228, The Academic Press, New York, 1962.

---

[3] Anderson, J. D., *Inclusion of General Relativity Theory in the Representation of Spacecraft Tracking Data,* SPS 37-50, Vol. III, pp. 39–47. Jet Propulsion Laboratory, Pasadena, Calif., Apr. 30, 1968.

B. Quantitative Confirmation of Planetary Defects in the Lunar Theory by Spectral Decomposition,

J. D. Mulholland, K. Garthwaite, and D. B. Holdridge

Efforts at improving the JPL lunar ephemeris (LE) have been continuing since early 1966, first by the incorporation of analytical corrections and later by the use of numerical integration techniques. It seemed evident, even in the earliest computer studies (SPS 37-48, Vol. III, pp. 33–39, SPS 37-49, Vol. III, pp. 21–23), that a major part of the difference between numerical integrations and the lunar source theories to which they were fit lay in the planetary perturbations. Clemence (Ref. 1) already had provided an estimate of the magnitude of the series truncation errors in the planetary terms of the Lunar Theory, and the integrations seemed to bear him out. Nonetheless, with only a 2-yr span of integration, it was not possible to perform any meaningful analysis of the residuals, even though one could visually estimate the existence of certain prominent periods that could be identified with planetary terms in the theory.

The lunar motion has now been integrated numerically over a 50-yr interval, coinciding with the standard span of the JPL Ephemeris Tape System. This integration (LE 15) was an intermediate step in the construction of JPL LE 16[1] (Ref. 2), and every possible effort was made to assure that it was consistent with the theory (LE 14) from which source positions were computed (SPS 37-57, Vol. II, pp. 51–53). The half-century of residuals (LE 15–LE 14) provide an adequate base for power spectrum analysis of periods up to at least 1000 days. Such an analysis has now been performed using a computer program written by Lieske, based on his own modification (Ref. 3) of the autocorrelation method described by Southworth (Ref. 4).

The spectral decomposition of the coordinate residuals amply confirms the conclusion that the theory suffers from significant truncation of the planetary perturbation terms. Within the range of periods from 6 to 1000 days, every local maximum of significant size in the spectral power density can be closely related to specific planetary perturbation periods. A few of the more noteworthy ones are summarized in Table 1. Earlier work had raised the expectation that periods around ten days would be in evidence, with arguments like $\ell + 2D + k(T - \text{Planet})$; the spectral analysis disclosed no period in that vicinity that was particularly strong, but there were numerous significant periods in the $9\overset{d}{.}1$–$10\overset{d}{.}6$ range corresponding to such arguments. Very little of any significance was found at shorter periods.

Table 1. Planetary perturbation periods corresponding to features in geocentric distance residuals

Argument[a]	Period, days	Value from analysis
$T - V$	584	585
$-T + 2J$	439	444
$-T + J$	399	400
$2T - 2V$	292	292
$-2T + 2J$	199	199
$4T - 4V$	146	146
$-T + S_n$	37.81	37.85
$-\ell + 2D + 2T - 2V$	35.70	35.71
$-\ell + 2D - T + J$	34.57	34.58
$-D + 4T - 3V$	27.57	27.59
$-16T + 18V$	27.55	27.52
$2\ell + 3T - 3V$	14.82	14.81
$2D - T + V$	14.40	14.41

[a] T = Earth, V = Venus, J = Jupiter, S_n = Saturn, ℓ = Moon, and D = Moon − Sun.

Table 1 is not meant to imply that the coefficients of the listed arguments are in need of revision in the theory. It is much more probable that the discrepancies arise from numerous very small terms whose arguments are closely related to, and whose periods differ only slightly from, those given here. These data appear to establish clearly the importance of truncation in the planetary terms since no features were found to be strongly associated with periods appropriate to the "main problem," which consists of Earth–Moon–Sun only.

References

1. Clemence, G. M., "Remarks on Current Lunar Theory," in *Proceedings of the JPL Seminar on Uncertainties in the Lunar Ephemeris*, Technical Report 32-1247. Edited by J. D. Mulholland. Jet Propulsion Laboratory, Pasadena, Calif., May 1968.
2. O'Handley, D. A., et al., *JPL Development Ephemeris Number 69*, Technical Report 32-1465. Jet Propulsion Laboratory, Pasadena, Calif., Dec. 1969.
3. Lieske, J. H., "On the Secular Change of the Obliquity of the Ecliptic," *Astron. Astrophys.*, Vol. 5, pp. 90–101, 1970.
4. Southworth, R. W., "Autocorrelation and Spectral Analysis," in *Mathematical Methods for Digital Computers: Volume I*. Edited by A. Ralston and H. S. Wilf. John Wiley & Sons, Inc., New York.

---

[1] Garthwaite, K., Holdridge, D. B., and Mulholland, J. D., *A Preliminary Special Perturbation Theory for the Lunar Motion* (to be published).

XVIII. Systems Analysis

MISSION ANALYSIS DIVISION

A. On Forming a Consensus of Individual Preferences or Consolidation of Pecking Orders, *R. G. Chamberlain*

1. Introduction

The problem dealt with in this article is that of combining several individual preference patterns into a single preference pattern for the society composed of those individuals. Luce and Raiffa (Ref. 1) have presented an excellent discussion of the difficulties of this problem. They have, in fact, cited Arrow's (Ref. 2) impossibility theorem, which states that under certain reasonable conditions the problem has no general solution. Later theoretical work (see Fishburn, Ref. 3, for an extensive bibliography) has investigated modifications to those conditions.

This article will not be so ambitious as to try to solve the problem in general. Instead, it is proposed that a social consensus be constructed to reflect all paired comparisons with which no individual disagrees. Construction of such an ordering requires recognition that society does not agree (or does not know) how some of the pairs should be ordered. The resultant consensus is quite general: interpersonal and intrapersonal comparisons of utility, at best difficult to obtain in practice, are not required. Many suggested consensus-forming techniques fail simply because they do not consider these factors.

2. The *Unknown* Relationship

There are three relationships between objects commonly recognized in utility theory: *preference*, *nonpreference*, and *indifference*.[1] Thus, $A >$ (is preferred to) B is true if and only if $B <$ (is not preferred to) A is true and $B \sim$ (is indifferent to) A is false.[2] To form a consensus of the type described earlier, another kind of relationship, *ignorance*, is needed.[3] Let us introduce the question mark to symbolize this relationship. Thus, (preference of) $A\,?$ (is unknown relative to) B if and only if neither a preference nor an indifference relation between A and B has been established. This relationship can also exist between partial orderings.

---

[1] See Ref. 3. The three relations are sometimes defined in terms of each other.

[2] Symbols $>$ and $<$ are used to denote "is preferred to" and "is not preferred to" because the symbols commonly used are not available to the typesetter.

[3] The ignorance relation, insofar as a society is concerned, can come about either by conflict between the preferences of two or more members of the society or by the lack of a stated preference by any member.

3. Symbolic Examples

Consider a society composed of two individuals whose preferences (among vacation spots, kinds of fruit, friends, or what have you) can be represented as follows:

$$\text{1st individual: } A > B > C > D > H$$

$$\text{2nd individual: } B > C > E > F > G > H$$

In this case, the preferences can simply be interleaved to give

$$\text{Society: } A > B > C > [D \mathrel{?} (E > F > G)] > H$$

Addition of a third individual to this society, with preferences

$$\text{3rd individual: } C > D > E$$

can resolve the ambiguity to give the new society a complete ordering:

$$\text{New society: } A > B > C > D > E > F > G > H$$

In the above example, it was merely fortuitous that the third individual simplified society's ordering. Often, addition of individuals will increase the complexity. Consider the following partial orderings:

$$\text{1st individual: } A > B > C > D$$

$$\text{2nd individual: } C > A > B > D$$

The result for this society is

$$\text{Society: } [(A > B) \mathrel{?} C] > D$$

And a third individual with $B > A > D > C$ leads to

$$\text{New society: } A \mathrel{?} B \mathrel{?} C \mathrel{?} D$$

Luce and Raiffa (Ref. 1, p. 337) have presented a particularly troublesome example, as follows:

$$\text{1st individual: } A > B > C > D > E > F > G$$

$$\text{2nd individual: } D > A > G > E > F > B > C$$

In this case, society's consensus is too complicated to express on a single line; although if D were removed, we could write society's preference as

$$A > [(B > C) \mathrel{?} (E > F) \mathrel{?} G]$$

It may be readily represented on a tree structure, however, where a (transitive)[4] arrow represents the (transitive) preference relation, and the absence of an arrow represents the ignorance relation. Thus,

Society:

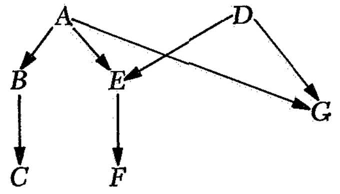

The simpler examples presented earlier can also be represented by trees, of course.

4. Applications

Illustrations of problems to which this concept might be applied follow:

(1) Not all college basketball teams face each other during a season. Yet, a national news service desires to rank the major teams relative to each other. The news service polls a selected group of coaches across the country to obtain a set of individual rankings. Not all of the coaches have opinions on all of the teams, some of the coaches may be better evaluators than others, and, further, the simple rankings do not indicate each coach's feelings about the magnitudes of the differences in ability. How should the news service combine the lists to produce the coaches' consensus?

(2) The president of the PDB Manufacturing Company has decided to expand the company's operations. To what extent do his vice presidents agree on the order in which new locations should be developed?

(3) A new manager wants to get a feel for the overall abilities of the people under him. He asks each of his subordinates to rank their people and his assistants to rank as many of the people that they each know about. What can be deduced from these rankings?

---

[4] A relation R is transitive if and only if $a\,R\,b$ and $b\,R\,c$ imply $a\,R\,c$. Thus, $A > B > C$ (or equivalently on the tree, $A \rightarrow B \rightarrow C$) means $A > B$, $B > C$, and $A > C$.

(4) A management consultant, in the initial stages of studying a new firm, asks each of the division managers to rank a set of likely objectives for the firm in order of importance. What is the consensus?

5. Other Techniques

A number of techniques have been devised to attempt to resolve the problem of combining individual preferences. The two most common of these, majority rule and the method of marks, will be mentioned briefly.

Majority rule assigns a preference for society whenever more individuals have one preference than have the other. One difficulty with this rule is that it can fail to provide a transitive result, as may be seen from the following example.

$$\text{1st individual: } A > B > C$$

$$\text{2nd individual: } B > C > A$$

$$\text{3rd individual: } C > A > B$$

Under majority rule, society's preferences are then

$$\text{Society: } A > B, \text{ and } B > C, \text{ but also } C > A$$

Another difficulty is that individual and interpersonal strengths of preference are ignored. Thus, if in the above example, the first individual greatly prefers *A*, all other preferences are weak, and if the first individual's influence in this society is not negligible, society should probably prefer *A*.

The other common technique, *the method of marks*, is frequently reinvented. The objects on each individual preference list are numbered sequentially; the objects are then scored by adding the resultant numbers; and society's preference is inferred by ranking the objects according to their scores. Even if more information is obtained from each individual, so the intrapersonal differences in utility are reflected in the scores to be added, interpersonal differences are neglected. The resultant scores are likely to be meaningless. Fishburn (Ref. 3, p. 365) notes an example published in 1785 where an object having a simple majority over all other objects cannot get the highest score regardless of the way in which marks are assigned in each individual pattern.

If, in addition, the partial orderings do not contain exactly the same objects, additional problems arise. How are objects missing from any of the lists to be scored? Placement among those in the list must be completely arbitrary—but so is placement at either end.

The real problem with any technique that provides a unique social order for all possible individual profiles is that such a unique order contains more information than the individual profiles. Bounds on interpersonal utilities could be derived from the proposed social order when considered with the partial orders. The partial orders themselves do not contain this information. Hence, such a technique cannot be a tautologic operation.

6. Conclusions

Occasionally, it is desirable to combine orderings from several sources into a single ordering that represents a consensus. Numerical techniques, often suggested, invariably try to produce results that contain more information than is present in the input.

In this article, it is suggested that if the statement, "The data does not specify the consensual relationship between certain objects," is admitted, then it is often possible to present a consensus that contains no more and no less information than can be inferred from the partial orderings.

References

1. Luce, R. D., and Raiffa, H., *Games and Decisions*, Chapter 14. John Wiley & Sons, Inc., New York, 1957.
2. Arrow, K. F., *Social Choice and Individual Values*, Cowles Commission Monograph 12. John Wiley & Sons, Inc., New York, 1951.
3. Fishburn, P. C., "Utility Theory", *Management Science*, Vol. 14, No. 5, pp. 335–378, January 1968.

Subject Index

Subject Index (contd)

NASA — JPL — Coml., L.A., Calif.